ABSTRACT

Title of dissertation: SYNCHRONIZATION OF CHAOTIC LASERS

David James DeShazer, Doctor of Philosophy, 2002

Dissertation directed by: Professor Rajarshi Roy
Department of Physics

Studying the nonlinear aspects and chaotic dynamics of lasers, as well as other systems of scientific and technological interest, allows us to understand the possible advantages they offer and the limits they impose. Of particular interest are the often subtle relationships and synchronous states of coupled chaotic optical systems. This dissertation is the culmination of investigations of nonlinear dynamics and synchronization, and their underlying physical mechanisms, in two solid state laser systems: Nd^{3+}:YAG laser arrays and injected Erbium Doped Fiber Ring Lasers (EDFRL).

Synchronization and chaos are studied in a three element, nearest neighbor coupled Nd^{3+}:YAG laser array. Identical synchronization is found only between the outer lasers of the array, with no clear relationship to the central laser which mediates the interaction. This synchronous state is stable irrespective of the level of external modulation, and is reproduced in numerical simulations. Analysis of

a simple model explains these results and predicts the observed anti-phase locked state of the Nd^{3+}:YAG laser array and the embedding dimension of its dynamics.

More refined analysis utilizing the concept of phase synchronization is required to uncover the relationship of the central and outer lasers. Frequency filtered phase variables are computed from the array's intensity time series. The frequency resolution provided by the phase definition permits the identification of frequency regimes and ratios of phase synchronization.

Giant intensity bursts, with a broad distribution of burst times and amplitudes, are induced in erbium doped fiber ring lasers by weak matched optical injection. This is in sharp contrast to the usual stabilizing effect of tuned injection. Time resolved heterodyne experiments reveal that the EDFRL modes wander over a range of MHz, leading to intermittent interactions with the injected optical signal, and the observed intensity bursts. A phenomenological model of the injected laser system qualitatively and quantitatively reproduces the bursting dynamics and their observed statistics.

Modulating the injection signal with unbiased noise induces burst synchronization of two matched EDFRLs with common injection. Analysis algorithms are developed to study the burst dynamics while neglecting their component fast fluctuations. Quantitative analysis shows a sharp transition to the synchronized state with increasing modulation.

SYNCHRONIZATION OF CHAOTIC LASERS

by

David James DeShazer

Dissertation submitted to the Faculty of the Graduate School of the
University of Maryland, College Park in partial fulfillment
of the requirements for the degree of
Doctor of Philosophy
2002

Advisory Commmittee:

Professor Rajarshi Roy, Chair/Advisor
Professor Edward Ott
Professor Daniel P. Lathrop
Professor Howard Milchberg
Professor Christopher Davis

Acknowledgments

The completion of my doctoral studies and this dissertation is a milestone I would not have been able to reach without the inspiration and support of many people. First and foremost I thank those who've known me the longest and have had the most influence on my life, my family. The love, guidance, support and friendship my parents, James and Alice DeShazer, and my sister Jean have given me over the years has made so many things in my life possible.

Much appreciation is owed to my Ph.D. advisory committee members, Dr. Rajarshi Roy, Dr. Edward Ott, Dr. Daniel Lathrop, Dr. Howard Milchberg and Dr. Christopher Davis. Dr. Lathrop, Dr. Ott and most especially my advisor Dr. Roy deserve special thanks for all the guidance they've given me. Thank you Raj for all the years you've been my mentor, and the patience and inspiration you've given me.

This dissertation was possible only through the efforts of many talented researchers I've had the pleasure and privilege of working with. Most notably, Dr. Roy and Dr. Ott have lent their considerable talents to many portions of this research. Additionally, I thank Dr. K. Scott Thornburg and Dr. Gregory VanWiggeren for their introductions to the experimental systems and many dynamic principles utilized in this research. Dr. John Terry also deserves recognition for his inspired contributions to this research and his continued friendship. The successes that have been achieved during my tenure are grounded in our time together at Georgia Tech.

Fruitful collaborations were found at the University of Maryland College Park as well. I thank Romulus Breban, Brian Tighe, Dr. Jürgen Kurths, and Dr. Jordi

García-Ojalvo for many hours of work and the insight they brought to these studies. I have great hopes for new discoveries and developments as Beth Rogers continues studying nonlinear dynamics in fiber lasers, and thank her for her work over the past several months.

I thank the other members of Dr. Roy's research group, Ryan McAllister, Bhaskar Khubchandani, Wing-Shun Lam, Christian Silva, Ming-Young Kim, and Beth Rogers for all of the insight, support, perspective, and most importantly. friendship they've given me over the past few years. Additionally, I thank alumni of the group, Dr. Larry Fabiny, Dr. Quinton Williams, Dr. Darlene Hart, and Dr. George Gray in addition to Dr. K. Scott Thornburg and Dr. Gregory VanWiggeren who provided the solid scientific foundations of upon which this dissertation was based.

Finally I thank all of my professors, family, fellow students, friends, workout partners, hiking buddies etc. who've helped keep me grounded throughout graduate school and in life. I look forward to many more years of friendship as I move on to the next phase of my life.

DAVID J. DeSHAZER

University of Maryland College Park

October 2002

TABLE OF CONTENTS

LIST OF FIGURES

LIST OF TABLES

Chapter 1

Introduction

1.1 Nonlinear Dynamics, Lasers and Synchronization

The common practice of viewing systems of scientific and technological interest as linear and well behaved while avoiding nonlinear regimes allows for easy analysis and application. However, most systems in physics, chemistry, communications, biology and many other disciplines are inherently nonlinear. In fact, classifying nonlinear dynamics as a subfield of science has been likened to classifying the study of non-elephant animals as a subfield of zoology. Studying the nonlinear aspects of lasers, as well as other systems of scientific interest, allows us to understand the possible advantages they offer and the limits they impose. If we do not pursue this understanding we are confining ourselves to a narrow view of the universe with similarly limited possibilities.

A traditional, colloquial interpretation relates chaos to random systems without any aspect of order. However, chaos as studied in physics, math and other disciplines describes deterministic systems that display aperiodic dynamics and a sensitivity to initial conditions and perturbations. So, there is order in chaos, it is just very subtle. Often, understandin the dynamics of a chaotic system is only possible using sophisticated analytic methods. Excellent texts on chaos and nonlinear dynamics include Refs. [1, 2], and various tools for studying chaotic time series are discussed in Refs. [3, 4].

Lasers are particularly rich dynamic systems that, in the proper parameter regimes, display chaotic dynamics. Since their first description in 1958 by Schawlow and Townes [5], and Maiman's demonstration of the ruby laser in 1960 [6] lasers have garnered significant attention thanks to their many scientific and technological applications . Studying laser dynamics is one avenue to gaining a better understanding of the fundamental physics behind lasers, as well as interactions of electromagnetic fields, and the interaction of light and matter. Useful texts on optical and laser systems include Refs. [7, 8, 9, 10]. Nonlinear dynamics in optical systems are addressed in Refs. [11, 12, 13]. In addition, studying chaos in lasers systems allows us to address, by analogy, the behavior of other complex dynamic systems which may not be experimentally accessible. Beyond determining the boundaries of chaos in laser systems so as to avoid the chaotic regions in linear applications, a deeper understanding of the laser systems allows for the development of applications that depend on the nonlinear nature of the system. An example is using the chaotic fluctuations of an erbium doped fiber ring laser to mask messages [14].

Using chaos to transmit information requires the synchronization of chaotic systems. Synchronization is a fundamental aspect of many systems of technological and scientific interest such as neural networks, chemical oscillators, computer and communication networks, astronomical phenomena, and of course lasers. Synchronization of chaos is a surprising, counterintuitive result due the parameter sensitive and aperiodic nature of chaos. Like chaos itself, synchronization of chaotic systems is often rather subtle and may manifest itself in various weak forms beyond the fa-

miliar identical synchronization. A review of chaotic synchronization is supplied by Refs. [15, 16]. Identifying synchronization in chaotic systems often requires sophisticated detection algorithms. The development and application of such algorithms and synchronization measures is a central aspect of this dissertation.

1.2 Dissertation Organization

This dissertation, made possible by the efforts of many talented researchers and collaborators, details experiments designed to study the nonlinear dynamics and synchronization properties of laser systems. During the course of this research, several surprising dynamical and synchronization regimes were discovered. Using the analytic tools mentioned above, including those developed as a part of this research, we investigate dynamic transitions in, and relationships between chaotic lasers. In this fashion, we were able to uncover dynamical relationships previously experimentally unavailable. While this dissertation is primarily experimental, the physical mechanisms responsible for the dynamics and relationships observed are investigated analytically and numerically, as well as experimentally.

The following two chapters provide introductions to chaotic dynamics and the experimental systems used in this research. Chapter 2 provides an introduction to chaos, including routes to chaos (Sec. 2.1.1) and the synchronization of chaotic dynamics (Sec. 2.2). Lasers and nonlinear dynamics in lasers are reviewed in Chapter 3. A basic derivation of the semiclassical Maxwell-Bloch equations is provided (Sec. 3.1), and their equivalence to the chaotic Lorenz system is noted (Sec. 3.2). The Arecchi classification scheme, which categorizes laser systems by their dynamics, is presented in Section 3.3. The laser systems studied are presented in Section 3.4, neodymium doped yttrium aluminum garnet (Nd:YAG), and Section 3.5, erbium doped fiber ring lasers (EDFRL).

Solid state laser arrays are introduced in the first section of Chapter 4. Studying chaos in a three Nd:YAG laser array described in Section 4.2, we find a surprising

synchronized state where the outer lasers of the array are identically matched and have no clear relation to the central laser that mediates the interaction [17]. Analysis of the laser model in Section 4.4 explains the stability of this synchronized state, and numerical simulations of the model in Section 4.5 show strong agreement with experimental observation.

Despite the strong agreement between experiment and theory, the dynamic relationship between the side and central lasers is unclear. Only by studying the system from the perspective of phase synchronization, a weak form of synchronization, using frequency filtered phase definitions and synchronization measures developed as part of this research, are we able to complete the picture of the relationships between the laser array elements (Section 5.2) [18, 19].

The discovery of the surprising phenomena of giant bursting dynamics induced by a weak, optical frequency-matched injection signal is presented in Chapter 6, Section 2 [20]. The physical origins of the bursting dynamics are investigated experimentally, finding that the slow wandering of the ring laser modes leads to intermittent interaction with the injection laser and the observed bursting dynamics (Section 6.3). A phenomenological model of the injected laser system is advanced in Section 6.4, and is found to have excellent qualitative and statistical agreement with the experimental dynamics in Section 6.5.

Noise induced burst synchronization in two matched EDFRLs with a common optical injection signal is studied in Chapter 7 [21]. Using data analysis techniques developed as part of this research, the bursting intensity time series is reduced to symbolic dynamics, and a burst synchronization measure is proposed (Sections 7.4-5). Studying burst synchronization as a function of modulation strength we find a sharp transition to burst synchronization.

In Chapter 8 we review the experimental, numerical and analytic results of this dissertation, identify open questions, and suggest numerical and experimental studies to address these questions while continuing to advance our understanding of the nonlinear properties, dynamics and synchronization of chaotic lasers.

Chapter 2

Chaos and Synchronization

2.1 Chaos

The French mathematician Henri Poincaré is often referred to as the founder of the study of chaotic dynamics. Following Newton, generations of mathematicians and physicists had concentrated on using Newton's laws of motion and the concept of universal gravitation to analyze and predict individual orbits in an attempt to solve the analytically intractable three body problem. At the end of the 19^{th} century, Poincaré broke away from this tradition and instead of trying to analyze and predict specific orbits in the solar system, he asked the question of whether or not orbits are necessarily stable. By taking a new approach and analyzing sets of possible initial conditions for a planetary body in the solar system, and discovering the possibility of complex, aperiodic orbits, Poincaré was the first to observe chaotic dynamics [1, 2].

Chaotic dynamics arise from deterministic systems with aperiodic behavior

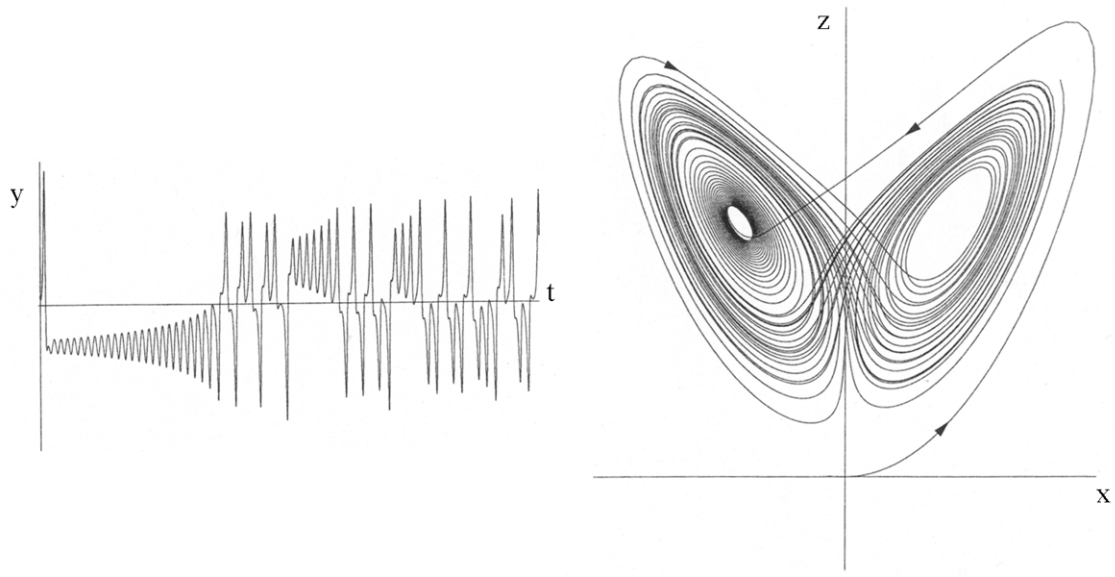

Figure 2.1: The chaotic time series $y(t)$ (left) and the strange attractor (right) resulting from the numerical integration of the Lorenz equations, Eqn. (2.1) with the parameter values $\sigma = 10$, $b = \frac{8}{3}$, and $r = 28$. [2]

that displays a sensitive dependence on initial conditions, exactly the situation that Poincaré studied. In equally famous work, Lorenz studied a simplified model of convection in the atmosphere in an attempt to understand and predict weather patterns. He discovered instead the three dimensional system of equations

$$\begin{aligned} \dot{x} &= \sigma(y - x), \\ \dot{y} &= rx - y - xz, \\ \dot{z} &= xy - bz, \end{aligned} \tag{2.1}$$

which displays chaotic dynamics, and confounded his hopes of improving weather predictions [22, 2]. The Poincaré-Bendixson theorem states that three is the minimum requisite number of dimensions for a dynamic system to display chaotic dynamics [2]. In these equations the over-dot indicates differentiation with respect to time, and σ, r, $b > 0$ are parameters. Choosing the values $\sigma = 10$, $b = \frac{8}{3}$, and $r = 28$ we observe aperiodic motion (left plot of Fig. 2.1), and the famous strange 'butterfly' attractor (right plot Fig. 2.1) [2].

Sensitivity to initial conditions is studied by examining trajectories with nearly identical initial conditions, as Poincaré did. If there is some small deviation between

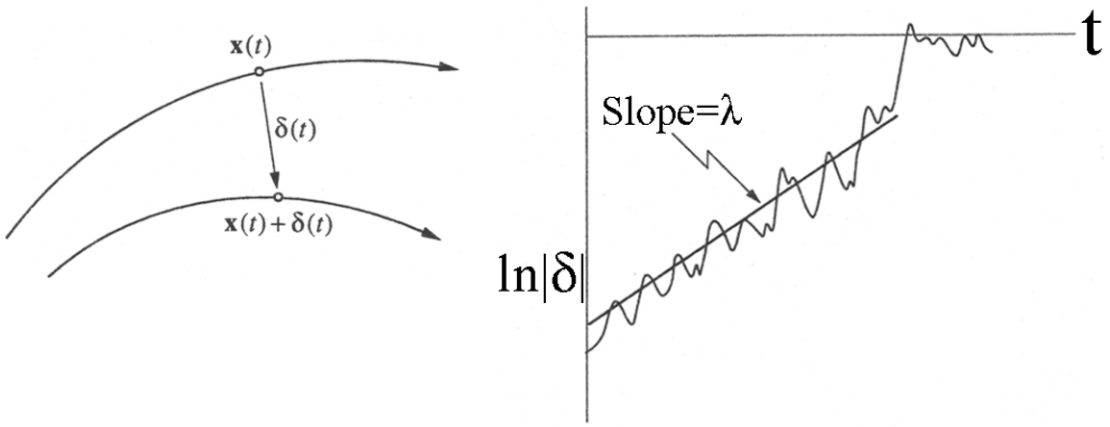

Figure 2.2: The sensitivity to initial conditions is observed by following two identical systems with slightly different initial conditions as they diverge in time (left plot). The exponential growth of $\delta(t)$ is described by the Lyapunov exponent λ, and saturates at a value equivalent to the dimension of the attractor (right plot). [2]

initial conditions $\delta_o = x(o) - x'(0)$ for two identical systems, then in a chaotic system the difference $\delta(t)$ between the two systems will grow in time. In Fig. 2.2, left figure, we see how $x(t)$ in two identical Lorenz systems diverges in time due to this initial discrepancy. Here the initial difference was on the order of $|\delta_o| = 10^{-15}$. It is found that the growth of $\delta(t)$ is exponential and we may characterize this growth with the relation

$$|\delta(t)| \sim |\delta_o| e^{\lambda t}, \tag{2.2}$$

where λ is the Lyapunov exponent and has units of inverse time. Sensitivity to initial conditions is quantified by the Lyapunov exponent [2, 1]. Plotting $ln|\delta|$ as a function of time, we are able to see the exponential growth described by Eqn. (2.2), which then saturates at a value of $|\delta|$ comparable to the size of the attractor, Fig. 2.2 right plot.

We shall continue encountering the Lorenz system throughout this dissertation, as it displays many significant aspects of chaos and often serves as a test system for new ideas. Another nonlinear system of equations that is widely studied in dynamics literature, including this dissertation, is the Rössler system. While its inspiration is perhaps more mundane than the systems studied by Poincaré and Lorenz – the stretching and pulling executed by a taffy pulling machine at a candy store – the

three dimensional Rössler system

$$\begin{aligned} \dot{x} &= -y - z, \\ \dot{y} &= x + ay, \\ \dot{z} &= b + z(x - c), \end{aligned} \tag{2.3}$$

it is perhaps more useful for this simplicity [23]. The only nonlinearity in the system is from the zx term in the third differential equation, allowing for simpler, though still chaotic, dynamics. Here a, b, and c are parameters.

2.1.1 Routes to Chaos

Initially stable systems enter chaotic regimes by various routes, such as series of bifurcations [1, 2, 24], quasiperiodicity [1, 25], and intermittent dynamics [1, 26, 24, 27]. These paths to chaos are not necessarily independent or exclusive of one another. The conditions in which chaos is possible and the routes to chaos are a continuing area of investigation. References [1, 2, 24] review these studies.

A variety of bifurcations have been identified and studied in numerical and experimental systems including Hopf, saddle-node, tangent, and pitchfork or period doubling bifurcations. Here, a smooth shift in a parameter of the system under investigation results in a sudden change in the dynamic nature of the system. The parameter value of this dynamic shift is the bifurcation point. Series of bifurcations may lead to the development of strange attractors and chaotic dynamics. Sometimes a single bifurcation is enough to enter a chaotic regime when the bifurcation destroys all of the stable orbits in a system, such as in the case of an inverse tangent or inverse saddle-node bifurcation. [1, 24].

The period-doubling cascade route to chaos is particularly interesting example due to the work of Feigenbaum [28, 29, 1, 2]. Investigating period doubling bifurcations in the logistic map

$$x_{m+1} = r x_m (1 - x_m), \tag{2.4}$$

and the sine map

$$x_{m+1} = r \sin(\pi x_m), \tag{2.5}$$

Feigenbaum noticed that both maps shared identical convergence rates of the bifurcation points and distances along x between the stable points. The relationships defining this universality are

$$\lim_{n\to\infty} \frac{r_n - r_{n-1}}{r_{n+1} - r_n} = \hat{\delta} = 4.6692..., \tag{2.6}$$

describing the convergence rate of the bifurcation points r_n, and the rescaling

$$\lim_{n\to\infty} \frac{d_n}{d_{n+1}} = \hat{\alpha} = -2.5029..., \tag{2.7}$$

where d_n describes the distance along x between stable points [2]. Hence, even though the two maps are very different – the logistic map displays a quadratic nonlinearity while the sine map is transcendental – they both follow the exact same route to chaos! The mathematical constants $\hat{\delta}$ and $\hat{\alpha}$ are in fact intrinsic to the period doubling route to chaos. Various experimental studies have measured values of $\hat{\delta}$ which show reasonable agreement to Feigenbaum's theory; Libchaber et al. obtained $\hat{\delta} = 4.4 \pm 0.1$ in a mercury convection experiment with four period doubling bifurcations [30], and Arecchi and Lisi measured $\hat{\delta} = 4.7 \pm 0.3$ studying a nonlinear transistor experiment with an equal number of bifurcations [31].

To better visualize the period doubling transition to chaos, we examine a Rössler system, Eqn. (2.3) with $a = b = 0.2$ and allow c to act as the bifurcation parameter, Fig. 2.3 [32]. When $c = 2.5$, the system trajectory is a simple closed loop, projected onto the xy-plane. Period doubling bifurcations occur as c increases to 3.5 and again on the path to $c = 4$ such that the system displays period 2 and 4 trajectories following the respective bifurcations. At $c = 5$ we observe the strange attractor for a chaotic Rössler system [32]. Fig. 2.4 displays the bifurcation diagram of this period doubling cascade. Each point represents a sampled local maximum of $x(t)$, so the speckle pattern indicates no stable maxima and a chaotic trajectory. It is interesting to note that an expansion in the periodic window of the region about $c = 5.5$ would reproduce the structure of the initial bifurcation cascade [32].

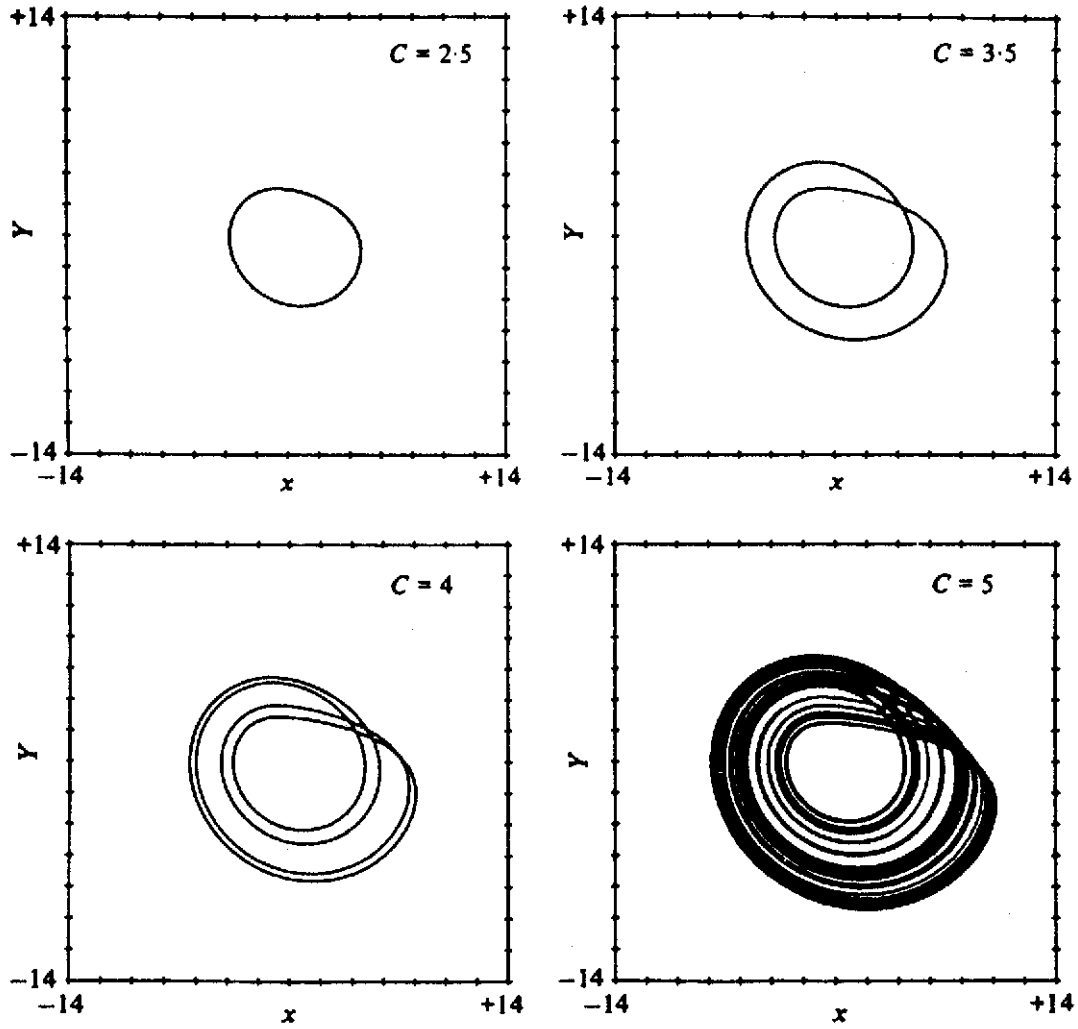

Figure 2.3: Period doubling cascade of the Rössler system Eqn. (2.3) to chaos with the parameter c acting as the bifurcation parameter. At $c = 2.5$ we observe a period 1 orbit, and at $c = 5$ we find the strange attractor for the Rössler system. Here $a = b = 0.2$. [32]

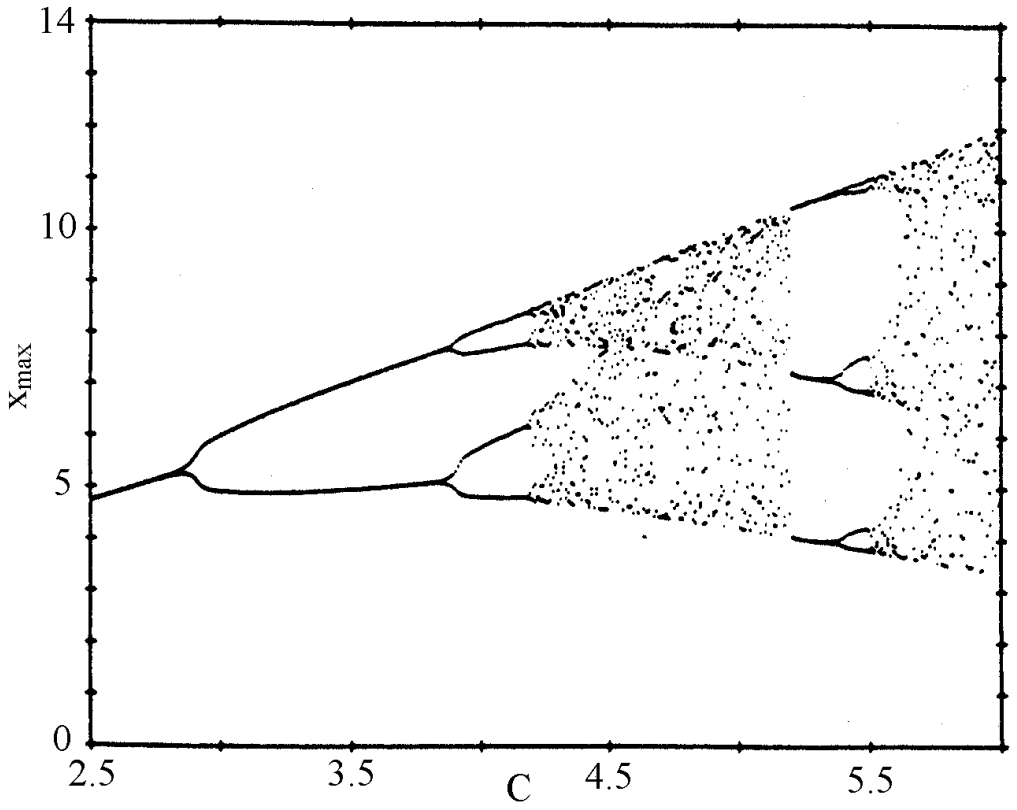

Figure 2.4: The bifurcation diagram of the Rössler system Eqn. (2.3) undergoing a period doubling cascade to chaos. The distance between bifurcation points determines the value of $\hat{\delta}$, Eqn. (2.6), and the distance along x between stable maxima determines $\hat{\alpha}$, Eqn. (2.7). The periodic window ($c \approx 5.5$) reproduces the original bifurcation cascade. [32]

The fact that all systems which display a period doubling cascade to chaos follow a similar path allows a tremendous freedom to scientists. In a perhaps overly broad extension of this universality, we are now able to justify inquiry into the nature of chaotic systems that may be difficult to study directly, using as an analog a study of other, more accessible systems with similar dynamic structure.

Quasiperiodicity provides an alternative route to chaos [1]. As the control parameter of the system is shifted towards a chaotic regime, additional frequency components develop. If the ratio of the primary frequency components is irrational, the closed behavior we saw in the period doubling bifurcation case will be absent. However, the dynamics of the system are not chaotic, as they are still essentially just the superposition of periodic oscillations; hence they are *quasiperiodic*.

As the value of the control parameter is increased further, the discrete frequency content of the signal is lost to a continuous spectrum. In the case of a deterministic system, such as in the case of the Taylor-Couette experiment reported by Gollub and Swinney [25], the continuous spectrum observed is a strong indicator of chaotic dynamics.

The intermittency route to chaos was originally studied by Pomeau and Manneville [33]. In this case, a parameter p of a nonlinear system is initially chosen such that the system will display periodic dynamics. However, above a certain threshold, p_{th}, the system is unstable, and may exhibit intermittent deviations (bursts) from the periodic orbit. As p increases further, the period between bursts decreases until the original periodic orbit is no longer observed and the system is fully chaotic.

The intermittency route to chaos is illustrated in Fig. 2.5 for an initially periodic time series of $z(t)$ in the Lorenz system, Eqn. (2.1). The parameters $\sigma = 10$ and $b = 8/3$ are fixed and r is the control parameter [33]. In this case, the bursting threshold is $r_{th} = 166.06$. Fig. 2.5(a) displays the periodic dynamics when the Lorenz system is integrated with $r = 166 < r_{th}$. Increasing r slightly and moving down the figure, we observe deviations from the initial periodic behavior. As the control parameter is increased further, the intermittent bursting increases in frequency.

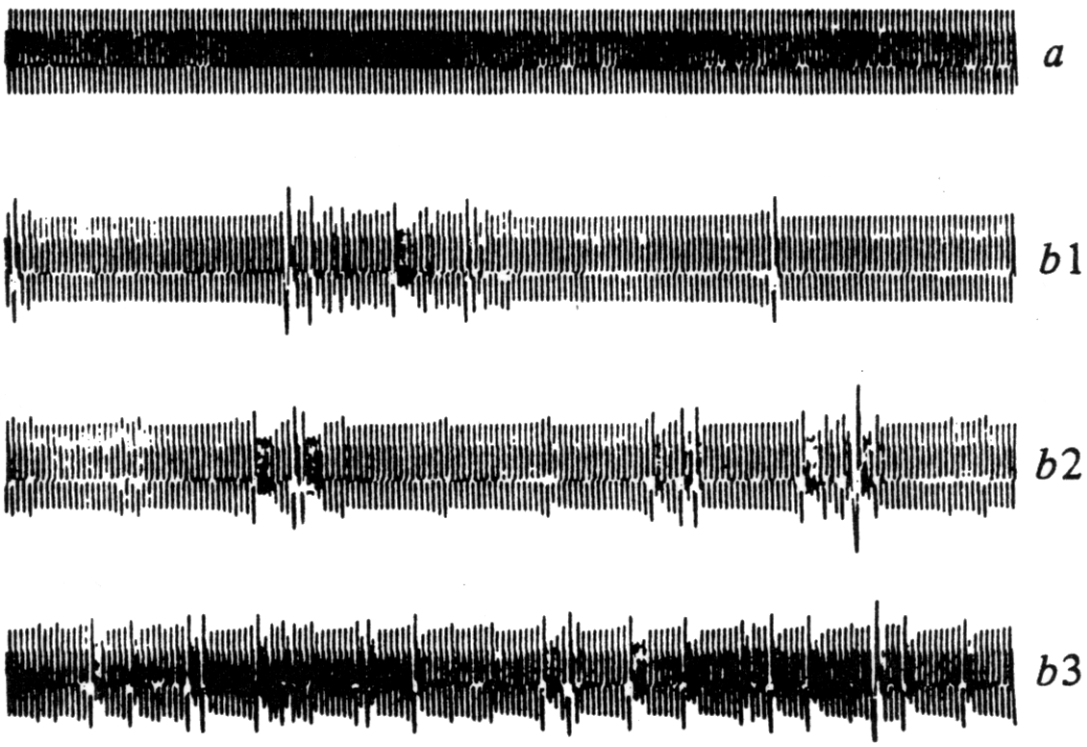

Figure 2.5: Intermittent transition to chaos. A periodic time series of the z coordinate of the Lorenz system is found with $r = 166 < r_{th}$ (a). Increasing r above the bursting threshold, we observe increasingly frequent bursts (b1-b3). The Lorenz system (2.1) is integrated with the parameters $\sigma = 10$ and $b = 8/3$ fixed. [33]

Pomeau and Manneville identified three species of intermittency due to three generic bifurcations: Type I saddle node, Type II Hopf and Type III inverse period doubling [33, 1]. As can be observed in Fig. 2.5, the interburst time decreases with the growth of the bifurcation parameter. Pomeau and Manneville found the power law scaling

$$\langle \Delta T \rangle \sim \begin{array}{ll} (p - p_{th})^{-1/2} & \text{Type I} \\ (p - p_{th})^{-1} & \text{Type II} \\ (p - p_{th})^{-1} & \text{Type III} \end{array} , \tag{2.8}$$

where $\langle \Delta T \rangle$ is the mean interburst time. While Type II and Type III intermittency share the same -1 decay exponent, their dynamics near p_{th} are characteristic of the underlying bifurcation.

Another intermittent route to chaos is found when changing a system parameter leads to collisions of chaotic attractors with other attractors or periodic orbits, or causes a sudden shift in the dimension of the attractor. In this case the system displays crisis induced intermittency as it jumps from one attractor to another [1].

In these intermittent routes to chaos, the bifurcation parameter was varied smoothly. However, an alternate form, labeled on-off intermittency, may result from the coupling of chaotic systems [26, 27, 34] or from driving a system with a stochastic signal [26, 35]. The latter case is in contrast to the other species of intermittency mentioned; now the bifurcation parameter is the element being stochastically driven. Despite the stochastic source, the statistics of intermittent events display a $-3/2$ power law distribution in time.

This distribution is evidenced in liquid crystal electroconvection experiments by John, Behn and Stannarius [35]. In Fig. 2.6(I) a $-3/2$ power law decay extends over several decades. Here, τ is the lifetime of laminar behavior, and α is a parameter of the stochastic driving. The labels (a), (b) and (c) in Fig. 2.6(I) correspond to increasing voltage, U, differences between the two charged plates in the experiment.

Power law distributions are found when examining the burst amplitudes in Fig. 2.6(II) as well. Here, a decay exponent of -1 identifies the voltage at which the Lyapunov exponent $\lambda = 0$, marking the transition to chaotic behavior [35].

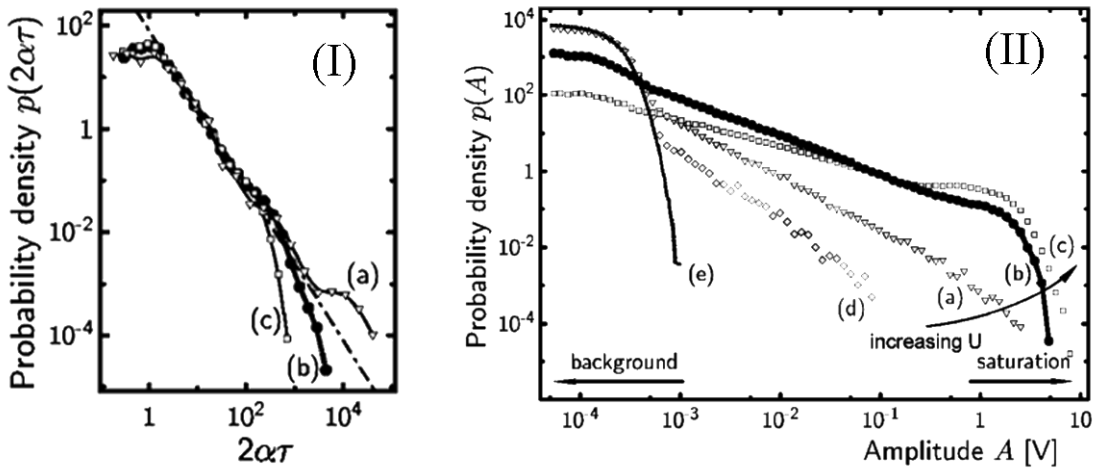

Figure 2.6: Characteristic statistics of On-Off Intermittency observed in liquid crystal electroconvection experiment. The interburst time distribution follows a $-3/2$ power law decay over several decades (I). Here, τ is the interburst time and α is a parameter of the stochastic driving. The labels (a), (b) and (c) correspond to increasing voltages, U. The slope of the log-log burst amplitude distribution shifts with increasing U, (II). A slope of -1 indicates a Lyapunov exponent of $\lambda = 0$.[35]

2.2 Synchronization

Synchronization in chaotic systems is a surprising phenomenon. The fundamental characteristics of chaotic systems, such as aperiodic dynamics and a sensitivity to initial conditions, would seem to preclude synchronization. However, numerical and experimental studies over the past decade have established the existence of synchronization of chaos in diverse systems.

The first reported observations of the synchronization of coupled chaotic systems were in studies by Yamada and Fujisaka [36, 37]. Shortly after Afraimovich, Verichev and Rabinovich [38] first advanced many of the tools necessary for understanding the synchronization of chaos. However, the field did not gain popular recognition until the seminal work of Pecora and Carroll in 1990 [39].

In this study, the authors examined the dynamics of coupled chaotic models including coupled Rössler systems, Eqns. (2.3), and coupled Lorenz systems, Eqns. (2.1), and chaotic circuits. These three-dimensional chaotic systems are unidirectionally coupled such that one component of the drive system replaces its coun-

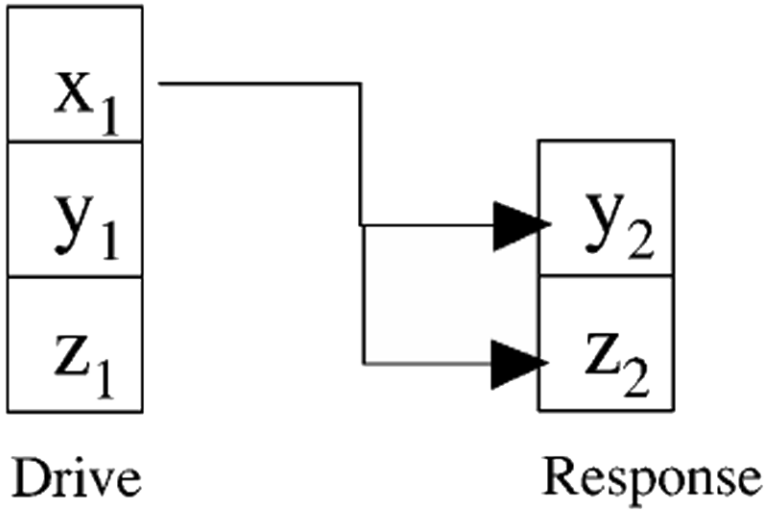

Figure 2.7: Geometric representation of the complete replacement coupling scheme used by Pecora and Carroll. One variable of the drive system replaces its counterpart in the response system, resulting in identical synchronization of chaotic dynamics.[15]

terpart in the response system. This coupling scheme is geometrically presented in Fig. 2.7. In this complete replacement scheme, and with the proper choice of coupling components, all of the Lyapunov exponents of the response system will become negative and the two systems will synchronize. Note that the dynamics of the drive system are unaffected and chaotic. This transition to synchronization for two Rössler systems is presented in Fig. 2.8. Here, the two systems begin with different initial conditions, but through the replacement of $y(t)$ the response (right) system synchronizes to the drive system (left) in only a few orbits.

While the deviation of trajectories was exponential in the uncoupled case, the rate of synchronization of identical coupled systems is actually exponential in time. This is apparent in Fig. 2.9(a) where the coupling variable for the identical Lorenz systems is $x(t)$. Here, the convergence of the two systems is seen as the differences $\Delta y = y_2 - y_1$ and $\Delta z = z_2 - z_1$ decay exponentially quickly [39]. However, identical synchronization is not always possible. With only a 5% parameter detuning between the drive and response Lorenz systems, Δz and Δy remain relatively constant after a brief decay time. This limited convergence of the nonidentical coupled attractors

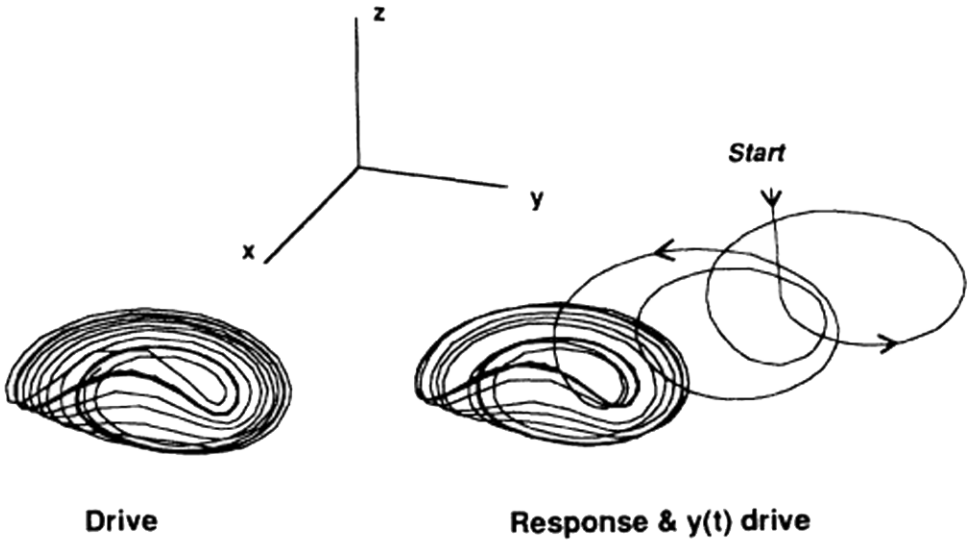

Figure 2.8: Synchronization of two chaotic Rössler systems through the replacement of $y(t)$ in the response system (right) with $y(t)$ from the drive system (left). [39]

is seen in Fig. 2.9(b).

The difference between the complete synchronization seen in Fig. 2.9(a) and the partial synchronization of Fig. 2.9(b) may be stated mathematically. The condition for complete synchronization is simply

$$\lim_{t\to\infty} |x_1(t) - x_2(t)| = 0. \tag{2.9}$$

Therefore, any dynamical differences between the two systems reduce to zero as the systems evolve in time. The weaker requirement for partial synchronization is then

$$\lim_{t\to\infty} |x_1(t) - x_2(t)| < \text{constant}. \tag{2.10}$$

The phase space where the condition $|x_1(t) - x_2(t)| = 0$ holds is called the *synchronization manifold.*

A more general view of synchronization does not require that all the dynamical characteristics of the studied systems match, merely that there is some relationship between their dynamics. A simple case of this is lag synchronization, where one system leads another [40]. In this case synchronization would be given by the relation

$$\lim_{t\to\infty} |x_1(t) - x_2(t-\tau)| \leq \text{constant}, \tag{2.11}$$

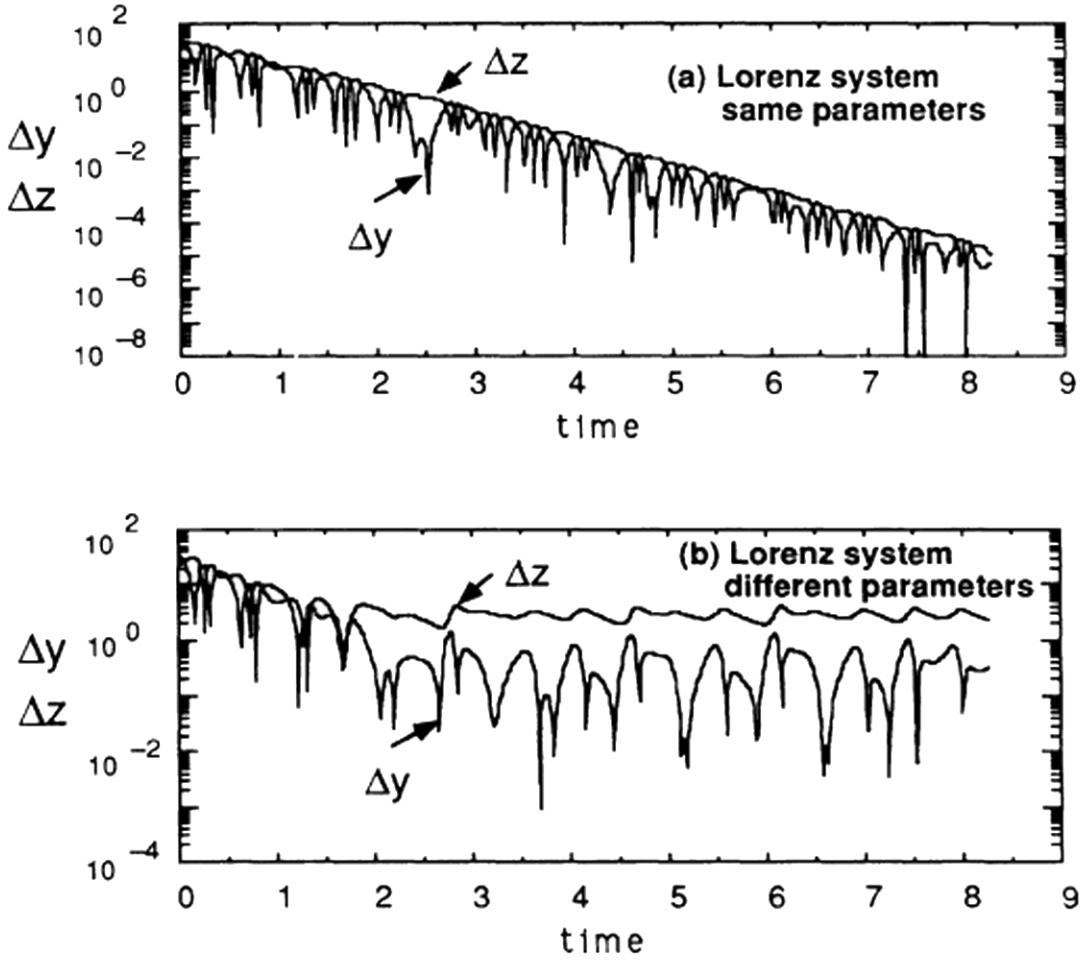

Figure 2.9: Synchronization of Lorenz attractors through complete replacement of $x(t)$. Identical systems exponentially converge to complete synchronization (a). However, a 5% parameter mismatch between the coupled systems allows only partial synchronization (b). [39]

where τ is the time lag between the systems. In the case of perfect lag synchronization, the constant on the right hand side of the equation is zero.

Phase synchronization is another weak form of synchronization, and was first recognized in chaotic systems by Pikovsky [41] and Stone [42]. In this case, we may decompose a times series as

$$x(t) = A(t)\sin\big(\phi(t)\big), \tag{2.12}$$

where $A(t)$ is the time varying amplitude and $\phi(t)$ is the time varying phase of $x(t)$, and $x(t), A(t), \phi(t) \in \boldsymbol{R}$. In the case of a complex time series $x(t)$, the term $\sin\big(\phi(t)\big)$ becomes $\exp[i\phi(t)]$ and $A(t)$ and $\phi(t)$ remain real. As the name implies, phase synchronization requires only that

$$\lim_{t\to\infty} |m\phi_1(t) - n\phi_2(t)| = 0, \tag{2.13}$$

and there is no bound on $A(t)$. The positive integers m and n define the locking ratio between dynamic systems. This concept of frequency locking ratios and regions is often studied using Arnold's Tongues [1]. We shall address phase synchronization further in Section 5.2.

Even weak forms of synchronization like phase and lag synchronization require a conceptually direct relationship between systems. Complex dynamical systems may not reveal such easy relationships despite being intimately related. By writing one dynamical system as a smooth function F of another

$$y(t) = F\big(x(t)\big), \tag{2.14}$$

then it is possible to consider a broad class of synchronization. This class of synchronization is somewhat mislabeled as *generalized synchronization* [43]. The requirement of Eqn. (2.14) that the functional relationship is smooth and unidirectional is a significant constraint.

This concept of generalized synchronization may be applied to a rich set of dynamical systems, but may be difficult to detect. One statistic proposed for its identification is mutual false nearest neighbors [43]. This statistic is related to

mutual information and false nearest neighbors [3] and depends on the conjecture that a set of nearest neighbor points in the phase space of $x(t)$ will correspond to neighboring points in the phase space of $y(t)$.

Mutual false nearest neighbors does not always provide a good indication of synchronization for complex systems. An intuitive and more robust tool is provided by the auxiliary system method [44]. In this case, if generalized synchronization is suspected, then a second response system, identical to the original response system, is coupled to the drive system. The two response systems are independent of each other. If the two response systems synchronize to each other, then they are each related to the drive system through generalized synchronization. This may be simply seen in the relations

$$\begin{array}{l} y(t) = F\big(x(t)\big) \\ y'(t) = F\big(x(t)\big) \end{array} \Rightarrow y(t) = y'(t), \tag{2.15}$$

where $y(t)$ and $y'(t)$ are the identical response systems that are related to the drive system $x(t)$ through the function F.

Chapter 3

Chaos in Lasers

Since they are monochromatic, unidirectional and often produce stable power outputs, lasers are considered benchmarks of stability with good reason. However, they do possess the potential for complex and chaotic dynamics. As lasers have become ubiquitous in modern technology and science, it is to our benefit to understand their dynamics and the potential benefits they offer, as well as any limitations they may impose.

3.1 Laser Equations

The basic equations of motion for laser systems are often derived using a semi-classical methodology; the electric field is treated classically using Maxwell's equations [45], and the gain medium is treated quantum mechanically [11, 9, 7]. The classical treatment of the electric field is easily justified by the large numbers of photons produced by lasers.

The simplest approach to deriving the basic laser equations is to consider the gain medium as a two-level atomic system which interacts with a classical electric field. This system is described by the time dependent wave equation

$$H\Psi = i\hbar\frac{d\Psi}{dt} \tag{3.1}$$

where H is the generally time dependent Hamiltonian and Ψ is the time dependent wave function. We may decompose the wave function into components describing the individual levels of the atom,

$$\Psi(\boldsymbol{r},t) = C_1(t)\Psi_1(\boldsymbol{r},t) + C_2(t)\Psi_2(\boldsymbol{r},t). \tag{3.2}$$

The coefficients C_1 and C_2 determine the probability of finding the system in either the first or second energy level, and are normalized such that $|C_1(t)|^2 + |C_2(t)|^2 = 1$. The density matrix for the system, $\rho = |\Psi\rangle\langle\Psi|$ may then be written as

$$\rho = \begin{pmatrix} |C_1|^2 & C_1C_2^* \\ C_1^*C_2 & |C_2|^2 \end{pmatrix}. \tag{3.3}$$

We may increase the transparency of Eqn. (3.1) further by separating the wave functions into time dependent and independent parts,

$$\Psi_n(\boldsymbol{r},t) = e^{-i\mathcal{E}_n t/\hbar}\psi_n(\boldsymbol{r}). \tag{3.4}$$

The difference of the energy levels $\mathcal{E}_n$ in the exponential term determines the transition frequency

$$\omega_o = \frac{1}{\hbar}(\mathcal{E}_2 - \mathcal{E}_1). \tag{3.5}$$

Finally, we may separate the Hamiltonian H into components describing the two level atom, H_o, and its interaction with the classical electric field, H_I, where

$$H_o = \begin{pmatrix} \mathcal{E}_1 & 0 \\ 0 & \mathcal{E}_2 \end{pmatrix}, \tag{3.6}$$

$$H_I = \begin{pmatrix} 0 & p \\ p & 0 \end{pmatrix} E(t). \tag{3.7}$$

Here, $E(t)$ is the complex electric field amplitude and p is the dipole moment of the atom along the direction of the electric field, and is defined as

$$p \equiv eX_{12}. \tag{3.8}$$

X_{12} is the displacement of the electron cloud about the atom along the direction of the electric field, and e is the charge of a single proton.

Using the Heisenberg picture [46],

$$\frac{d\rho}{dt} = -\frac{i}{\hbar}[\rho, H], \tag{3.9}$$

we find the material rate equations

$$\begin{aligned} \frac{d(\rho_{22}-\rho_{11})}{dt} &= -\gamma_{\parallel}\big[(\rho_{22}-\rho_{11}) - (\rho_{22}-\rho_{11})^{eq}\big] \\ &\quad + \frac{i2p}{\hbar}\big[E^* e^{-i\omega t}\rho_{12} + \text{c.c.}\big], \qquad (3.10) \\ \frac{d\rho_{12}}{dt} &= -(\gamma_{\perp} + i\omega_o)\rho_{12} + \frac{ip}{\hbar}E(\rho_{22}-\rho_{11}), \qquad (3.11) \end{aligned}$$

where c.c. indicates the complex conjugate of the previous term. We have phenomenologically added the decay terms $\gamma_{\parallel}$ and $\gamma_{\perp}$, the population inversion decay rate and the dephasing rate, respectively. Both terms naturally appear in a more rigorous quantum mechanical derivation [47, 48]. Equations (3.10 & 3.11) are known as the optical Bloch equations. Their macroscopic forms are found through the relations

$$N = N_{tot}(\rho_{22} - \rho_{11}), \tag{3.12}$$

$$P = N_{tot}p(\rho_{12} + \rho_{21}). \tag{3.13}$$

Here N is the population inversion, P is the polarization, and N_{tot} is the total density of atoms which may contribute to the action of the laser. The macroscopic material rate equations are

$$\begin{aligned} \frac{dN}{dt} &= -\gamma_{\parallel}(N - N^{eq}) + \frac{i2}{\hbar}(E^*P + \text{c.c.}), \qquad (3.14) \\ \frac{dP}{dt} &= -(\gamma_{\perp} + i\omega_o)P + \frac{i|p|^2}{\hbar}EN. \qquad (3.15) \end{aligned}$$

Using the rotating wave approximation, we shift the complex polarization, Eqn. (3.15), to a reference frame rotating at ω, the frequency of the interacting electric field.

Eqn. (3.15) now becomes

$$\frac{dP}{dt} = -(\gamma_\perp + i\Delta\omega)P + \frac{i|p|^2}{\hbar}EN, \tag{3.16}$$

where $\Delta\omega = \omega_o - \omega$.

The classical electric field obeys the one dimensional wave equation

$$\frac{\partial^2 E'}{\partial z^2} - \frac{1}{c^2}\frac{\partial^2 E'}{\partial t^2} = \mu_o \frac{\partial^2 P'}{\partial t^2} \tag{3.17}$$

derived from Maxwell's equations. We may write the complex electric field as $E'(z,t) = E(z,t)\exp[i(\omega t - \beta z)]$ and the complex macroscopic polarization $P' = \frac{1}{2}P(z,t)\exp[-i\beta z] + \text{c.c.}$, where $E(z,t)$ is the slowly varying complex amplitude and $P(z,t)$ is the complex slowly varying amplitude of the polarization. Using these definitions as well as the slowly varying envelope approximation we find the simpler wave equation

$$v_g\frac{\partial E}{\partial z} + \frac{\partial E}{\partial t} = \frac{-i\omega}{\epsilon}P. \tag{3.18}$$

Here, ϵ is the permittivity of the laser medium, and v_g is the group velocity of light through that medium. In most laser systems the electric field amplitude does not significantly vary over the length of the laser cavity, hence the uniform field approximation allows $\frac{\partial E}{\partial z} \to 0$. With this final approximation, and phenomenologically introducing the photon decay rate K, which may be determined through a rigorous analysis of the laser cavity geometry and boundary conditions [49, 8], we obtain the Maxwell-Bloch semiclassical laser equations

$$\frac{dE}{dt} = -KE - \frac{i\omega}{\epsilon}P, \tag{3.19}$$

$$\frac{dN}{dt} = Q - \gamma_\parallel N + \frac{i2}{\hbar}(E^*P + \text{c.c.}), \tag{3.20}$$

$$\frac{dP}{dt} = -(\gamma_\perp + i\Delta\omega)P + \frac{i|p|^2}{\hbar}EN. \tag{3.21}$$

Q is a constant pump term.

3.2 Maxwell-Bloch, Lorenz System Correspondence

An interesting aspect of the Maxwell-Bloch equations is that they have a direct correspondence to the Lorenz equations [50, 11, 12]. In this comparison, E and P are assumed to be real. This amazing coincidence of dynamical systems was the impetus for studying chaos in optical systems. However, it was largely regarded as a practical curiosity, as the requirement for a laser system to display instabilities is [12]

$$K > \gamma_{\parallel} + \gamma_{\perp}. \tag{3.22}$$

This is the so called 'bad cavity' condition, so named as it requires that the photon decay rate from the cavity must be greater than the relaxation rate of the laser medium, therefore requiring intense pumping to reach threshold. A relatively transparent output coupler is the simplest way to achieve this condition for a given active medium. Beyond the system requirement of Eqn. (3.22), a stability analysis of the Maxwell-Bloch equations, Eqns. (3.19-3.21), reveals the laser must be pumped 10-20 times above threshold to reach the 'second laser threshold', which marks the onset of dynamic instabilities [12]. The 'first laser threshold' simply marks the onset of lasing action.

With the bad cavity condition, Eqn. (3.22), a large pump input is required to even reach the first threshold, and it was thought that the second was out of reach. However, Weiss and co-workers [51] were able to meet these system requirements and demonstrate instabilities in an ammonia ring laser operated at $\lambda = 100\mu m$. The dynamics found show strong qualitative and quantitative agreement with the Lorenz system in a similar parameter regime. Figure 3.1[51, 12] displays a comparison of the phase spaces of the Lorenz system, x vs. dx/dt, Fig. 3.1(a), and the phase space E vs. dE/dt for the ammonia laser, Fig. 3.1(b).

Beyond evidencing chaos in laser systems, this demonstration of a Lorenz-like strange attractor also hints at the possibility of synchronizing chaotic lasers. Pecora and Carroll's seminal work demonstrating synchronization of chaos used Lorenz systems among others [39] that we discussed in Section 2.2.

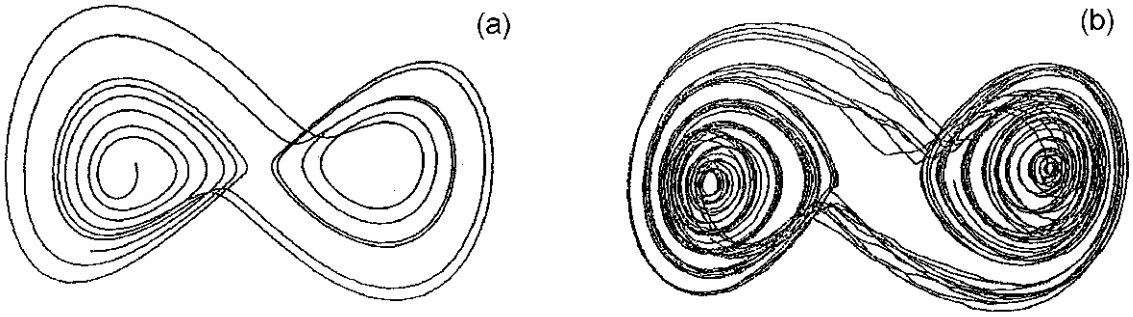

Figure 3.1: Comparison of the phase space of a chaotic Lorenz system (x vs. dx/dt) (a) and the phase space (E vs. dE/dt), an ammonia ring laser with similar scaled parameters (b).[51, 12]

3.3 Laser Classifications

In the course of studying a stable CO_2 laser's transition to chaos, Arecchi and co-workers advanced a classification scheme of single mode laser systems based on the range of dynamics available to the laser [52]. A system which requires the full Maxwell-Bloch equations to describe its dynamics is classified as a Class C laser. This is the only class of lasers which may autonomously display chaotic dynamics as a system must consist of at least three dynamic variables for chaos to be present [2]. For independent laser systems these three variables are the complex electric field amplitude $E(t)$, the real population inversion $N(t)$, and the complex macroscopic material polarization $P(t)$. Class C lasers include lasers such as argon ion, krypton ion, and the ammonia laser addressed above.

Class C lasers are systems where the time scales of all three Maxwell-Bloch equations are similar, i.e. $K \sim \gamma_{\parallel} \sim \gamma_{\perp}$. Only in this case may the field equation display chaotic dynamics. If one dynamical variable evolves on a much faster time-scale than the other two, then this 'fast' variable will track the slower variables virtually instantaneously. Therefore, it will no longer have a perceivable effect on the dynamics of the system, and we may adiabatically eliminate this equation from the model. Typically, the polarization term will evolve on a faster time scale such that $\gamma_{\perp} \gg \gamma_{\parallel} K$. In this case, the polarization terms in Eqns. (3.19&3.20) are set to

the steady state value

$$P_o = \frac{i|p|^2 EN}{\hbar(\gamma_\perp + i\Delta\omega)}, \tag{3.23}$$

and the laser equations become

$$\frac{dE}{dt} = -KE + (\gamma_\perp - i\Delta\omega)\frac{\omega|p|^2}{\hbar\epsilon(\gamma_\perp^2 + \Delta\omega^2)}EN, \tag{3.24}$$

$$\frac{dN}{dt} = Q - \gamma_\parallel N - \frac{4|p|^2\gamma_\perp}{\hbar^2(\gamma_\perp^2 + \Delta\omega^2)}|E|^2 N. \tag{3.25}$$

Lasers that are described by this set of two coupled equations are known as Class B lasers. The lasers studied in this dissertation, Nd:YAG and erbium doped fiber ring lasers, are included in this classification along with CO_2, semiconductor, and ruby lasers.

If the population inversion evolves on a sufficiently fast time scale, then it too will track the electric field virtually instantaneously. This condition leads to a Class A laser system, and possesses time scales that obey the inequality $\gamma_\perp, \gamma_\parallel \gg K$. In this case we may adiabatically eliminate Eqn. (3.25). The steady state value of the population inversion is

$$N_o = \frac{Q\hbar^2(\gamma_\perp^2 + \Delta\omega^2)}{4|p|^2\gamma_\perp|E|^2}, \tag{3.26}$$

and the laser is now described by the single equation

$$\frac{dE}{dt} = -KE + \frac{Q(\gamma_\perp - i\Delta\omega)\hbar\omega}{4\epsilon\gamma_\perp}\frac{E}{|E|^2}. \tag{3.27}$$

Class A lasers include helium-neon lasers and dye lasers.

While only Class C lasers may autonomously display chaotic dynamics, it is possible to generate chaotic dynamics in Class B lasers by increasing the number of degrees of freedom in the laser system. This may be achieved by modulating a system parameter such as the pump or cavity loss, increasing the number of lasing modes, adding a feedback signal, introducing inhomogeneous broadening to the system, injecting the laser with a detuned optical injection (the topic of Arecchi and Lisi's work, Ref. [52]), or adding some other nonlinearity or dynamical variable to the Class B laser system.

3.4 Nd:YAG Lasers

A significant portion of this dissertation concerns experiments and analysis of dynamics of a linear array of neodymium doped yttrium aluminum garnet (Nd:YAG) lasers. Nd:YAG lasers have a long history in the study of nonlinear dynamics and chaos. Just six years after Geusic et. al produced the first Nd:YAG laser in 1964 [53], Kimura and Otsuka reported period doubling bifurcations and chaotic spiking dynamics in a modulated Nd:YAG laser [54]. We now summarize some of this Class B laser's properties and present a simple model which effectively describes a single Nd:YAG laser.

3.4.1 Nd:YAG Properties

The prominence of Nd:YAG lasers in industry, research, medicine and military applications is due in large part to the excellent properties of the host material, yttrium aluminum garnet. The chemical formulation of the host is $Y_3Al_5O_{12}$, and forms a cubic crystalline structure, as do most garnets [55]. The crystal is colorless and optically isotropic, beneficial properties in a laser crystal, and possesses sufficient hardness that it does not routinely fracture during fabrication. The structure generally is stable from very low temperatures to its melting point. Some thermal properties of Nd:YAG are listed in Table (3.1) [55]. Of particular importance is the thermal dependence of the index of refraction, $\partial n/\partial T$ which allows thermal lensing to occur. Thermal lensing is required for the formation of stable laser cavities for the linear Nd:YAG array described in Section 4.2 and studied in Chapters 4 and 5 [56].

In a Nd:YAG crystal the trivalent ion Nd^{3+} replaces Y^{3+}. As the two ions possess the same positive charge there is no need for charge compensation. However, the dimensions of the two ions differ by approximately 3%, so the doping concentration of Nd^{3+} is limited to 1% to restrict lattice distortions in the crystal. Table (3.2) [55] lists some physical and optical properties of Nd:YAG.

Nd:YAG is a four-level laser system. This allows a population inversion to be

Property	Units	$300K$	$200K$	$100k$
Thermal conductivity	$Wcm^{-1}K^{-1}$	0.14	0.21	0.58
Specific heat	$Wsg^{-1}K^{-1}$	0.59	0.43	0.13
Thermal diffusivity	cm^2s^{-1}	0.046	0.10	0.92
Thermal expansion	$K^{-1} \times 10^{-6}$	7.5	5.8	4.25
$\partial n/\partial T$	K^{-1}	7.3×10^{-6}	–	–

Table 3.1: Thermal properties of Nd:YAG. [55]

Chemical formula	Nd:$Y_3Al_5O_12$
Weight % Nd	0.725
Atomic % Nd	1.0
Knoop hardness	1215
Thermal expansion coefficient	
[100] orientation	$8.2 \times 10^{-6}C^{-1}$, $0 - 250C$
[110] orientation	$7.7 \times 10^{-6}C^{-1}$, $10 - 250C$
[111] orientation	$7.8 \times 10^{-6}C^{-1}$, $0 - 250C$
Linewidth	4.5Å
Stimulated emission cross section	
$4F_{3/4}(R_2)$-$4I_{11/2}(Y_3)$	$\sigma_{21} = 6.5 \times 10^{-19}cm^2$
Fluorescence lifetime	$230 - 240\mu s$
Index of refraction	1.82(at $\lambda = 1.0\mu m$)

Table 3.2: Physical and optical properties of Nd:YAG. [55]

achieved relatively easily, since the terminating level of the laser transition is not the ground level, and hence is nearly unpopulated. Any electron population present in this terminal level is due primarily to thermal excitations from the ground state. The decay times of the initial ($4F_{3/4}$, $\tau_f = 240\mu s$) and terminal ($4I_{11/2}$, $\tau_f = 30ns$) levels of the laser transition further assist the generation of a population inversion. A simplified energy level diagram for Nd:YAG is shown in Fig. 3.2, and indicates the lasing transition from the R_2 sublevel of $4F_{3/4}$ to the Y_3 sublevel of $4I_{11/2}$, generating photons with a center wavelength of $\lambda = 1.064\mu m$. The $1.064\mu m$ transition corresponds to the dominant peak of the fluorescence spectrum of Nd:YAG. In Fig. 3.3 [55], this peak is labeled (5). The labels indicate the transitions between sublevels of $4F_{3/4}$ and $4I_{11/2}$ shown in the subfigure.

The absorption spectrum of Nd:YAG is plotted in Fig. 3.4 [55]. Pumping the laser crystal at wavelengths that are short compared to $\lambda = 1.064\mu m$ and correspond to strong absorption peaks results in efficient lasing. However, due to experimental considerations we choose to pump the Nd:YAG laser array studied in Chapters 4 and 5 at $\lambda = 514.5nm$, which lies on a relatively weak absorption peak.

3.4.2 Nd:YAG Rate Equations

As mentioned above, Nd:YAG is a Class B laser, as the polarization decay rate ($\gamma_\perp \approx 10^{11}s^{-1}$) is much greater than the population inversion decay rate ($\gamma_\parallel \approx 4 \times 10^3 s^{-1}$) and the photon decay rate ($K \approx 10^7 s^{-1}$). After adiabatic elimination of the polarization, the Nd:YAG laser is described by two coupled ordinary differential equations. The form of these equations may differ, depending on the choice of normalization parameters, and the details of the laser systems. Here we describe a single Nd:YAG laser with the transparent set of laser equations

$$\frac{dE}{dt} = \frac{1}{\tau_c}(G - \epsilon_1)E + i\omega_1 E, \tag{3.28}$$

$$\frac{dG}{dt} = \frac{1}{\tau_f}(p - G - G|E|^2). \tag{3.29}$$

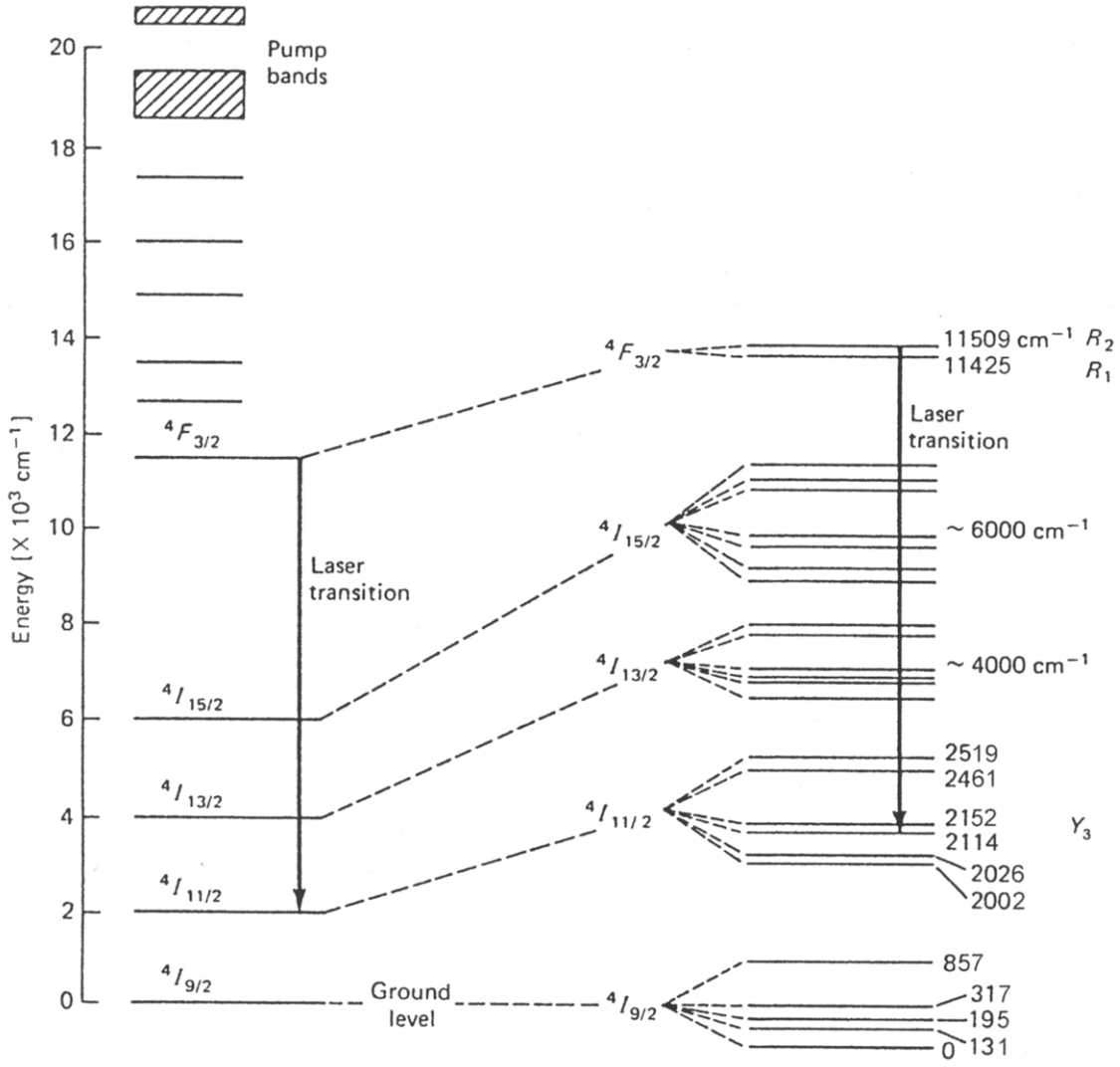

Figure 3.2: Simplified energy level diagram of the Nd:YAG, a four level laser medium. The laser transition from the R_2 sublevel of $4F_{3/4}$ to the Y_3 sublevel of $4I_{11/2}$ generates photons with a center wavelength of $\lambda = 1.064\mu m$. [55]

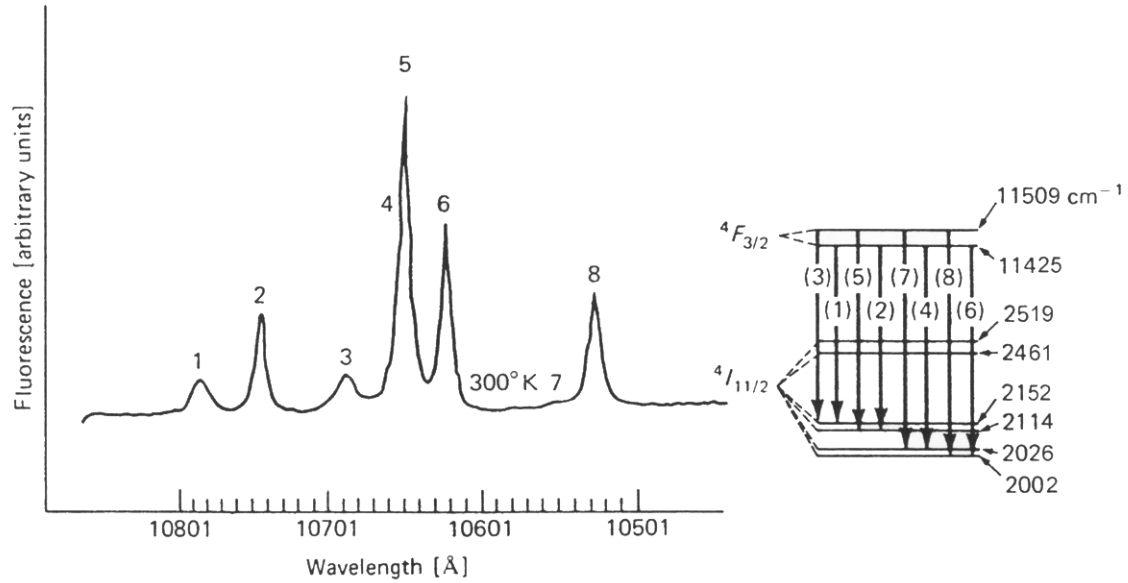

Figure 3.3: Fluorescence spectrum of Nd:YAG at $T = 300K$. The $1.064\mu m$ transition is corresponds to the dominant peak, labeled (5). The individual peaks in the spectrum result from transitions between the various sublevels of $4F_{3/4}$ and $4I_{11/2}$ shown in the subfigure to the right. [55]

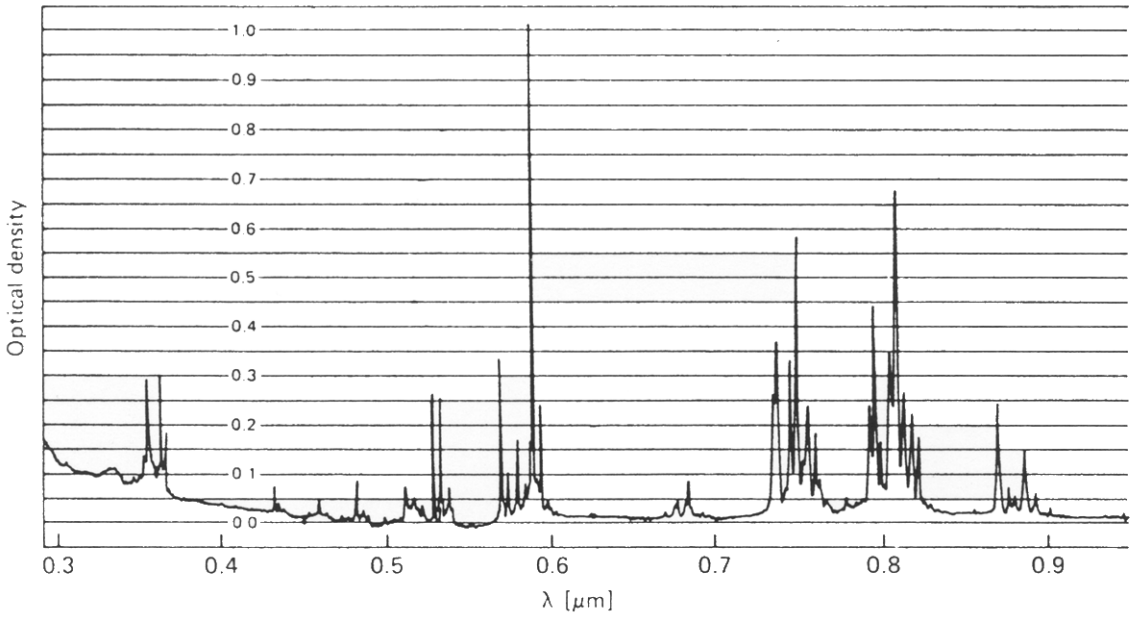

Figure 3.4: Absorption spectrum of Nd:YAG at $T = 300K$. Efficient laser action is observed when the Nd:YAG crystal is pumped at a strong absorption wavelength. Due to experimental considerations, we choose a pump wavelength of $\lambda = 514.5nm$, a relatively weak absorption peak. [55]

E is the normalized complex slowly varying electric field envelope, and G is the real gain and is proportional to the population inversion. The time scales of the laser equations are determined by the cavity round trip time, $\tau_c = 400 - 500ps$, and the fluorescence time of the upper level of the laser transition, $\tau_f = 230 - 240\mu s$. p is the pump parameter, ϵ_1 is the loss coefficient of the single laser, and ω_1 is the detuning of the laser from a fundamental cavity mode.

3.5 Erbium Doped Fiber Ring Lasers

The lasing ion of erbium, like neodymium is a trivalent lanthanide [57], and forms Class B laser systems as well. Erbium lasers have received significant attention, as they generate light at $\lambda = 1.5\mu m$, the minimum loss wavelength of fused silica (optical fiber)[58]. This peak wavelength and broad gain bandwidth have earned Er^{3+} systems a prominent role in telecommunications and research.

3.5.1 Erbium Doped Fiber Properties

An erbium doped fiber ring laser (EDFRL) is a three-level laser system whose terminal level of the laser transition is identical to the Er^{3+} ground state. Achieving a population inversion in such a system is especially difficult, as it requires moving the majority of the electrons from the ground state. Fortunately, the excited energy level's amazingly long fluorescence time ($\tau_f = 10ms$) makes laser action possible. The polarization decay time of Er^{3+} is $\tau_p \approx 1fs$, which easily justifies the Class B laser approximation. Table 3.3 lists some of the properties of erbium doped fiber systems.

The energy level diagram presented in Fig. 3.5 [57] displays the absorptive and radiant transitions of erbium doped glass. The corresponding optical wavelengths are given in nanometers for the absorption and experimentally observed radiative transitions. We are concerned with a pump mechanism that will allow stimulated emission near $\lambda = 1.5\mu m$, the $4I_{13/2} \rightarrow 4I_{15/2}$ radiant transition. The two primary

Ion	Er^{3+}
Absorption cross section, $4I_{15/2} \rightarrow 4I_{11/2}$	$\sigma_a^{peak} = 7.9 \times 10^{-21} cm^2$
Stimulated emission cross section $4I_{13/2} \rightarrow 4I_{15/2}$	$\sigma_e^{peak} = 6.7 \times 10^{-21} cm^2$
Fluorescence lifetime	$10ms$
Polarization lifetime	$2.1fs$
Lineshape function	$g(\nu_s) = 9.3 \times 10^{-16}$
Index of refraction	1.46 (at $\lambda = 1.5\mu m$)

Table 3.3: Properties of Er:glass. [57, 59]

possibilities are optically pumping the doped fiber at $\lambda = 1.48\mu m$ or at $\lambda = 980nm$. In the former case, electrons are excited to energetic sublevels of the $4I_{13/2}$ energy level, and quickly decay to lower sublevels. It is from these minimal sublevels that the radiant transition occurs. Pumping with $\lambda = 980nm$ raises electrons to $4I_{11/2}$, where they undergo a fast 'non-radiating' transition to $4I_{13/2}$. The EDFRLs utilized for this research use semiconductor pump lasers operating at $\lambda = 980nm$.

Figure 3.6 displays the absorption spectrum of erbium doped fiber [57]. The absorption peaks are labeled with their corresponding raised energy levels. We utilized the absorption peak labeled $4I_{13/2}$ ($\lambda = 980nm$) for optical pumping in this research.

Although the radiant transitions take place between quantized energy levels of Er^{3+}, the resulting spectrum extends over many nanometers. This broadening is due in part to several mechanisms which break degeneracies in the energy level diagrams. These include electron-electron interactions and spin-orbit coupling inherent to the erbium ion, and most significantly the Stark effect [57, 59], due to interactions with the host material. The Stark effect is also known as the crystal field interaction in doped materials. Here, the host material generates local electric fields peculiar to its crystal structure. These electric fields may lift additional degeneracies in the Er^{3+} energy levels. On a macroscopic scale, the glass host may be viewed as amorphous. However, there exist microcrystal structures throughout. Since the details and composition of these local lattices vary throughout the material, then the local electric

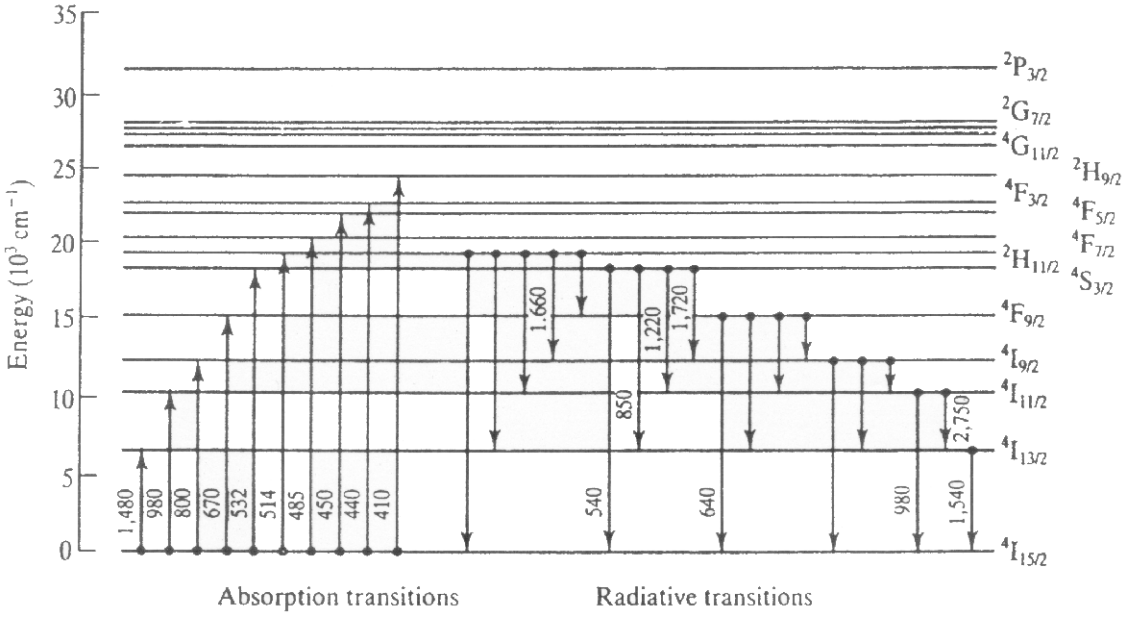

Figure 3.5: Energy level diagram of erbium doped optical fiber displaying absorptive and radiant transitions. Wavelengths in nanometers are given for those transitions observed experimentally. [57]

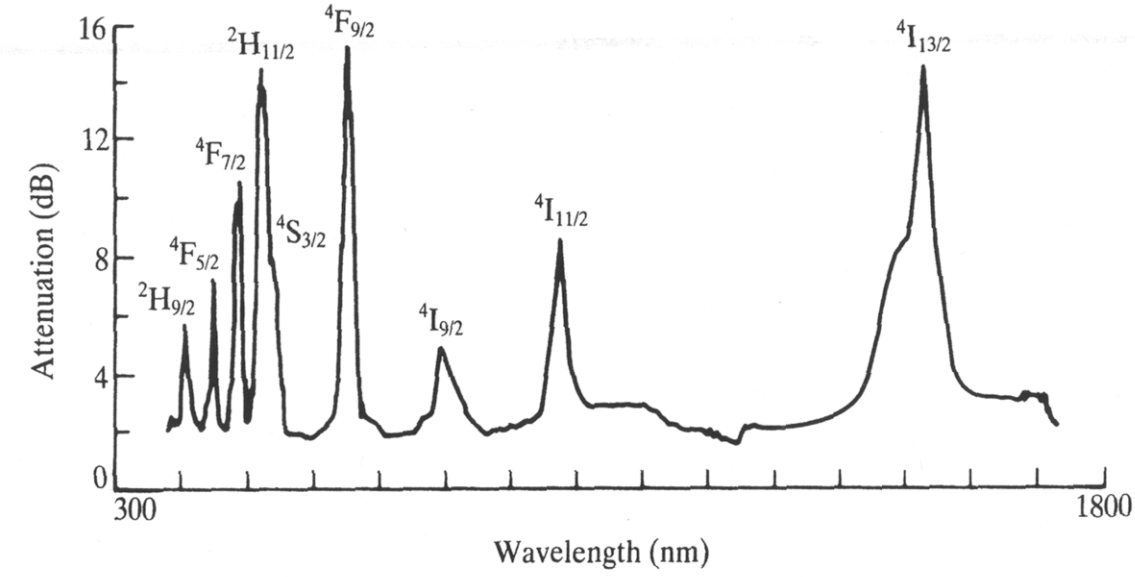

Figure 3.6: Absorption spectrum of erbium doped fiber. We utilized the absorption peak labeled $4I_{13/2}$ ($\lambda = 980nm$) for optical pumping in this research. [57]

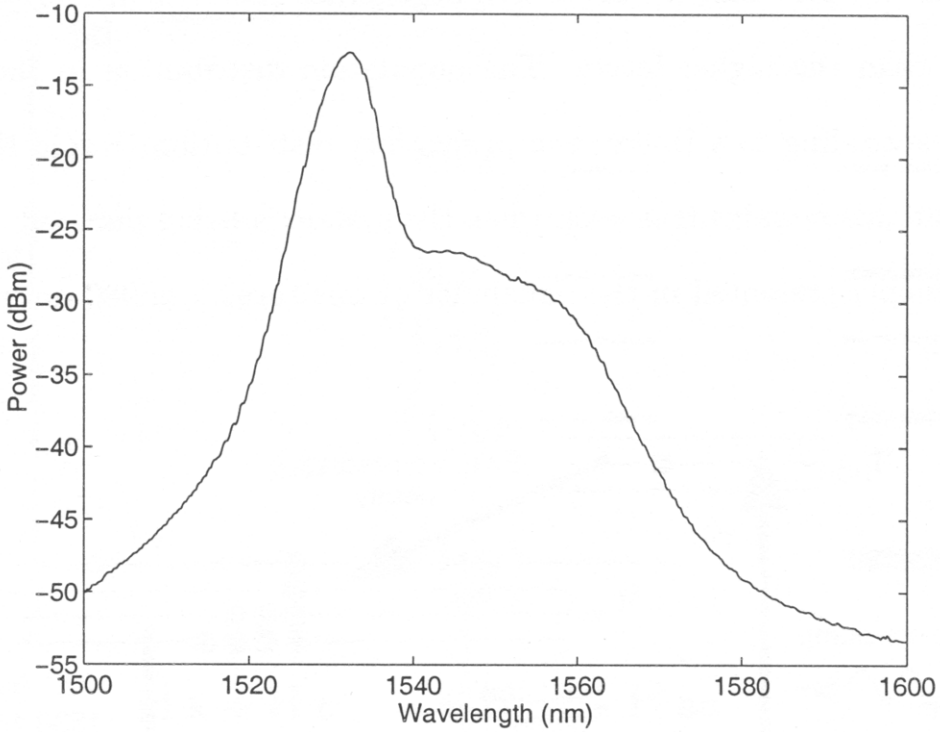

Figure 3.7: Amplified spontaneous emission spectrum of erbium doped fiber optically pumped at $\lambda = 980nm$. The broadening due to the crystal field interaction (Stark effect) produces a gain region extending from $\lambda = 1525nm$ to $\lambda = 1560nm$.

fields change, allowing an expansive broadening of the amplified spontaneous emission spectrum. This broadening is apparent in the amplified spontaneous emission optical spectrum of erbium doped fiber pumped at $\lambda = 980nm$, Fig. 3.7. We observe that the $4I_{13/2} \rightarrow 4I_{15/2}$ transition may now allow significant gain of optical signals with $\lambda = 1525 \rightarrow 1560nm$.

Exhaustive treatments of erbium doped fiber are contained in Refs. [57, 59].

3.5.2 Properties of Optical Fiber

The single-mode nonpolarization-maintaining optical fiber that forms the ring cavity has significant effects on the laser field as well. As the very designation of the fiber suggests, the polarization state of light may be affected by the optical fiber [60].

A length of nonpolarization maintaining fiber may be thought of as a collection of randomly oriented optical waveplates, leading to some net birefringence over the length of the optical fiber. The effect of a length l of optical fiber on the polarization state of the light is expressed by the equation

$$\begin{pmatrix} E_1(l) \\ E_2(l) \end{pmatrix} = \begin{pmatrix} f & g \\ -g^* & f^* \end{pmatrix} \begin{pmatrix} E_1(0) \\ E_2(0) \end{pmatrix}, \tag{3.30}$$

where E_1 and E_2 are the projections of the complex electric field amplitude onto two orthogonal linearly polarized states. The unitary Jones matrix $\begin{pmatrix} f & g \\ -g^* & f^* \end{pmatrix}$ defines the polarization transformation [60]. While the birefringence is sensitive to mechanical and environmental stresses, in a vibration isolated, temperature controlled laboratory the birefringence may be taken to be constant.

An additional effect is due to the fact that the index of refraction $n(\omega)$ is frequency dependent, so when a pulse of light containing a range of frequencies is launched down a fiber, it will become broadened as the component frequencies of the pulse experience a range of $n(\omega)$. This pulse broadening is known as group velocity dispersion, and is quantified by $\beta_2 = d^2\beta/d\omega^2$. $\beta(\omega)$ is defined in the complex electric field by the relation $E'(z,t) = E(z,t)\exp[i(\omega t - \beta(\omega)z)]$ where $E'(z,t)$ is the complex electric field and $E(z,t)$ is its complex amplitude. For single mode optical fiber $\beta_2 \approx -20ps^2/km$ [58].

An additional family of nonlinearities are introduced by the Optical Kerr Effect [61] that describes how the index of refraction is shifted by an intense field. This intensity dependence is written as

$$n(\omega, |E|^2) = n_1(\omega) + n_2|E|^2. \tag{3.31}$$

In optical fiber $n_1(\lambda = 1.5\mu m) = 1.44$ and $n_2 = 2.2 - 3.4 \times 10^{-20} m^2/W$. This nonlinearity leads to self phase modulation and cross phase modulation where one laser mode may modulate the optical phase of another [62]. Additionally, n_2 is not necessarily identical along orthogonal transverse axes of the optical fiber. Therefore, the Optical Kerr Effect may lead to an additional birefringence term in the system.

A final nonlinearity present in optical fiber is four wave mixing where tightly spaced laser modes may generate additional modes [62]. Abarbanel et al. [63] considered these nonlinear effects in a model similar to Eqns. (3.45, 3.46, & 3.47) and concluded the Optical Kerr Effect is the source of chaotic fluctuations in EDFRL intensity time series.

3.5.3 Erbium Doped Fiber Ring Laser

A conventional laser system consists of a linear cavity containing the active medium, with mirrors on either end. The output beam is transmitted through a partially reflecting mirror. In a fiber ring laser, the cavity is not defined by mirrors, and it is far from linear. Instead the two ends of the erbium doped fiber are connected with a length of passive fiber, forming a ring. Light may be coupled from the cavity using an evanescent field coupler. One potential advantage of EDFRLs is the extremely long cavity lengths that they make possible. Typical solid-state laser cavities are only centimeters long. However, EDFRLs may be tens of meters long. This leads to round-trip times on the order of hundreds of nanoseconds, allowing resolution of sub-round trip dynamics [59, 14, 64, 63].

A typical setup of a basic erbium doped fiber ring laser is presented in Fig. 3.8. The active medium of the ring laser is the erbium doped fiber amplifier which contains a length of doped fiber. Figure 3.9 is a schematic of the components of an erbium doped fiber amplifier. The doped optical fiber is optically pumped with a $980nm$ semiconductor diode laser. The pump laser field is injected into the erbium doped fiber using a wave division multiplexing coupler. Also internal to the erbium doped fiber amplifier is a pair of Faraday optical isolators which act as 'diodes' for light. This ensures the unidirectional circulation of the laser field in the ring cavity in the direction of the arrow in Fig. 3.8.

If the ring laser is constructed from nonpolarization maintaining fiber (as the ones used in this research were), then the laser will possess some general elliptical polarization state. By adjusting the net birefringence of the cavity using a polar-

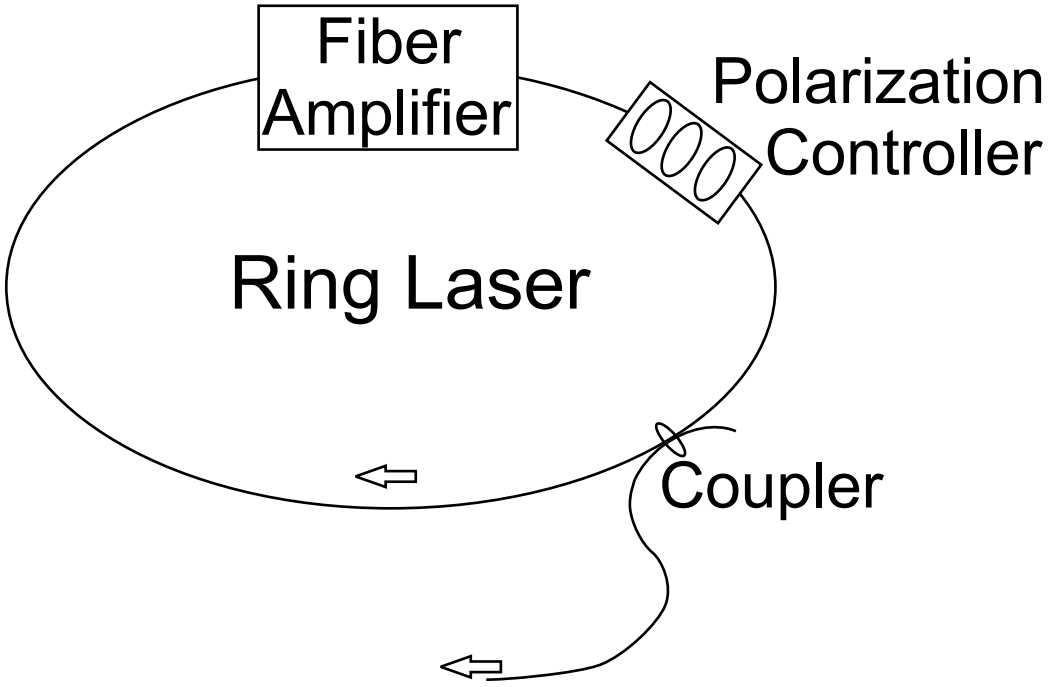

Figure 3.8: Simple erbium doped fiber ring laser setup. The doped fiber amplifier acts as the active medium of the laser. The components are detailed in Fig. 3.9. Light propagates unidirectionally in the ring, and may be coupled out using an evanescent field coupler. The net birefringence of the ring may be adjusted using a polarization controller, affecting a number of experimental observables.

ization controller, it is possible to adjust the polarization state of the ring laser, select from various dynamic regimes, and even tune the optical frequency of the laser. There are two dominant types of polarization controllers. The first type is an all-fiber polarization controller, where mechanical stresses on the fiber (twisting, compression) induce a local shift in birefringence. The second type is an optical wave plate polarization controller consisting of $\lambda/4, \lambda/2, \lambda/4$ optical wave plates. By rotating the plates to adjust their relative orientations, the net birefringence of the cavity is affected.

While an EDFRL operating above threshold possesses a much narrower optical spectrum, it still demonstrates gain over a very wide region. An sample spectrum of an EDFRL is presented in Fig. 3.10. In this case the ring cavity length is $41.5m$ and the system is pumped well above threshold. An optical waveplate polarization controller was used to tune the laser wavelength to a single, well defined peak.

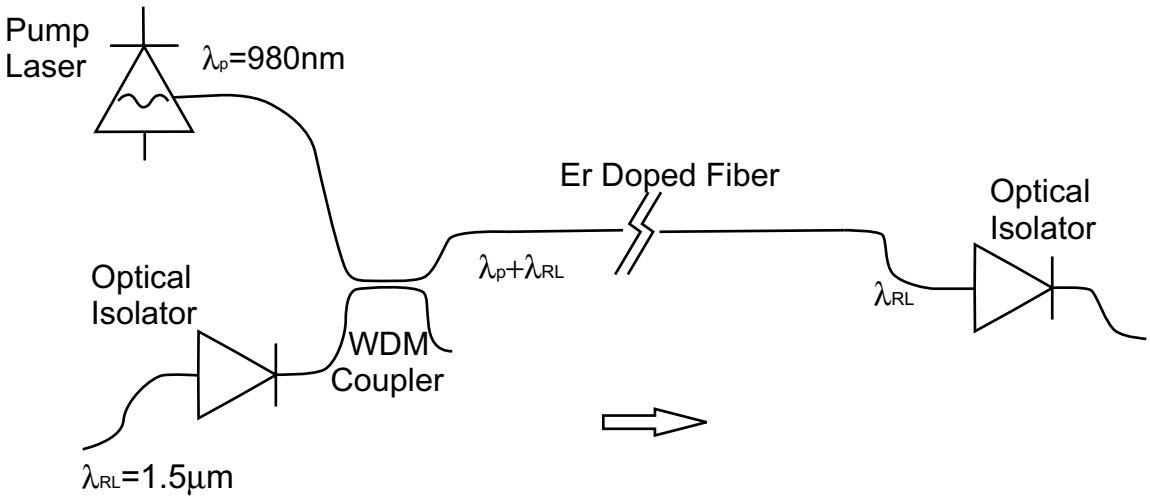

Figure 3.9: Basic component structure of an erbium doped amplifier. A $980nm$ pump laser excites the erbium doped fiber. The pump field is injected into the doped fiber using a wave division multiplexing (WDM) coupler. Two Faraday optical isolators enforce the direction of propagation of the lasers in Fig. 3.8.

The full width at half max of the peak is $\Delta\lambda \approx 600pm$ while the longitudinal mode spacing (determined by the cavity length) is $\approx 40fm$. So the lasing EDFRL possesses approximately 15000 modes!

3.5.4 EDFRL Rate Equations

Due to the length of the ring laser cavity and the division of passive and active fiber, a delay differential representation of the fiber ring laser system is necessary for an accurate representation of the dynamics. Similar equations were presented in Refs. [59, 14], and details of the derivation are corrected here. As mentioned above, we may adiabatically eliminate the polarization term from the EDFRL rate equations. Additionally, we are interested in the case where there is no well defined polarization state. Hence, we begin our derivation of the delay differential laser equations with a system similar to the Class B equations we derived in Sections 3.1

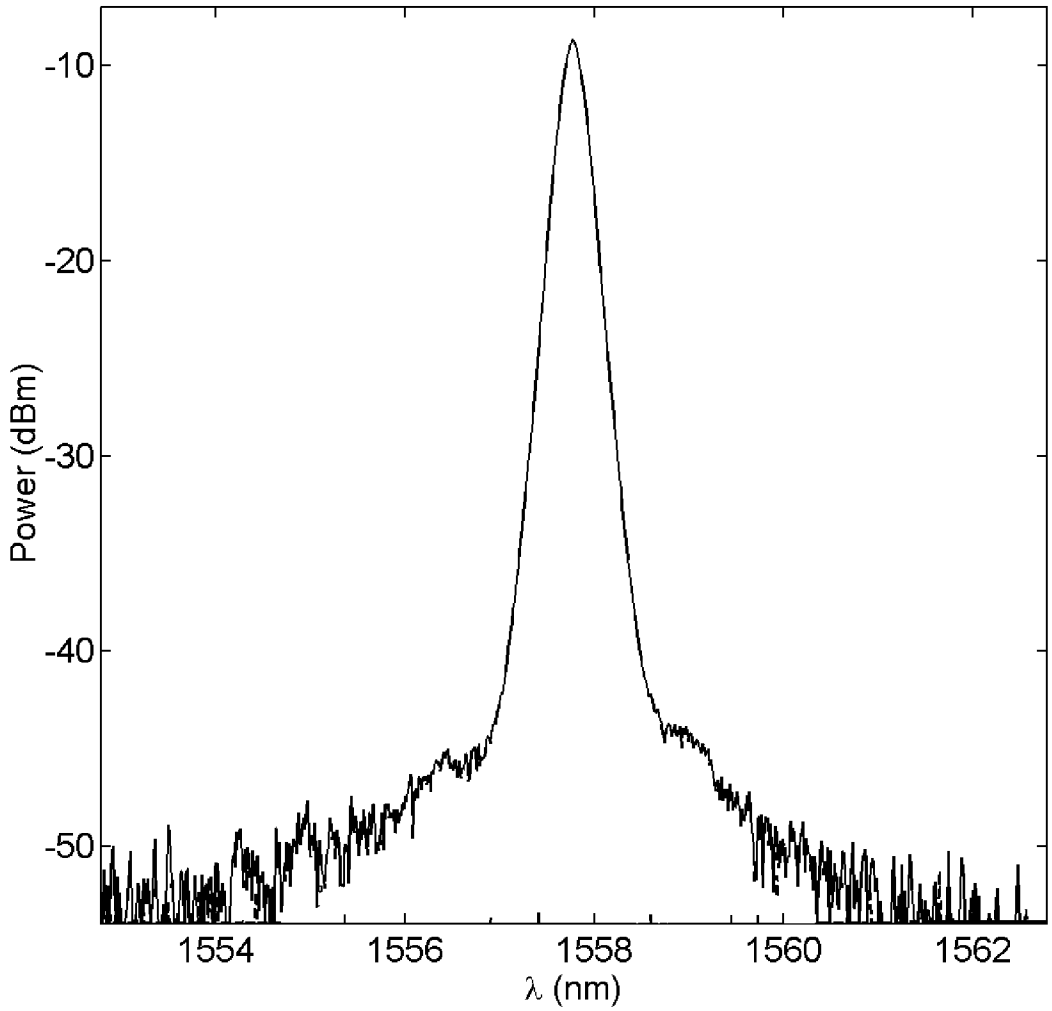

Figure 3.10: Optical spectrum of EDFRL pumped well above threshold. Polarization controllers tuned to produce a single well defined peak. The full width at half max is $\Delta\lambda = 600pm$ while the longitudinal mode spacing is just $40fm$.

& 3.3, Eqns. (3.24 & 3.25),

$$\frac{\partial E_1}{\partial t} = -v_g\frac{\partial E_1}{\partial z} + (\gamma_\perp - i\Delta\omega_1)\frac{\omega_1|p|^2}{\hbar\epsilon(\gamma_\perp^2+\Delta\omega_1^2)}E_1 N, \tag{3.32}$$

$$\frac{\partial E_2}{\partial t} = -v_g\frac{\partial E_2}{\partial z} + (\gamma_\perp - i\Delta\omega_2)\frac{\omega_2|p|^2}{\hbar\epsilon(\gamma_\perp^2+\Delta\omega_2^2)}E_2 N, \tag{3.33}$$

$$\frac{\partial N}{\partial t} = Q - \gamma_\parallel(N+N_{tot}) - \frac{4|p|^2\gamma_\perp}{\hbar}\left(\frac{|E_1|^2}{(\gamma_\perp^2+\Delta\omega_1^2)} + \frac{|E_2|^2}{(\gamma_\perp^2+\Delta\omega_1^2)}\right)N. \tag{3.34}$$

We have decomposed the laser field into two orthogonally polarized fields which are identified by numerical subscripts. The group velocities, v_g, of light along orthogonal polarization directions are identical as we are considering propagation in homogeneous, nonpolarization maintaining, single-mode optical fiber. The decay term for the electric field has been eliminated for the moment, but will be addressed in the boundary conditions of the ring cavity. The consideration of the N_{tot} term is required by the three-level nature of erbium lasers, in which the terminal level of the laser transition is also the ground state. All other variables and parameters are defined as in Section 3.1.

We may simplify these equations by introducing the following change of variables and definitions:

$$N \to N - N_o, \qquad Q = Q + \gamma_\parallel N_o$$
$$a_m = \frac{4|p|^2\gamma_\perp\omega_m}{\hbar\epsilon v_g(\gamma_\perp^2+\Delta\omega_m^2)}, \qquad \Delta_m = \frac{\Delta\omega_m}{\gamma_\perp}.$$

The index $m = 1, 2$ indicates the polarization state and N_o is the threshold population inversion. The ring laser equations now read,

$$\frac{\partial E_1}{\partial t} = -v_g\frac{\partial E_1}{\partial z} + (1-i\Delta_1)v_g\frac{a_1}{4}E_1(N-N_o), \tag{3.35}$$

$$\frac{\partial E_2}{\partial t} = -v_g\frac{\partial E_2}{\partial z} + (1-i\Delta_2)v_g\frac{a_2}{4}E_2(N-N_o), \tag{3.36}$$

$$\frac{\partial N}{\partial t} = Q - \gamma_\parallel(N+N_{tot}) - \epsilon v_g\left(a_1\frac{|E_1|^2}{\hbar\omega_1} + a_2\frac{|E_2|^2}{\hbar\omega_2}\right)(N-N_o). \tag{3.37}$$

In general E_m and N depend on t and z.

This description of the ring laser depends on coupled partial differential equations that may be difficult to approach numerically. By changing coordinates to a

retarded reference frame that moves in step with a light wave circulating in the ring cavity,

$$\tau \equiv t - z/v_g, \tag{3.38}$$

we are able to consider a numerically simpler set of delay and ordinary differential equations. In this reference frame, the field equations may now be written

$$\frac{\partial E_1(z,\tau+\frac{z}{v_g})}{\partial z} = (1-i\Delta_1)\frac{a_1}{4}E_1(z,\tau+\frac{z}{v_g})\big(N(z,\tau+\frac{z}{v_g})-N_o\big), \tag{3.39}$$

$$\frac{\partial E_2(z,\tau+\frac{z}{v_g})}{\partial z} = (1-i\Delta_2)\frac{a_2}{4}E_2(z,\tau+\frac{z}{v_g})\big(N(z,\tau+\frac{z}{v_g})-N_o\big). \tag{3.40}$$

Proper construction of the delay differential equations requires that we treat the active and passive lengths of fiber separately. We now consider the effect of the doped fiber length. Making the simplifying and naive assumption that the active fiber is non-birefringent, the effect of the gain medium on the electric fields in the retarded reference frame may be found by integrating over the length of the active fiber $\mathcal{L}$. We find

$$E_1(\mathcal{L},\tau+\frac{\mathcal{L}}{v_g}) = E_1(0,\tau)\exp\Big[\frac{a_1}{4}(1-i\Delta_1)(W(\tau+\frac{\mathcal{L}}{v_g})-W_o)\Big], \tag{3.41}$$

$$E_2(\mathcal{L},\tau+\frac{\mathcal{L}}{v_g}) = E_2(0,\tau)\exp\Big[\frac{a_2}{4}(1-i\Delta_2)(W(\tau+\frac{\mathcal{L}}{v_g})-W_o)\Big], \tag{3.42}$$

where $W(\tau+\mathcal{L}/v_g)=\int_0^{\mathcal{L}} N dz(z,\tau+z/v_g)$ is the total population inversion for the doped fiber laser, and $W_o = N_o\mathcal{L}$. Integrating Eqn. (3.37) over the doped length of fiber, we find the rate equation

$$\begin{aligned}\frac{dW(\tau)}{d\tau} &= Q\mathcal{L} - \gamma_{\|}(W(\tau)+W_{tot}) \\ &\quad -v_g\epsilon\frac{|E_1(0,\tau)|^2}{\hbar\omega_1}\big(\exp[a_1\{W(\tau+\frac{\mathcal{L}}{v_g})-W_o\}]-1\big) \\ &\quad -v_g\epsilon\frac{|E_2(0,\tau)|^2}{\hbar\omega_2}\big(\exp[a_2\{W(\tau+\frac{\mathcal{L}}{v_g})-W_o\}]-1\big),\end{aligned} \tag{3.43}$$

where $W_{tot} = N_{tot}\mathcal{L}$.

The boundary conditions due to the passive fiber are found by considering the effect the fiber has on the electric field as it travels its length. The losses in the ring laser may be isolated in the passive fiber and are represented by the return

coefficient R. For a EDFRL of total length L and active fiber length $\mathcal{L}$ the boundary conditions are

$$\begin{pmatrix} E_1(0,\tau) \\ E_2(0,\tau) \end{pmatrix} = R \begin{pmatrix} f & g \\ -g^* & f^* \end{pmatrix} \begin{pmatrix} E_1(\mathcal{L}, \tau - \frac{L-\mathcal{L}}{v_g}) \\ E_2(\mathcal{L}, \tau - \frac{L-\mathcal{L}}{v_g}) \end{pmatrix}. \tag{3.44}$$

This set of boundary conditions defines the electric field at the input of the doped fiber ($z = 0$) as a time delayed, attenuated version of the field leaving the gain medium that has undergone some polarization rotation. This polarization rotation is defined by the unitary Jones matrix $\begin{pmatrix} f & g \\ -g^* & f^* \end{pmatrix}$, and accounts for the birefringent nature of optical fiber [60]. Applying these boundary conditions to Eqns. (3.41, 3.42, & 3.43) the completed delay-differential EDFRL model is

$$\begin{aligned} E_1(\mathcal{L}, \tau + \frac{\mathcal{L}}{v_g}) &= R\Big(fE_1(\mathcal{L}, \tau - \frac{L-\mathcal{L}}{v_g}) + gE_2(\mathcal{L}, \tau - \frac{L-\mathcal{L}}{v_g})\Big) \times \\ &\quad \exp\Big[\frac{a_1}{4}(1 - i\Delta_1)(W(\tau + \frac{\mathcal{L}}{v_g}) - W_o)\Big], \qquad (3.45) \\ E_2(\mathcal{L}, \tau + \frac{\mathcal{L}}{v_g}) &= R\Big(-g^*E_1(\mathcal{L}, \tau - \frac{L-\mathcal{L}}{v_g}) + f^*E_2(\mathcal{L}, \tau - \frac{L-\mathcal{L}}{v_g})\Big) \times \\ &\quad \exp\Big[\frac{a_2}{4}(1 - i\Delta_2)(W(\tau + \frac{\mathcal{L}}{v_g}) - W_o)\Big], \qquad (3.46) \\ \frac{dW(\tau)}{dt} &= Q\mathcal{L} - \gamma_{\parallel}(W(\tau) + W_{tot}) \\ &\quad -v_g\epsilon R^2 \frac{|fE_1(\mathcal{L}, \tau - \frac{L-\mathcal{L}}{v_g}) + gE_2(\mathcal{L}, \tau - \frac{L-\mathcal{L}}{v_g})|^2}{\hbar\omega_1} \\ &\quad \big(\exp[a_1\{W(\tau + \frac{\mathcal{L}}{v_g}) - W_o\}] - 1\big) \\ &\quad -v_g\epsilon R^2 \frac{|-g^*E_1(\mathcal{L}, \tau - \frac{L-\mathcal{L}}{v_g}) + f^*E_2(\mathcal{L}, \tau - \frac{L-\mathcal{L}}{v_g})|^2}{\hbar\omega_2} \\ &\quad \big(\exp[a_2\{W(\tau + \frac{\mathcal{L}}{v_g}) - W_o\}] - 1\big). \qquad (3.47) \end{aligned}$$

Note that the time delay in the field equations is equal to L/v_g, the round trip time of light in the ring cavity. This leads to chaotic structures which will nearly repeat on round trip timescales. We shall see evidence of this dynamic feature in power spectra of EDFRL intensity time series in Sections 6.2 & 6.3. For a discussion of the sub-round trip dynamics of EDFRLs, see Refs. [59, 14]

Chapter 4

Synchronization of Chaos in a Three Laser Array

4.1 Laser Arrays

Lasers are an incredible tool for research, and they have many practical applications. This is due, in large part, to their unique ability to produce highly directional, monochromatic, coherent light. However, many applications are power-intensive, and there are limitations to the output of a single laser, because of technical (e.g. material breakdown due to large local fields) and practical considerations (e.g. cost, ease of construction). Fortunately, an array of relatively weak lasers may be coupled together in such a way that they are phase locked, producing peak powers that are far beyond what can be produced by a single laser, while maintaining the desirable properties of a single laser. Since intensity is the square of the electric field amplitude, the peak intensity of a phase-locked array is given

$$I = |E|^2 = \left|\sum_{j=1}^{N} E_j\right|^2 = N^2|E_o|^2. \tag{4.1}$$

Here, E and E_j are the complex electric fields of the laser array and array elements, respectively. We assume each of the N lasers is of equal intensity, such that $E_j = E_o$. In the case of an unlocked array, the fields add incoherently, so the peak intensity of the array is simply the sum of the individual intensities of the component lasers, $I = N|E_o|^2$ [65].

The first investigations into coupled arrays of lasers were conducted by Basov and co-workers in 1965 [66, 67], in their attempts to produce coherent light with an array of semiconductor diode lasers. Advanced, high power semiconductor arrays are commonplace today in laboratories and industry.

Synchronization is another important consequence of coupling lasers. Synchronized chaotic lasers allow the possibility of hiding messages in the chaotic waveforms. Such a communication scheme was demonstrated by VanWiggeren and Roy using erbium-doped fiber ring-lasers [68, 14]. Recently Tang et al. have demonstrated transmission of pseudo-random bits at $2.5GHz$ using synchronized, chaotic semiconductor diode lasers [69].

However, semiconductor diode laser arrays do not always lend themselves to easy study. The fast evolution of their electric fields, combined with the inability to modify coupling of the array elements, makes detailed, thorough experiments difficult. Constructing a coupled solid state laser array in neodymium doped yttrium aluminum garnet (Nd:YAG), where the relaxation oscillations are on the order of $100kHz$, allows greater experimental resolution of the laser dynamics. Additionally, the distance between lasers in the array and hence the coupling, may be varied in this solid state array, allowing greater experimental flexibility. A study of synchronization in such an array makes up the remainder of this chapter and the following chapter, with the notable exception of Section 4.1.5. We begin by reviewing coupling, instabilities and synchronization found in previous studies of a two element Nd:YAG laser array [70, 71, 72]. We also review predictions of synchronization in a three element semiconductor laser array model studied by Winful and Rahman [73] in Section 4.1.5.

4.1.1 Two Coupled Laser Model

It is straightforward to expand the Class-B laser equations describing a single Nd:YAG laser presented in Section 3.4.2 to an array of two mutually coupled, single mode lasers, resulting in the system [70]

$$\begin{aligned}
\frac{dE_1}{dt} &= \tau_c^{-1}[(G_1 - \epsilon_1)E_1 - \kappa E_2] + i\omega_1 E_1, \\
\frac{dG_1}{dt} &= \tau_f^{-1}[p_1 - G_1 - G_1|E_1|^2], \\
\frac{dE_2}{dt} &= \tau_c^{-1}[(G_2 - \epsilon_2)E_2 - \kappa E_1] + i\omega_2 E_2, \\
\frac{dG_2}{dt} &= \tau_f^{-1}[p_2 - G_2 - G_2|E_2|^2].
\end{aligned} \tag{4.2}$$

As before, E_n is the slowly varying complex electric field, and G_n is the real gain. The index $n = 1, 2$ designates the array element. The time scales of the lasers are largely determined by $\tau_c \approx 400 - 500ps$ and $\tau_f \approx 240\mu s$, the cavity round trip time and the population decay time, respectively. ϵ_n is the loss coefficient, and p_n is the pump rate. The critical deviations from the single laser equations are the coupling parameter κ, and the detuning ω_n of laser n from some common cavity mode. Notice that the coupling is confined to the field equations. The negative sign preceding κ is due to the observed stable state of anti-phase locking, where the two lasers are locked π out of phase. We shall discuss this term in more detail in the following section.

By decomposing the complex electric field such that $E(t) = \mathcal{E}(t)exp[i\phi(t)]$, where $\mathcal{E}(t)$ is the real, time varying electric field amplitude and $\phi(t)$ is the real

phase we may re-write Eqns. (4.2) in the more transparent form

$$\begin{aligned}
\frac{dI_1}{dt} &= 2\tau_c^{-1}[(G_1-\epsilon_1)I_1 - \kappa\sqrt{I_1 I_2}\cos(\phi_2-\phi_1)], \\
\frac{dG_1}{dt} &= \tau_f^{-1}[p_1 - G_1 - G_1 I_1], \\
\frac{d\phi_1}{dt} &= \omega_1 - \frac{1}{\tau_c}\sqrt{\frac{I_2}{I_1}}\kappa\sin(\phi_2-\phi_1), \\
\frac{dI_2}{dt} &= 2\tau_c^{-1}[(G_2-\epsilon_2)I_2 - \kappa\sqrt{I_2 I_1}\cos(\phi_1-\phi_2)], \\
\frac{dG_2}{dt} &= \tau_f^{-1}[p_2 - G_2 - G_2 I_2], \\
\frac{d\phi_2}{dt} &= \omega_2 - \frac{1}{\tau_c}\sqrt{\frac{I_1}{I_2}}\kappa\sin(\phi_1-\phi_2).
\end{aligned} \tag{4.3}$$

The individual laser intensities are given by $I_n = |E_n|^2$. As we are interested in the synchronization of two identical, mutually coupled lasers, we allow $\epsilon_n = \epsilon$ and $p_n = p$.

4.1.2 Coupling and Coherence

A population inversion, and hence laser action, in the experiment is achieved by optically end-pumping the Nd:YAG crystal with two identical beams from an argon ion laser operating at $\lambda = 514.5nm$. in this fashion we generate two parallel Nd:YAG lasers. In the Nd:YAG crystal the pump beam have waists of $w_o \approx 20\mu m$, and the dimension of the infrared Nd:YAG lasers ($\lambda = 1064nm$) are $w_o \approx 200\mu m$. Assuming a Gaussian intensity distribution, w_o is the $1/e^2$ radius of the beam. Even in the strongly coupled case where the two Nd:YAG lasers are separated by just $d = 0.6mm$, we clearly see that coupling is solely due to the overlap of the electric fields of the Nd:YAG lasers, Fig. 4.1, as there is no overlap of the fields of the pump beams. The gain region of the crystal is defined by the extent of the pump beam, and hence there is no coupling by gain sharing, either. This fact is apparent in the model, Eqns. (4.2). The profile and dimension of the lasers are experimentally verified using a photodiode with a rotating slit aperture.

The level of coupling between the infrared lasers is determined by calculating the overlap integral of the transverse fields. With a Gaussian intensity distribution,

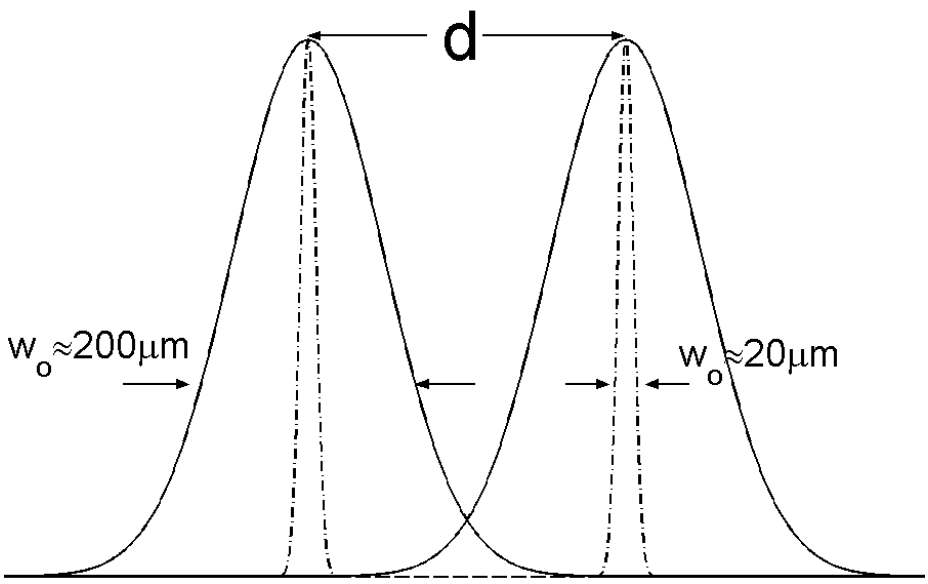

Figure 4.1: Coupling in the laser array is due solely to the overlap of the fields of the Nd:YAG lasers. The transverse electric field amplitudes of the coupled Nd:YAG lasers (solid lines) and the Ar^+ pump lasers (dash-dot lines) are plotted assuming Gaussian intensity distributions and a separation of $d = 0.6mm$. This corresponds to a strongly coupled case with $\kappa \approx 10^{-3}$.

a constant phase front, and a $1/e^2$ radius of w_o we write the transverse electric field of a single laser as

$$E_n'(x,y,t) = \frac{E_n(t)}{\pi w_o^2} e^{\left[-\frac{x^2+y^2}{w_o^2}\right]}. \tag{4.4}$$

Then the overlap integral of the fields of the two Nd:YAG lasers separated by a distance d is

$$\int_{-\infty}^{\infty}\int_{-\infty}^{\infty} dxdy E_1'(x+d,y,t)E_2'(x,y,t) = \frac{E_1(t)E_2(t)}{2\pi w_o^2}\exp\Big[-\frac{d^2}{2w_o^2}\Big]. \tag{4.5}$$

With proper normalization such that for a separation of $d = 0$, $\kappa = 1$, we then define [70]

$$\kappa \equiv \exp\Big[-\frac{d^2}{2w_o^2}\Big]. \tag{4.6}$$

With sufficiently large coupling κ, the two lasers of the experimental array lock and synchronize [70]. In this case, intensities and gains of the two lasers are identical, and Eqns. (4.3) reduce to just three equations describing the intensity,

gain and phase difference $\Phi = \phi_1 - \phi_2$ of the two lasers. This final equation,

$$\frac{d\Phi}{dt} = (\omega_1 - \omega_2) + 2\kappa\tau_c^{-1} \sin\Phi, \tag{4.7}$$

is the Adler equation [74] and has been frequently used to study coupled oscillators [75]. In the limit of small detuning, $\Delta\omega = \omega_1 - \omega_2 << 2\kappa\tau_c^{-1}$, the two laser array is stable only in the anti-phase locked state corresponding to $\Phi = \pi$. Instabilities and relative phase jumps were reported at the critical value of $\Delta\omega \approx 2\kappa\tau_c^{-1}$ [70, 71] and shall be discussed in the next section. Large detunings preclude phase locking.

Experimentally, the stable anti-phase locked state is easily observable in the far-field intensity distribution. In Fig. 4.2 [70] the two-lobed structure shows destructive interference along the line of symmetry, demonstrating that the two lasers are locked with a phase difference of $\Phi = \pi$. A single lobe would be seen in the case of locking with $\Phi = 0$. The separation of the two lasers is $d = 0.6mm$.

As the coupling of the two lasers increases, the level of mutual coherence increases as well. Coherence may be quantified experimentally by measuring the visibility V, the depth of interference fringes resulting in overlapping the two lasers. Visibility is defined by the relation

$$V \equiv \frac{\langle I\rangle_{max} - \langle I\rangle_{min}}{\langle I\rangle_{max} + \langle I\rangle_{min}}, \tag{4.8}$$

where I_{max} is the peak intensity and I_{min} is the minimum intensity due to constructive and destructive interference of the laser fields [70]. A value of $V = 0$ indicates uncoupled, mutually incoherent beams, and $V = 1$ corresponds to the locked, mutually coherent case.

Analytically, we may calculate the time averaged interference pattern resulting from overlapping two laser fields using the equation

$$\langle I\rangle = \langle|E_1|^2\rangle + \langle|E_2|^2\rangle + 2|\langle E_1^* E_2\rangle| \cos(\omega(t_1 - t_2) + \varphi), \tag{4.9}$$

where φ is some initial phase difference [9]. It may be shown that Eqn. (4.8) is equivalent to the analytically more convenient definition

$$V \equiv \sqrt{\langle\cos(\Phi)\rangle^2 + \langle\sin(\Phi)\rangle^2} \tag{4.10}$$

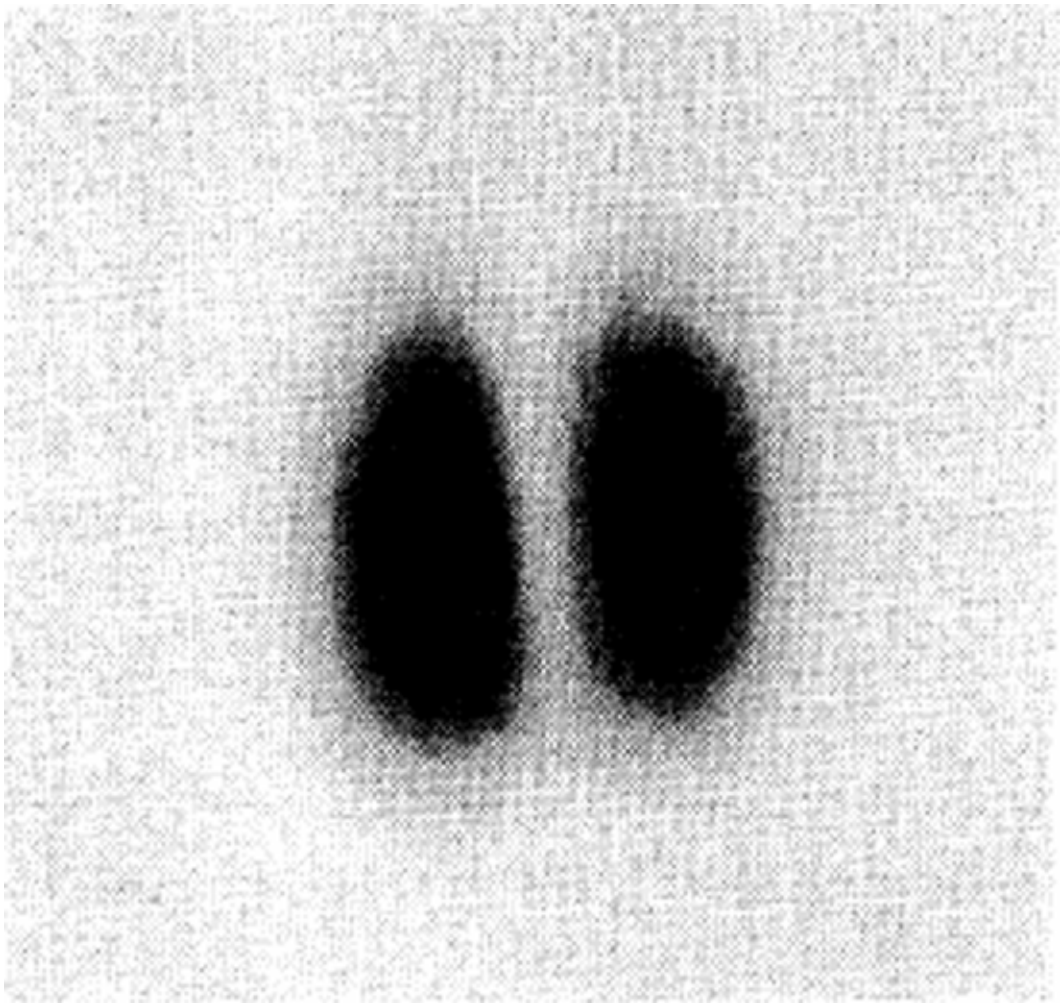

Figure 4.2: The far-field intensity distribution of two anti-phase locked Nd:YAG lasers. The two lobed structure shows destructive interference along the line of symmetry, demonstrating that the two lasers are locked with a phase difference of $\Phi = \pi$. Increasing intensity is represented by darker shading. The lasers are separated by $d = 0.6mm$. [70]

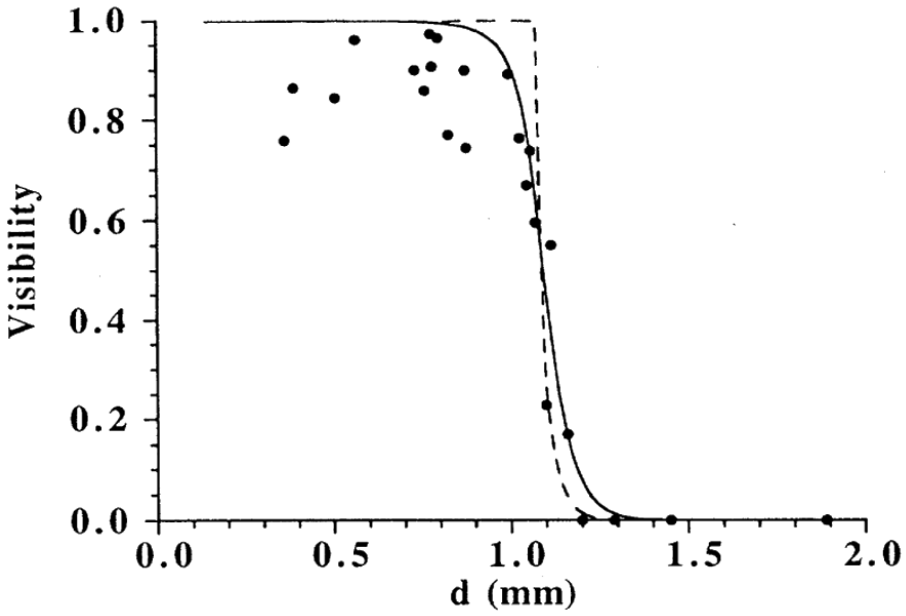

Figure 4.3: Comparison of experimental and theoretical measurements of visibility as a function of beam separation. The discrete points correspond to experimental measurements with $w_o \approx 200\mu m$. The dashed visibility curve is calculated by choosing a detuning $\Delta\omega = 5000\, rad/s$ and beam size $w_o = 200\mu m$. Increasing the beam size to $w_o = 250\mu m$, the solid visibility curve is predicted. [70]

We find good agreement between experimental measurements of visibility and the theoretically predicted values in Fig. 4.3 [70]. The discrete points represent experimental measurements of visibility at increasing beam separations (decreasing coupling). The dashed visibility curve is calculated by choosing a detuning $\Delta\omega = 5000\,rad/s$ and beam size $w_o = 200\mu m$. Increasing the beam size to $w_o = 250\mu m$ the solid visibility curve is predicted.

4.1.3 Amplitude Instabilities

We now return to the critical value of detuning in the Adler equation, Eqn. (4.7), where $\Delta\omega \approx 2\kappa\tau_c^{-1}$. In this case the intensities of the coupled lasers are periodically modulated due to the $\cos(\Phi)$ term in Eqns (4.3). The modulation frequency is simply given by

$$\omega_{mod} = \sqrt{\Delta\omega^2 - (2\kappa\tau_c^{-1})^2}. \tag{4.11}$$

In the situation that ω_{mod} is close to the relaxation frequency of the laser elements of the array, subharmonic resonances may occur, inducing amplitude instabilities and deterministic chaos [76, 77]. We observe these instabilities in the three laser array in Section 4.3 as well. The destabilizing effect of tuned modulation on laser systems has been widely studied [78, 79, 80, 81].

In the two element Nd:YAG laser array under consideration, the relaxation oscillation frequency is $\nu_{rel} \approx 100kHz$. Amplitude instabilities are observed, Fig. 4.4(a), when the lasers are positioned with an intermediate separation of $d = 1.03mm$, producing a coupling of $\kappa \approx 2 \times 10^{-5}$, and an experimentally determined detuning of $\Delta\omega \approx 2\pi \times 1MHz$. Additionally, large variations of the detuning frequency of the two lasers on the order of $10MHz$ were observed in the amplitude instability regime. [71]

In order to model the laser array dynamics in this unstable regime, a stochastic colored noise term is added to the detuning of the lasers in Eqns. (4.2). Varying the frequency shift of each of the lasers from the common cavity mode independently, $\omega_n = \omega_{0,n} + \xi_n(t)$. The mean detuning from the common mode is given by $\omega_{0,n}$.

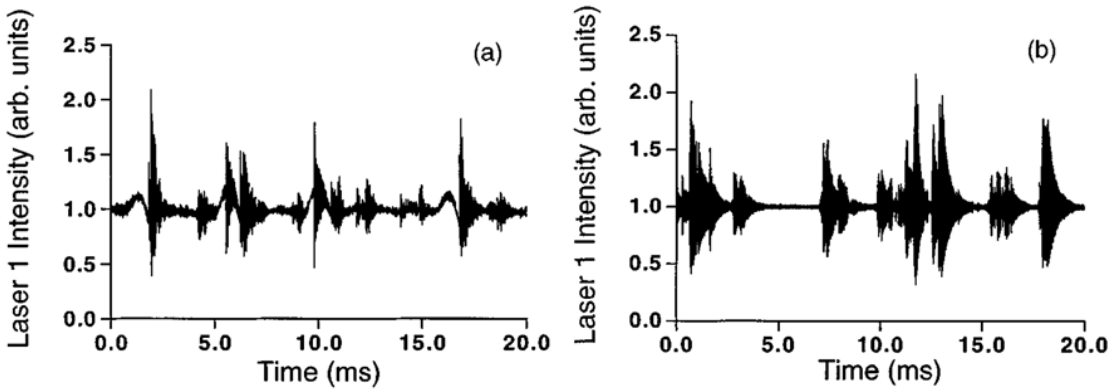

Figure 4.4: Experimental (a) and numerical (b) intensity time series displaying amplitude instabilities. The instabilities are due to subharmonic resonances between the individual relaxation oscillation frequencies and periodic modulations found at intermediate levels of coupling between the two lasers of the array. The experimental time series (a) was obtained with a beam separation of $d = 1.03mm$. The simulated time series (b) was calculated using stochastically varying detuning with a mean of $\overline{\Delta\omega} = 5 \times 10^5 s^{-1}$. The variation was supplied by a zero mean colored noise of strength $D = 5 \times 10^9 s^{-1}$ and a correlation time $\theta = 3ms$. [71]

$\xi_n(t)$ is the colored noise term with a zero mean, strength D and correlation time θ such that $\langle \xi_n(t)\xi_m(t')\rangle = \delta_{nm}\frac{D}{\theta}\exp[-|t'-t|/\theta]$ [82]. Choosing $D = 5 \times 10^9 s^{-1}$ and $\theta = 3ms$ with a mean relative detuning of $\overline{\Delta\omega} = 5 \times 10^5 s^{-1}$, simulations of the laser equations show good agreement with experimental results, Fig. 4.4(b) [71].

4.1.4 Synchronization of Two Coupled Lasers

With increased coupling, resulting in phase locking and mutual coherence of the laser array elements, it is only natural to expect synchronization of the intensity dynamics to follow. To justify this expectation, we briefly study the stability analysis of Eqns.(4.2)[14]. Changing variables to the sum and difference variables $I_+ = I_1 + I_2$,

$I_- = I_1 - I_2$, $G_+ = G_1 + G_2$, and $G_- = G_1 - G_2$ we find the system

$$\begin{aligned}
\frac{dI_+}{dt} &= 2\tau_c^{-1}\left[\frac{G_+I_+}{2} + \frac{G_-I_-}{2} - \epsilon I_+ + \kappa\sqrt{I_+^2 - I_-^2}\right], \\
\frac{dG_+}{dt} &= \tau_f^{-1}\left[2p - \frac{G_+I_+}{2} - \frac{G_-I_-}{2} - G_+\right], \\
\frac{dI_-}{dt} &= 2\tau_c^{-1}\left[\frac{G_+I_-}{2} + \frac{G_-I_+}{2} - \epsilon I_-\right], \\
\frac{dG_-}{dt} &= \tau_f^{-1}\left[-\frac{G_+I_-}{2} - \frac{G_-I_+}{2} - G_-\right], \\
\frac{d\Phi}{dt} &= \Delta\omega + \kappa\tau_c^{-1}\left(\frac{2I_+}{\sqrt{I_+^2 - I_-^2}}\right).
\end{aligned} \tag{4.12}$$

Here, $\Phi = \phi_1 - \phi_2$ as before. We may refer to the sum and difference variables as the tangential and transverse variables, respectively, as they describe movement along and orthogonal to the synchronization manifold. The stable, anti-phase locked state corresponds to the fixed points $\Phi' = (2j+1)\pi$, and $I'_- = G'_- = 0$, where j is some integer. The fixed points for the tangential variables are calculated by setting $dI_+/dt = dG_+/dt = 0$, resulting in the complete set of fixed points

$$\begin{aligned}
I'_+ = \tfrac{2p}{\epsilon-\kappa} - 2,\ G'_+ = 2(\epsilon - \kappa), \\
I'_- = 0,\ G'_- = 0, \\
\Phi' = (2j+1)\pi.
\end{aligned} \tag{4.13}$$

Linearizing Eqns. (4.12) about these fixed points, we compute the tangential Lyapunov exponents

$$\lambda_+ = \frac{1}{2}\left(-\frac{2+I'_+}{2\tau_f} \pm \sqrt{\frac{(2+I'_+)^2}{4\tau_f^2} - \frac{2G'_+I'_+}{2\tau_f\tau_c}}\right), \tag{4.14}$$

and the transverse Lyapunov exponents

$$\lambda_- = \frac{1}{2}\left(-\frac{2\kappa}{\tau_c} - \frac{2+I'_+}{2\tau_f} \pm \sqrt{\left(-\frac{2\kappa}{\tau_c} - \frac{2+I'_+}{2\tau_f}\right)^2 - \frac{\kappa(2+I'_+)}{\tau_c\tau_f} - \frac{2G'_+I'_+}{2\tau_f\tau_c}}\right). \tag{4.15}$$

As the real parts of both sets of exponents are negative, the set of fixed points in Eqns. (4.13) are stable, and the dynamics of the two laser array will remain on the synchronization manifold.

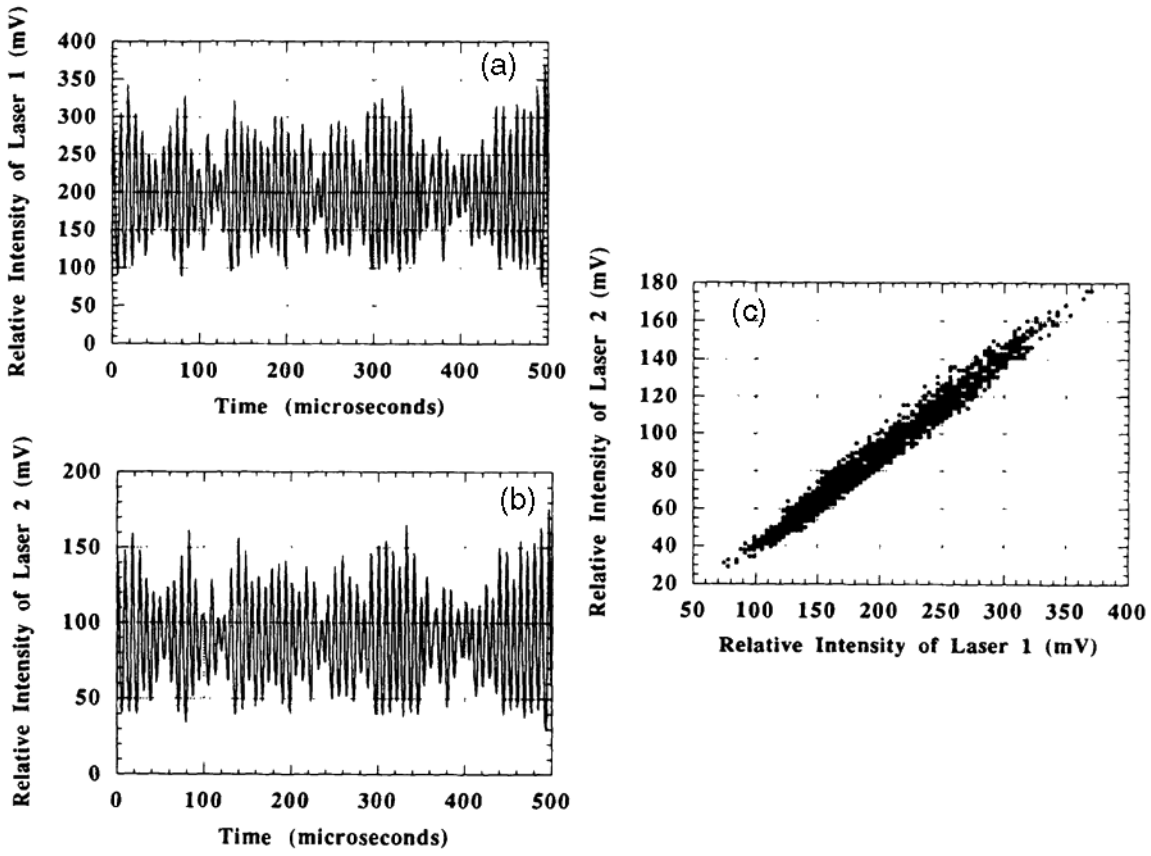

Figure 4.5: Synchronization of chaotic intensity dynamics in a coupled two laser array. The pump beams are separated by $d = 0.75mm$, and pump beam 1 is modulated near the relaxation oscillation frequency of $\nu_{rel} \approx 130kHz$ to induce chaotic fluctuations in the array. Due to the coupling of the Nd:YAG lasers, the intensity time series of laser 1 (a) and laser 2 (b) show matched fluctuations. The x-y synchronization plot (c) of the dynamics demonstrates the strength of the synchronization as there are only minimal deviations from the diagonal.[72]

Perhaps a more interesting question is "What will happen if the coupled lasers display chaotic dynamics?". In Ref. [72], the pump beam of laser 1 is modulated near the relaxation oscillation frequency $\nu_{rel} \approx 130kHz$, resulting in chaotic intensity fluctuations. With large separations, $d > 1.2mm$, laser 2 is unaffected and continues steady state operation. Decreasing the separation to $d = 0.75mm$, hence increasing the coupling strength to $\kappa = 8.8 \times 10^{-4}$, the two lasers are anti-phase locked and demonstrate synchronized chaotic intensity fluctuations. Fig. 4.5 [72] displays the intensity time series of the two lasers (a & b) and the x-y synchronization plot (c), where the intensity of laser 2 is plotted against the intensity of laser 1. A cursory inspection of the intensity time series reveals nearly identical dynamical behavior, and is verified by the x-y synchronization plot where there are only minimal deviations away from the diagonal in Fig. 4.5(c) [72].

4.1.5 Synchronization in a Model of Three Coupled Semiconductor Lasers

Numerically studying a nearest neighbor coupled array of three semiconductor diode lasers Winful and Rahman in 1990 [73] found identical synchronization between the outer two lasers of the array. Surprisingly, this synchronous relationship was not observed between either side laser and the central laser. The model

$$\begin{aligned} \frac{dE_j}{dt} &= \frac{1}{2}\Big[G(N_j) - \tau_p^{-1}\Big](1 - i\alpha)E_j + i\kappa(E_{j+1} + E_{j-1}), \\ \frac{dN_j}{dt} &= P - \frac{N_j}{\tau_s} - G(N_j)|E_j|^2, \end{aligned} \tag{4.16}$$

describes a linear array of laser elements where E_j is the complex slowly varying electric field, $G(N_j)$ is the real gain term that depends on the population inversion N_j, and j is some integer. The level of nearest neighbor coupling is given by κ, α is the line-width enhancement factor, and P is the pump rate. Note that in Nd:YAG and most other solid state lasers, $\alpha = 0$. The time scales of the laser are determined by the photon lifetime $\tau_p \approx 1ps$ and the population inversion decay time $\tau_s \approx 2ns$ [73]. Notice that these typical semiconductor laser time-scales are far faster than

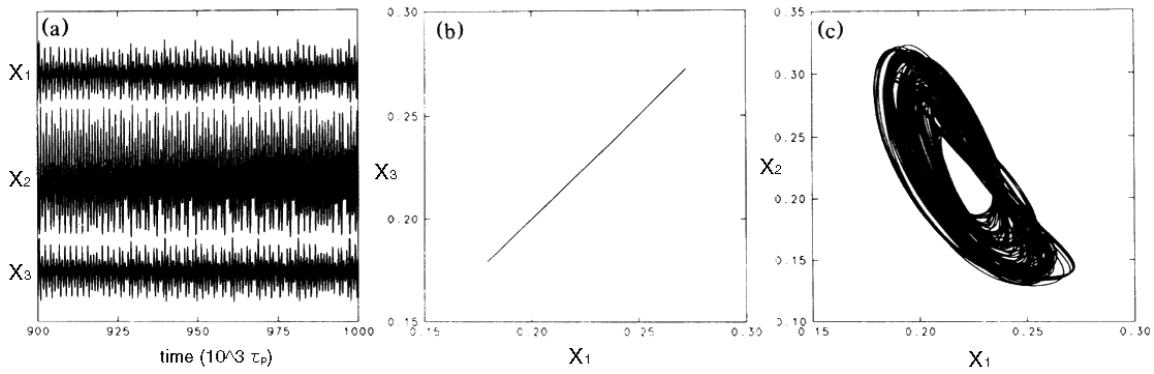

Figure 4.6: Synchronized chaotic dynamics of a simulated three element semiconductor diode laser array. The field amplitude times series X_1, X_2, and X_3 (a) are studied with coupling of $\eta = 10^{-3.5}$. Synchronization is observed between the outer pair, X_1 and X_3 (b), but not between X_1 and X_2 (c). Here the system is simulated with $p = 0.05$, $T = 2 \times 10^3$, and $\alpha = 5$. [73]

those present in Nd:YAG lasers, resulting in quickly evolving intensity dynamics in the semiconductor case.

Transforming variables to obtain a real, unitless system of equations, we find

$$\begin{aligned} \frac{dX_j}{d\tau} &= Z_j X_j - \eta[X_{j+1}\sin(\phi_j - \phi_{j+1}) - X_{j-1}\sin(\phi_{j-1} - \phi_j)], \\ T\frac{dZ_j}{d\tau} &= p - Z_j - (1 + 2Z_j)X_j^2, \\ \frac{d\phi_j}{d\tau} &= \alpha Z_j - \eta\Big[\frac{X_{j+1}}{X_j}\cos(\phi_j - \phi_{j+1}) + \frac{X_{j-1}}{X_j}\cos(\phi_j - \phi_{j-1})\Big]. \end{aligned} \tag{4.17}$$

Here, τ is the reduced time variable, normalized to the photon lifetime, $X_j = \sqrt{0.5g\tau_s}|E_j|$ is the normalized, real field amplitude, $Z_j = 0.5gN_{th}\tau_p(N_j/N_{th} - 1)$ is the normalized population inversion, and ϕ_j is the real phase of the complex field E_j. We have used the definition $g = \delta G/\delta N$, the differential gain, and N_{th} is the threshold population inversion that permits lasing action. The scaled pumping rate is given by $p = 0.5gN_{th}\tau_p(P/P_{th} - 1)$, $\eta = \kappa\tau_p$ describes the coupling, and $T = \tau_s/\tau_p$. [73]

The authors restrict the array to three identical coupled lasers, increasing the coupling beyond the threshold value of $\eta = 10^{-4.43}$, where the laser array shifts from steady state operation to periodically pulsing dynamics. Through a series of period doubling bifurcations, the individual lasers become chaotic. Throughout this

cascade, the outer pair of lasers remain synchronized. In Fig. 4.6(a) [73] we see the chaotic field amplitudes of the three lasers with $\eta = 10^{-3.5}$, $p = 0.05$, $T = 2 \times 10^3$, and $\alpha = 5$. By examining the x-y synchronization plots of the outer pair (X_1 and X_3) Fig. 4.6(b) we verify perfect synchronization; however the relationship of laser 1 with laser 2 does not show this synchronicity, Fig. 4.6(c).

4.2 Experimental Setup

To study the intensity and synchronization dynamics of a loss modulated linear three laser array, we constructed the experimental system shown in Fig. 4.7 [17]. The laser array consists of three parallel, linearly separated neodymium doped yttrium aluminum garnet (Nd:YAG) lasers ($\lambda = 1064nm$) formed in a single crystal $5mm$ in length and diameter. The laser crystal is doped such that it has a 1% concentration of Nd^{3+} by weight. A high power argon ion laser ($\lambda = 514.5nm$, TEM_{00}) serves as the optical pump source, and is divided into three equal intensity beams using the zeroth- and first-order modes of a custom designed fan-out grating donated by Digital Optics Corporation. Only negligible intensities are found elsewhere. The three Ar^+ laser beams are focused and positioned using a simple refracting microscope, constructed from antireflection coated lenses with focal lengths of $fl_1 = 19mm$ and $fl_2 = 100mm$. The resulting configuration is three equal intensity Ar^+ lasers parallel to and symmetric about the axis of the YAG rod. The pump beams have waists of $w_o \approx 20\mu m$ in the YAG crystal. A Coherent Innova 200-15 argon ion laser ($15W$ multi-line and $6.5W$ single line, $\lambda = 514.5nm$) is used as the pump source.

The end-pumped Nd:YAG laser cavity consists of the doped YAG rod with a dielectric, high reflection coating evaporated onto one end, an intra-cavity acousto-optic modulator (AOM) (IntraAction Corp. Model AQS-271AG15 AOM driven at $27MHz$ with a IntraAction Model ME-27D driver), and flat output coupler (OC) with 2% transmittance. The sum power of the three pump beams is approximately $5W$. Beyond allowing us to uniformly loss-modulate the linear laser array, the AOM

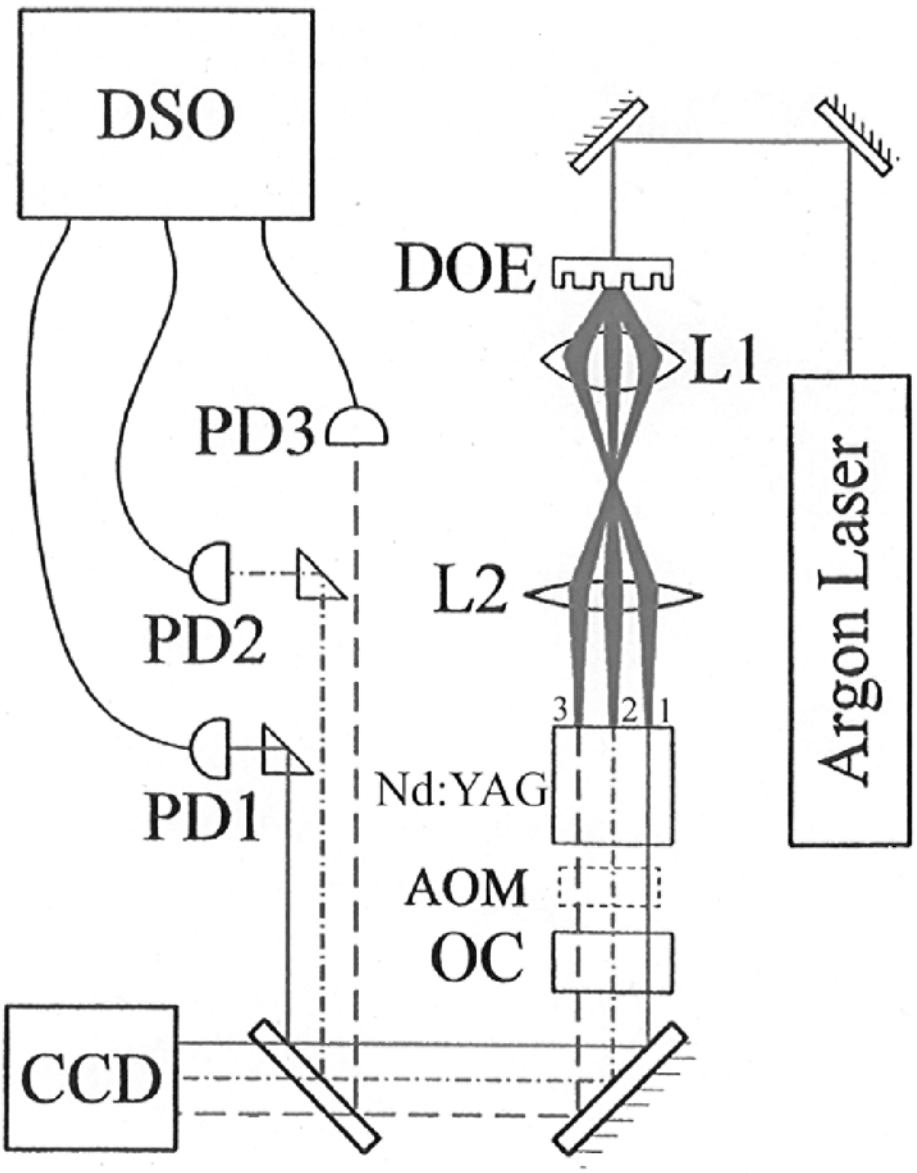

Figure 4.7: Experimental configuration to study the intensity and synchronization dynamics of a linear array of three laterally coupled chaotic lasers generated in a single Nd:YAG rod. The rod is optically end-pumped with three equal intensity argon-ion laser beams. The beams are formed using a diffractive optic element (DOE) where essentially all the power is transmitted to the zeroth- and first-order modes. The separation d of the array of pump beams is controlled using the simple microscope formed by lenses L1 and L2, with focal lengths of $19mm$ and $100mm$, respectively. The Nd:YAG crystal has a high reflection coating on the input side, and an anti-reflection coating on the other. The output coupler (OC) has a 2% transmittance. The intra-cavity acousto-optic modulator (AOM) is used to loss modulate the laser array and serves as a thick étalon. The individual intensity dynamics of the three coupled lasers are sampled with three fast photodetectors (PD1, PD2, and PD3) and recorded using a digital sampling oscilloscope (DSO).

serves as a thick étalon. It's orientation in the laser cavity is adjusted to ensure single longitudinal mode operation, which is verified using a confocal scanning Fabry-Pérot interferometer (Burleigh SA-200-A with a free spectral range of $2GHz$ and a finesse of 200). With these system parameters, the relaxation oscillation frequency of the Nd:YAG lasers is $\nu_{rel} = 140kHz$.

Thermal lensing due to the high intensity pump beams allows the generation of three separate stable cavities in a single Nd:YAG rod [55, 83, 70]. The three TEM_{00}, $\lambda = 1064nm$ lasers possess waists of $w_o \approx 200\mu m$. Each laser is separated from its nearest-neighbor(s) by $d = 0.64mm$; hence, significant coupling is only possible for nearest-neighbor Nd:YAG lasers, and there is no overlap of the pump laser fields. Laser separations and dimensions are measured directly using a photodiode with a rotating slit-aperture (Photon Inc. 1080-10 BeamScan). In this configuration, even without modulation, the infrared lasers display intermittent instabilities due to resonance of the optical phase dynamics with the relaxation oscillations of the laser array [71].

As the stability of the Nd:YAG cavity is provided by thermal lensing, active temperature control of the laser crystal is necessary. This was provided by a temperature controller donated by Spectra-Physics in conjunction with a $10k\Omega$ thermistor (Techno Sfernice, Inc. Model 10TCJ103) and two Melcor FCO, 6-12-05 thermo-electric coolers.

The laser radiation transmitted by the output coupler is a mixture of the green pump beams and the infrared lasers. The remnants of the pump laser are removed with an absorptive Schot glass notch filter (Earling Corp.). The Nd:YAG lasers are isolated by a series of non-polarizing beam-splitting cubes and 90^o prisms. The complex intensity dynamics of the individual infrared lasers are recorded simultaneously at $12.5 \times 10^6 samples/sec$ with three fast photodiodes (Liconix 40D) and a four channel digital sampling oscilloscope (Lecroy 7200).

4.3 Synchronization of a Three Laser Array

The dynamics of individual lasers in the array depends on the depth of loss modulation due to the AOM. With the addition of this dynamic element into the Nd:YAG laser cavity, we now write the time varying loss term in the field equation as

$$\epsilon_n(t) = \epsilon_o + \epsilon_{mod} \sin(2\pi\nu_{mod}t), \tag{4.18}$$

where $\epsilon_o \approx 0.17$ is the intrinsic cavity loss for a given laser in the array ($n = 1, 2, 3$), $\nu_{mod} = 166kHz$ is the modulation frequency, and ϵ_{mod} is the amplitude of the modulation. Fig. 4.8 displays the intensity dynamics of laser 1 with a sample of modulation strengths, ϵ_{mod}. The additional degree of freedom provided by the coupling allows chaotic, intermittent intensity fluctuations even in the unmodulated laser array (top intensity time series, Fig. 4.8). Softly modulating the losses of the cavity at $\nu_{mod} = 166kHz$, the coupled laser displays sustained chaotic dynamics (middle intensity time series, Fig. 4.8). We define soft modulation as a modulation level that never induces enough losses in the cavity to prohibit lasing action. The time series presented was modulated with $\epsilon_{mod} = 0.07$. Hard modulation is therefore loss modulation that is deep enough to preclude lasing action and leads to Q-switched pulse dynamics (bottom intensity time series, Fig. 4.8). The hard modulation time series corresponds to a modulation of $\epsilon_{mod} = 0.23$.

While the various levels of loss modulation lead to striking differences in the behavior displayed by the individual lasers they always display similar synchronous relationships. The experimental measurements of all three lasers with soft loss modulation shown in Fig. 4.9 exemplify this synchronization. The three lasers are simultaneously sampled every $80ns$ for 25000 samples, covering a span of $2ms$. The chaotic intensity time series of the individual lasers of the array are plotted in Figs. 4.9(a-c) with their corresponding power spectra plotted directly below in Figs. 4.9(d-f) respectively. Upon inspection, it is clear the two outer lasers (1 & 3) are nearly identical to each other, but distinctly different from the central beam (laser 2). This observation is confirmed with xy-synchronization plots of the laser dynamics, Figs. 4.9(g-i). Fig. 4.9(h) shows the nearly identical synchronization

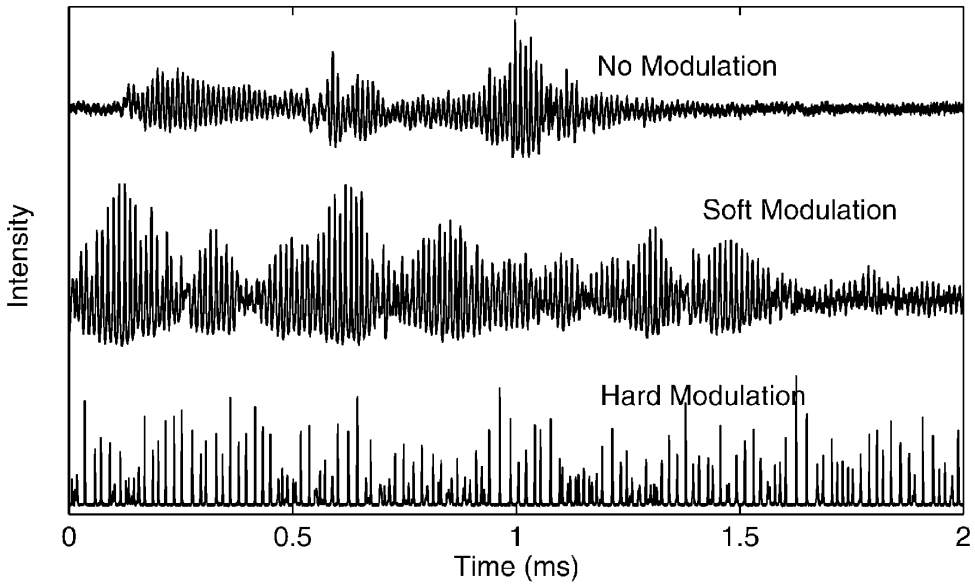

Figure 4.8: Intensity dynamics of the laser array depend on the loss modulation strength. Intermittent complex fluctuations are seen with No Modulation due to the interactions within the coupled laser array. Sustained chaotic behavior is observed with Soft Modulation and the system shifts to Q-switched pulsed dynamics with Hard Modulation.

between the outer pair of lasers. These lasers are only able to interact through the central laser, which, in Figs. 4.9(g & i) reveals no easily discernable relationship with laser 1 or laser 3.

We find differences between the power spectra of the side and central lasers as well, Fig. 4.9(d-f). It is interesting to note the harmonic relationships between the side lasers, 1 and 3, and the central beam, laser 2. The dominant peak for lasers 1 and 3 is at $\nu = 80kHz$. The dominant peak in laser 2's power spectrum is at $\nu = 140kHz$, a peak missing in the two side lasers' power spectra. All three lasers display sharp peaks at $\nu_{mod} = 166kHz$.

The intensity time series dynamics of all three lasers is numerically estimated to be five dimensional, Fig. 4.10, using the false nearest neighbor method [3]. The intensity times series utilized contain 25000 data points spanning $2ms$. The embedding delay time of $\tau \approx 2.2\mu s$ is determined from the first minima of the average mutual information of the intensity time series [3]. This dimensional estimate

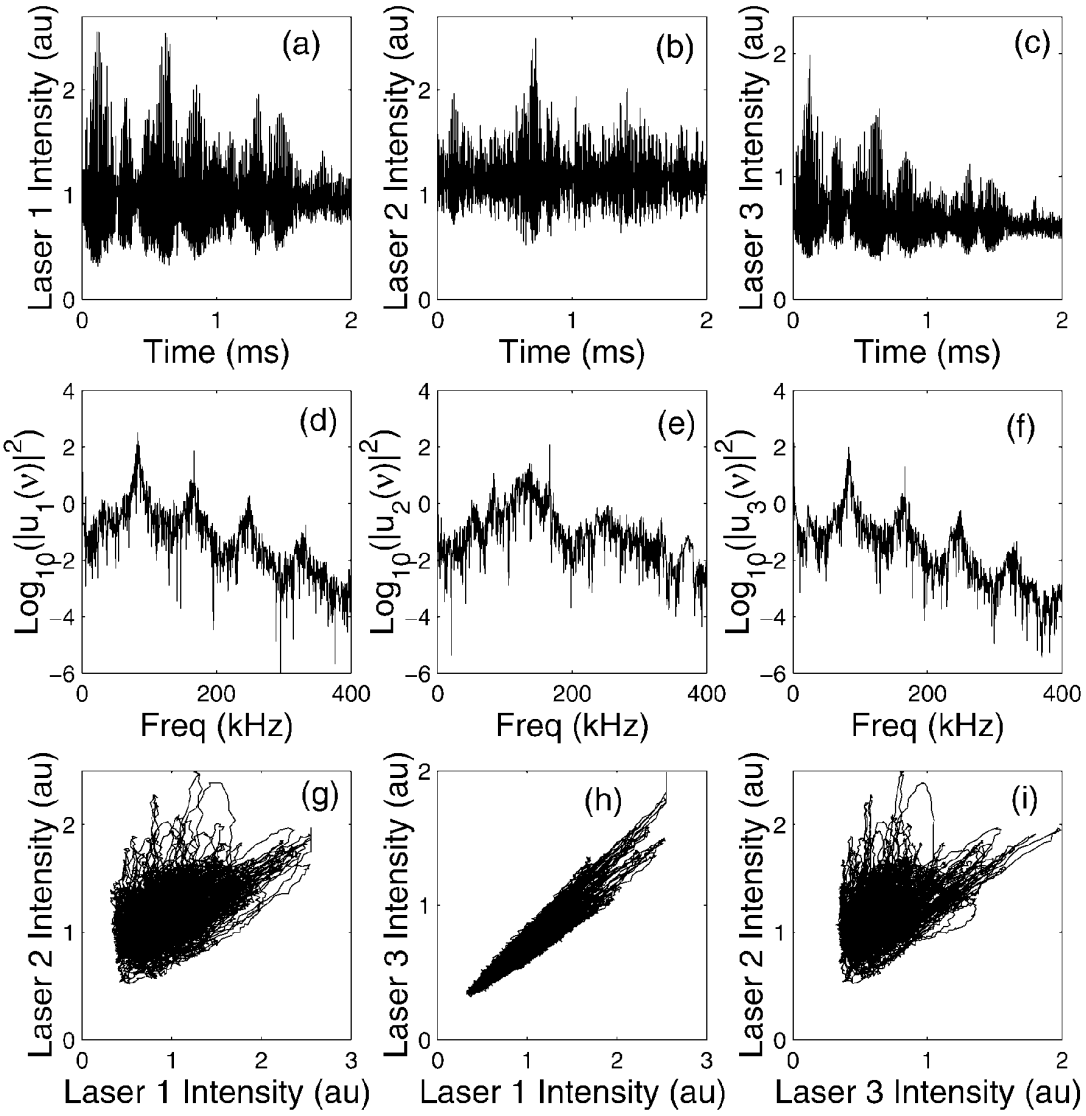

Figure 4.9: Chaotic intensity dynamics of the three laser array with soft loss modulation ($\epsilon_{mod} = 0.07$). Intensity time series (a-c) of the individual lasers and their respective power spectra (d-f). Peak at $166kHz$ in all three power spectra is due to loss modulation at this frequency. The two side lasers (1 & 3) demonstrate striking similarities to each other, and distinct differences from the central laser (2). The synchronicity of the outer laser pair is shown by plotting laser 1 vs. laser 3 (h). The xy-synchronization plots of the side lasers with the central beam (g&i) do not show any obvious relationship.

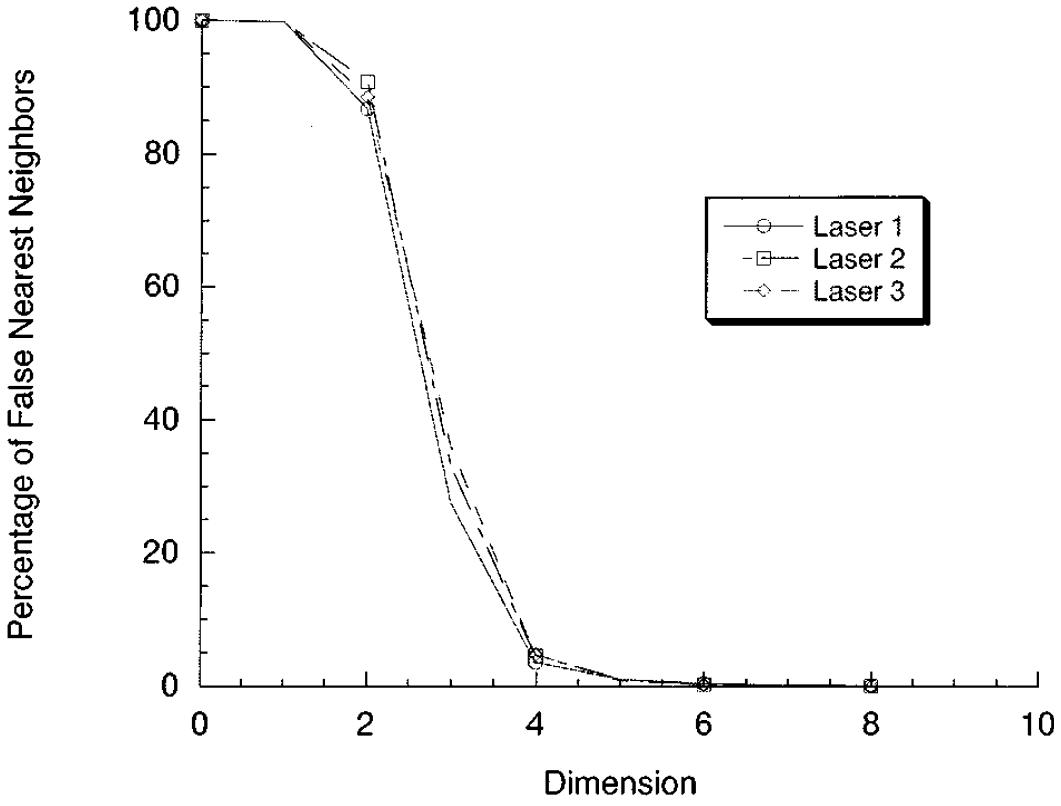

Figure 4.10: Using the false nearest-neighbors method, we numerically estimate the dimensionality of the experimental system, using measured time series of the intensity fluctuations. The 1% level of false nearest neighbors suggests the system is five dimensional, giving good agreement between the experiments and the dimension of the amplitude anti-synchronized subspace, Table 4.1.

agrees with the dynamically invariant state labeled amplitude anti-synchronized in Table 4.1, corresponding to a system with amplitude synchronization and equal left and right detunings present.

4.4 Equations of Motion

The equations describing the time evolution of the slowly varying complex electric field amplitude E_n and the real gain G_n of laser $n = 1, 2, 3$ in a linear array of three spatially coupled, loss modulated single-mode class-B lasers are similar to those discussed in Sections 4.1.1 and 4.1.4, [72]. The extension to a three laser array is

$$\begin{aligned}
\frac{dE_1}{dt} &= \tau_c^{-1}[(G_1(t) - \epsilon(t))E_1(t) - \kappa E_2(t)] + i\omega_1 E_1(t), \\
\frac{dG_1}{dt} &= \tau_f^{-1}(p - G_1(t) - G_1(t)|E_1(t)|^2), \\
\frac{dE_2}{dt} &= \tau_c^{-1}[(G_2(t) - \epsilon(t))E_2(t) - \kappa(E_1(t) + E_3(t))] + i\omega_2 E_2(t), \\
\frac{dG_2}{dt} &= \tau_f^{-1}(p - G_2(t) - G_2(t)|E_2(t)|^2), \\
\frac{dE_3}{dt} &= \tau_c^{-1}[(G_3(t) - \epsilon(t))E_3(t) - \kappa E_2(t)] + i\omega_3 E_3(t), \\
\frac{dG_3}{dt} &= \tau_f^{-1}(p - G_3(t) - G_3(t)|E_3(t)|^2).
\end{aligned} \tag{4.19}$$

Time scales in the coupled laser equations are determined by the cavity round-trip time, $\tau_c = 0.4 - 0.5ns$, and the fluorescence time of the upper lasing level of Nd^{3+}, $\tau_f = 240\mu s$. Coupling between the lasers in the array is calculated from the overlap integral of adjacent beams' electric fields, Eqn. (4.5), and is given by $\kappa \equiv \exp(-d^2/2w_o^2)$. Here, κ is normalized to unity for separation $d = 0$ and a Gaussian intensity profile where w_o is the $1/e$ radius of the electric field amplitude. The negative sign preceding κ follows from the observed π optical phase shift between nearest neighbor beams, as seen in Fig. 4.2. The level of optical pumping p is constant for all three lasers, while the modulated cavity loss is given by $\epsilon_n(t) = \epsilon_o + \epsilon_{mod}\sin(2\pi\nu_{mod}t)$, where $\nu_{mod} = 166kHz$ is the loss modulation frequency. The intrinsic cavity loss is $\epsilon_o \approx 0.17$ and the level of loss modulation ϵ_{mod} is dependent

on the strength of the signal driving the intra-cavity AOM. ω_n is the detuning of laser n from a common cavity mode.

We now follow the analysis of Eqn. (4.19) performed by Dr. John Terry and reported in Ref. [17]. While we only consider the loss modulation case here, the analysis that is presented is equally valid for a pump modulated laser array.

We first let $E_n = X_n \exp[i\phi_n]$, where X_n is the real amplitude and ϕ_n the real phase of the complex electric field of laser n. Time is scaled to the round-trip time τ_c. We subsequently introduce the change of variables $\Phi_L = \phi_2 - \phi_1$ and $\Phi_R = \phi_2 - \phi_3$, and $\Omega_L = \omega_2 - \omega_1$ and $\Omega_R = \omega_2 - \omega_3$. With these definitions and changes of variables we rewrite Eqn. (4.19) as a system of eight real ordinary differential equations

$$\begin{aligned}
\frac{dX_1}{dt} &= [F_1 - \epsilon_1(t)]X_1 - \kappa X_2 \cos(\Phi_L), \\
\frac{dF_1}{dt} &= \gamma(A - F_1 - F_1 X_1^2), \\
\frac{dX_2}{dt} &= [F_2 - \epsilon_2(t)]X_2 - \kappa(X_1 \cos(\Phi_L) - X_3 \cos(\Phi_R)), \\
\frac{dF_2}{dt} &= \gamma(A - F_2 - F_2 X_2^2), \\
\frac{dX_3}{dt} &= [F_3 - \epsilon_3(t)]X_1 - \kappa X_2 \cos(\Phi_R), \\
\frac{dF_3}{dt} &= \gamma(A - F_3 - F_3 X_3^2), \\
\frac{d\Phi_L}{dt} &= \Omega_L + \kappa\Big[\Big(\frac{X_2}{X_1} + \frac{X_1}{X_2}\Big)\sin(\Phi_L) + \frac{X_3}{X_2}\sin(\Phi_R)\Big], \\
\frac{d\Phi_R}{dt} &= \Omega_R + \kappa\Big[\Big(\frac{X_3}{X_2} + \frac{X_2}{X_3}\Big)\sin(\Phi_R) + \frac{X_1}{X_2}\sin(\Phi_L)\Big].
\end{aligned} \tag{4.20}$$

Here F_n is the real gain, $\gamma = \tau_c/\tau_f$ and A is the scaled pump rate.

The issue of synchronization between the two outer lasers may be addressed by introducing the sum and difference variables of these lasers and assuming that all three lasers are equally detuned, i.e., $\Omega_L = \Omega_R = 0$. Introducing an additional change of variables $X_+ = 0.5(X_1 + X_3)$, $X_- = 0.5(X_1 - X_3)$, $F_+ = 0.5(F_1 + F_3)$, and $F_- = 0.5(F_1 - F_3)$, synchronization between the two outer lasers occurs when $X_- = F_- = 0$ in the non-trivial case of $X_+, F_+ \neq 0$, i.e. the lasers are operating and the electric field amplitudes and gains of the outer pair are identical.

Symmetry	Representative point	Dim.	Name
$\boldsymbol{Z}_2(\xi) \times \boldsymbol{Z}_2(\mu)^{00}$	$(X_+, F_+, X_2, F_2, 0, 0, 0, 0)$	4	synchronized
$\boldsymbol{Z}_2(\xi) \times \boldsymbol{Z}_2(\mu)^{\pi\pi}$	$(X_+, F_+, X_2, F_2, 0, 0, \pi, \pi)$	4	anti-synchronized
$\boldsymbol{Z}_2(\mu\xi)$	$(X_+, F_+, X_2, F_2, 0, 0, \phi, -\phi)$	5	amplitude anti-synchronized
$\boldsymbol{Z}_2(\mu)^{00}$	$(X_+, F_+, X_2, F_2, X_-, F_-, 0, 0)$	6	optical phase synchronized
$\boldsymbol{Z}_2(\mu)^{\pi\pi}$	$(X_+, F_+, X_2, F_2, X_-, F_-, \pi, \pi)$	6	optical phase anti-synchronized

Table 4.1: Dynamically invariant subspaces contained in Eqn. (4.20), a symmetric array of three nearest neighbor, evanescent field coupled lasers. Experimental measurements correspond to the dimension 5, amplitude anti-synchronized subspace.

The transformed system is equivariant under the action of the symmetries

$$\xi(X_+, F_+, X_2, F_2, X_-, F_-, \Phi_L, \Phi_R) = (X_+, F_+, X_2, F_2, -X_-, -F_-, \Phi_L, \Phi_R),$$

corresponding to the exchange of the outer pair of lasers, and

$$\mu(X_+, F_+, X_2, F_2, X_-, F_-, \Phi_L, \Phi_R) = (X_+, F_+, X_2, F_2, X_-, F_-, -\Phi_L, -\Phi_R),$$

corresponding to taking the complex conjugate of the electric fields of all three lasers in the array.

There is also a parameter symmetry involving the coupling parameter κ, $(\kappa, \Phi_L, \Phi_R) \to (-\kappa, \Phi_L + \pi, \Phi_R + \pi)$ which adds π to the phase of the middle laser while reversing the sign of κ. It is interesting to note that all three lasers are phase synchronized when κ is negative, corresponding to $\Phi_L = \Phi_R = 0$, and only the two outer lasers are synchronized when κ is positive. The second case of a positive κ corresponds to the experimentally observed case of the nearest neighbor pairs of lasers locked π out of phase.

From these symmetries, the dynamically invariant subspaces cataloged in Table 4.1 exist. Notice the five-dimensional subspace labeled 'amplitude anti-synchronized', corresponding to the case where the μ symmetry has been broken through equal detuning of the two outer beams from a common cavity mode. This subspace agrees with the dimensionality of the experimental system as determined by the false nearest neighbor method, Fig. 4.10, and the synchronization and anti-phase locked state

observed, and supports our assumptions of the parameter regimes considered.

Note that although there are several invariant subspaces where the phases of all three lasers are locked, there are *no* invariant subspaces forced by symmetry such that all the amplitude and gains are equal, $X_+ = X_2$ and $F_+ = F_2$. We may examine this synchronization state using two approaches: first, by examining the set of such points in the phase space and showing that it is not invariant as in Ref. [84], and second, by reducing the system of three lasers to one of two lasers with unequal coupling.

To this end, we define the manifold

$$\mathcal{M}_{12} = \{(X_1, F_1, X_2, F_2, X_3, F_3, \Phi_L, \Phi_R) : X_1 = X_2, F_1 = F_2 : \& : \Phi_R = 0, \pi\}, \tag{4.21}$$

corresponding to perfect (anti)synchronization between lasers 1 and 2 in terms of the original variable.

4.4.1 Instability of Central-Side Laser Intensity Synchronization

In the case of coupling $\kappa \neq 0$ between the laser array, a trajectory can only be in $\mathcal{M}_{12}$ instantaneously, by assuming that X_1 and X_2 are nonzero and examining the evolution of their difference, $x_- = 0.5(X_1 - X_2)$, and sum, $x_+ = 0.5(X_1 + X_2)$. The time differential equation for x_- is then given by

$$\frac{dx_-}{dt} = \frac{F_1 + F_2}{2} x_- + \frac{F_1 - F_2}{2} - \epsilon(t) x_- + \kappa x_- \cos(\Phi_L) + \frac{1}{2}\kappa X_3 \cos(\Phi_R). \tag{4.22}$$

If the system state lies on $\mathcal{M}_{12}$, this means that $x_- = 0$ and $F_1 = F_2$; so the trajectory at this point will obey

$$\frac{dx_-}{dt} = \frac{1}{2}\kappa X_3 \cos(\Phi_R). \tag{4.23}$$

Thus, the trajectory must leave $\mathcal{M}_{12}$, unless $\kappa = 0$, $X_3 = 0$, and/or $\Phi_R = \pi/2 + j\pi$, where j is some integer. As we are interested in the study of a coupled laser array,

we assume $\kappa \neq 0$. In the case of $X_3 = 0$,

$$\frac{dX_3}{dt} = -\kappa X_2 \cos(\Phi_R), \tag{4.24}$$

and so X_3 always exits $\mathcal{M}_{12}$, as we have defined the subspace such that $\Phi_R = 0, \pi$. Hence, no trajectories are supported by the subspace as long as there is nonzero coupling and field amplitudes between and for the three lasers of the array.

4.4.2 Reduction to a Two Laser Array with Asymmetric Coupling

We consider only amplitude synchronized subspaces similar to that observed experimentally where the two side lasers (1 & 3) are synchronized. Then $X_1 = X_3$ and $F_1 = F_3$, and we may reduce the array of eight, real coupled ordinary differential equations describing the coupled three laser array, Eqns. (4.20), to a set of five coupled equations describing a two laser array with asymmetric coupling.

$$\begin{aligned}
\frac{dX_1}{dt} &= [F_1 - \epsilon(t)]X_1 - \kappa X_2 \cos(\Phi), \\
\frac{dF_1}{dt} &= \gamma(A - F_1 - F_1 X_1^2), \\
\frac{dX_2}{dt} &= [F_2 - \epsilon(t)]X_2 - 2\kappa X_1 \cos(\Phi), \\
\frac{dF_2}{dt} &= \gamma(A - F_2 - F_2 X_2^2), \\
\frac{d\Phi}{dt} &= \kappa\Big(\frac{X_2}{X_1} + 2\frac{X_1}{X_2}\Big)\sin(\Phi).
\end{aligned} \tag{4.25}$$

While the loss is uniform for the reduced two laser system, the influence of laser 1 ('side' laser) on laser 2 ('central' laser) is double of that in the reverse direction. Redefining the sum and difference variables for the reduced laser system, $X_- = 0.5(X_1 - X_2)$, $X_+ = 0.5(X_1 + X_2)$, $F_- = 0.5(F_1 - F_2)$, and $F_+ = 0.5(F_1 + F_2)$, we

now find the transformed system of equations

$$\begin{aligned}
\frac{dX_+}{dt} &= X_+[F_+ - \epsilon(t)] + F_-X_- - \kappa\cos(\Phi)(3X_+ + X_-), \\
\frac{dF_+}{dt} &= \gamma[A - F_+(1 + X_+^2 + X_-^2) - 2F_-X_-X_+], \\
\frac{dX_-}{dt} &= X_-[F_- - \epsilon(t)] + F_+X_+ + \kappa\cos(\Phi)(3X_- + X_+), \\
\frac{dF_+}{dt} &= \gamma[A - F_-(1 + X_+^2 + X_-^2) + 2F_+X_-X_+], \\
\frac{d\Phi}{dt} &= \frac{3\left(X_+^2 + \frac{2}{3}X_+X_- + X_-^2\right)}{X_+^2 - X_-^2}\kappa\sin(\Phi).
\end{aligned} \tag{4.26}$$

Examining the synchronized case, we find that

$$\begin{aligned}
\frac{dX_-}{dt} &= \kappa\cos(\Phi)X_+, \\
\frac{dF_-}{dt} &= 0, \\
\frac{d\Phi}{dt} &= 3\kappa\sin(\Phi).
\end{aligned} \tag{4.27}$$

In the interesting case of nonzero coupling with the two lasers operating above threshold, $\kappa \neq 0$ and $X_+ \neq 0$, and X_- quickly moves away from 0 in the experimentally observed case of a phase difference of $\Phi = \pi$ between nearest neighbor lasers. Note that this is a fixed point for Φ. Even in the general case where X_- has a zero differential, $\cos(\Phi) = 0$ then $\Phi \mathrm{mod} \pi = \pi/2$, the resulting differential

$$\frac{d\Phi}{dt} = 3\kappa \tag{4.28}$$

would drive the reduced laser array out of synchronization. Therefore synchronization of the asymmetrically coupled two laser array is not observed, and thus not present in the original three laser array.

4.5 Comparison of Numerical and Experimental Results: Pump Modulation

While the previous analysis considered a loss modulated laser array, the conclusions are equally valid in the case of pump modulation [85]. Experimentally, we simply remove the acousto-optic modulator from inside the cavity, and place it in the path of the argon ion pump laser before the fan-out grating. In this way, all three pump beams are modulated equally. Pump modulation is considered numerically by allowing the pump term $p(t)$ to vary in time, giving the real gain expression

$$\frac{dG_n}{dt} = \tau_f^{-1}(p(t) - G_n - G_n|E_n|^2) \tag{4.29}$$

replacing the gain expression in the class-B laser Equations (4.19). The pump modulation is given by the expression $p(t) = p_o + p_{mod}\sin(2\pi\nu_{mod}t)$, where $\nu_{mod} = 100kHz$ is chosen to be near the relaxation oscillation frequency of the lasers in order to induce chaotic intensity fluctuations. The loss term ϵ in the complex field expressions Eqns. (4.19) is now constant and equal to the intrinsic cavity loss ϵ_o.

Experimental measurements of the pump modulated laser array display similar dynamics and relationships as those observed in the loss modulated case. Fig. 4.11 displays the intensity time series of the three coupled lasers (a-c) and their x-y synchronization plots (d-f). Nearly identical synchronization is observed between the two side lasers (Figs. 4.11(a, c & e)), while no clear relationship between the side and central lasers is observed. The depth of the pump modulation, is $p_{mod} = 0.20$ for all three beams. The nearest neighbor separations are approximately $d = 0.975mm$.

Numerical integration of the pump modulated three laser array was carried out using a Runge-Kutta integrator with a variable time step. The results of this integration is displayed in Fig. 4.12. The simulated intensity time series of the laser array are shown in Figs. 4.12(a-c) with their corresponding x-y synchronization plots, Figs. 4.12(d-f). In good agreement with the experimental results for both loss and pump modulation we again observe identical synchronization between the two side lasers, Fig. 4.12(e), and no obvious relationship with the center laser, Figs. 4.12(d

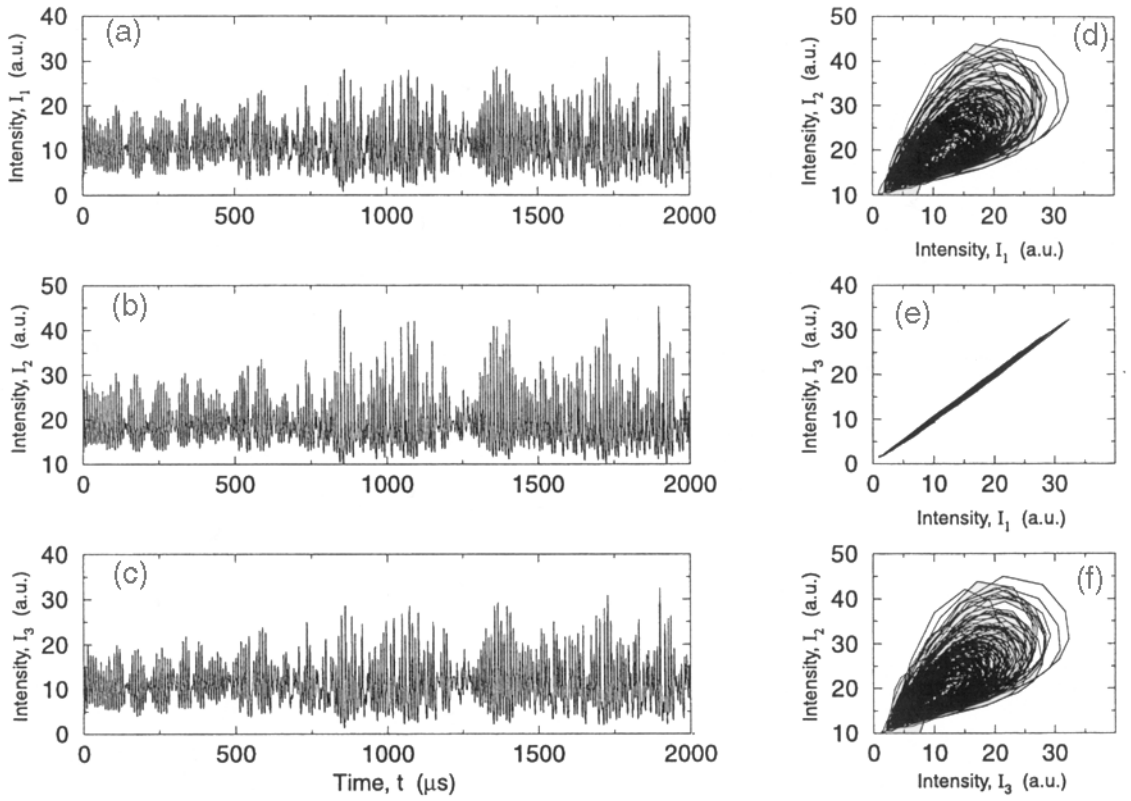

Figure 4.11: Experimental measurements of the relative intensities of three coupled lasers with pump modulation and nearest neighbor separations of $d = 0.975mm$. The intensity time series of the three lasers, (a-c), display sustained chaotic fluctuations. The x-y synchronization plots of the three times series, (d-f), displays a high degree of intensity synchronization only between lasers 1 and 3, (a). [17]

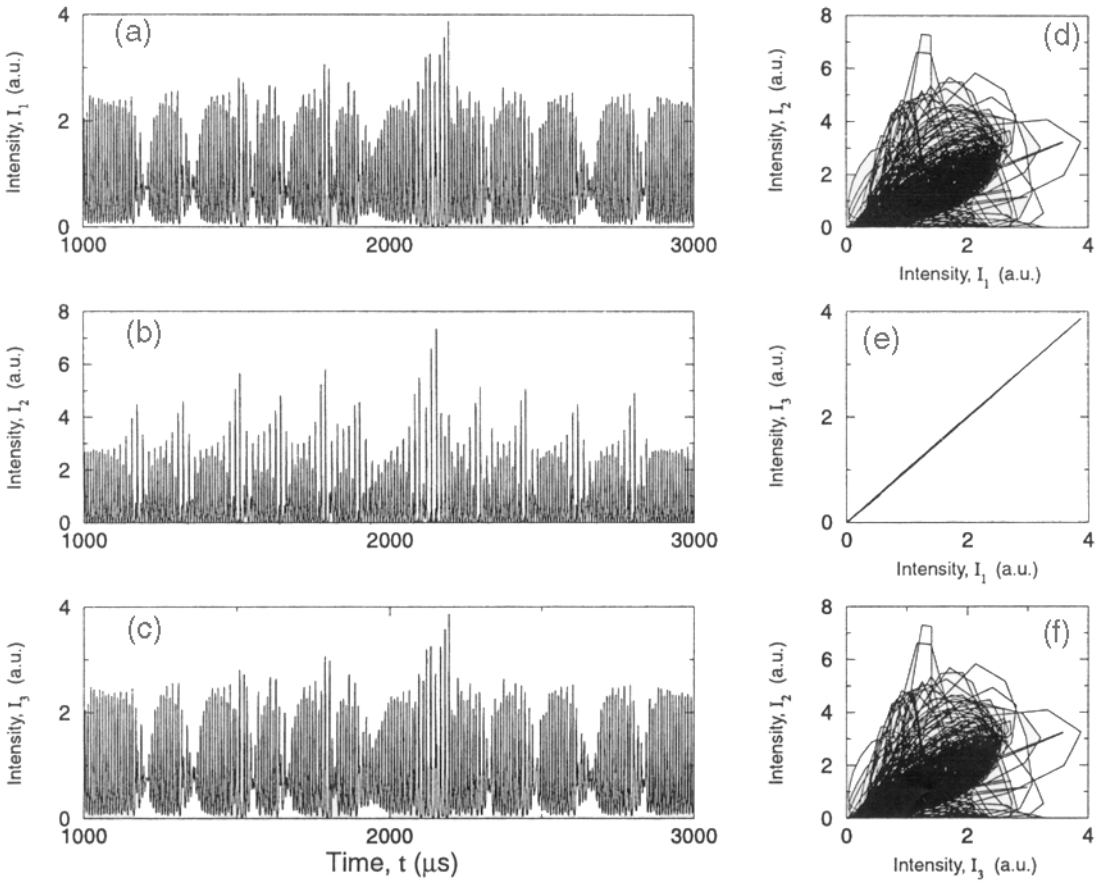

Figure 4.12: Results of numerical integration of the three Nd:YAG laser array model with pump modulation. The intensity time series of the three lasers, (a-c), display sustained chaotic fluctuations as the pump modulation rate $\nu_{mod} = 100kHz$ was chosen to be close to the relaxation oscillation frequency of the coupled lasers. The x-y synchronization plots of the three times series, (d-f), display a high degree of intensity synchronization only between lasers 1 and 3, (a). [17]

& f).

4.6 Discussion

Strong synchronization has been found in experimental and numerical observations between the pair of outer lasers in the three laser array (1 & 3), without any clear relationship of these side lasers with the central laser (2). The dominance of this dynamic state has been explained by analyzing the equations of motion, Eqns. (4.19), of the nearest neighbor coupled linear laser array. Winful and Rahman observed similar behavior in a model of three coupled semiconductor lasers [73]. Additionally, experimental measurements and observations of the dynamics agree with the dimension five, amplitude anti-synchronization subspace found in the analysis of Eqns. (4.19).

Despite the strong agreement of our experimental, numerical and analytic results, we are still left with the question of how the central laser is related dynamically to the two side lasers. As the linear laser array is constructed such that only nearest neighbors are coupled, the synchronization of side lasers depends on the mediation of the central laser. The relationship of a side laser and the central laser is a more general form of synchronization, and requires a more subtle analysis of the dynamics to uncover this relationship. In Section 5.2, we examine the nature of this interaction using a Gaussian frequency filtered analytic signal phase. The shifting nature of the laser dynamics with increasing strengths of loss modulation and their entrainment to the sinusoidal modulation signal is studied in Section 5.1.

Chapter 5

Entrainment and Phase Synchronization in a Three Laser Array

5.1 Entrainment of Chaotic Dynamics

5.1.1 Introduction

Perhaps the most famous characteristic of chaos is the sensitive dependence of chaotic systems on initial conditions and to small perturbations, as we discussed in Section 2.1. This defining property makes it impossible to predict the behavior of a chaotic system over long time periods. An interesting and surprising result of this sensitivity is the possibility of controlling chaotic dynamics with specific perturbations. A technique to control chaotic systems based only on the observed dynamics of a system was advanced in 1990 by Ott, Grebogi, and Yorke [86]. Known as OGY, the control technique was implemented in a number of experimental systems

including stabilizing the dynamics of a frequency doubled Nd:YAG laser [87], and returning an arrhythmic rabbit heart to periodic behavior [88, 89].

A more common and conceptually simpler method of maintaining healthy heart function is using a periodic signal from an implanted pacemaker to ensure regular beating. In such a situation, the contractions of the heart are entrained to the pace-maker output. A somewhat exotic, well studied example of complex synchronization and entrainment is exhibited by large assemblies of male fireflies in parts of South-East Asia that will flash in unison to attract a female. Ref. [90] provides a review of firefly synchronization research. When exposed to a light flashing at a frequency close to its natural repetition rate of $0.9s$ a firefly will become entrained to the artificial flashing [91]. However, if the period of the perturbing flashes is too far removed from the natural pace of the firefly, then only intermittent periods of entrainment, interspaced with 2π phase slips, are observed [91].

Phase entrainment to a periodic signal has been reported for deterministically chaotic systems. Originally recognized in an experimental study [41], theoretical studies of the Rössler [92] and Lorenz systems [93, 94] have been conducted as well. Recently, entrainment of homoclinic chaos in a CO_2 laser (a Class-B laser) [95] to sinusoidal loss modulation was demonstrated [96].

5.1.2 Loss Modulation Entrainment

As we saw in the previous chapter, the dynamics of individual lasers in the array depends on the depth of the loss modulation due to the acousto-optic modulator (AOM). With the addition of this dynamic element into the Nd:YAG laser cavity, we now write the time varying loss term in the field equation as

$$\epsilon_n(t) = \epsilon_o + \epsilon_{mod} \sin(2\pi\nu_{mod} t), \tag{5.1}$$

where $\epsilon_o \approx 0.17$ is the intrinsic cavity loss, the array index array $n = 1, 2, 3$, $\nu_{mod} = 166kHz$ is the modulation frequency, and ϵ_{mod} is the amplitude of the modulation. Fig. 4.8 displays the intensity dynamics of laser 1 with a sample of modulation

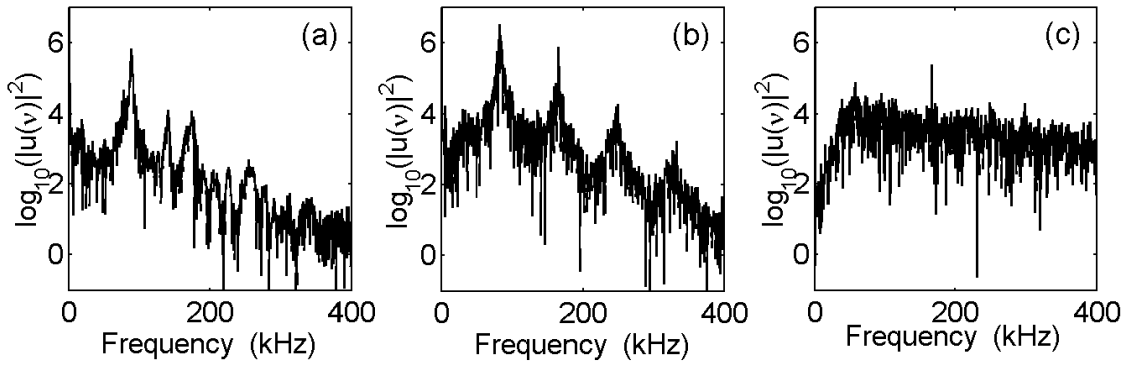

Figure 5.1: Power Spectra for laser 1 of the array with No Modulation (a), Soft Modulation $\epsilon_{mod} = 0.07$ (b), and Hard Modulation $\epsilon_{mod} = 0.23$ (c). Both (b) and (c) display strong peaks at $\nu_{mod} = 166kHz$.

strengths, ϵ_{mod}. The additional degree of freedom provided by the coupling allows complex, intermittent intensity fluctuations even in the unmodulated laser array (top intensity time series, Fig. 4.8).

The loss modulation of the laser array results in a shift of dynamics in frequency space, as well as in the nature of the intensity time series. Simply examining the power spectra, Fig. 5.1, of the three time series, we witness the effect increasing loss modulation has on the laser dynamics. Figs. 5.1(a), (b) and (c) display the power spectra for unmodulated, soft modulated ($\epsilon_{mod} = 0.07$) and hard modulated ($\epsilon_{mod} = 0.23$) infrared laser intensity time series respectively. In addition to a more uniform spectral profile with modulation, we easily see a sharp peak at $\nu_{mod} = 166kHz$, indicating the possibility of phase entrainment of the dynamics to the sinusoidal modulation.

By examining the spectrogram representations of the frequency content of these intensity time series, Fig. 5.2, we gain additional insight into how loss modulation affects the dynamics of the laser array. Here we have calculated the power spectra of successive segments of 2500 points, or $0.2ms$, of the intensity time series in question. The resulting spectra are formed into a matrix, allowing us to view the intensity spectral evolution in time. Here color represents the Log_{10} of the power contained in a frequency component – horizontal axis – at a given time – vertical axis. A simple bilinear interpolation between the vertices of the resulting pixels is

used to simulate improved resolution.

Consistent with Fig. 4.8, the unmodulated spectrogram Fig. 5.2(a) displays a shifting power spectrum during the course of the measurement. The high power red band in Fig. 5.2(a&b) correspond to natural frequency peaks of the Nd:YAG laser. The soft loss modulated spectrogram Fig. 5.2(b) displays a more consistent spectrum in time, corresponding to the relatively sustained chaotic behavior observed in the intensity time series. Additionally, a dramatic high power red streak at $\nu_{mod} = 166kHz$ is apparent, evidencing the Nd:YAG frequency response and perhaps phase entrainment to the modulation signal. The spectrogram of the hard modulated laser dynamics Fig. 5.2(c) is relatively constant in both frequency and time, although a streak at ν_{mod} is still easily seen.

To determine if phase entrainment to the sinusoidal modulation signal is present, as well as the observed frequency entrainment and a shift in laser dynamics, it is necessary to identify a phase marker and compare its behavior in time to the rotating phase of the $166kHz$ modulation signal. Peaks in the laser intensities – defined by maxima of the dynamics above the mean of the signal – are a physically obvious choice for the phase marker. By tracking the location of the peaks in time relative to the phase of the modulation signal we observe a significant confinement of the phase locations of the peaks in the modulated time series. Peak phase location is simply defined as $peaktime \times 166kHz \times 2\pi$.

Fig. 5.3 displays infrared laser intensity time series with identified peaks and their phase histograms. Figs. 5.3(a), (b) and (c) display intensity time series of laser 1 of the coupled laser array with no modulation, soft modulation and hard modulation respectively. Due to the Q-switched nature of hard loss modulated lasers the mean of the dynamics rests relatively close to the minimum intensity shown in Fig. 5.3(c). The peaks of the laser intensities are indicated with open diamonds. The phase histogram for the unmodulated laser, Fig. 5.3(d) has a nearly uniform distribution. The histogram for the soft modulated laser, Fig. 5.3(e), displays significant confinement of the phase location of the intensity time series peaks, and hence phase entrainment of the laser to the $166kHz$ sinusoidal modulation signal.

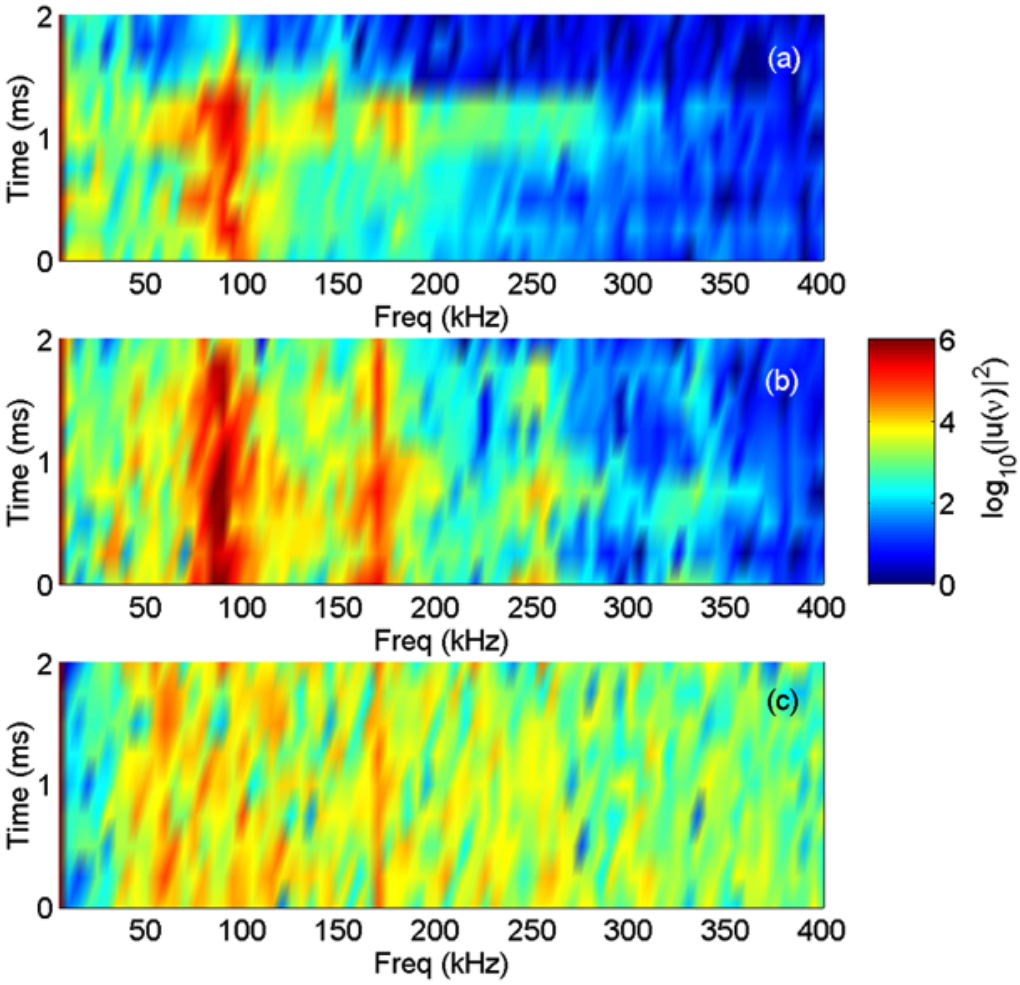

Figure 5.2: Spectrograms for the unmodulated (a), soft loss modulated (b) and hard modulated (c) coupled Nd:YAG laser dynamics. The modulated plots display frequency entrainment to the modulation frequency $\nu_{mod} = 166kHz$ as well as a more consistent power distribution in time and frequency.

The hard modulated peak phase location histogram, Fig. 5.3(f) evidences an even greater degree of phase entrainment.

A quantitative measure Q of phase entrainment is easily obtained from the normalized entropy S of the peak phases and is defined by

$$\begin{aligned} Q &\equiv 1 - S, \\ \text{where} & \\ S &= -\frac{\sum_{l=1}^{N} P_l ln P_l}{ln N}. \end{aligned} \tag{5.2}$$

Here, P_l is the probability that a peak phase will be found in bin l. The normalization factor $ln(N)$, where N is the number of bins, normalizes the Shannon entropy to 1. Hence, Q ranges from 0, for no entrainment, to 1, indicating perfect phase entrainment to the modulation signal.

Using Eqn. (5.2) we are able to study phase entrainment as a function of the loss modulation strength. Fig. 5.4 demonstrates the approximately linear increase in phase entrainment with an increasing modulating signal strength. Each filled diamond represents the phase entrainment value for one of three repeated measurements. Soft modulation time series plotted above correspond to a modulation strength of $\epsilon_{mod} = 0.07$, while the hard modulation time series were obtained with a modulation of $\epsilon_{mod} = 0.23$.

5.2 Phase Synchronization

Recently, a weak form of synchronization, phase synchronization, has been shown to be a useful tool for the analysis of chaotic signals arising in a variety of situations. Phase synchronization of chaos was originally pointed out by Pikovsky [41] and Stone [42] for the case of a chaotic oscillator perturbed by an external periodic signal, similar to the entrainment studied in the previous section. More recently, the idea of phase synchronization between coupled chaotic oscillators has been introduced [97], choosing coupled Rössler attractors [23] as a test system. We review this work

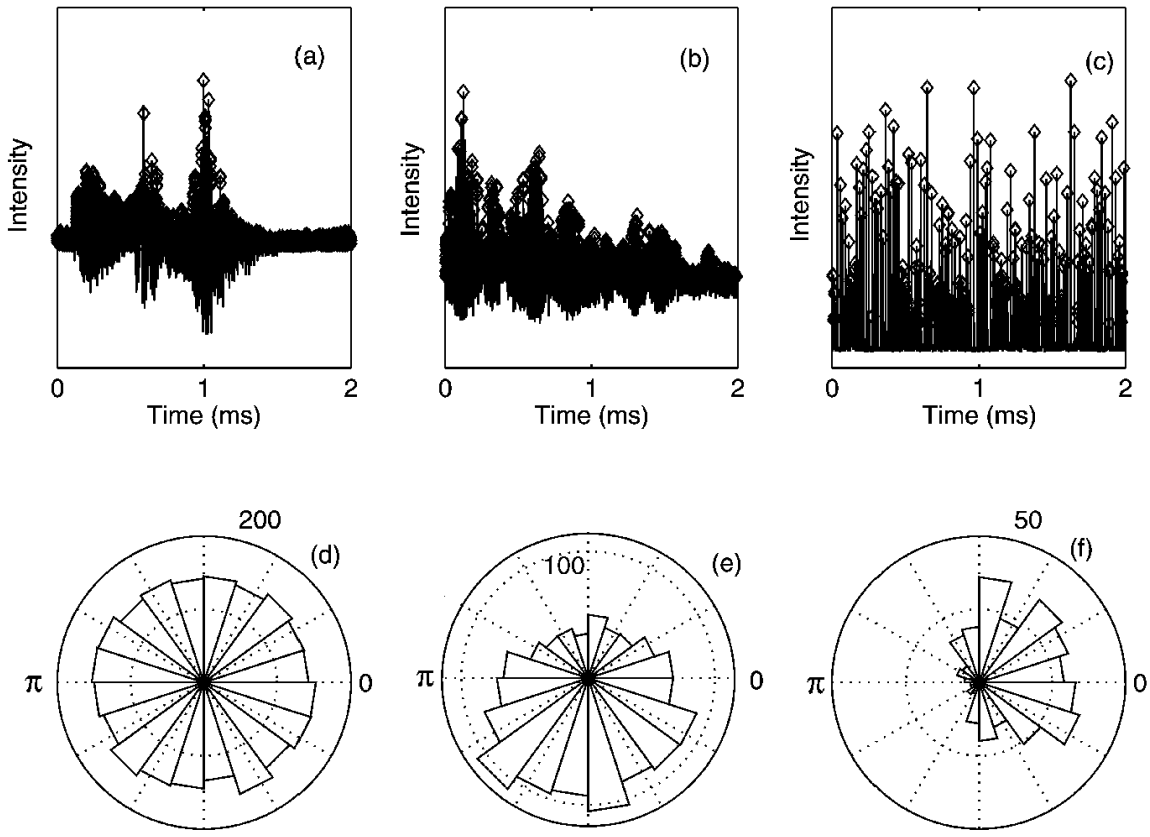

Figure 5.3: Loss modulation of the Nd:YAG laser array leads to phase entrainment of the laser dynamics to the sinusoidal modulation signal. Intensity time series of laser 1 of the coupled array with No Modulation (a), Soft Modulation (b), and Hard Modulation (c) are shown with their peaks identified with hollow diamonds. It is straightforward to calculate the value of a phase rotating at $\nu_{mod} = 166kHz$ at each peak. A histogram of the unmodulated laser peak phases (d) shows a nearly uniform distribution. The soft modulated laser peak phase histogram (e) is angularly confined, displaying phase entrainment to the loss modulation signal. Phases of the hard modulated laser peaks (f) shows and even greater degree of phase entrainment.

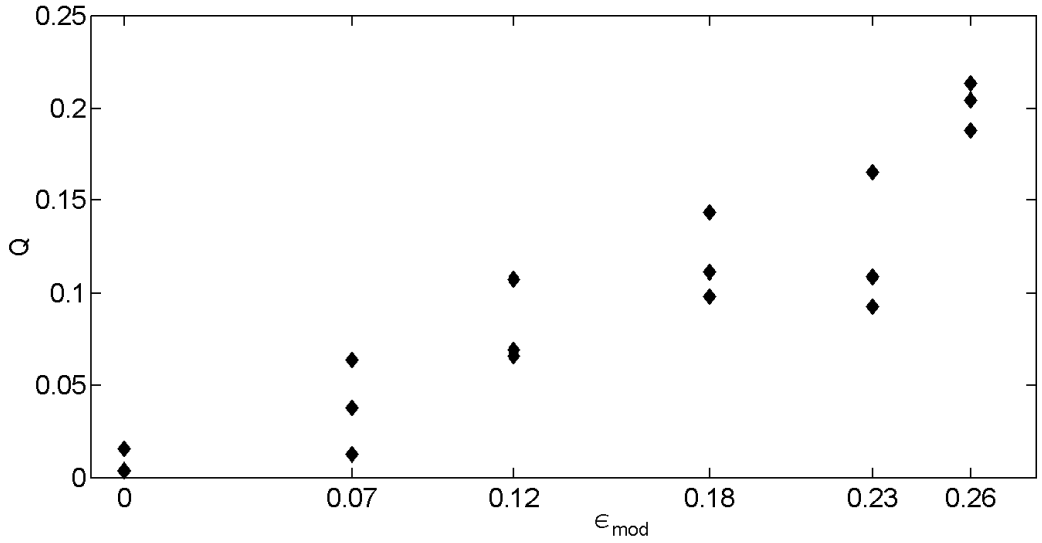

Figure 5.4: Phase entrainment increases monotonically with modulation strength. Measurements at each modulation value were repeated three times.

below. This concept has proven to be very useful, especially in the analysis of biological data (e.g., Ref. [98]). Experimental observation of phase synchronization in chaotic physical systems has been recently reported [96, 99, 100]. For a review of research in phase synchronization of chaos see Ref. [16, 23].

5.2.1 Phase Synchronization of Rössler Attractors

Inspired by the stretching and folding action of a taffy-pulling machine Otto Rössler developed a system of three ordinary differential equations [23, 2]

$$\begin{aligned} \dot{x} &= -y - z, \\ \dot{y} &= x + ay, \\ \dot{z} &= b + z(x - c), \end{aligned} \tag{5.3}$$

which define a particularly simple attractor with a single xz quadratic nonlinearity. In this system, the over-dot $(\cdot)$ indicates a differential with respect to time, and a, b and c are constant system parameters. Integrating these equations in the case of $a = b = 0.2$ and $c = 5.7$ and projecting the dynamics onto the xy-plane we observe

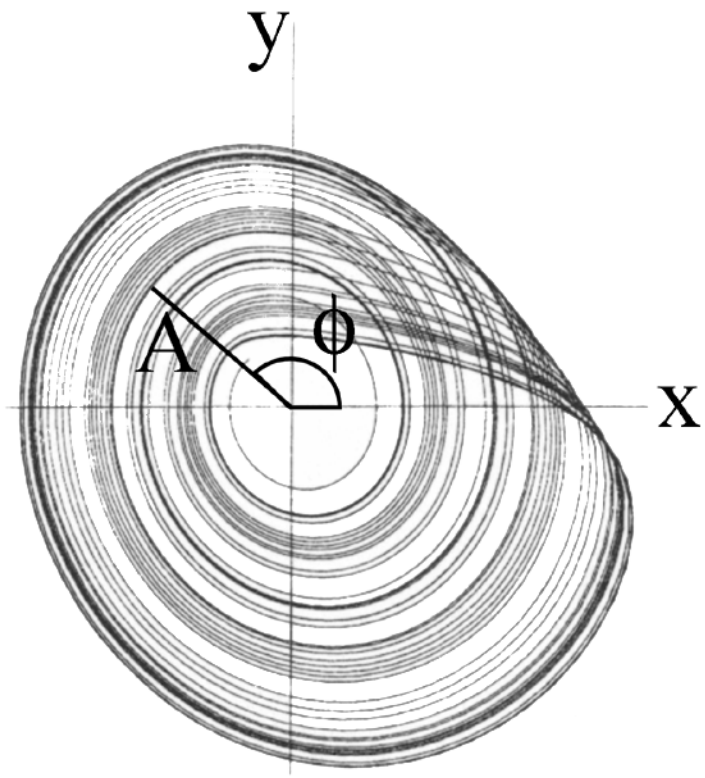

Figure 5.5: X-Y projection of Rössler attractor with $a = b = 0.2$ and $c = 5.7$. The labels A and ϕ show possible, physically intuitive definitions of amplitude and phase for the system. [2]

the particularly simple rotations performed by the system, Fig. 5.5 [2]. It is easy to see how a phase ϕ and amplitude A may be defined for the system from these rotations.

However, most experimental and numerical systems do not possess such easily defined phases. Hence, Rosenblum, Pikovsky and Kurths [97] choose to study the relative phase dynamics of two coupled Rössler attractors using an equivalent phase derived from the complex analytic signal $V(t)$ originally advanced by Gabor [101],

$$V(t) = x(t) + ix_H(t) = A(t)e^{i\phi(t)}, \tag{5.4}$$

where $x(t), x_H(t), A(t), \phi(t) \in \boldsymbol{R}$. One may calculate the analytic signal from any real time series. Choosing the time series $x(t)$, $\phi(t)$ is identical to that defined in Fig. 5.5. However, the amplitudes in Fig. 5.5 and Eqn. (5.4) need not match. The real and imaginary parts of the analytic signal are related through the Hilbert

transform

$$x_H(t) = \frac{1}{\pi} P \int_{-\infty}^{\infty} \frac{x(t')}{t - t'} dt', \tag{5.5}$$

where P indicates the principle part of the integral. The system of two coupled, nonidentical Rössler attractors are defined similarly to Eqn. (5.3)

$$\begin{aligned} \dot{x}_{1,2} &= -\omega_{1,2} y_{1,2} - z_{1,2} + C(x_{2,1} - x_{1,2}), \\ \dot{y}_{1,2} &= -\omega_{1,2} x_{1,2} + a y_{1,2}, \\ \dot{z}_{1,2} &= b + z_{1,2}(x_{1,2} - c), \end{aligned} \tag{5.6}$$

with the addition of the coupling and detuning parameters C and $\omega_{1,2} = 1 \pm \Delta\omega$, respectively [97]. Choosing an initial detuning $\Delta\omega = 0.015$ and system parameters $a = 0.15$, $b = 0.2$, and $c = 10$, we can examine the relative phase $\phi_1 - \phi_2$ of the two systems as C is increased. Beginning with only minimal coupling, $C = 0.01$, the two chaotic systems do not display phase synchronization as $\phi_1 - \phi_2$ increases monotonically, Fig. 5.6(a) [97]. Increasing the level of coupling to $C = 0.027$, phase synchronization is observed with intermittent jumps of 2π. Strong coupling $C = 0.035$ produces constant phase synchronization. However, the analytic amplitudes $A_{1,2}(t)$, Eqn. (5.4), calculated from the x coordinates of the coupled attractors, do not display any hint of synchronization even at this strong coupling value, Fig. 5.6(b) [97].

For a review of research in phase synchronization of chaos see Ref. [16].

5.2.2 Definition of Phase from Array Intensities

While it is simple to identify identical synchronization of intensities as we did in the previous chapter, it is much more difficult to discern relationships between the dynamics of elements of the array that are not identically synchronized. Typical experimental measurements record intensity time series without any determination of the phases of the fields of the laser elements. The relative *optical* phases of the array elements determine the intensity distributions in the far field (e.g. Fig. 4.2). Phase dynamics and chaotic intensity time series were studied experimentally and

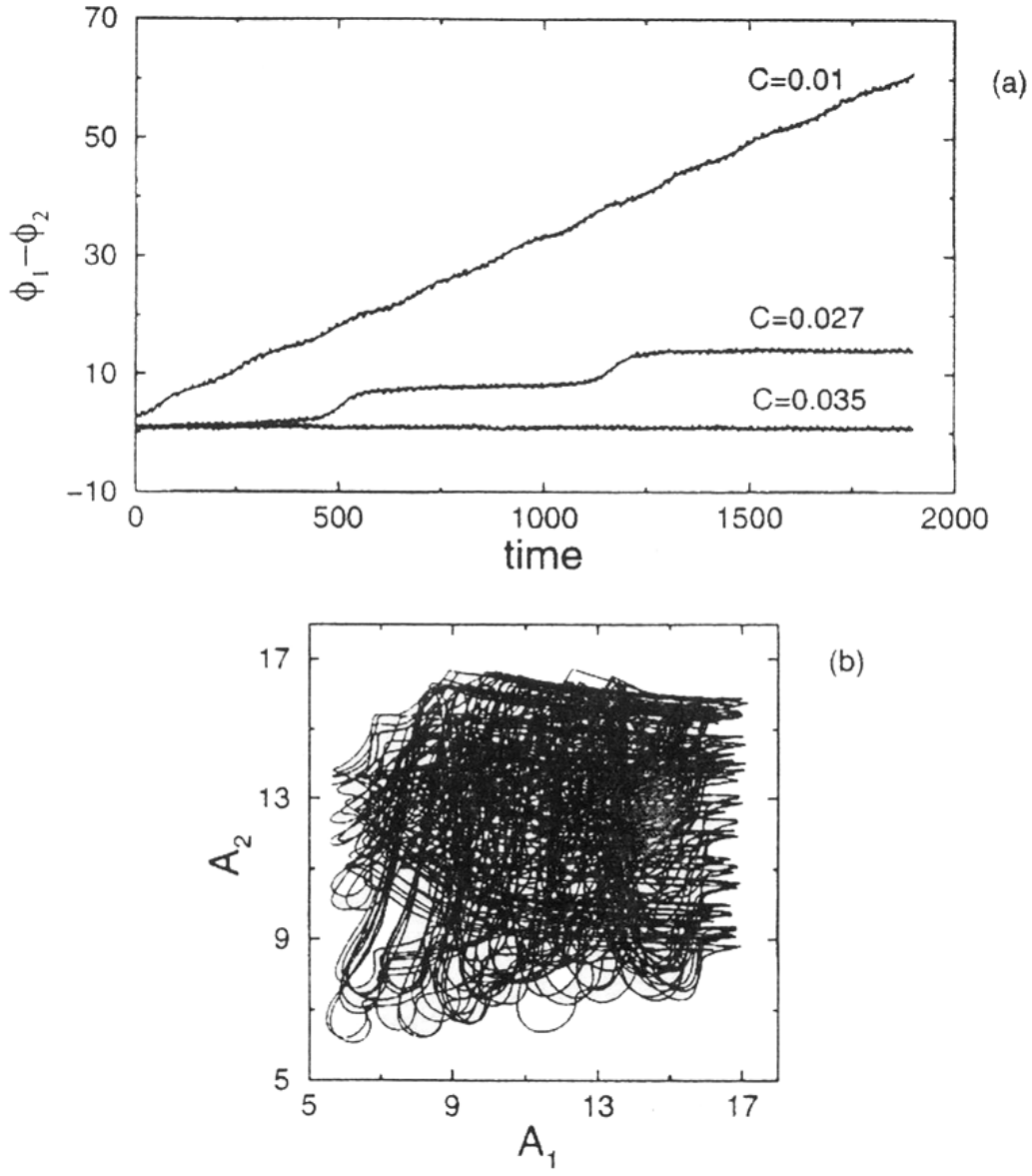

Figure 5.6: The relative phase of two nonidentical, coupled Rössler systems for unsynchronized, $C = 0.01$, intermittent phase synchronized $C = 0.027$, and phase synchronized, $C = 0.035$, states (a). Even with relatively strong coupling and phase synchronization the analytic amplitudes $A_{1,2}$ remain chaotic and unsynchronized (b).[97]

numerically for two spatially coupled lasers [70, 72], where phase-locking was determined from the far-field intensity profile and through measurements of interference fringe visibilities. It is difficult, however, to acquire and analyze dynamically evolving interference patterns at time scales comparable to those of the fluctuations of the fields (microseconds or shorter). Therefore, it is important to define new, experimentally accessible phase variables that will allow quantitative detection of phase synchronization between the array elements.

We consider now, with some repetition of the previous Section, a fairly general means by which a phase may be associated with a real scalar signal, $I(t)$ [18]. Representing $I(t)$ by its Fourier transform $u(\nu)$, $I(t) = (2\pi)^{-1} \int_{-\infty}^{\infty} \exp(i\nu t) u(\nu) d\nu$, we note that the time variation of each Fourier component, $u(\nu)e^{i\nu t}$, is a complex number whose phase continually increases (decreases) with time for $\nu > 0$ ($\nu < 0$). However, the symmetry of the Fourier components and the integration from $\nu \to -\infty$ to $\nu \to \infty$ eliminates the imaginary components and destroys the phase information. Thus, one way to introduce a phase is to suppress the negative ν components by replacing $u(\nu)$ by $2\theta(\nu)u(\nu)$ (where $\theta(\nu)$ is the unit step function, $\theta(\nu) = 1$ for $\nu > 0$ and $\theta(\nu) = 0$ for $\nu < 0$). In this case we obtain a superposition of rotating complex numbers all of which have increasing phase,

$$V_A(t) = \pi^{-1} \int_0^{\infty} e^{i\nu t} u(\nu) d\nu. \tag{5.7}$$

Thus we may reasonably expect $V_A(t)$ to execute rotations in the complex plane with continually increasing phase. The function $V_A(t)$ is Gabor's 'analytic signal'[101], which has been recently introduced for the purpose of the study of phase synchronization of chaos in Ref. [97]. Noting that the inverse transform of $2\theta(\nu)$ is $\delta(t) + \frac{i}{\pi} P\frac{1}{t}$, we can express the analytic signal as

$$V_A(t) = I(t) + iI_H(t) = I(t) + \frac{i}{\pi} I(t) \odot P\frac{1}{t}, \tag{5.8}$$

where $I_H(t)$ and $I(t)$ are related by the Hilbert transform $I_H(t) = \pi^{-1} P \int_{-\infty}^{\infty} dt' I(t')/(t - t')$, $\odot$ denotes convolution, and $P\frac{1}{t}$ is the principal part of $1/t$. Writing

$$V_A(t) - \langle V_A \rangle = R_A(t) e^{i\Phi_A(t)} \tag{5.9}$$

where $R_A(t)$ and $\Phi_A(t)$ are real, and $\langle V_A \rangle$ is the time average of $V_A(t)$, we call $\Phi_A(t)$ the *analytic phase*. Here we note that it is useful to consider more general choices. In particular, we can replace $u(\nu)$ in the original Fourier transform by $f(\nu)u(\nu)$, where $f(\nu)$ is suitably chosen (Eqn. (5.8) corresponds to $f(\nu) = 2\theta(\nu)$). Specifically, we will be interested in the choice of a Gaussian for $f(\nu)$, $f(\nu) = \exp[-(\nu - \nu_o)^2/2\sigma^2]$; this gives

$$V_G(t) \equiv \frac{1}{2\pi} \int_{-\infty}^{\infty} d\nu e^{i\nu t} e^{-\frac{(\nu-\nu_o)^2}{2\sigma^2}} u(\nu) = I(t) \odot F(t), \tag{5.10}$$

where $F(t) = \sigma(\sqrt{2\pi})^{-1} exp[-i\nu_o t + \sigma^2 t^2/2]$. We then define a Gaussian phase by

$$V_G(t) - \langle V_G \rangle = R_G(t) e^{i\Phi_G(t)}. \tag{5.11}$$

The Gaussian's center frequency ν_o and its width σ are parameters in the definition of $\Phi_G(t)$. Note that, like the choice $f(\nu) = 2\theta(\nu)$ resulting in the analytic signal, the choice of a Gaussian again emphasizes positive frequencies (we take $\nu_o > 0$). We find that application of a frequency bandpass filter as in Ref. [98] produces similar results for our data. Other choices that give previously mentioned means of defining a phase are $f_1(\nu) = 1 - ie^{i\nu T}$, yielding $V(t) = I(t) - iI(t - T)$, and $f_2(\nu) = 1 + \nu\alpha$ yielding $V(t) = I(t) + i\alpha\frac{dI(t)}{dt}$. Again, both of these choices may be thought of as emphasizing positive frequencies: $|f_2(\nu)| > |f_2(-\nu)|$ for $\nu > 0$ (we assume $\alpha > 0$), and for a spectrum peaked at $\nu \sim \frac{\pi}{2T}$ we note that $f_1(\frac{\pi}{2T}) = 2$ while $f_1(-\frac{\pi}{2T}) = 0$.

Examining $V_A(t)$ and $V_G(t)$ from the same intensity time series we see immediately the advantage of Gaussian filtering. In Fig. 5.7 the real part of an analytic signal is plotted versus the imaginary part of the signal for both $V_A(t)$ (a) and $V_G(t)$ (b). $V_A(t)$, Fig. 5.7(a), is obviously less symmetric, and close inspection reveals multiple spurious rotations about an arbitrary point, causing phase slips of 2π, and trajectories that pass through the center of rotation, causing slips of π. Choosing a Gaussian filter with $\sigma = 18kHz$ and $\nu_o = 80kHz$, eliminates the most of these occurences, providing a much improved definition of phase.

We find the Gaussian filtered phase superior for our purposes, and we believe this may also be the case in other situations involving nonstationary, noisy time series of limited duration. For our experimental data set, we have tested for phase

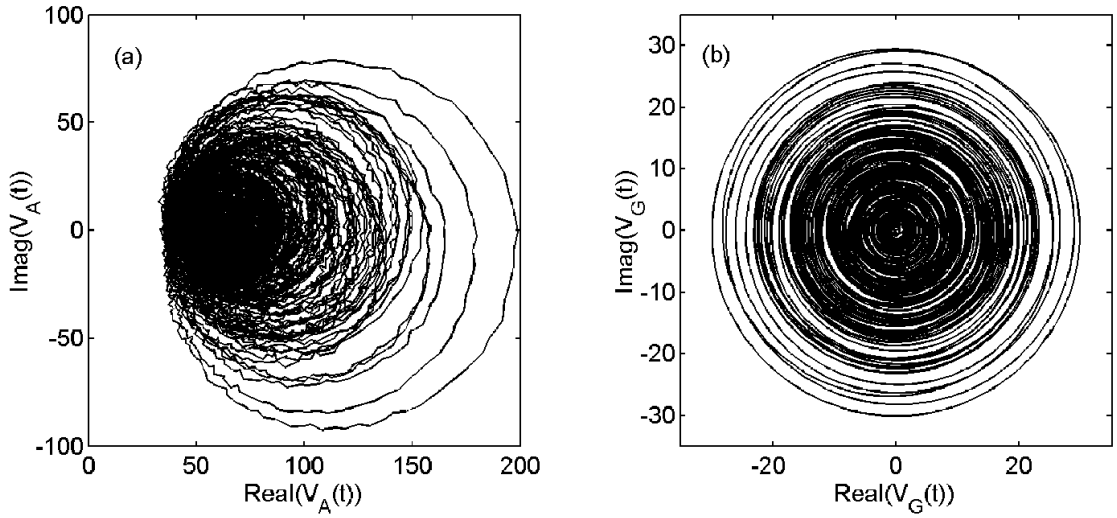

Figure 5.7: Contrasting the analytic signal $V_A(t)$ (a) with the Gaussian filtered analytic signal $V_G(t)$ (b) for a soft modulated laser we are able see how filtering will provide an improved phase definition. $V_G(t)$ was determined with a filter centered at $\nu_o = 80kHz$ and a standard deviation of $\sigma = 18kHz$. Angular position determines phase.

synchronization using the phase definitions $\Phi_A(t)$ and $\Phi_G(t)$, as well as some others. One could use other band-limited forms for $f(\nu)$ and obtain results similar to our Gaussian choice. For example, we have found this is the case for $f(\nu) = (2\sigma)^{-1}\theta(\sigma - |\nu - \nu_o|)$. In this case, we calculated $V(t)$ by Fourier transforming $I(t)$, replacing $u(\nu)$ by $f(\nu)u(\nu)$, and inverse transforming. In the case where the calculation is done directly in time, via a convolution, the convolution is numerically easier to perform for the Gaussian choice, since the Gaussian kernel is better localized in time.

5.2.3 Phase Synchronization of a Three Laser Array

Using the definitions of $\Phi_{A,G}(t)$ above, we are now able to study phase synchronization between the individual lasers in the array [18, 19]. We know that the side lasers (1&3) display identical synchronization, Fig. 4.9, so phase synchronization, a comparatively weak form of synchronization necessary for identical synchronization, is present. But what about the interaction of the outer lasers (1 & 3) with the

central laser (2)? Will a phase variable derived from the intensity time series of the individual lasers allow us to test for interdependence of these lasers? We concentrate on lasers 1 and 2 for the remainder of this section and investigate their interaction using the concept of phase synchronization.

In the previous section we introduced an analytic phase $\Phi_A(t)$ and a Gaussian filtered phase $\Phi_G(t)$. To determine these variables from an experimental data set, we generate $V_{A,G}(t)$ by first applying an appropriate fast Fourier transform algorithm to $I(t)$. The resulting $u(\nu)$ is multiplied by $2\theta(\nu)$, in the analytic case, or $\exp[-(\nu - \nu_o)^2/2\sigma^2]$ for the Gaussian filtered case, before applying the inverse fast Fourier transform to obtain our complex signal $V(t)$. $V_{A,G}(t)$ is then used to determine $\Phi_{A,G}(t)$ as defined in Eqns. (5.9 & 5.11). The phase variables are defined such that they are continuous in time, i.e. $\Phi_{A,G}(t)$ increases continuously in time and is not discontinuously reset to 0 as it passes through 2π. In the Gaussian case, the physical relevance of the phase is guaranteed by always choosing $f(\nu)$ such that $\sigma \times$ *duration of time series* $\gg 1$.

Let us first examine the case of an unmodulated laser array. Phase synchronization of an outer laser (1) and the central laser (2) with is determined by plotting the relative phase, $\Delta\Phi(t) \equiv \big(\Phi_1(t) - \Phi_2(t)\big)/2\pi$ versus time. In Fig. 5.8(a), the analytic signal relative phase $\Delta\Phi_A(t)$ varies over a broad range of values (≈ 130 rotations), including discontinuous jumps, and only very limited flat regions. In short, phase synchronization is not observed using the unfiltered analytic phases. However, phase synchronization is observed plotting $\Delta\Phi_G(t)$ in Fig. 5.8(b). Nearly perfect phase synchronization is observed with a Gaussian filter centered at $\nu_o = 140kHz$ (solid line), while significant phase synchronization with intermittent phase slips is seen with $\nu_o = 80kHz$ (dotted line). These values of ν_o were chosen because they correspond to significant peaks in the power spectra of the lasers. This guarantees the phases calculated correspond to dominant frequency components of the intensity dynamics. In both cases $\sigma = 15kHz$. No synchronization was detected when one of the component phases of $\Delta\Phi_G(t, \nu_o = 140kHz, \sigma = 15kHz)$ was replaced with a surrogate phase vector from another intensity time series sampled under identical

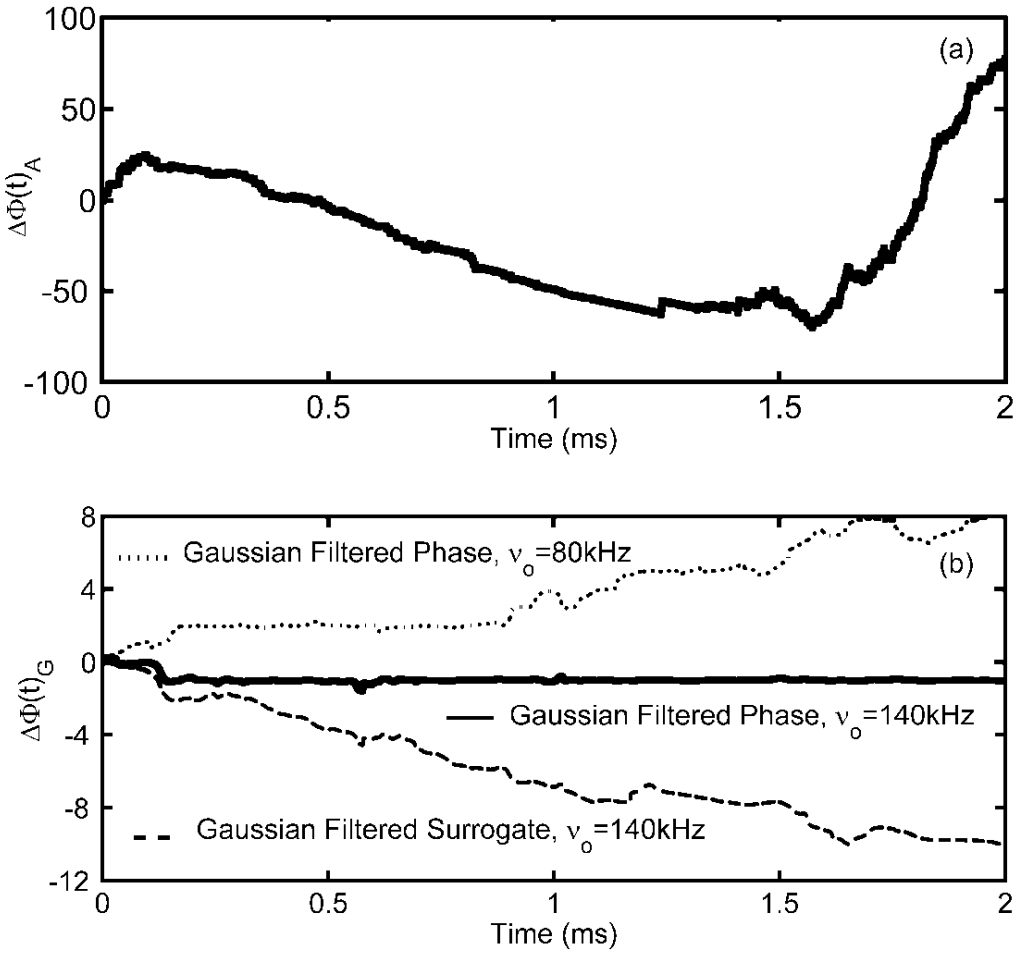

Figure 5.8: Time series for relative phases of (a) $\Delta\Phi_A(t)$ and (b) $\Delta\Phi_G(t)$ for lasers 1 and 2 of the unmodulated laser array. Phase synchronization is not seen for $\Delta\Phi_A(t)$ (a), but is easily observable for $\Delta\Phi_G(t)$ (b) with the Gaussian filter centered at $\nu_o = 140kHz$ (solid line). Intermittent phase slipping and synchronization is observed with $\nu_o = 80kHz$ (dotted line). No synchronization is observed, as expected, when Gaussian filtered surrogate phase is introduced as a replacement for one of the component phases of $\Delta\Phi_G(t)$ with $\nu_o = 140kHz$ (dashed line). Here $\Delta\Phi(t) = (\Delta\Phi_1(t) - \Delta\Phi_2)/2\pi$, and for all traces in (b) the Gaussian filter width is $\sigma = 15kHz$.

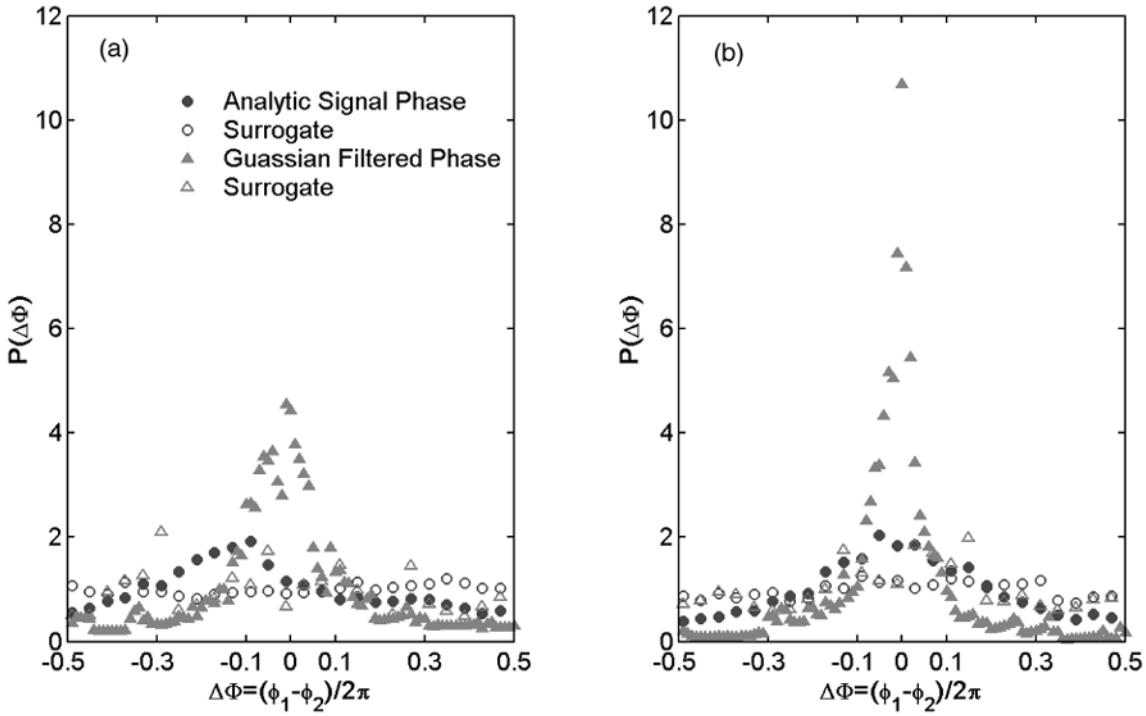

Figure 5.9: Normalized probability distributions of $\Delta\Phi(t)$ for laser arrays with no modulation (a) and soft modulation (b). Gaussian filtered phases display strong peaks (filled gray diamonds) while the analytic phases (filled black circles) show only slight peaks in the distributions. The surrogate cases (open symbols) display nearly uniform distributions. The Gaussian filter was defined with $\nu_o = 80kHz$ and $\sigma = 18kHz$.

conditions (dashed line).

The dramatic effect of loss modulation, as well as the improved detection of phase synchronization may be examined using the normalized probability distribution of the relative phases ($\Delta\Phi(t)$mod1, where $\Delta\Phi$ has already been normalized by 2π). Figure 5.9 displays results for the laser array with no modulation (a) and with soft modulation (b). In both cases the Gaussian filtered ($\nu_o = 80kHz$, $\sigma = 18kHz$) relative phase (filled gray diamonds) displays the dominant peak, though it is larger in the soft modulated case (b). The analytic signal relative phase (filled black circles) shows only slight peaks in the distributions. Relative phases calculated with surrogate signals (open symbols) have nearly uniform distributions.

As in Section 5.1.2, when examining entrainment of the dynamics to the modulation signal, we are able to quantify the level of phase synchronization using the

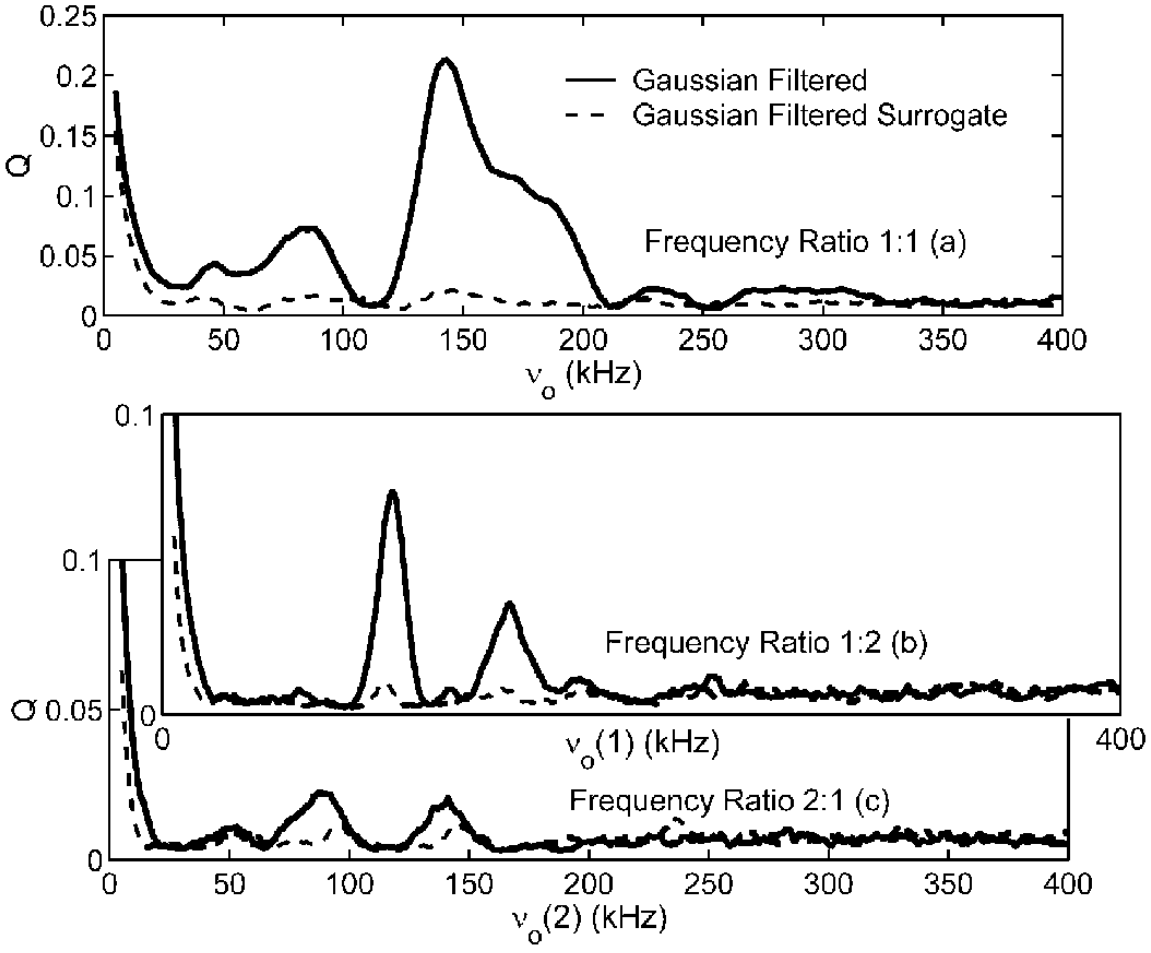

Figure 5.10: Phase synchronization of unmodulated laser 1 with laser 2 for frequency ratios of $\nu_o(laser1) : \nu_o(laser2)$ = 1:1 (a), 1:2 (b) and 2:1 (c), solid lines. Significant 1:1 phase synchronization occurs primarily between $125kHz$ and $200kHz$ (a), with weaker and more restricted synchronization present at higher frequency ratios (b & c). All synchronization measurements used a $\sigma = 18kHz$ Gaussian filter. The dashed lines represent synchronization results using surrogate time series.

normalized Shannon entropy calculated from the probability distributions of the relative phases. Recalling Eqn. (5.2), we define our synchronization measure $Q \equiv 1 - S$ where $S = \sum_{l=1}^{N} P_l \ln P_l / \ln(1/N)$ (where P_l is the probability of $\Delta\Phi_G \mathrm{mod} 1$ being in bin l). By plotting the Q as a function of ν_o we are able to study the phase synchronization of lasers 1 and 2 in a range of frequency regimes and ratios. In Fig. 5.10(a) we see that for a 1:1 frequency ratio, strong phase synchronization is observed for frequency bands less than $200kHz$, and is strongest between $125kHz$ and $200kHz$ (solid line). The dashed line indicates the base level provided by the surrogate measurement. The synchronization ranges for frequency ratios of $\nu_o(laser1) : \nu_o(laser2)$ =1:2 and 2:1 are more restricted and weaker than observed in the 1:1 case, as seen in Figs. 5.10(b) and (c) respectively. In all cases $\sigma = 18kHz$.

Scanning the center frequencies of the Gaussian filters in lockstep and at set ratios, as in Fig. 5.10, suggests a method to obtain a more global picture of phase synchronization in the three laser array. By shifting the filter centers for both lasers independently, we are able to identify frequency regimes and ratios of phase synchronization at a single glance. In Fig. 5.11 we see this method applied and the synchronization ratios identified in Fig. 5.10 are again observed, and labeled. Fig. 5.11(a) plots the phase synchronization results on a three dimensional plot with $\nu_o(2)$ and $\nu_o(1)$ on the x- and y-axes, and our phase synchronization measure Q on the z-axis. The color scaling is preserved in Fig. 5.11(b) where we see the 'bird's-eye-view' of the global phase synchronization plot of the first two lasers of the unmodulated laser array. The synchronization peak near $\nu_o(1), \nu_o(2) = 0$ is due to the strong, low frequency content of the unmodulated power spectrum, see Fig. 5.1(a). This synchronization is 'false' as it is present in the surrogate case, see Fig. 5.10. Along both axes ν_o is advanced by $5kHz$ increments while maintaining a filter width of $\sigma = 18kHz$. This produces the dotted lines for higher frequency ratios in the regimes of phase synchronization.

By applying a soft loss modulation ($\epsilon_{mod} = 0.07$) to the laser array, we observe a dramatic increase in over-all synchronization, Fig. 5.12. While the maximum level of phase synchronization for a given frequency regime is basically unchanged,

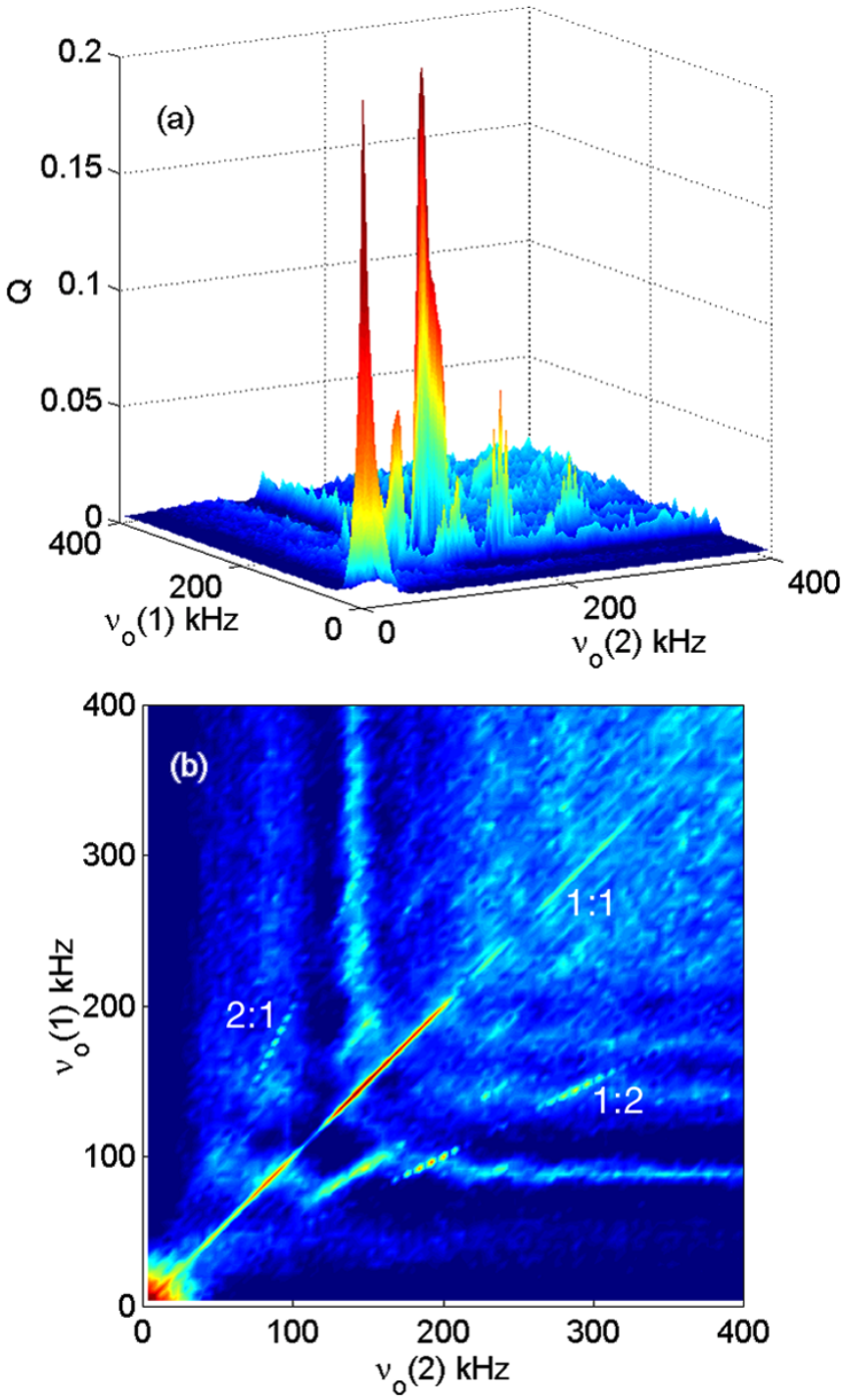

Figure 5.11: Global phase synchronization of unmodulated laser 1 with laser 2. Three dimensional synchronization profile (a) displays Q (z-axis) as the Gaussian filter centers, ν_o, for laser 1 (y-axis) and laser 2 (x-axis) are shifted independently. Significant synchronization is observed along ratios of 1:1, 2:1 and 1:2. The top-down view (b) preserves the color-scaling of Q in (a). ν_o is shifted in increments of $5kHz$ for both lasers, causing the dotted lines for higher frequency ratios of synchronization. Selected frequency ratios that display synchronization are labeled.

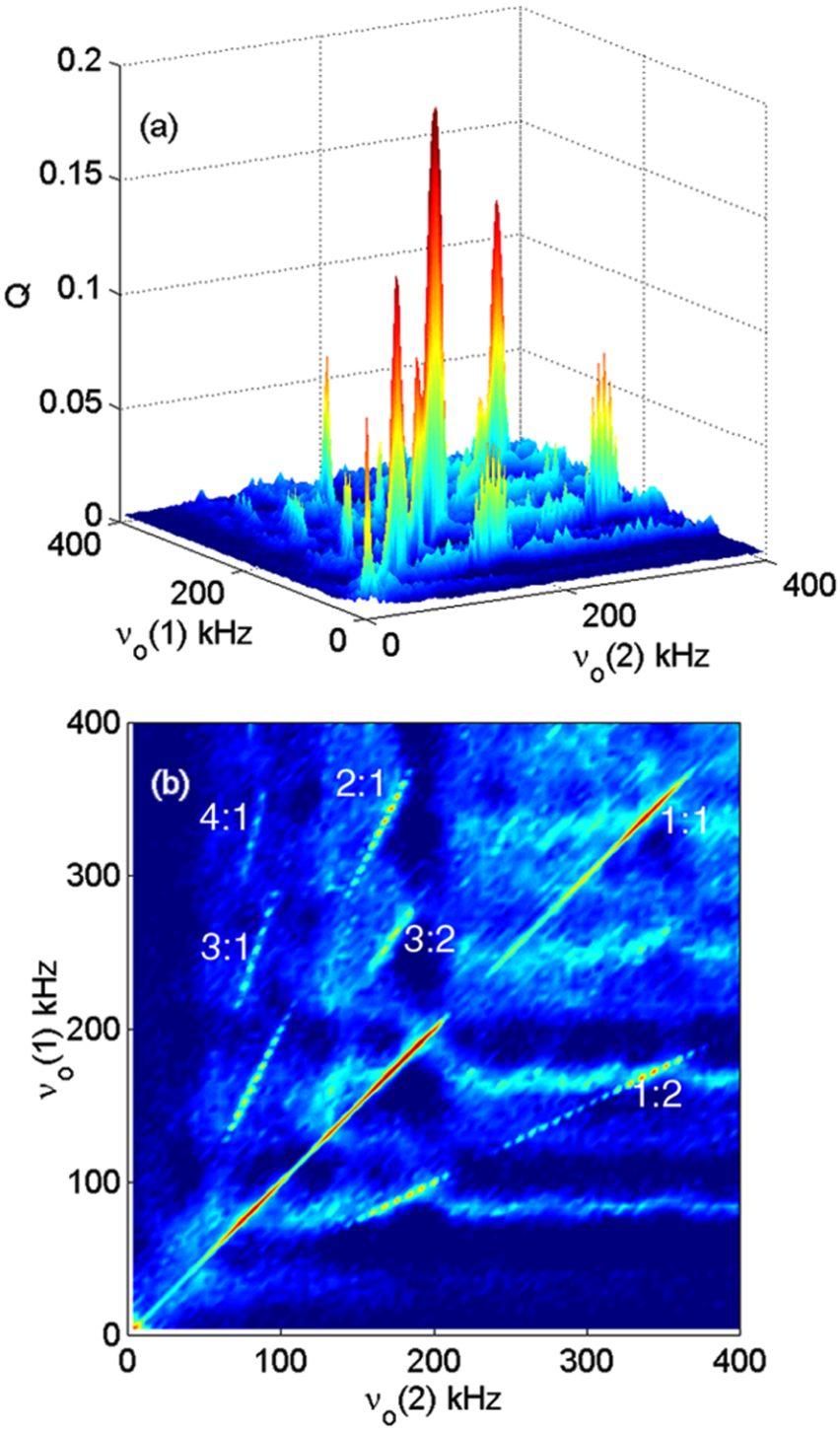

Figure 5.12: Global phase synchronization of soft modulated ($\epsilon_{mod} = 0.07$) dynamics of laser 1 and laser 2. Three-dimensional synchronization profile (a) displays Q (z-axis) as the Gaussian filters for laser 1 (y-axis) and laser 2 (x-axis) are shifted independently. The top-down view (b) preserves the color-scaling of Q in (a). The soft loss modulation of the laser cavity increases the frequency range of synchronization and the number of higher frequency ratios displaying significant synchronization.

significant synchronization is observed for a broader frequency range of the 1:1 ratio. Synchronization is induced in additional higher frequency ratios with greater magnitude as well. The 'false' (present in the surrogate cases) low frequency synchronization observed in the unmodulated array has disappeared. As observed in the intensity time series presented in Fig. 4.8, soft modulation results in sustained chaotic oscillations, eliminating much of the dynamics' low frequency components. As in the unmodulated plots, Fig. 5.12(a) provides the global three-dimensional phase synchronization plot, while Fig. 5.12(b) presents the top-down view, preserving the color scaling of Q of the three-dimensional plot. Again, ν_o is shifted by increments of $5kHz$ for both lasers independently with $\sigma = 18kHz$.

Hard modulation ($\epsilon_{mod} = 0.23$) of the laser array results in q-switched pulse dynamics. The discontinuous nature of these dynamics predictably suppresses phase synchronization between the lasers, as observed in Fig. 5.13. However, the phase synchronization is more uniform in frequency space. The higher frequency ratios of synchronization also show a greater range of synchronization. As before, the top-down synchronization plot Fig. 5.13(b) preserves the color scaling of Q in the three dimensional plots. The center of the Gaussian frequency filters are shifted by $5kHz$ steps, with $\sigma = 18kHz$.

5.3 Discussion

Phase synchronization and entrainment is studied in a loss modulated linear Nd:YAG three laser array, where the elements of the array are nearest neighbor coupled. The intensity dynamics of individual lasers in the array display amplitude instabilities without modulation, and shift to sustained chaotic dynamics with soft loss modulation. Increasing the level of modulation, the individual lasers move to chaotic Q-switched spiking behavior. Entrainment of the intensity dynamics to the sinusoidal modulation signal is demonstrated. Defining a measure of entrainment using the normalized Shannon entropy, we show the entrainment monotonically increases

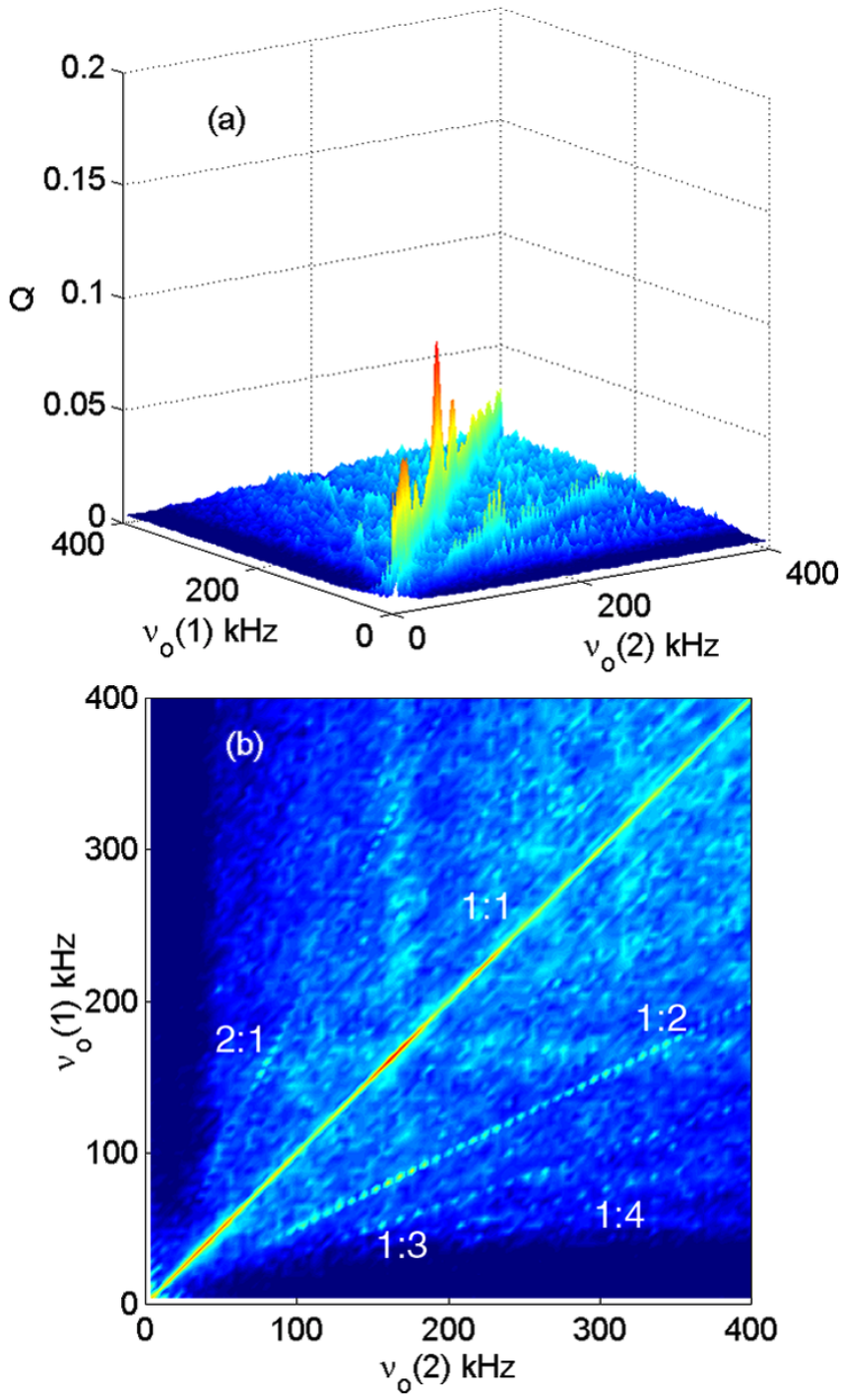

Figure 5.13: Global phase synchronization of hard modulated ($\epsilon_{mod} = 0.23$) dynamics of laser 1 and laser 2. Three dimensional synchronization profile (a) displays Q (z-axis) as the Gaussian filters for laser 1 (y-axis) and laser 2 (x-axis) are shifted independently. The top-down view (b) preserves the color-scaling of Q in (a). Hard modulation results in q-switching intensity dynamics, whose discontinuous nature results in reduced phase synchronization peaks. However, phase synchronization is more consistent on the frequency ratios indicated.

with modulation strength.

Significant synchronization of the intensity dynamics of the outer lasers of the array was found [17]. However, the intensity dynamics alone do not reveal the relationship of the central laser with the two side lasers. By defining phase variables from the intensity time series, we are able to investigate the relationship of the central and side lasers of the array. The phases are calculated using a positive peaked Gaussian frequency filtered complex Gabor analytic signal. This definition of phase for the array elements allowed the discovery of relationships between the lasers that are not otherwise apparent. Additionally, the frequency confined nature of the phase variables, due to the filter, permitted investigations of various frequency components and frequency ratios of the dynamics of the laser array. A phase synchronization measure, again based on a normalized Shannon entropy, allowed the visualization of a global picture of phase synchronization. Phase synchronization increased dramatically, and the synchronized frequency components shifted with soft modulation. However, hard loss modulation, which resulted in Q-switched intensity time series suppressed the level of phase synchronization due to the discontinuous nature of the pulsing dynamics.

Introducing a Gaussian frequency filtered phase variable to study nonstationary noisy data is clearly advantageous. Relationships in the experimental example of a chaotic linear laser array are clearly evidenced that are otherwise obscured. This technique should be applicable to a wide range of physical and biological investigations.

Chapter 6

Injection Induced Bursting in an Erbium-Doped Fiber Ring Laser

The occurrence of large bursts is ubiquitous in nature – astrophysical objects [102, 103], neurons [104], and lasers [52, 105, 106, 71] – all display bursting dynamics under certain conditions. Great effort has been made to understand the origin of bursts in specific systems. For example, detailed models have been constructed for neural systems, where it is thought that bursts of electrical activity are responsible for conveying information to different parts of an organism [107, 108]. By studying injection induced bursting dynamics in erbium-doped fiber ring-lasers (EDFRL) insight into these dynamical systems and others may be gained, as well as improved understanding of EDFRLs.

6.1 Injected Lasers

The study of the effect of injected light fields on laser properties and dynamics reaches back to the early years of laser research. In 1972, Spencer and Lamb presented the first theoretical study of a laser with optical injection [109]. Practical applications of introducing a monochromatic injection signal to a laser system has driven investigations into similar systems. Benefits of laser injection include increased power output and stabilization through injection seeding [110], control of polarization states [111], and, perhaps most importantly, stabilizing and tuning the optical spectrum of the injected laser through frequency locking [112, 113]. One ingenious application of injection frequency locking is preventing phase-detuning in an array of non-identical solid state lasers [114]. By frequency locking the entire array to a common injection signal peak intensities reach $N^2 I$, identical to the performance of a perfectly phase-locked laser array. N corresponds to the number of lasers in the array and I is the individual laser intensity.

Successful frequency locking is dependent on the detuning of the injection source with respect to the injected laser. Lariontsev et al. [115] used a class-B, injected laser model to examine injection locking in a Nd:YAG microchip laser. Utilizing the uniform field approximation and the slowly varying envelope approximation for a single longitudinal mode solid state laser the rate equations are

$$\frac{d\mathcal{E}}{dt} = \big[\Gamma\big(N\frac{1-i\delta}{1+\delta^2}-1\big) - i(\omega_{inj}-\omega_n)\big]\mathcal{E} + \kappa\frac{\mathcal{E}_{inj}}{T_c}, \tag{6.1a}$$

$$\frac{dN}{dt} = \frac{1}{T_1}\big[N_o - N\big(1+\frac{|\mathcal{E}|^2}{1+\delta^2}\big)\big]. \tag{6.1b}$$

Here the field equation, using the slowly varying envelope approximation, has been shifted to a frame where the complex electric field rotates with the injection laser frequency such that $E = \mathcal{E}\exp[i\omega_{inj}t]$. The subscript inj differentiates the complex injected field from the complex laser field. Γ is the photon decay rate from the laser cavity, and $\delta = (\omega_n - \omega_o)/\gamma$ is the relative detuning of the lasing mode n with the line-center ω_o, where 2γ is the linewidth. The ratio of the injected field to the intracavity field is given by κ. T_c is the cavity round-trip time. Hence, the final

term of the field equation determines the rate of injection into the cavity. N is the population inversion density normalized to threshold, and T_1^{-1} is its decay rate. N_o corresponds to the pump strength, and is normalized to the laser threshold value with $\omega_n = \omega_o$ such that $N_o = \eta_o + 1$ and η_o is the excess pump above threshold.

The stability of the injected laser's intensity dynamics is dependent on the terms $i(\omega_{inj} - \omega_n)$ and κ in Eqn. (6.1a). First investigating the stable frequency locked regime, Lariontsev et al. write the stationary solutions for Eqn. (6.1) where $d\mathcal{E}/dt = 0$ and $dN/dt = 0$,

$$S^2 = |\mathcal{E}|^2\big[\big(\frac{N}{1-\delta^2} - 1\big)^2 + \big(\Omega + \delta\big(\frac{N}{1+\delta} - 1\big)\big)^2\big], \tag{6.2}$$

$$N = \frac{1+\eta_o}{1+|\mathcal{E}|^2/(1+\delta 2)}. \tag{6.3}$$

Here $\Omega = (\omega_{inj} - \omega_n)/\Gamma$ is the normalized detuning between the injection laser and the frequency of the independent laser. $S = \kappa\mathcal{E}_{inj}/(\Gamma T_c\sqrt{I_s})$ is the normalized injected field amplitude with I_s an intensity saturation parameter derived from the finite gain of the active medium [115]. Considering small perturbations to $|\mathcal{E}|^2$ and N and with the ansatz $|\mathcal{E}|^2, N \sim \exp[\lambda t\Gamma]$ we find the characteristic equation

$$\lambda^3 + a_2\lambda^2 + a_1\lambda + a_o = 0, \tag{6.4}$$

using the definitions

$$a_2 = b - 2N_1, \tag{6.5}$$

$$a_1 = N_1^2 - 2bN_1 + N_2^2 + N_3, \tag{6.6}$$

$$a_o = b(N_1^2 + N_2^2) - N_3(N_1 + \delta N_2), \tag{6.7}$$

and

$$b = (\Gamma T_1)^{-1}\big(1 + \frac{|\mathcal{E}|^2}{1+\delta^2}\big), \tag{6.8}$$

$$N_1 = \frac{N}{1+\delta^2} - 1, \tag{6.9}$$

$$N_2 = \delta N_1 + \Omega, \tag{6.10}$$

$$N_3 = \frac{1}{\Gamma T_1}\frac{2N|\mathcal{E}|^2}{(1+\delta^2)^2}. \tag{6.11}$$

With Eqns. (6.3) we find stable frequency locking while the inequalities

$$a_o > 0,\ a_1 > 0,\ a_1 a_2 - a_o > 0 \tag{6.12}$$

hold.

However, the injected laser is not free from the influence of the injected light field when the detuning shifts slightly beyond the stable frequency locked regime. A broader range of injection locking allows for instabilities and dynamics due to interactions of the light fields. This broader locking range is defined by the band of detunings where the inequality

$$|\mathcal{E}|^2 > |\mathcal{E}_{free}|^2 \tag{6.13}$$

holds and encompasses the stable frequency locked range. Here $\mathcal{E}_{free}$ is the complex electric field of the laser with out injection. As long as the injection is enhancing the power of the laser, the injected laser system is locked in some fashion. From Eqn. (6.13) one may derive the broad injection locking range for $\delta < 0$ [110]

$$-\frac{S\sqrt{1+\delta^2}}{\sqrt{\eta_o - \delta^2}} \leq \Omega \leq \frac{S}{\sqrt{\eta_o - \delta^2}}. \tag{6.14}$$

Figure 6.1 from Ref. [115] displays the frequency locking regimes with increasing normalized injection amplitude S, and pump excesses of $\eta_o - \delta^2 = 0.01$ (label 1), $\eta_o - \delta^2 = 0.25$ (label 2), and $\eta_o - \delta^2 = 9.84$ (label 3). The subject system is a Nd:YAG microchip laser with a cavity length of $1mm$, and a cavity loss of 2%. The stable boundary (solid line) coincides with the boundary determined by Eqn. 6.14 (dotted line) for the lower boundaries of (1) and (2) and all of (3).

Outside of the stable frequency locking regime, the introduction of an external light field to a laser may result in instabilities and chaotic dynamics in the injected laser. Arecchi and co-workers examined theoretically the case of a homogeneously broadened CO_2, laser where optical injection resulted in period doubling cascades and deterministic chaos [52, 105, 12]. Careful and extensive work mapping bifurcations, routes to chaos and dynamics in injected semiconductor laser systems has been pursued by Krauskopf, Lenstra, Simpson and co-workers in recent years [116, 117, 118, 119, 120].

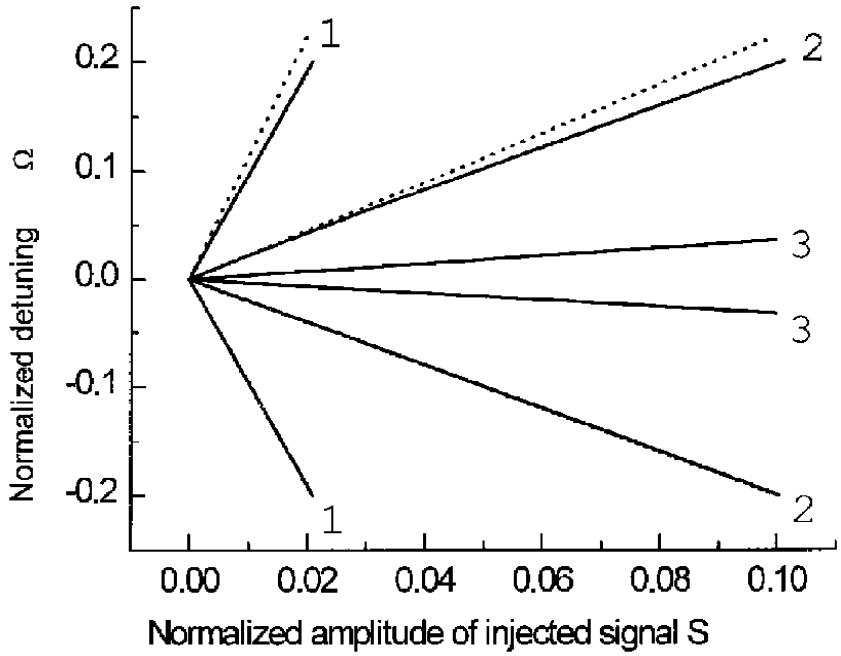

Figure 6.1: Stable (solid lines) and unstable (dotted lines) locking regimes for pump excesses of $\eta_o - \delta^2 = 0.01$ (label 1), $\eta_o - \delta^2 = 0.25$ (label 2), and $\eta_o - \delta^2 = 9.84$ (label 3) for the modeled Nd:YAG microchip laser. An unstable locking regime beyond the stable frequency locked boundaries only occurs above the upper boundaries of the two weakly pumped cases. [115]

Beyond the range of any frequency locking, the injected laser dynamics may still be modified by the injected light field. The injected light may still sample the population inversion, beat with the lasing mode, and non-linear interactions such as four-wave mixing may occur between the injected frequency and the lasing frequency [121] to produce additional lasing peaks in the optical spectrum of the injected laser.

6.2 Injected EDFRL Bursting Dynamics

Bursting is induced in the erbium-doped fiber ring-laser by a constant intensity, monochromatic injection from an external cavity semiconductor diode laser [20]. Fig. 6.2 displays the experimental setup used to study injection-induced bursting dynamics. The active element of the ring laser is an erbium-doped fiber amplifier (EDFA) containing $17m$ of erbium-doped fiber pumped with a $980nm$ semiconductor diode laser. The fiber amplifiers (Model OFA-1203-17) used for this research were constructed by Oprel Corporation, which has since been purchased by JDS Uniphase. The ring-laser is operated far above threshold, with a pump power of $130mW$. Lasing threshold occurs at about $10mW$. Under these conditions, the optical power circulating in the ring laser is $P_{RL} \approx 9mW$. The uni-directionality of light propagation within the ring cavity in the direction of the arrow is enforced by Faraday optical isolators internal to the EDFA. The total fiber ring length is approximately $41.5m$. All passive (Corning, SMF) and doped fiber is single mode, non-polarization maintaining. A $(\lambda/4, \lambda/2, \lambda/4)$ optical waveplate polarization controller (PC) allows tuning of the net birefringence of the ring laser, and hence its lasing frequency, among other characteristics. The optical waveplates are mounted on a gradient refractive index lens coupled fiber bench, forming the polarization controller (Optics For Research, PC-FFB-S/S-1550-Y). We select a mode of operation where the EDFRL displays a single-peaked spectrum centered at $\lambda = 1557.8nm$, with a full width at half maximum of approximately $0.6nm$.

A common constant optical signal, also at $\lambda_{inj} = 1557.8nm$, is injected into

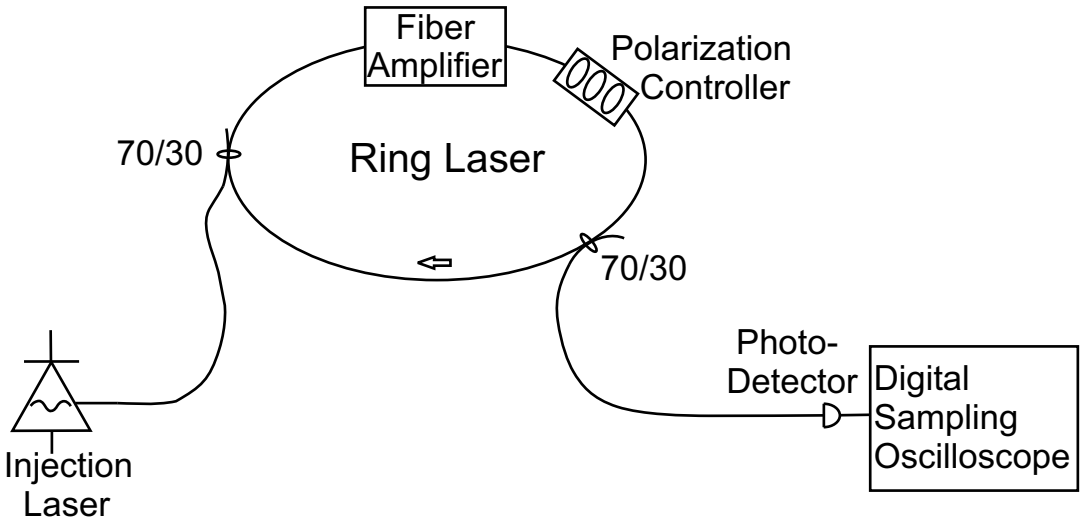

Figure 6.2: An injected Erbium-Doped Fiber Ring-Laser (EDFRL) with total fiber length of $41.5m$ displays bursting dynamics. The injection laser is a tunable External Cavity Semiconductor Diode Laser (ECSL). The EDFRL intensity dynamics are measured using a $125MHz$ bandwidth photo-detector and a $1GHz$ bandwidth Digital Sampling Oscilloscope.

the ring cavity using 70/30 fiber-optic evanescent field couplers (Gould Fiber Optics, Single Mode Coupler/Splitter 1550nm, 50-1 35-30-2-31-6-1), stimulating large intensity bursts in the ring-laser. The constant signal source is a tunable external cavity semi-conductor diode laser (ECSL) (Photonics Inc., Tunics-BT tunable diode laser).

Light from the EDFRL is extracted with a 70/30 coupler, and the dynamics are studied by measuring the intensity with a $125MHz$ bandwidth photodetector (New Focus Corp. Model 1811 IRDC) and a $1GHz$ bandwidth digital sampling oscilloscope (LeCroy, LC534).

The large bursts in intensity from a weak, constant injection signal are shown in Fig. 6.3. The top intensity time series displays injection induced bursting dynamics that may be contrasted with the free running EDFRL dynamics plotted below. While the burst events are large, and relatively slow, they each contain many fast intensity fluctuations. These fluctuations are the relaxation oscillations of the ring laser as the burst is damped and the ring laser returns to 'steady state' operation. The relaxation oscillation frequency is approximately $45kHz$.

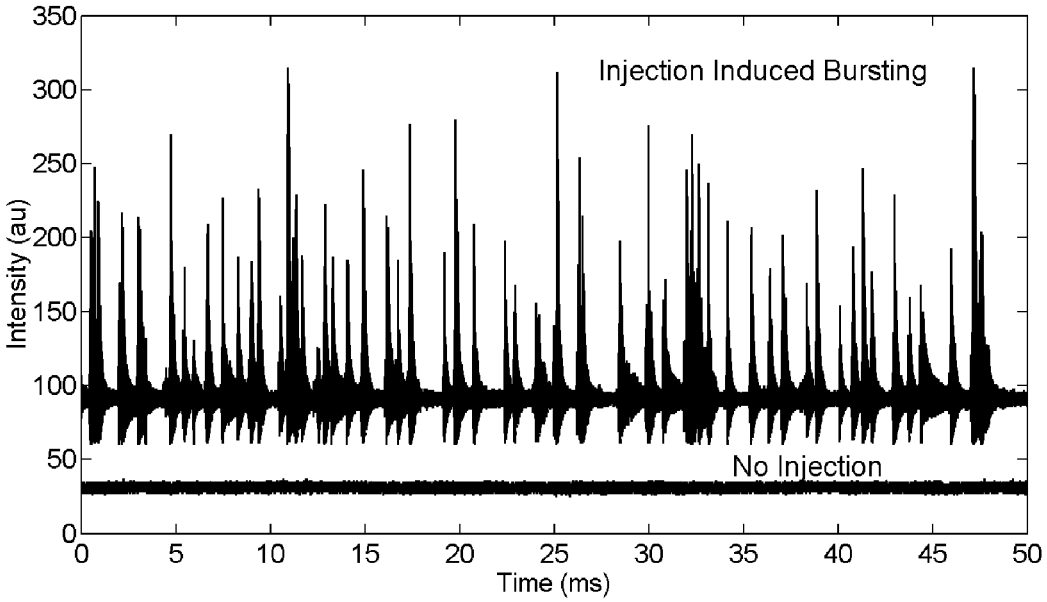

Figure 6.3: Optical injection induced bursting dynamics in the EDFRL (top) contrasted with the steady state output of the EDFRL with out injection (bottom).

Every burst in the ring-laser does not immediately return to steady state behavior. Often, as the initial burst relaxes, an additional burst or a train of additional bursts may occur before the laser finally returns to a state of relatively stable operation. Here the power ratio of the frequency matched optical injection signal to the intra-ring power is $P_{inj}/P_{RL} = 2.8 \times 10^{-3}$.

The optical spectra of the injection laser (dashed line) and the ring laser (solid line) are plotted on a log-linear scale in Fig. 6.4. Here, the injection laser and the EDFRL (without injection) are tuned such that their intensities as well as their peak frequencies are matched, $\lambda_{inj} = \lambda_{RL} = 1557.8nm$. The full width at half-maximum (FWHM) of the ring laser spectrum is $\Delta\lambda \approx 0.6nm$, or $\Delta\nu \approx 74GHz$. The width of the injection laser's optical spectrum (dashed line) is due to the $60pm$ resolution of the optical spectrum analyzer. The reported FWHM of the single mode external cavity semiconductor laser is $\Delta\nu = 150kHz$ or $\Delta\lambda = 1.21fm$ [122]. Note that in dBm a difference of -3 corresponds to a factor of two decrease in power. The FC/PC fiber coupled optical spectrum analyzer used is Agilent Technology's Model 86141B OSA.

The difference in the spectral widths of the two lasers is simply due to the

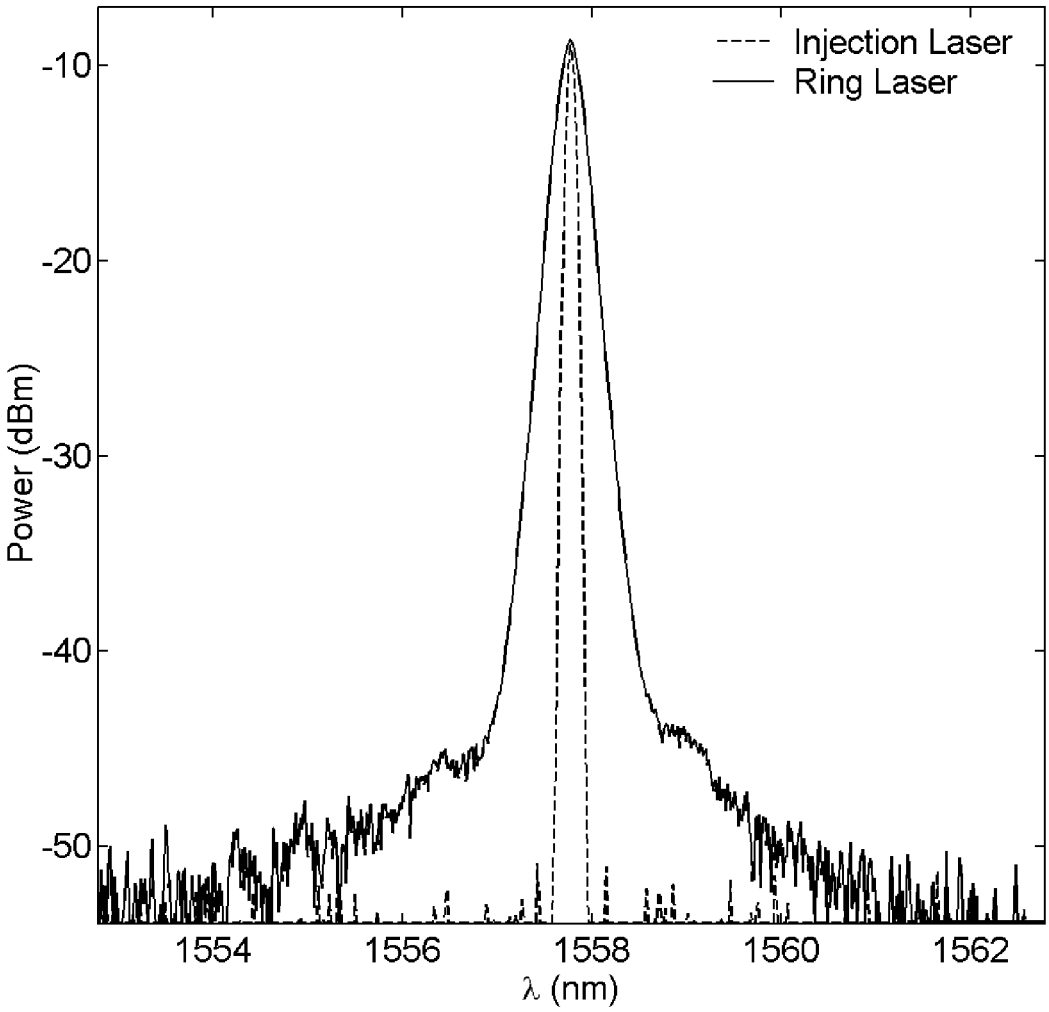

Figure 6.4: Optical spectra of EDFRL (solid line) and monochromatic injection laser (dashed line) with powers and frequencies matched. The width of the injection laser spectrum is due to instrumentation limitations. $\Delta\lambda_{RL} = 600pm$, $\Delta\lambda_{inj} = 1.21fm$

single mode nature of the external cavity injection laser and the multi-mode nature of the fiber ring laser. Recall that the ring cavity length is $L = 41.5m$, which corresponds to a free spectral range of $\Delta\nu_{sp} = 5MHz$. The free spectral range determines the optical mode spacing in a laser, and, for a ring cavity, is defined by $\Delta\nu_{sp} = c/nL$, where c is the speed of light in vacuum, $n = 1.44402$ is the index of refraction of fused silica (optical fiber), and L is the total length of the ring laser. Therefore, just the FWHM tip of the EDFRL spectrum contains ≈ 15000 modes contributing to the total intensity of EDFRL. It is also important to note that there exists a broad gain region beyond the lasing peak. Recalling Fig. 3.7, strong optical gain is available from $1530nm$ to $1560nm$ and beyond.

By successively injecting the EDFRL with different wavelengths of light and comparing the resulting dynamics, we are able to examine the effects of detunings between the injection and ring-lasers' spectral peaks on the bursting dynamics. In Fig. 6.5 we observe that the amplitude and frequency of bursts depend on the relative wavelengths of the laser. Starting with the injection laser matched to the EDFRL wavelength of $\lambda_{RL} = 1557.8nm$ (top intensity time series) the injection laser is progressively tuned towards the blue such that $\lambda_{inj} < \lambda_{RL}$ (moving down Fig. 6.5). As the detuning between the two lasers increases, the amplitude and the frequency of the bursts decreases. However, it is important to note that significant bursts still occur even after λ_{inj} has moved beyond the EDFRL spectral peak. Eventually, with the injection laser tuned to $\lambda_{inj} = 1545.0nm$ the EDFRL intensity dynamics are nearly identical to a ring laser without injection (bottom plot), with only minor, infrequent instabilities. For all intensity time series, $P_{inj}/P_{RL} = 2.8 \times 10^{-3}$, with both laser powers held constant. Note that the DC offsets of the intensity time series are artificial.

By choosing the ratio of the standard deviation of the intensity time series with its mean, $\sigma(I(t))/\langle I(t)\rangle$, as an intuitive measure of the bursting dynamics, we combine the amplitude and frequency of the bursting dynamics. By stepping through injection laser power as well as optical detuning, we observe a peaked structure in the top plot of Fig. 6.6. Here, the z-axis is the ratio $\sigma(I(t))/\langle I(t)\rangle$, the x-axis is the

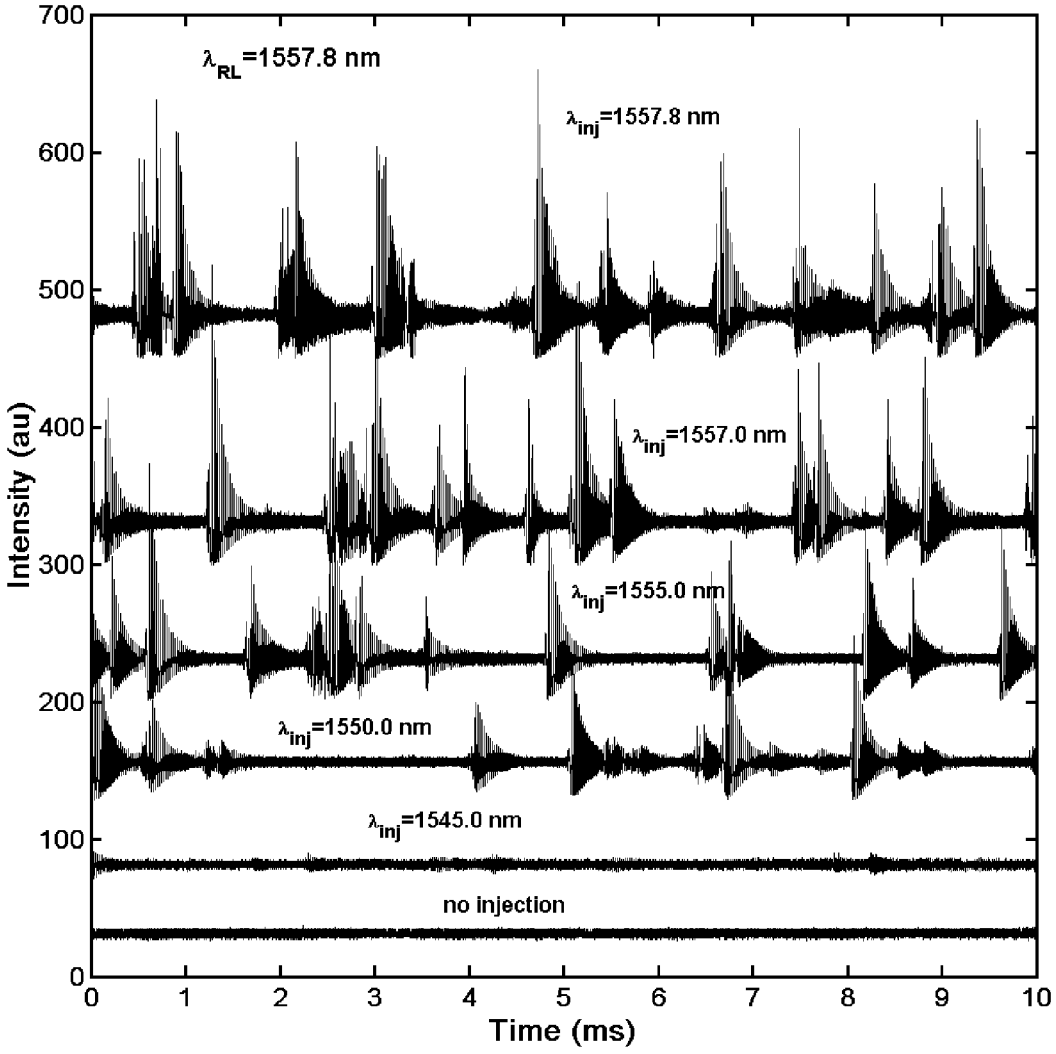

Figure 6.5: Injection induced bursting dynamics with increasing detuning. As the injection wavelength is moved away from the lasing peak of the EDFRL the amplitude and frequency of bursts decrease, until the intensity time series of the injected ring laser resembles that of a EDFRL without injection.

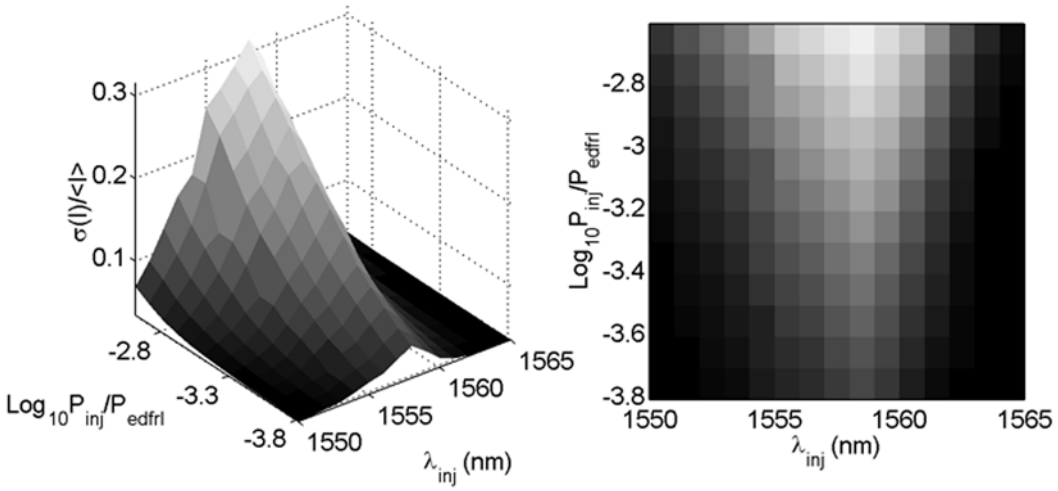

Figure 6.6: Profile of the standard deviation of the bursting intensity time series normalized by the mean intensity ($\sigma(I(t))/\langle I(t)\rangle$) as a function of injection power and wavelength. The peak is found at the maximal injection power, and near zero detuning. The gray-scale is preserved between the three dimensional and two dimensional plots.

injection laser's peak wavelength, and the y-axis is the logarithm of the ratio of laser powers $\log_{10} P_{inj}/P_{RL}$. Preserving the gray-scale encoding of the z-axis, the right plot of Fig. 6.6 provides a top-down view of the structure. As expected, the apex of the peak is located on resonance with the ring-laser, at the maximum injection power, $P_{inj}/P_{EDFRL} = 2.8 \times 10^{-3}$. The measure $\sigma(I(t))/\langle I(t)\rangle$ increases linearly to this peak at resonance as a function of the $\log_{10} P_{inj}/P_{RL}$. Additionally we observe an asymmetry between blue ($\lambda_{inj} < \lambda_{RL}$) and red ($\lambda_{inj} > \lambda_{RL}$) detuned injection induced dynamics. The nonlinear slope drops more quickly on the red detuned slope. This is likely due to the reduced gain in this region (see Fig. 3.7). Again, bursting is present with λ_{inj} beyond the lasing peak of the EDFRL, Fig. 6.4.

6.3 Origins of Bursting Dynamics

Beyond just observing the phenomena of injection induced bursting dynamics we need to understand its origins. Without this understanding we would be missing a significant piece of the overall picture of erbium doped fiber ring lasers. Uncovering

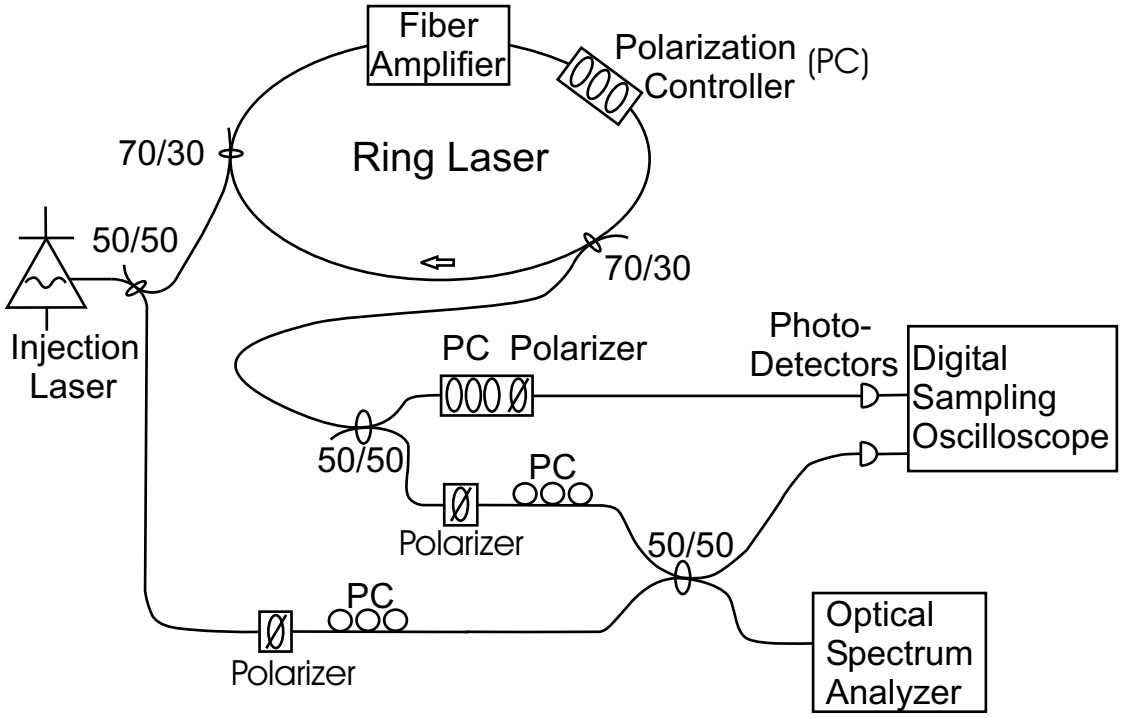

Figure 6.7: Fiber heterodyne experimental setup to study the optical mode dynamics of the erbium doped fiber ring laser. half of the output of the stable external cavity injection laser acts as a frequency signal (bottom channel). The output of the ring laser is divided into two channels. The top channel acts as a dynamics reference, carrying the pure EDFRL dynamics. The second half of the ring laser output is combined with the frequency reference signal using a 50/50 coupler, forming the heterodyne channel. The intensity dynamics of the heterodyne channel is compared with the pure EDFRL intensity dynamics to study the ring laser mode dynamics.

the source of these large intensity fluctuations may point the way to improved stability in fiber ring lasers and fiber laser arrays, both important in many applications. Additionally, understanding the complex bursting observed here provides a possible tool for understanding bursting dynamics in other systems with similar behavior, such as neurons [108].

The complex multi-mode character of EDFRLs provides a clue as to the origins of the ring-laser bursting. As discussed in Section 6.1, locking to and interactions with an injected laser field may cause significant changes in the behavior of the laser system. Therefore, we need to understand how the single-mode injected laser field interacts with the multiple lasing modes in the EDFRL.

To reveal the optical mode structure of the EDFRL and its dynamics, we

conduct a simple heterodyne experiment using the experimental setup diagramed in Fig. 6.7. The erbium-doped fiber ring-laser is identical to the one described above, with an active medium consisting of $17m$ of erbium doped fiber which is pumped with a $980nm$ emitting semiconductor diode laser. The ring laser is operated far above threshold with an intracavity power of approximately $9mW$. Faraday optical isolators internal to the fiber amplifier ensure the unidirectional circulation of light in the ring cavity in the direction indicated by the arrow. The total length of the single-mode, non-polarization maintaining optical fiber that forms the ring laser is $41.5m$, resulting in a free spectral range of $\Delta\nu_{sp} = 5MHz$. A $(\lambda/4, \lambda/2, \lambda/4)$ optical waveplate polarization controller allows tuning of the net birefringence of the fiber ring laser, and hence its lasing frequency, among other characteristics. Using this polarization controller, we tune the ring-laser such that it has a single dominant peak centered at $\lambda_{RL} = 1557.8nm$. Light is extracted from the ring cavity using a 70/30 evanescent field coupler. Bursting dynamics are stimulated by injecting light from a tunable external cavity semiconductor diode laser (ECSL) into the EDFRL using another 70/30 coupler.

The external cavity injection laser provides an ideal, stable reference laser for the heterodyne experiment. Tuned to the peak wavelength of the EDFRL, a 50/50 coupler (Gould Fiber Optics, single mode, 1550nm 2x2 splitter/combiner) diverts one half of the ECSL output to the fiber optic heterodyne. The EDFRL output is also split into two equal parts using a 50/50 coupler. The top fiber optic channel in Fig. 6.7 carries the baseline, pure EDFRL dynamics to be detected and recorded using a $125MHz$ photo-detector and a $1GHz$ bandwidth digital sampling oscilloscope. The other half of the ring laser output is combined with the reference laser light in the heterodyne channel using another 50/50 fiber optic coupler. All fiber lengths in the experimental setup are matched for simultaneous detection.

Light from the two lasers possess slightly different optical frequencies, and hence the optical phases of the two lasers rotate at different rates. As these phases slide in and out of phase with respect to one another, the laser fields constructively and destructively interfere, resulting in periodic fluctuations of the total intensity of

the combined beam. Due to the fact that the EDFRL output consists of thousands of lasing modes, the combined beam will have intensity fluctuations that correspond to a superposition of the detunings of each of these modes with respect to the stable reference frequency of the external cavity laser. In this case, we choose AC coupling so the only effect of mixing the laser fields is the beat induced modulations on the EDFRL intensity dynamics.

The second arm of the final 50/50 coupler also carries the combined EDFRL injection laser signal. By connecting this channel to a fiber coupled optical spectrum analyzer and blocking the EDFRL and the reference laser output in turns, the peak frequencies and powers entering the heterodyne channel are matched. This state corresponds to the optical spectrum observed in Fig. 6.4. Variable attenuator tweeker modules (not shown) (Optics For Research, Model HW-XY-1.5IR) are used to match peak powers.

As the entire experimental setup is constructed from non-polarization maintaining optical fiber, it is necessary to actively match the polarization state of the laser fields mixed and sampled. The ring laser generally lases in an elliptically polarized state [123, 14]. Lasing along orthogonal polarization directions in the ring laser may be thought of as two independent lasers sampling the same gain [59]. Additionally, optical fiber is intrinsically birefringent; every segment of fiber may be thought of as a randomly oriented polarization waveplate of indeterminate strength [124]. Fortunately, in a vibration isolated, temperature controlled laboratory environment, this collection of randomly oriented 'waveplates' is static for time scales of many minutes. Therefore, using both waveplate (Optics For Research) and fiber polarization controllers (PC) (Fiber Control Industries) in addition to linear polarizers (Optics For Research, Model PCB-IR1), it is possible to match the polarization states of the EDFRL and reference laser fields combined along the heterodyne channel. The polarized projection of the ring laser field in the heterodyne channel is matched with a polarization controller and linear polarizer in the pure EDFRL arm, ensuring the baseline intensity dynamics of the two arms are identical. Variable attenuator 'tweeker' modules (not shown) that do not affect polarization are used

to match the amplitudes of the baseline EDFRL dynamics.

Figure 6.8 illustrates the procedure for isolating the dynamics due to beating the EDFRL and injection laser, allowing the study of the EDFRL optical mode dynamics. Here, we concentrate on just a few relaxation oscillations of the single burst of the pure EDFRL output in Fig. 6.8(a). Fig. 6.8(b) displays just these oscillations, while Fig. 6.8(c) shows the beated EDFRL/reference laser signal. The oscillations in the intensity time series due to the time variable interference of the two lasers are readily apparent. Both the pure ring laser and beat dynamics are normalized to the standard deviation of the pure EDFRL intensity time series. When we subtract the pure ring laser intensity time series, from the heterodyne intensity time series we recover the dynamics solely due to the interaction of optical modes of the EDFRL and the injection/reference laser, Fig. 6.8(d). Figs. 6.8(e-g) display the power spectra of the pure EDFRL dynamics, beat dynamics and their difference respectively. A dominant peak at $5MHz$, corresponding to the free spectral range of the ring laser and indicative of the round-trip time repeating dynamics mentioned in Section 3.5.4, is apparent in both Figs. 6.8(e & f). The subtraction of the two signals greatly suppresses this feature, as may be seen in the power spectrum of the difference time series, Fig. 6.8(g) . The intensity time series is sampled at a rate of 500×10^6 $samples/second$. The power ratio of the injected optical signal to the circulating power is $P_{inj}/P_{RL} = 7.4 \times 10^{-2}$.

First, we examine the somewhat simpler mode dynamics of the fiber ring laser without injection. Fig. 6.9(a) displays the pure intensity time series of the EDFRL. Both the AC coupled EDFRL and the beated EDFRL/reference laser intensity time series are normalized to the standard deviation of the pure ring laser dynamics. The spectrogram of the difference of these data sets, the isolated beat dynamics due to the interaction of the EDFRL modes with the reference laser, is plotted in Fig. 6.9(b). The $2ms$ data set, sampled at 500×10^6 $samples/second$, is divided into 100 time steps with no overlap, and the power spectra for each of the $20\mu s$, $10,000$ point time segments is calculated and formed into a matrix. The logarithm of the power spectra amplitudes are encoded in color.

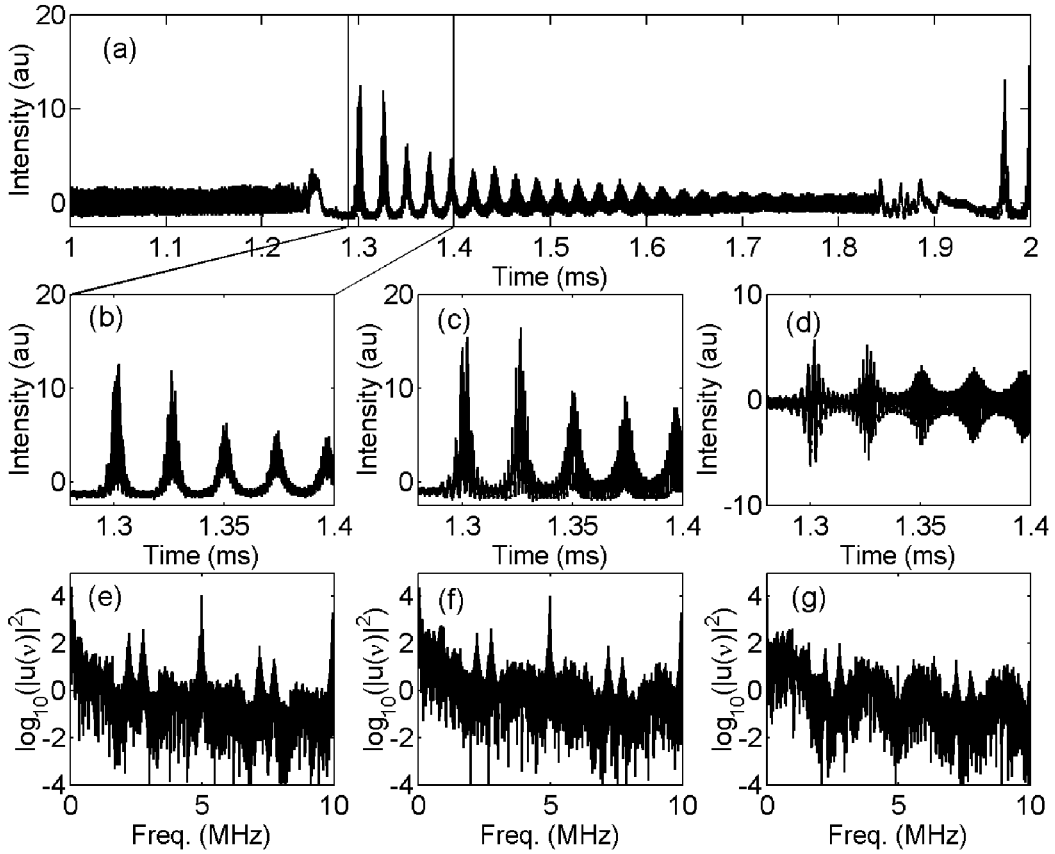

Figure 6.8: Isolating intensity dynamics due to the interaction of the optical modes of the EDFRL and the injection laser outputs. Initial relaxation oscillations of an injection induced burst are isolated (a & b). The corresponding oscillations from the EDFRL, mixed with the external cavity laser output, displays large intensity oscillations due to the beating of the two lasers (c). Taking the difference between the two intensity time series, the dynamics due to the beating of the two lasers are isolated (d). Suppression of the dominant features due the EDFRL intensity dynamics seen in power spectra (e & f) is observed in the power spectrum of the isolated beat dynamics (g).

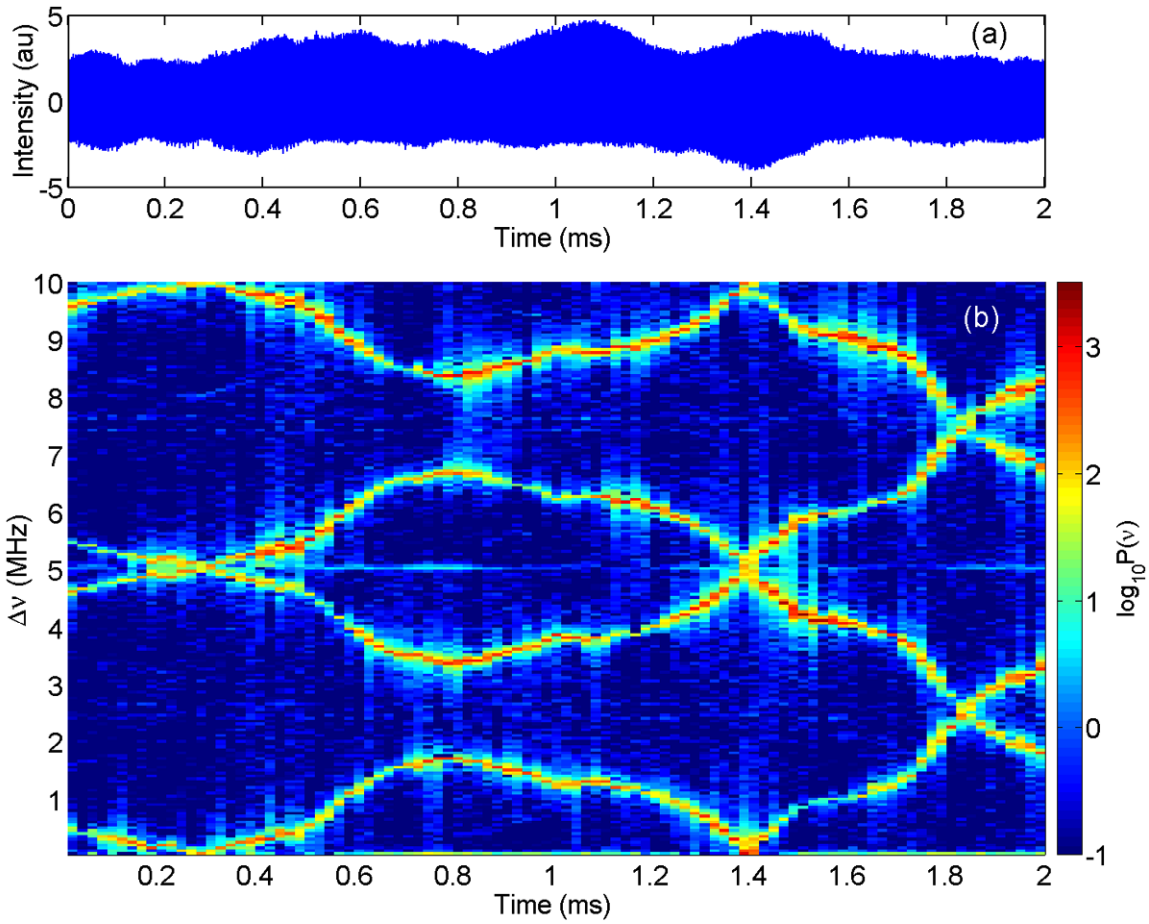

Figure 6.9: Longitudinal optical mode structure of the EDFRL without injection. The pure baseline ring laser dynamics are plotted in (a). The individual modes wander over several MHz in the spectrogram of the isolated beat dynamics of the ring laser with the external cavity reference laser (b). The duplicate, mirror image modes within the free spectral range of $5MHz$ results from only being able to measure the magnitude of the optical mode detunings, not their signs. The mode 'reflection' at $1.4ms$ is simply that particular ring laser mode passing through the optical frequency of the reference laser and shifting from a positive detuned to a negative detuned mode, or vice versa.

In Fig. 6.9(b) each of the wandering red and yellow trajectories represents an optical mode of the free running EDFRL. Again, the free spectral range of the fiber ring laser is $\nu_{sp} = 5MHz$, and dictates the longitudinal mode spacing. Note that within a detuning range, vertical axis, of $5MHz$ there are two modes whose wandering seems to mirror each other. The number of expecte modes doubles because the frequency of the intensity fluctuations in the heterodyne signal gives the magnitude of the detuning between EDFRL modes and the reference laser. Therefore, a negatively detuned EDFRL mode is folded over to a positive detuning in the spectrogram, and appears as the near mirror image of the positively detuned EDFRL mode. Additionally, the apparent reflection of the minimally detuned mode off of the zero-detuning reference at $0.3ms$ and $1.4ms$ is simply that particular ring laser mode passing through the optical frequency of the reference laser and shifting from a positive detuned to a negative detuned mode, continuing to evolve, and then passing through the reference frequency again. The ring laser modes maintain their $\Delta\nu_{sp}$ spacing as they wander over several MHz, without any apparent deterministic behavior. The horizontal line at $\Delta\nu = 5MHz$ is due to imperfect subtraction of the base line EDFRL intensity dynamics.

We now turn to a study of the mode dynamics of the EDFRL with injection. Fig. 6.10(a) displays the intensity time series of a pair of injection induced bursts, sampled at 500×10^6 $samples/second$ for a span of $2ms$. Again, the AC coupled EDFRL and the beated EDFRL/reference laser intensity time series are both normalized to the standard deviation of the pure EDFRL dynamics. The spectrogram of the difference of these data sets, the isolated beat dynamics due to the interaction of the EDFRL modes with the reference laser, is plotted in Fig. 6.10(b). As before, the $2ms$ 'difference' time series displayed in Fig. 6.10(a) is divided into 100 time segments with no overlap between the segments. The spectrogram is formed by calculating the power spectrum for each of the time slices and arranging the results in a matrix. The result is plotted with the amplitude of the power spectrum encoded as color. The horizontal lines are due to imperfect suppression of the EDFRL intensity dynamics. The faint ghost images forming additional sets of lasing modes

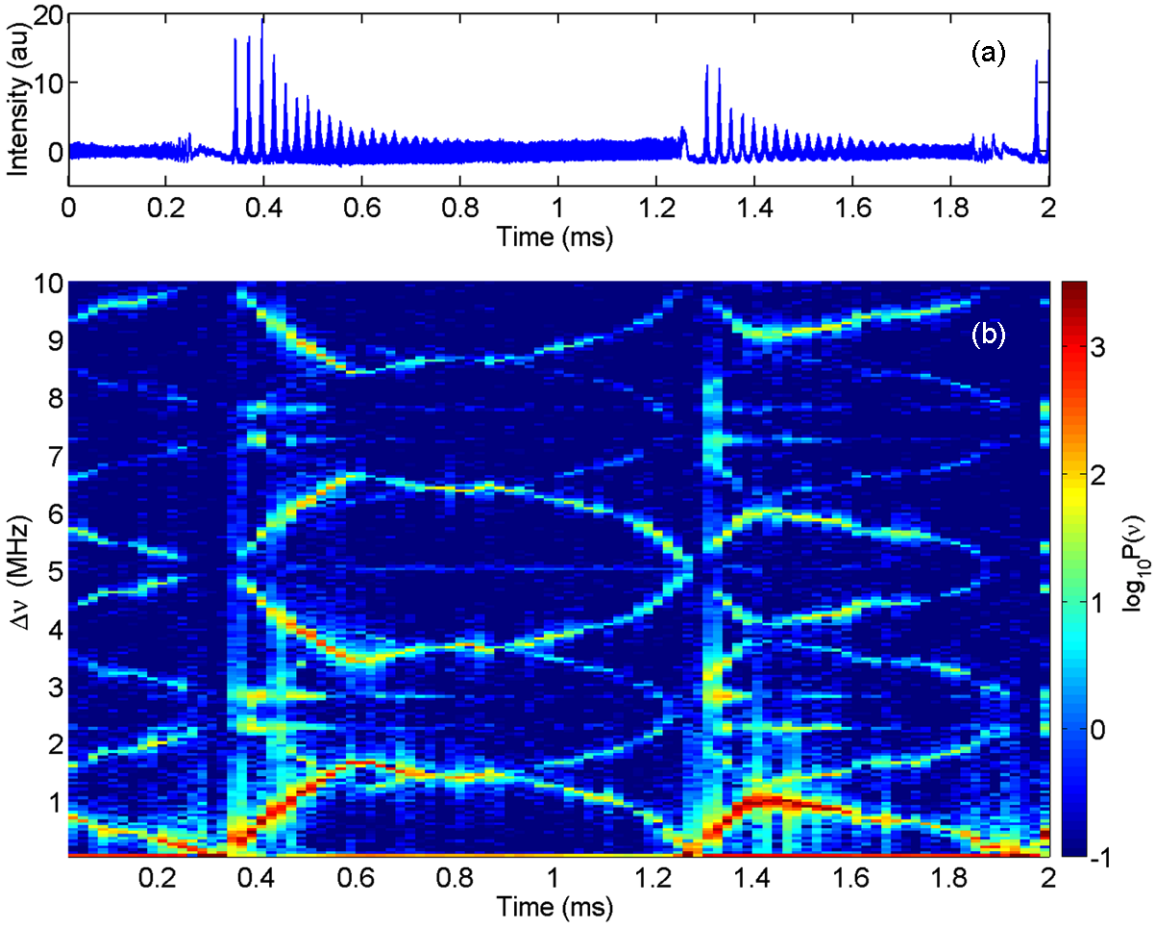

Figure 6.10: Longitudinal optical mode structure of an injected EDFRL. Injected induced bursting dynamics are plotted in (a). Individual optical modes wander relatively independent of the injection laser (b). Intermittently the minimum detuned EDFRL mode moves within locking range of the injection laser and locks. The locked mode monopolizes the gain provided by the erbium doped fiber, extinguishing lasing in all other modes. Large amplitude bursts in the EDFRL output occur when the minimum detuned mode escapes the locked state. At all times, optical power is concentrated near the injection laser frequency. Ghost images of orthogonally polarized lasing modes are observable.

are due to orthogonally polarized laser light fields, which are projected on the linear polarization state sampled by the linear polarizers shown in Fig. 6.7.

The critical development in the optical mode dynamics of the EDFRL with injection, and the difference between the uninjected case, is the interaction of the injection laser with its nearest neighbor EDFRL mode. While the detuning is relatively large, the mode evolution proceeds similarly to that observed in Fig. 6.9(b) for the uninjected laser. However, instead of merely passing through the injection laser frequency, it locks to the injected laser. At this point, all the power in the EDFRL is contained in this locked mode and all the other modes in the ring laser disappear. Ever so briefly, the injected EDFRL is a stable single-mode laser. Locking is evident in the intensity time series as the extent of the intensity fluctuations for this period are tightly confined, Fig. 6.10(a). When the 'natural' trajectory of the EDFRL mode moves beyond the locking regime, the laser bursts free of the injection frequency. The many EDFRL modes that were robbed of gain re-initiate lasing and the intensity undergoes relaxation oscillations in returning to its initial state, similar to that of the independent EDFRL. The ring laser modes then continue to wander, relatively independent of the injection, until the minimum detuned mode again momentarily locks to the injection laser, and subsequently initiates a burst upon release from the single mode locked state. Therefore, it is evident that the injection-induced burst dynamics are due to strong, intermittent interactions of the least detuned EDFRL mode with the reference injection laser, consisting of brief periods of locking, followed by bursts upon release of the EDFRL mode from the injection laser frequency.

The modes of the injected EDFRL are never completely free of the influence of the injected light field. Examining the magnitude of the minimally detuned EDFRL mode compared to the others within the $2\Delta\nu_{sp}$ range of Fig. 6.10(b), we see a significant decrease of power in modes removed from the injection laser frequency. Returning to the freely wandering EDFRL modes in Fig. 6.9(b) we observe there is nearly equal power in all the modes represented. There is always a confinement of the optical spectrum of the ring laser around the injection laser.

6.4 Injected EDFRL Model

We have observed experimentally that injection induced bursting dynamics are due to intermittent interaction of the minimally detuned mode of the erbium-doped fiber ring-laser and the single, stable mode of the injection laser. We also note that the bursting dynamics and relaxation oscillations are on time scales of milliseconds and tens of microseconds; many hundreds of times greater than the ring laser round trip time $\tau_c = 200ns$. With these two considerations in mind, we are free to take the uniform field approximation and model the injected ring laser as single mode class-B laser. We propose a simplified phenomenological model more similar to that describing a Nd:YAG laser, Eqns. (3.28 & 3.29), than to the model describing the sub-round trip dynamics of an EDFRL, Eqns. (3.45, 3.46, & 3.47),

$$\begin{aligned} \frac{dE}{dt} &= (G-\alpha)E - i\Delta\omega(t)E + E_{inj} + \eta(t), \\ \frac{dG}{dt} &= \frac{1}{T}(p - G - G|E|^2). \end{aligned} \tag{6.15}$$

Here E is the slowly varying complex electric field of the ring laser, and G is the normalized real gain of the doped fiber. We have chosen a rotating reference frame with a rate identical to the frequency of the injection laser, ω_{inj}, and normalized the time variable t by τ_c. The dimensionless detuning of the 'natural' lasing frequency ω_c of the ring laser, with respect to the injection laser frequency ω_{inj} is given by $\Delta\omega = (\omega_{inj} - \omega_c)\tau_c$, as determined by the ring cavity geometry and the properties of the lasing medium. The cavity loss coefficient is α, while the pump rate is p, and the threshold pump rate for laser action is $p_{th} = \alpha$. The amplitude of the injected field is given by E_{inj}. Spontaneous emission noise is given by $\eta(t)$, an independent Gaussian white noise source of zero mean with correlation $\langle \eta(t)\eta(t') \rangle = 2D_{sp}\delta(t-t')$ and strength D_{sp}. T, the time scale ratio in the gain term of Model (6.15), is defined by $T = \tau_f/\tau_c = 5 \times 10^4$, where $\tau_f = 10ms$ is the fluorescing time of the upper lasing level of the population inversion in Er^{3+}.

As discussed in Section 6.2, the EDFRL possesses many thousands of closely spaced longitudinal lasing modes with generally elliptic polarization states [14].

These properties are neglected in the above phenomenological model, which examines only a single linearly polarized longitudinal mode. As such, we must empirically match the majority of the model parameters such that simulations display dynamics similar to those of the actual laser system. The fluorescence time $\tau_f = 10ms$ and the cavity round trip time $\tau_c = 200ns$ used in the model correspond to those of the laser.

We are primarily concerned with understanding the bursting behavior observed in the injected EDFRL. Therefore, the relaxation oscillation frequency $\nu_{rel} \approx 45kHz$ and the damping rate of the bursts $T_{damp} \approx 0.2ms$ observed experimentally must be reproduced in the model. We use the relations

$$\begin{aligned} \nu_{rel} &= \tfrac{1}{2\pi\tau_c}\sqrt{2\tfrac{p-\alpha}{T}}, \\ T_{damp} &= 2\tfrac{T\alpha\tau_c}{p}, \end{aligned} \tag{6.16}$$

obtained from linear stability analysis of Model (6.15) in the absence of injection, to tune the parameters p and α. We find the pump rate $p = 80$ and the loss coefficient $\alpha = 0.8$ provide the necessary values for T_{damp} and ν_{rel}. This pump is eight times that of the experimental value, possibly due to an underestimation of the gain of the laser due to the single mode and uniform field approximations inherent in Model (6.15).

The injected power ratio for the simulated system may be determined by the relation

$$\frac{P_{inj}}{P_{RL}} = \frac{|E_{inj}|^2}{\langle |E|^2 \rangle}. \tag{6.17}$$

In the experimental studies, a typical injected power ratio was on the order of 10^{-4}. At this level, the stable locking range [115], Eqn. (6.12), is only $\pm 0.01MHz$, and much smaller than the observed wandering of the ring laser modes, Figs 6.9&6.10. Therefore, the shifting modes of the ring laser result in the minimally detuned mode traveling through all possible locking regimes with respect to the injection laser: beyond the influence of the injection laser, in the stable locking range, and in the dynamically complex intermediate locking range [52, 12, 75].

We phenomenologically approximate this frequency wandering using exponentially correlated Gaussian noise, specifically Ornstein-Uhlenbeck colored noise $\xi(t)$ [82] such that

$$\Delta\omega(t) = (\omega_{inj} - \omega_c)\tau_c = \Delta\omega_o + \xi(t). \tag{6.18}$$

Here, $\Delta\omega_o$ is the unitless detuning constant about which the ring laser frequency wanders. The wandering, given by Ornstein-Uhlenbeck noise, may be calculated with the simple ordinary differential equation

$$\frac{d\xi}{dt} = -\frac{1}{\tau_\omega}\xi + \frac{1}{\tau_\omega}\eta_\omega(t). \tag{6.19}$$

The correlation time of $\xi(t)$ is $\tau_\omega = 2 \times 10^3 = \tau_c^{-1} \times 0.4ms$, and $\eta_\omega(t)$ is the Gaussian white zero mean seed noise. The delta-correlated seed noise is described by $\langle \eta_\omega(t)\eta_\omega(t')\rangle = 2D_\omega\delta(t-t')$ and has a strength $D_\omega = 2 \times 10^3$. $\xi(t)$ is described by the correlation $\langle \xi(t)\xi(t')\rangle = D_\omega\tau_\omega^{-1}\exp[-|t-t'|/\tau_\omega]$. The experimental equivalents of D_ω, τ_ω, and $\Delta\omega_o$ should all be independent of the injection amplitude. It is important to note that we are not able to control the exact value of $\Delta\omega_o$ experimentally, though it is confined to within a few MHz because the mode spacing is determined by $\Delta\nu_{sp} = 5MHz$.

A comparison in Fig. 6.11 of numerical (left panel) and experimental (right panel) results verifies that Model (6.15), with the detuning wandering given by Eqn. 6.19, reproduces the essential features of the injected ring laser dynamics. Beyond displaying similar intermittent bursting dynamics, the amplitude of the bursts grows with the level of injection. The injected power ratios, P_{inj}/P_{RL}, used in the simulations were 2.50×10^{-5}, 1.59×10^{-4}, and 1.44×10^{-3} in Figs. 6.11(a), (b) and (c), respectively. The experimental values were 1.53×10^{-4}, 4.82×10^{-4}, and 1.92×10^{-3} in Figs. 6.11(d), (e) and (f) respectively. Note that the model produces large amplitude bursts with significantly lower injection. To allow a more direct comparison, all intensity time series have been normalized by their mean intensity, which is unaffected by the injection amplitude.

Examining a single pair of bursts, we are able to observe that, as in the experimental system, the bursting dynamics in the simulations are due to intermittent

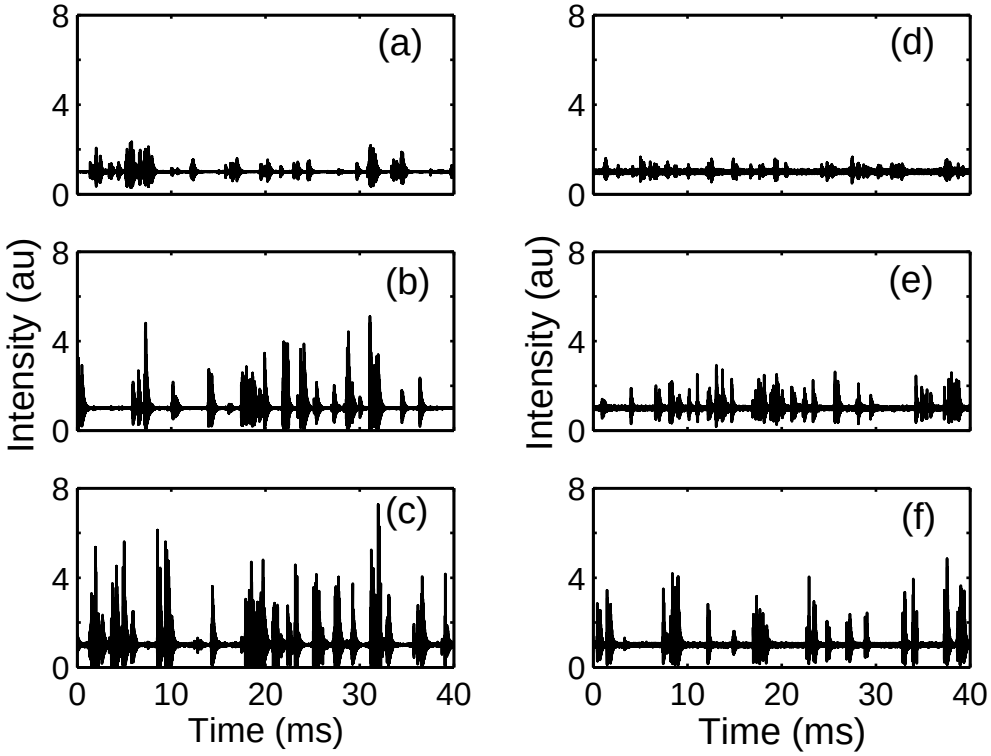

Figure 6.11: Bursting dynamics produced by numerical integration of Model (6.15) (left panel), qualitatively reproduce the intermittent bursting dynamics of the experimental time series (right panel). Additionally, the burst intensities scale with increased injection power. The simulated injected power ratios, P_{inj}/P_{RL}, were 2.50×10^{-5} (a), 1.59×10^{-4} (b), and 1.44×10^{-3} (c). The experimental values were 1.53×10^{-4} (d), 4.82×10^{-4} (e), and 1.92×10^{-3} (f).

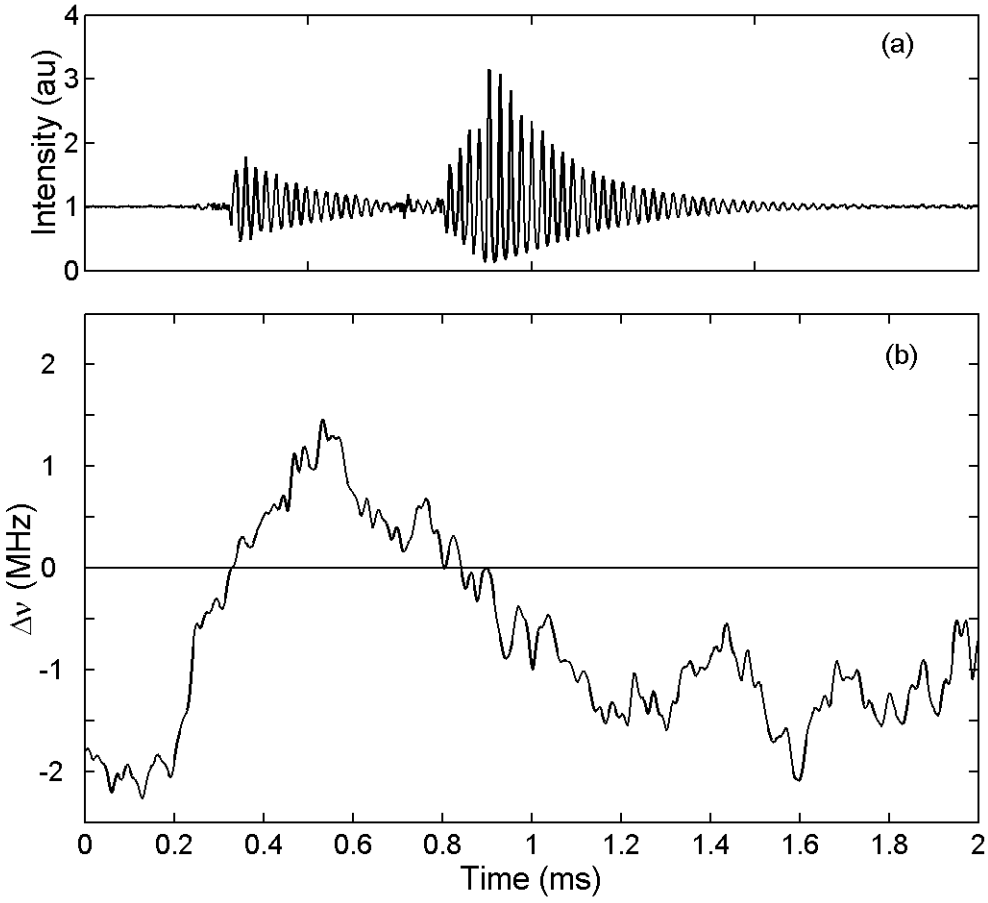

Figure 6.12: Intermittent interaction between the wandering ring laser mode and the injected field (b) result in bursting dynamics (a). The detuning, $\Delta\nu$ is determined from the rotation rate of the complex field $E(t)$ in Model (6.15). The frequency evolution is frequency filtered at $50kHz$ in order to match the resolution of the experimental heterodyne measurements.

interactions of the wandering ring laser mode and the injection laser, Fig. 6.12. The detuning is determined by calculating the instantaneous time derivative of the complex field $E(t)$. Recalling that Model (6.15) was constructed in a frame rotating with ω_{inj}, the rotation rate of the lasing field is identical to the detuning between the ring and injection lasers. This is completely analogous to how the ring laser mode dynamics were obtained in the experimental heterodyne measurements, Figs. 6.9&6.10, except we are able to determine the sign of the detuning in the simulations. The frequency evolution is frequency filtered at $50kHz$ in order to match the resolution of the experimental heterodyne measurements. The mean of the wandering mode is $\Delta\omega_o = -1MHz$. In Fig. 6.12(a) we observe a pair of bursts which are obviously correlated with the intersections of the laser mode and the injection laser frequency in Fig. 6.12(b). Here, the horizontal line marks the resonance between the ring and injection lasers. The locking region of $\pm 0.01MHz$ about this line is too small to display. The first burst in the series is initiated as the simulated EDFRL mode passes through locking region. Here, $P_{inj}/P_{RL} = 1 \times 10^{-4}$ so any locking between the two lasers is too brief to detect, as is the case in the experimental system with equivalent injection levels. Recall that, in the experimental heterodyne measurement, $P_{inj}/P_{RL} = 7.8 \times 10^{-2}$, resulting in a locking range of $\pm 0.28MHz$ which allows the frequency locking observed in Fig. 6.10. It is interesting to observe how multiple intersections of the ring and injection lasers combine to form a relatively complex second burst. Additionally, we observe that even with a relatively large detuning, the injected field may affect the dynamics of the system. Between the two bursts, slightly before $0.75ms$, a momentary dip of the ring laser mode towards resonance produces a low amplitude instability in the intensity time series. As discussed in Section 6.1, dynamics arise due to interactions of a laser with an injected field near the boundaries of the stable locking regime.

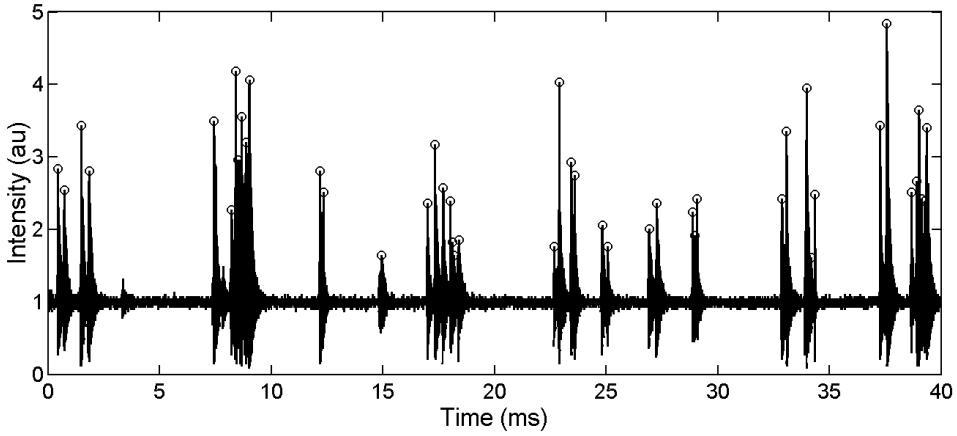

Figure 6.13: Identification of burst times and amplitudes in a bursting time series. The open circles locate the dominant peak in a given burst.

6.5 Statistical Comparison of Experiment and Model

We have observed similar bursting dynamics resulting from the intermittent interaction of the ring laser with an injection laser in the phenomenological model and experiments. However, we still need to analyze the statistics of the bursting dynamics to gain a quantitative comparison of the model and experiment, and hopefully gain further insight into the bursting dynamics themselves. Surprisingly, we find excellent statistical agreement between the experimental bursting time series and noise-driven dynamics of the numerical simulations.

The bursting dynamics presented throughout this chapter, in both experimental and numerical systems, are highly irregular in time and burst amplitude. The first step in analyzing the nature of these dynamics is to identify the burst times and intensities. This is most successfully achieved by determining the dominant peak in a given burst. An illustration of this method is presented in Fig. 6.13, where the open circles mark the selected peaks in the experimental time series. We require that the selected peaks be above the adaptive threshold $I_{th} = \langle I \rangle + 2\sigma(I)$. The algorithm allows for multiple bursts to be identified within a larger train.

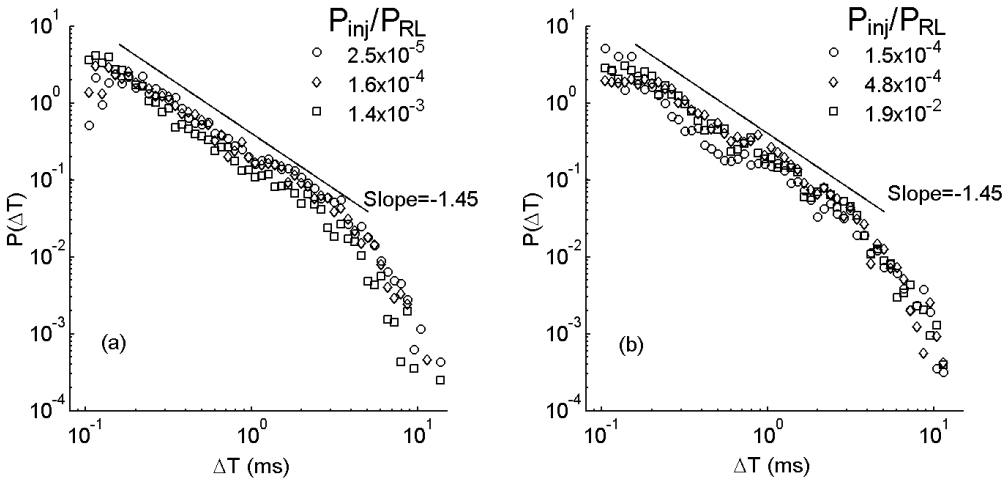

Figure 6.14: Normalized interburst time probability distributions for numerical (a) and experimental (b) time series. In both cases, the distributions are unaffected by the injection level and display a power law decay with an exponent ~ -1.45. Symbols and injection power ratios P_{inj}/P_{RL} are matched in the figure legends.

Using the burst times from the peak detection algorithm, we calculate the normalized probability distribution of the interburst times ΔT. The interburst time distributions for the numerical and experimental bursting time series presented in Fig. 6.11 are plotted in Figs. 6.14(a & b), respectively, and are quite similar to each other. The full time series are two seconds long and contain approximately 2500 bursts. While the burst intensities increase in Fig. 6.11 with increasing injection, it is apparent that the burst distributions are unaffected by the injection level. This supports our conclusion that the bursts are due to the wandering of the lasing frequency of the ring laser mode over a range on the order of MHz. Both the numerical and experimental cases show a distinct power law decay with an exponent of approximately -1.45 that extends approximately one and a half decades from $\Delta T = 10^{-1}$. A similar power law decay has been found in noise driven systems displaying on-off intermittency [26, 27], such as electroconvection in liquid crystals [35]. The injection levels in the numerical case (Fig. 6.14(a)) are $P_{inj}/P_{RL} = 2.50 \times 10^{-5}$, 1.59×10^{-4}, and 1.44×10^{-3} and are represented by open circles, diamonds and squares, respectively. In the experimental plot (Fig. 6.14(b)) $P_{inj}/P_{RL} = 1.53 \times 10^{-4}$, 4.82×10^{-4}, and 1.92×10^{-3} and are again represented by open circles,

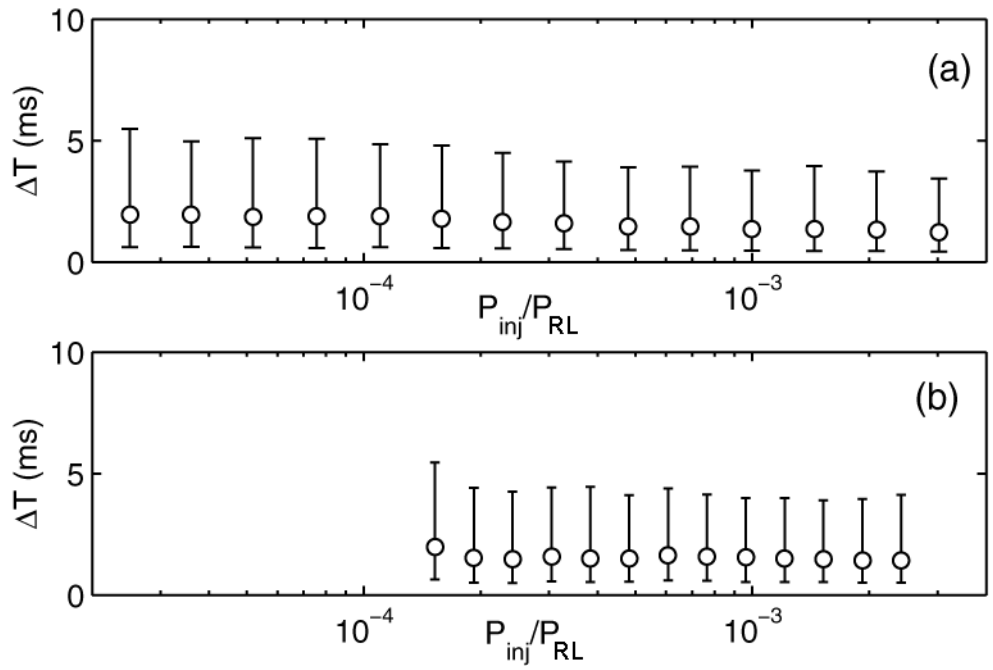

Figure 6.15: The average inter-burst time ΔT (open circles) is essentially constant with respect to P_{inj}/P_{RL} for both simulations (a) and experiments (b). The large error bars reflect the aperiodic nature of the bursting intensity time series in both cases.

diamonds and squares, respectively.

The relative invariability of the bursting behavior in time with respect to the level of injection, Fig. 6.14, is observed over a broader range in Fig. 6.15. Here, we look at the mean interburst times (open circles), ΔT, for the numerical simulations, Fig. 6.15(a), and experimental measurements, Fig. 6.15(b), for a sample of P_{inj}/P_{RL} including those examined in Fig. 6.14. As one would expect, $\langle \Delta T \rangle$ is nearly constant ($1.3ms < \langle \Delta T \rangle < 2.0ms$ in both cases) over the entire range of injection strengths. The large errorbars reflect the aperiodic nature of the bursting time series.

Using the burst peak intensities, I_p we found using our burst detection algorithm (Fig. 6.13), we are able to examine the normalized probability distribution of the burst intensities in Fig. 6.16. Here we study the same numerical (a) and experimental (b) data sets that we examined in Figs. 6.11&6.14. The increase in bursting amplitudes with increased injection is demonstrated by the distributions shifting towards the right in both cases. Both numerical and experimen-

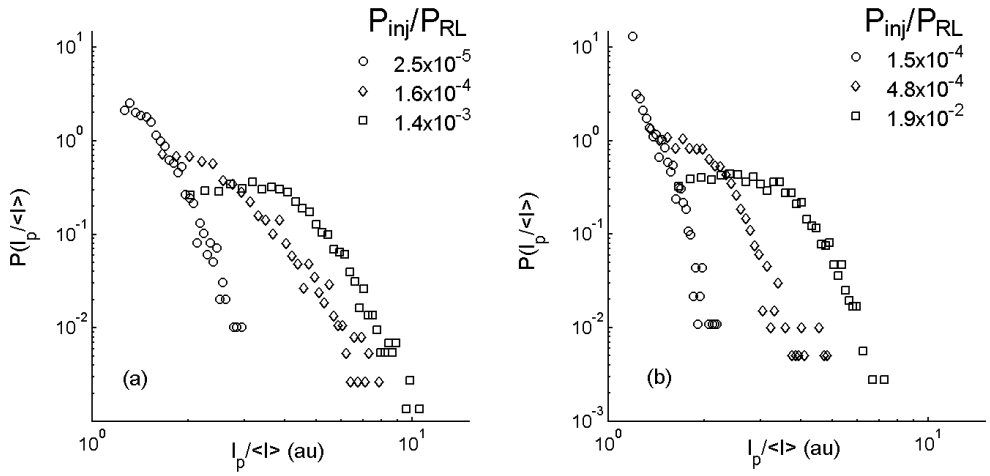

Figure 6.16: Normalized probability distributions of the peak burst intensities I_p (a) and experimental (b) data sets display the same qualitative features and trends for increasing values of P_{inj}/P_{RL} The data sets studied are identical to those examined in Figs. 6.11&6.14. P_{inj}/P_{RL}'s and corresponding symbols are matched in the figure legends.

tal plots show a similar change in overall distribution shape with increased injection, however in all cases a region of power-law decay is readily apparent. These power-law tails again agree with previous observations of systems exhibiting on-off intermittency [35]. The injection levels in the numerical case (Fig. 6.14(a)) are $P_{inj}/P_{RL} = 2.50 \times 10^{-5}$, 1.59×10^{-4}, and 1.44×10^{-3} and are represented by open circles, diamonds and squares, respectively. In the experimental plot (Fig. 6.14(b)) $P_{inj}/P_{RL} = 1.53 \times 10^{-4}$, 4.82×10^{-4}, and 1.92×10^{-3} and are again represented by open circles, diamonds and squares, respectively.

6.6 Discussion

The surprising experimental observation of irregular bursting dynamics initiated by a weak, frequency matched optical injection signal has been investigated and phenomenologically modeled. Experimental heterodyne measurements reveal that the lasing modes of the ring laser slowly wander over a range of MHz independent of injection. The intermittent interaction of the minimally detuned ring laser mode and

the monochromatic injected light field leads to brief periods of the EDFRL locking to the injection laser. The EDFRL then escapes the frequency locking range, producing bursts in the intensity time series. A phenomenological model of the injected laser system, considering a single, linearly polarized mode with Ornstein-Uhlenbeck noise driven detuning, qualitatively and statistically reproduces the most important features of the injected ring laser dynamics. Both numerical and experimental intensity time series produce normalized probability distributions displaying power-law decays, possibly indicative of on-off intermittency.

While we have identified the origin of the bursting dynamics as the intermittent interaction of the ring laser and injection laser fields and have modeled the dynamics successfully, the actual cause of the frequency wandering in the ring laser is undetermined, and under current investigation.

Chapter 7

Noise-Induced Burst Synchronization

The synchronization of bursting systems is highly relevant to understanding aspects of communication. A question of great general interest is whether two dynamical systems subject to a common noise background will synchronize their bursts, and if so, is there a noise threshold at which the synchronization occurs? Here, we report experiments carefully designed to study these questions quantitatively in a way that is currently difficult, if not impossible, with many complex, bursting systems. We note that the synchronization of uncoupled chaotic dynamical systems driven by a common noise source is a topic that has raised much controversy over the years [125, 126, 127, 128, 129, 130].

7.1 Noise-Induced Synchronization

Constructive effects of noise on dynamic systems have been reported, including noise induced-pattern formation [131] and stochastic resonance [132, 133, 134, 135]. Noise

induced order may be observed when the noise signal shifts the chaotic dynamics of the system onto a more periodic trajectory, reducing the largest Lyapunov exponent of the system to below zero [136, 137, 126, 138]. This allows for identical noise-induced synchronization, as matched systems with common noise would shift to identical trajectories.

The first report of such behavior [125] considered a noisy logistic map and the Lorenz attractor. However, the conclusion of noise induced synchronization in this case was due to finite precision in the numerical integration of the models; in fact, the largest Lyapunov exponent for the logistic map example never dipped below zero [126, 127]. This initial misstep, followed by studies examining systems where synchronization required a biased noise source [139, 140, 141], culminated in a supporting experimental study of a Chua circuit [128] and the premature general conclusion that unbiased noise could not induce synchronization.

However, counterexamples of unbiased noise-induced identical synchronization have been reported in recent years [129, 142, 143], including a study of a self-excited neuron model [144]. In an recent experimental and numerical studies, identical noise induced synchronization was demonstrated in a CO_2 laser displaying homoclinic bursting dynamics.

Recently Zhou and Kurths [130] have shown that weak synchronization, specifically noise induced phase synchronization of non-identical Rössler systems, may be induced by unbiased noise without driving $\lambda_1 \leq 0$.

Like phase synchronization, burst synchronization is an example of weak synchronization – the individual oscillations within a burst need not be synchronized in amplitude or phase – only the burst envelopes are correlated between the systems. In this chapter, we study noise induced synchronization of burst dynamics in erbium-doped fiber ring-lasers (EDFRLs). The intensity bursts are initiated by injection of a common, weak, optical signal into two nearly identical EDFRLs. When the injected monochromatic signal is constant in power, the intensity bursts in the two lasers are unsynchronized with a broad distribution of interburst times, as should be expected. In these experiments, we show that a small level of unbiased broadband

noise modulation of the common injected optical signal is sufficient to synchronize the bursts that occur in the two lasers to a remarkable extent. We then examine the synchronization of bursts when a weak sinusoidal modulation is applied to the injected signal. Synchronization occurred at about the same level of modulation strength as in the case of noise modulation. The statistical characteristics of the bursts in a single system are unchanged from the case of constant injection for both noise and sinusoidal modulation. [21]

7.2 Experimental Setup

The experimental set-up is displayed in Fig. 7.1. The components of the EDFRLs are described in Section 6.2. The intracavity optical power for the EDFRLs is approximately $9mW$, and the total fiber ring lengths are approximately $41.5m$ and are matched to within 1% of each other. We select a mode of operation where both EDFRLs display a single-peaked spectrum and are tuned to within $5GHz$ of each other and centered at $\lambda = 1557.7nm$, with a full width at half maximum of approximately $0.6nm$.

A common, constant, optical signal, also at $\lambda_{inj} = 1557.7nm$, is injected into the rings using 70/30 fiber-optic evanescent field couplers, stimulating large intensity bursts in the ring-lasers. The constant signal source is a tunable external cavity semi-conductor diode laser (ECSL). This signal may be amplitude modulated with a lithium-niobate electro-optic modulator (EOM) (JDS-Uniphase, Model MZ-150-002103). An all-fiber polarization controller ensures maximum transmittance through the modulator. A function generator (Stanford Research Systems, Model DS345, $30MHz$) is used to drive the EOM with noise or periodic waveforms. The injection signal is split equally between the two ring-lasers using a 50/50 coupler.

Light from the EDFRLs is extracted with 70/30 couplers, and the dynamics are studied by measuring the intensities with $125MHz$ bandwidth photo-detectors (PD) and a $1GHz$ digital sampling oscilloscope. All experimental data sets studied

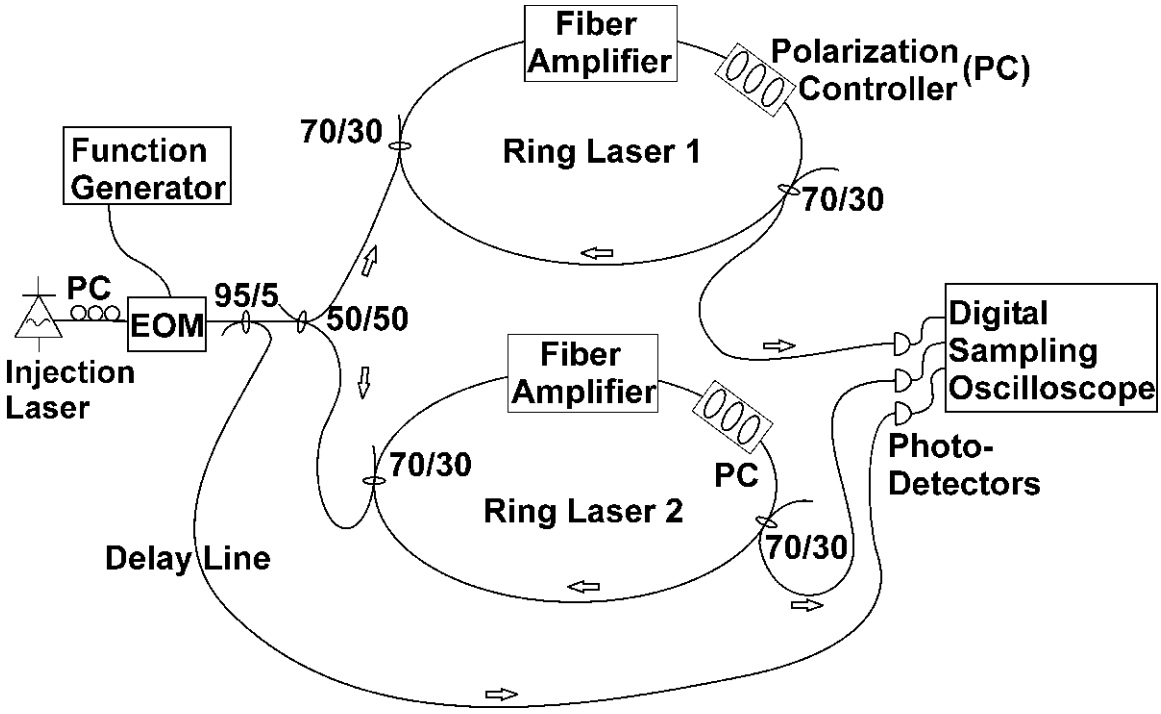

Figure 7.1: Experimental Setup: Two nearly identical Erbium-Doped Fiber Ring-Lasers (EDFRLs) of cavity length $\approx 41.5m$ are injected with a common, weak optical signal. The EDFRLs are pumped about ten times above threshold. Injection from the External Cavity Semiconductor diode Laser (ECSL), frequency matched to the EDFRLs, induces bursting in the EDFRLs. The ECSL output may be amplitude modulated with the Electro-Optic Modulator (EOM) driven by the Function Generator. Optical isolators integrated in the Erbium-Doped Fiber Amplifiers (EDFA) ensure light-wave propagation in the direction indicated by the arrows only. The EDFRL output intensities are measured using $125MHz$ photo-detectors (PD) and a $1GHz$ bandwidth Digital Sampling Oscilloscope (DSO).

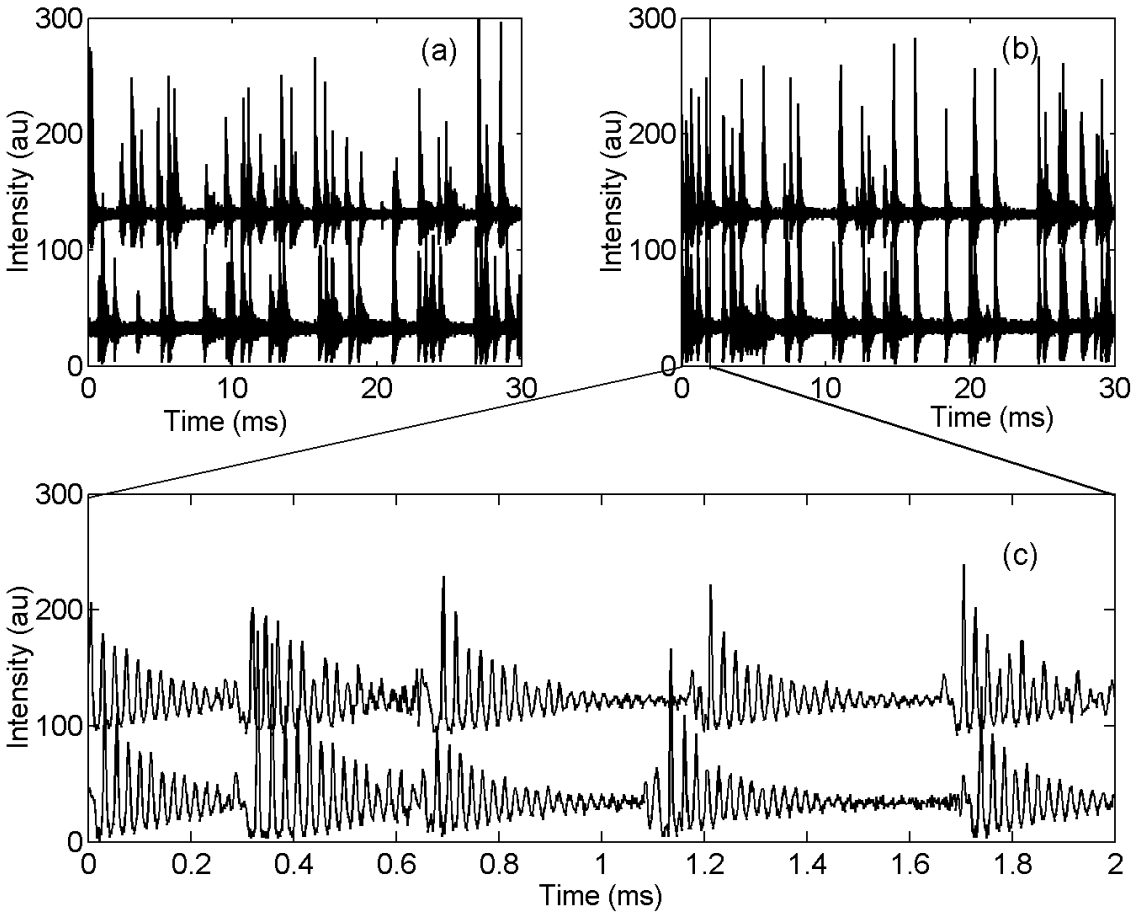

Figure 7.2: The bursting dynamics of the EDFRLs are uncorrelated with constant injection (a), but shift to synchronized behavior with unbiased noise modulation of the optical injection signal (b). The component intensity fluctuations are not necessarily matched in amplitude or phase (b).

here span a two second window and contain one million data points, with a sampling rate of 5×10^5 samples/sec.

7.3 Noise-Induced Burst Synchronization

The bursting dynamics of the EDFRLs, with an injection power $P_{inj} = 32\mu W$ and a circulation power of $P_{RL} \approx 9mW$ circulating in the ring cavity, are plotted in Fig. 7.2. Fig. 7.2(a) displays the case when the injected signal is unperturbed, resulting in the expected uncorrelated bursting. When a small amplitude, unbiased

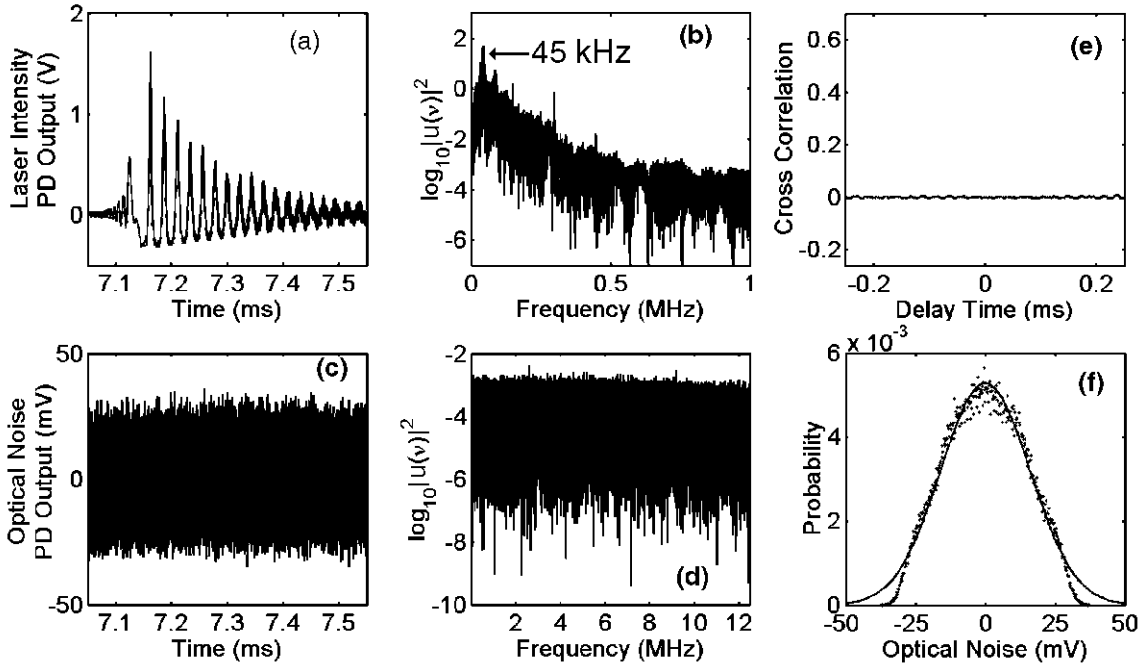

Figure 7.3: High resolution (~ 13 bits), AC coupled measurements of a single EDFRL injected with noise modulated optical signal (a), and the optical noise signal (c) are displayed with their power spectra (b&d, respectively). The EDFRL spectrum peaks at $\nu_{rel} \approx 45kHz$, and the noise is effectively white, at the $25MHz$ sampling frequency. The EDFRL is pumped well above threshold and $M_{noise} = 2 \times 10^{-2}$. The normalized probability distribution of the unbiased optical noise (f) shows a clipped, nearly-Gaussian profile. An ensemble averaged cross correlation of individual burst-noise pairings (e) is nearly featureless, showing no indication of identical or phase synchronization of the EDFRL dynamics to the optical noise.

noise-modulation is applied to the injection signal, a dramatic shift to burst synchronization is observed, as seen in Fig. 7.2(b). The strength of the noise modulation is measured by the ratio of the standard deviation of the injected power to its mean, $M_{noise} \equiv \sigma(P_{inj})/\langle P_{inj} \rangle = 2 \times 10^{-2}$. Contrasting Figs. 7.2(a) and (b), the shift from uncorrelated to synchronized bursting is qualitatively evident.

The EDFRL intensities display bursts, consisting of large amplitude relaxation oscillations at about $\nu_{rel} = 45kHz$. The relative amplitudes and phases of these fluctuations are not necessarily matched, as is illustrated in Fig. 7.2(c), a magnification of a slice of the dynamics in Fig. 7.2(b).

High resolution ($\sim$ 13bit), AC coupled simultaneous measurements of a single bursting ring laser and the modulated optical injection signal were taken in an

attempt to discern if there are any simple correlations between the two time series. A single injection induced burst is shown in Fig. 7.3(a), where the injection strength is quantified by the ratio $P_{inj}/P_{RL} = 3.6 \times 10^{-3}$ with a noisy modulation of $M_{noise} = 2 \times 10^{-2}$. The power spectrum of the bursting time series shows a strong peak at $\nu_{rel} \approx 45kHz$, Fig. 7.3(b). As always, $u(\nu)$ represents the Fourier transform of an intensity time series.

Figure 7.3(c) shows a sample of the unbiased noise modulation. The noise modulation has a near Gaussian intensity probability distribution, and a bandwidth of approximately $15MHz$ which is effectively white noise for the dynamical times scales involved. The flat aspect of the modulation spectrum is demonstrated in Fig. 7.3(d). The normalized probability distribution of the optical noise intensities is plotted in Fig. 7.3(f) with the experimental values represented by asterisks, and the solid line is a χ^2 fit of a unbiased Gaussian function.

To examine the possibility of a simple correlation between the bursting dynamics and the modulation signal, approximately 30 bursts were isolated with leading and lagging buffers of $0.1ms$. The matching portions of the optical noise signal are identified, forming burst-noise pairs. The ensemble average of cross correlations of these burst-noise pairs is shown in Fig. 7.3(e) and is nearly featureless. Neither a spike, indicating intensity synchronization, nor periodic oscillations, indicating phase synchronization, are observed. Similar results are found when we perform the same ensemble cross-correlation calculation with burst-sinusoidal modulation pairs, or with low band-pass filtered noise modulation.

While the relative behavior of the ring dynamics shifts dramatically towards synchronization, the statistics of the bursting dynamics of an individual ring remain unaffected. Normalized probability distributions of the interburst times, ΔT, and normalized burst intensities, $I_p/\langle I \rangle$, are plotted in Fig. 7.4(a) and (b), respectively, for the constant injection case (circles) and Gaussian white noise modulated injection (squares) as well as unbiased sinusoidal modulation (diamonds) at $\nu_{mod} = \nu_{rel} = 45kHz$. As in Section 6.5, the interburst times were found by determining the time of the dominant peak within individual bursts. This method was demonstrated in

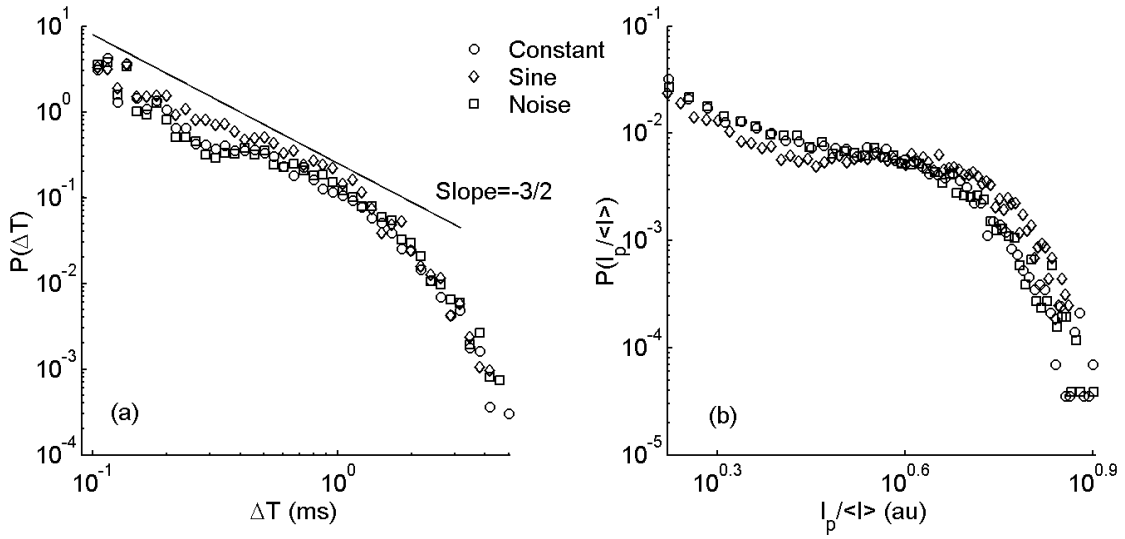

Figure 7.4: The normalized probability distributions of inter-burst times ΔT (a) and normalized burst intensities $I_p/\langle I \rangle$ (b) for the constant injection case (circles) and Gaussian white noise modulated injection (squares) as well as unbiased sinusoidal modulation (diamonds) at $\nu_{mod} = \nu_{rel} = 45kHz$. In all three cases the burst times follow similar distributions. The slope -1.5 power law behavior from $\Delta T = 3 \times 10^{-1}ms$ to $1ms$ is a possible indication of stochastically driven on-off intermittency [26, 35]. The injection modulated data sets were obtained with modulation strengths of $M_{noise} = M_{sine} = 2 \times 10^{-2}$.

Fig. 6.13. The burst intensity, I_p, is the intensity of this peak. The strength of the noise and sine modulations are matched, $M_{noise} = M_{sine} = 2 \times 10^{-2}$, where $M_{sine} \equiv 0.5\Delta P_{inj}/\langle P_{inj} \rangle$ and $\Delta P_{inj} = max(P_{inj}) - min(P_{inj})$. In all three cases the burst times follow similar distributions. Therefore, even though modulation of the injection signal induces burst synchronization, it does not appreciably modify the overall bursting dynamics!

It is also important to note that for ΔT ranging from $3 \times 10^{-1} ms$ to $1ms$ the inter-burst times closely follow a power law with slope $-3/2$. This is a possible indication that the injection induced bursting displays on-off intermittency [26, 35], and was noted in Section 6.5 as well. On-off intermittency is a stochastically driven class of dynamics and is discussed in Sec 2.1.1.

7.4 Definition and Application of a Burst Envelope

While the presence of burst synchronization is qualitatively evident in Fig. 7.2(b), the fluctuations of the EDFRL dynamics at $\nu_{rel} = 45kHz$ obscure direct attempts to determine the degree of synchronization. However, it is relatively straightforward to define a burst envelope for the dynamics using the low pass filtered analytic signal [101, 8] introduced in Section 5.2.2, Eqn. (5.7), and repeated here;

$$V(t) = \frac{1}{\pi} \int_0^{\nu_c} e^{i\nu t} u(\nu) d\nu. \tag{7.1}$$

$V(t)$ is the low-pass filtered complex analytic signal and $u(\nu)$ is the Fourier transform of the intensity time-series. We are not concerned with the nanosecond time-scale fluctuations intrinsic to the EDFRL dynamics. We only wish to maintain the integrity of the bursting dynamics observed in the injected ring laser. Therefore, we select a cut-off frequency, $\nu_c = 50kHz$, slightly larger than the relaxation oscillation components of the individual bursts. Burst synchronization is studied using the real

amplitude $A(t)$ of the centered complex analytic signal,

$$V(t) - \langle V(t) \rangle = A(t)e^{i\phi(t)}. \tag{7.2}$$

Hence $A(t)$ defines an envelope over the bursting intensity dynamics of a ring-laser.

For clarification, we present the definition of the burst envelope graphically in Fig. 7.5. Plotting the low-pass filtered analytic signal, Fig. 7.5(b), of two injection induced bursts, Fig 7.5(a), we observe large amplitude rotations in the complex, $Re(V(t))$ vs. $Im(V(t))$, plane at the burst times. These rotations damp to near zero amplitude as the bursts decay. Plotting only the amplitudes of these rotations we define the burst envelope, Fig. 7.5(c).

Re-examining burst synchronization, we again observe the shift from unsynchronized bursting with a constant injection signal, Fig. 7.6(a), to burst synchronization with noise modulated injection, Fig. 7.6(b). In Figs. 7.6(c) and (d) we have shown the xy-synchronization plots of the burst envelopes, $A_2(t)$ vs. $A_1(t)$. It is clear that burst synchronization is not present in the constant injection case, Fig. 7.6(c). The application of noise modulation centers the plot about the diagonal, demonstrating the shift to burst synchronization, Fig. 7.6(d). Viewed from this perspective, burst synchronization of the two systems driven by common noise may be regarded as an example of generalized synchronization [43, 44, 145, 146].

7.4.1 Intermittent Phase Synchronization

Phase synchronization of the intra-burst fluctuations may be studied using the phase $\phi(t)$ of the analytic signal $V_A(t)$[97, 147, 18]. Here we have chosen to shift our cut-off frequency to infinity, returning to the unfiltered complex analytic signal. Again we observed unsynchronized and synchronized bursting in the unmodulated Fig. 7.7(a) and noise modulated Fig. 7.7(b) intensity time series respectively. Here, the initial $5ms$ of the dynamics displayed in Figs. 7.2 & 7.6 are plotted. In Figs. 7.7(c) and (d) the relative phase difference $\Delta\phi(t) = (\phi_1(t) - \phi_2(t))/2\pi$ is plotted for the unmodulated injection and noise modulated injection cases respectively. The nearly

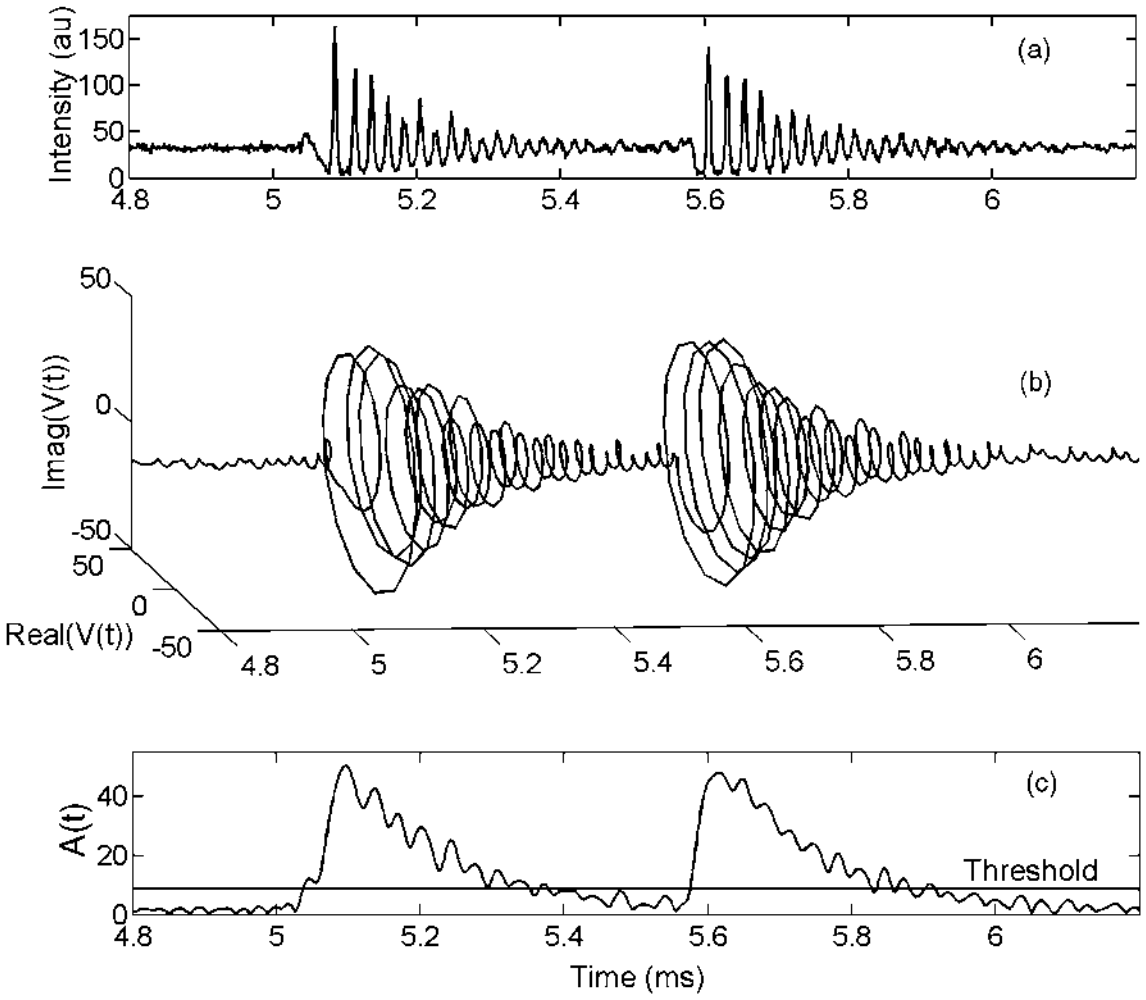

Figure 7.5: Definition of the burst envelope using the low-pass filtered analytic signal $V(t)$, Eqn. (7.1). $V(t)$ performs large amplitude rotations in the complex plane (b) corresponding to individual bursts seen in the intensity time series (a). The amplitudes of these rotations define the burst envelope (c).

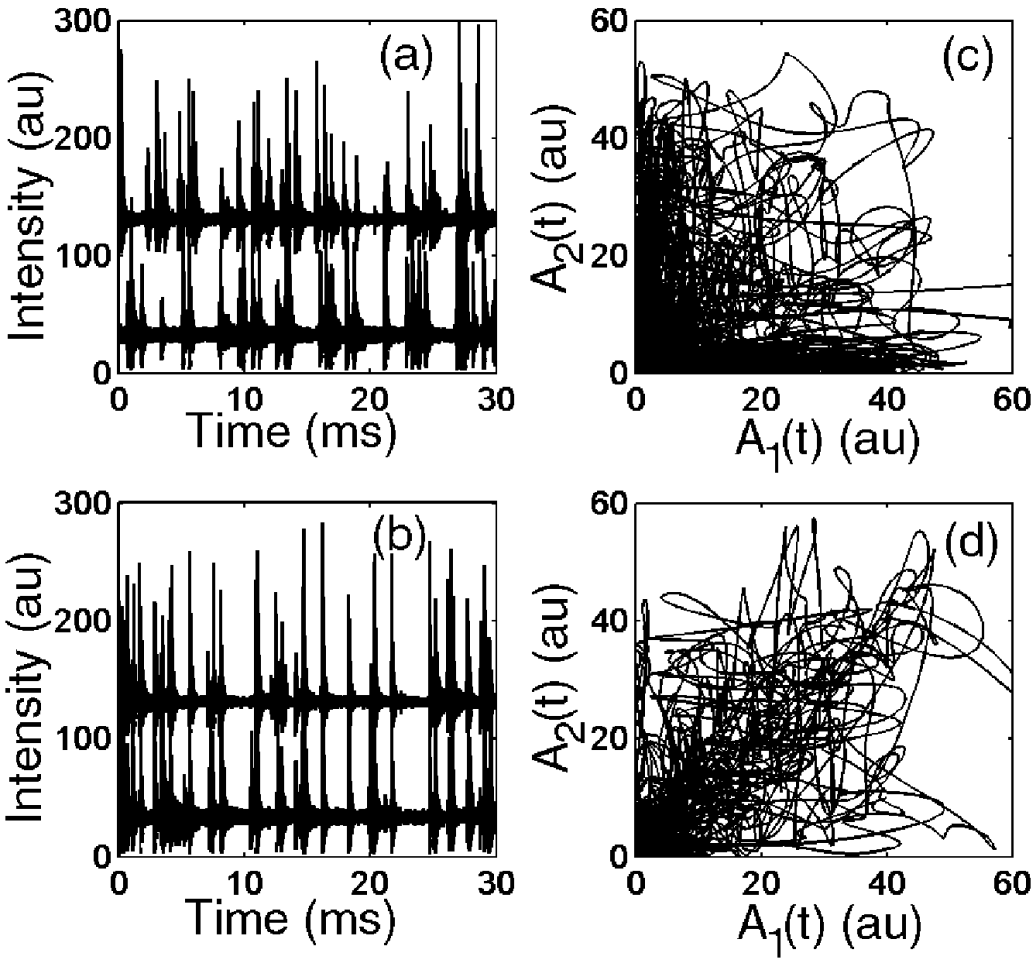

Figure 7.6: Bursting dynamics of the EDFRLs with unmodulated injection (a) and noise modulated injection (b). The shift to burst synchronization with noise modulation is evident. (c) and (d) are xy-synchronization plots for the burst envelopes for (a) and (b) respectively and illustrate burst synchronization with noise modulation.

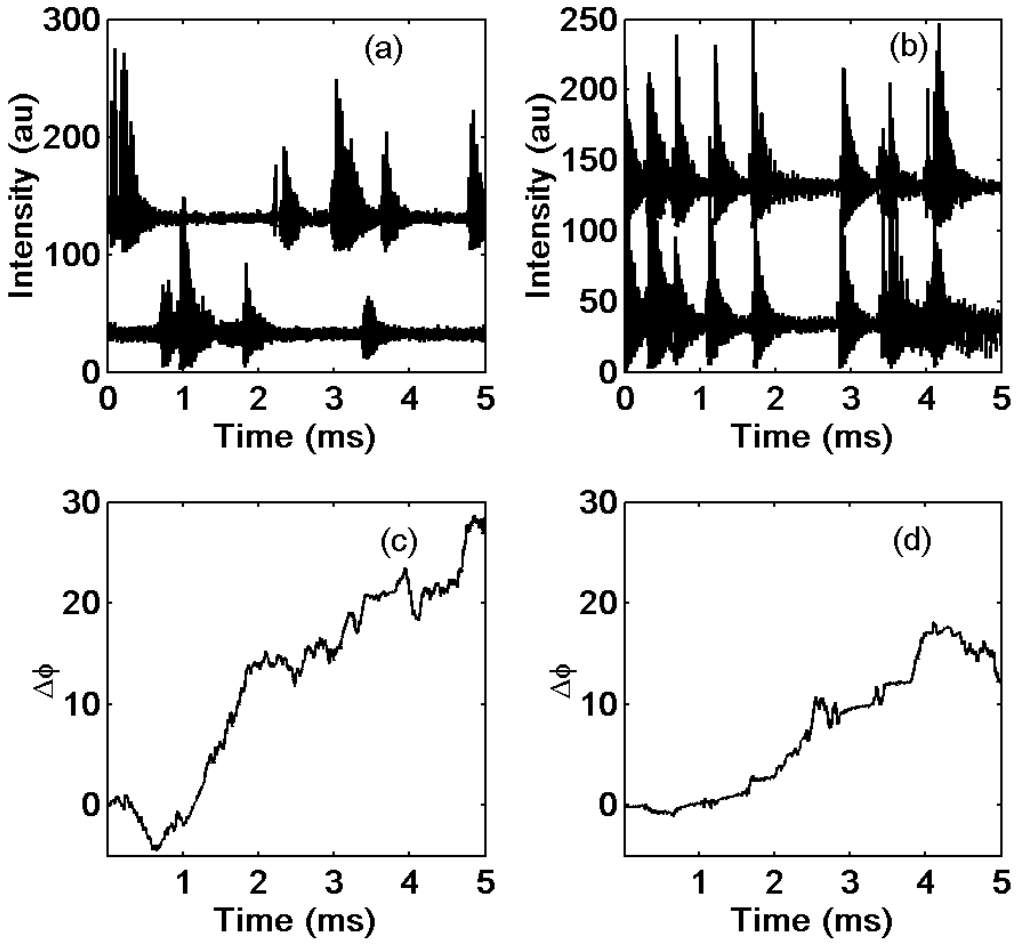

Figure 7.7: Intermittent phase synchronization of the bursting ring-laser dynamics are seen with the application of noise modulation. Unmodulated (a) and noise modulated (b) intensity time series are shown for the initial $5ms$ of the dynamics displayed in Fig. 7.2. The relative phase differences of the two EDFRLs are shown in (c) and (d). Nearly continuous phase slipping with varying slopes is observed in (c), indicating an absence of phase synchronization. The relatively flat sections in (d) indicate intermittent phase synchronization.

continuous phase slipping with varying slopes observed in Fig. 7.7(c) demonstrates a lack of phase synchronization in the constant injection case. In Fig. 7.7(d) we note that $\Delta\phi(t)$ is roughly constant within bursts, suggesting intermittent phase synchronization. Closer inspection shows that these phase synchronized time segments may have non-zero slopes, indicating imperfect phase synchronization.

7.5 Quantifying Burst Synchronization

7.5.1 Defining a Synchronization Measure

In determining a level of burst synchronization, we are not necessarily concerned with the amplitude or phase of the bursting dynamics, merely whether or not the bursts occur at the same time. Therefore, we reduce the time series to symbolic dynamics, indicating whether or not the ring lasers are bursting at a given point in time. We define an appropriate threshold A_{th} (see Fig. 7.5(c)) to identify bursts, and generate a new time series $B(t)$, where

$$B(t) \equiv \begin{cases} 1, & A(t) > A_{th} \\ -1, & A(t) \leq A_{th} \end{cases}. \tag{7.3}$$

The amplitudes of the bursts and phases of the fluctuations within the bursts have been eliminated in the time series $B(t)$. Burst synchronization is easily identified and quantified with this simplified burst time-series, which has the character of a random telegraph signal [148]. To determine the level of burst synchronization we calculate the zero-delay, normalized cross-correlation

$$C \equiv \frac{1}{N} \frac{\sum_{n=1}^{N} (B_1(n) - \langle B_1 \rangle)(B_2(n) - \langle B_2 \rangle)}{\sigma(B_1)\sigma(B_2)}. \tag{7.4}$$

Here B_1 and B_2 are the burst time series for EDFRL 1 and EDFRL 2, respectively, and N is the total number of sampled values in the time series. With these definitions for $B(t)$ and C we have a particularly transparent measure of synchronization; $C = 1$ represents perfect synchronization, $C = -1$ indicates complete anti-synchronization,

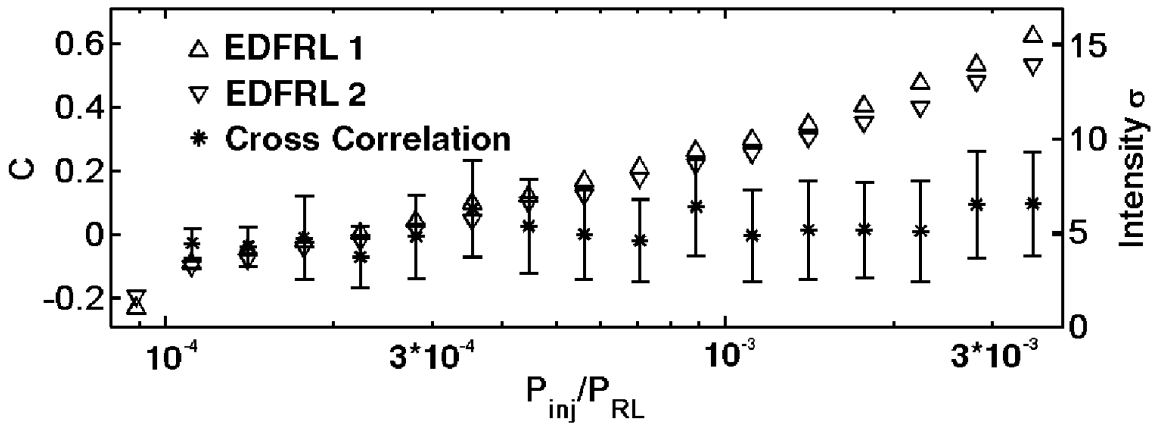

Figure 7.8: An increase in the constant injected signal power results in an increase in the standard deviation of the EDFRL intensity fluctuations (triangles, right vertical axis). The bursts in the two lasers remain essentially uncorrelated (asterisks, left vertical axis) for the entire range of injection power investigated.

and for $C = 0$ there is no relation on the average between the bursts of EDFRL 1 and EDFRL 2.

7.5.2 Injection Power

Adjustments in the power of the constant injected optical signal does not affect the synchronization of the bursts. However, the standard deviation of the intensity time series increases as P_{inj} increases. This is shown in Fig. 7.8. The right vertical axis corresponds to the standard deviations of the intensities of EDFRLs 1 and 2, marked by the triangles and inverted triangles, respectively. As above, the stable-state intracavity power of the EDFRLs is held constant at $P_{RL} = 9mW$. Only the injection power is varied, and is measured directly in the ring-lasers. The left vertical axis corresponds to the cross correlation C of the bursts, calculated from $B_1(t)$ and $B_2(t)$, Eqn. (7.4). The asterisks indicate the mean values of C for four repeated measurements at a given injection power. Each measurement is 2 seconds long and contains several thousand burst events. To calculate the error bars, we first determine C for $100ms$ time slices. The standard deviation of this set of cross-correlations is calculated and plotted for a given constant injection power. Hence, the error bars represent changes of burst correlation over short time scales – between

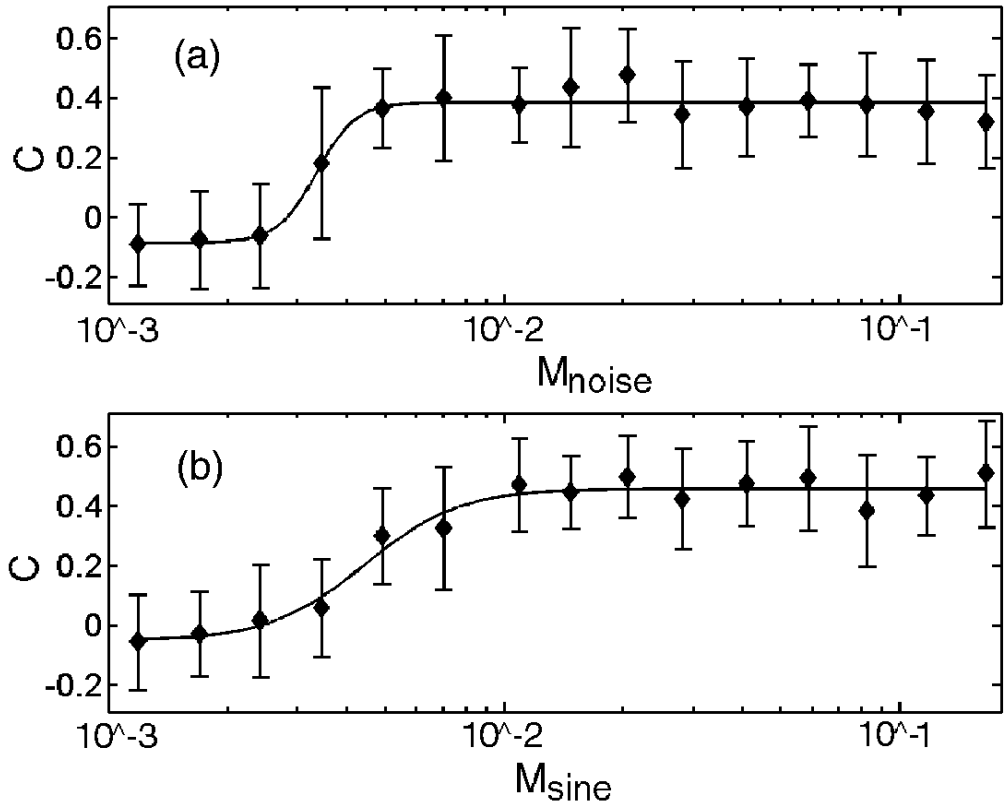

Figure 7.9: Burst synchronization is studied as a function of modulation strength. Both white-noise modulation (a) and sine modulation at $45kHz$ (b) show a significant transition to synchronization with increasing modulation strength. The solid lines are empirical fits to a sigmoidal function. M_{noise} is the ratio of the standard deviation of the noise fluctuations to the average injected power, and M_{sine} is the ratio of the amplitude of the sinusoidal modulation to the average power.

individual $100ms$ time slices within a long measurement – as well as changes between the long 2 second measurements. Therefore, we are able to see clearly that, while the bursts grow substantially with injection power, the mean value of C varies only slightly about zero. The minimum P_{inj}/P_{RL} value corresponds to no injection from the ECSL.

7.5.3 Synchronization with Modulation Strength

Burst synchronization is studied as a function of the modulation strength of the injected power in Fig. 7.9. The effect of an increasing noisy modulation is displayed in

Fig. 7.9(a), and increasing sinusoidal modulation amplitude in Fig. 7.9(b). The noisy modulation strength is measured by the ratio $M_{noise} \equiv \sigma(P_{inj})/\langle P_{inj}\rangle$, and the size of the sinusoidal modulation is given by $M_{sine} \equiv 0.5\big((max(P_{inj}) - min(P_{inj})\big)/\langle P_{inj}\rangle$. The minimal modulation point corresponds to no modulation in both cases. Six consecutive experimental runs, each 2 seconds long, were used to determine the corelation C and its error bars. As above, time slices of $100ms$ from the burst time series were considered in calculating the standard deviations. The mean injected power $\langle P_{inj}\rangle$ and the pumping of the EDFRLs are held constant, such that $\langle P_{RL}\rangle = 9mW$, and $\langle P_{inj}\rangle/\langle P_{RL}\rangle = 3.6 \times 10^{-3}$, the maximum injection reported in Fig. 7.8. The solid lines in both figures represent the χ^2 fit of the observed data points to an empirical sigmoidal function. A transition from uncorrelated bursts (C $\sim$ 0) to significant synchronization (C $\sim$ 0.4) is found to occur at modulation strengths of about 4×10^{-3}.

7.6 Discussion

We have demonstrated that unbiased modulation is sufficient to induce burst synchronization, as well as intermittent phase synchronization in an experimental system of two nearly identical, uncoupled lasers. A clear transition to synchronization was demonstrated for both broad-band noise and sinusoidal modulation. Surprisingly, the noise modulation was as effective as the sinusoidal modulation. While the transition to burst synchronization is clear, the mechanism of synchronization is not. There are no obvious correlations between the modulation signals and the EDFRL intensity time series. The burst synchronization suggests generalized synchronization of the EDFRLs to the modulation signal, as indicated by the auxiliary system method [44].

Chapter 8

Conclusions and Future Research

Ongoing experimental, numerical, and analytic studies of synchronization and chaos in a diverse set of dynamic systems continues to expand our understanding of the physical world, and suggest novel applications of these systems. Of particular interest are the often subtle relationships and synchronous states of coupled chaotic optical systems. In this dissertation we studied the nonlinear dynamics and synchronization, and their underlying physical mechanisms, in two solid state laser systems: Nd^{3+}:YAG laser arrays and optically injected Erbium Doped Fiber Ring Lasers (EDFRL).

8.1 Synchronization of a Linear Nd:YAG Three Laser Array

Experiments investigating the dynamics and synchronization of a linear three-laser array were performed [17]. This was the first investigation of synchronization in a system of more than two lasers. The array is nearest neighbor coupled through overlapping evanescent fields. The low relaxation oscillation frequency of the Nd:YAG lasers allowed for excellent resolution of the array dynamics. Without modulation, the array experienced amplitude instabilities, due to the coupling of the lasers. Soft modulation induced sustained chaotic dynamics, and hard loss modulation resulted in chaotic Q-switched pulses.

Experimental and numerical observations revealed strong synchronization between the pair of outer lasers in the three laser array (1&3), without any clear relationship with the central laser (2). This synchronized state persisted at all modulation levels. Analysis of Eqns. (4.19) showed that the intensity synchronization manifold for the side lasers is stable, and that there is no stable manifold where all three lasers are identically synchronized.

The intensity dynamics of the three lasers were estimated to be five-dimensional using the false nearest neighbor method [3]. This dimension agrees with the amplitude anti-synchronization subspace found in the analysis of Eqns. (4.19). This subspace corresponds to the state where the side lasers are identically synchronized, and the array is phase-locked π out of phase. This is exactly the experimentally observed state, and is confirmed by the far field intensity profile of the laser array.

8.2 Phase Synchronization Entrainment of a Nd:YAG Three Laser Array

There was strong agreement between the numerical and analytic results with experimental observations of identical synchronization between the two side lasers the system. Despite this fact was not fully understood. Since the linear laser array was constructed such that only nearest neighbors were coupled, synchronization of the side lasers must depend on the mediation of the central laser, and we were still left with the question of what dynamical relationship was involved in this dependence. The relationship of a side laser and the central laser is a more general form of synchronization, and so a more subtle analysis of the dynamics was required in order to uncover this relationship.

By defining phase variables from the intensity time series we were able to investigate the relationship of the central and side lasers of the array. The phases were calculated using a Gaussian frequency-filtered complex Gabor analytic signal. This definition of phase for the array elements allowed the discovery of relationships between the lasers that were not otherwise apparent. Additionally, the frequency confined nature of the phase variables, due to the Gaussian filter, allowed investigations of various frequency regimes and ratios of the dynamics of the laser array. We developed a phase synchronization measure, based on a normalized Shannon entropy, that allowed the visualization of a global phase synchronization picture. Phase synchronization was observed in the unmodulated array in several frequency regimes, and along a limited number of frequency ratios, Fig. 5.13. With soft modulation, the magnitude of phase synchronization increased dramatically, the synchronized frequency components shifted, and additional frequency ratios evidenced synchronization, Fig. 5.14. However, hard loss modulation, which resulted in Q-switched intensity time series, suppressed the level of phase synchronization, due to the discontinuous nature of the pulsing dynamics, Fig. 5.15.

Studying phase synchronization allowed relationships in the chaotic linear laser

array that were otherwise obscured to be clearly evidenced. Introducing a Gaussian frequency-filtered phase variable to study nonstationary noisy data is clearly advantageous. This technique, developed as part of this dissertation, should be applicable to a wide range of physical and biological investigations.

Additionally, we studied phase entrainment of the laser array to the sinusoidal modulation signal. Peaks in the intensity time series were used as phase markers. A confined distribution of the discrete phase markers with respect to a reference phase rotating at the modulation frequency indicates phase entrainment. We defined a measure of entrainment using the normalized Shannon entropy, and found entrainment monotonically increased with modulation strength.

8.3 Injection Induced Bursting in an Erbium-Doped Fiber Ring Laser

We observed the surprising phenomena of bursting in an EDFRL due to a weak, frequency-matched optical injection signal. In most systems, a tuned injection signal would stabilize intensity fluctuations. However, instead of constraining the fast, low amplitude fluctuations intrinsic to the EDFRL, the optical injection induced giant intensity bursts, irregularly spaced in time. The bursting dynamics were investigated experimentally and numerically.

The EDFRL output is composed of thousands of longitudinal modes, resulting in the FWHM of $600pm$ observed in Fig. 3.10. Experimental time-resolved heterodyne measurements revealed that the lasing modes of the ring laser slowly wander over a range of MHz, independent of injection, Fig. 6.11. The intermittent interaction of the minimally detuned mode and the monochromatic injected light field lead to brief periods during which the EDFRL locks to the injection laser, after which it escapes the frequency-locking regime. This produces bursts in the intensity time series, Fig. 6.12. Since only this single mode of the ring laser interacted with the

injected field, a phenomenological model of the injected laser system was developed that considered only the minimally detuned mode of the ring laser. The wandering of the EDFRL modes was modeled using exponentially correlated Ornstein-Uhlenbeck noise. Numerical simulations using this model reproduced the critical qualitative and statistical features of the injected ring laser's burst dynamics. Both numerical and experimental intensity time series produced normalized probability distributions displaying power-law decays with a slope of $-3/2$, which is possibly indicative of on-off intermittency.

8.4 Noise Induced Burst Synchronization in Erbium-Doped Fiber Ring Lasers

Beyond examining bursting dynamics induced by a constant optical injection, we also studied the effects of unbiased noise modulation of the injection signal on the bursting dynamics. Specifically, we were addressed a question of great general interest, "Will two dynamically bursting systems subject to a common unbiased noise background synchronize their bursts?" The synchronization of bursting systems is highly relevant to understanding aspects of communication. The research conducted for this dissertation included experiments carefully designed to answer this question quantitatively.

Two nearly identical independent EDFRLs, injected with a common optical injection signal, produced dynamically similar, but uncorrelated bursting dynamics. Modulation of the injection signal using unbiased Gaussian-white noise resulted in a dramatic shift to burst synchronization. While burst synchronization was qualitatively evident, the decaying intensity fluctuations which formed the bursts prevented easy quantitative analysis of the noise induced synchronization. These internal fluctuations were neglected through the definition of a burst envelope from the amplitude of the low-pass frequency-filtered analytic signal, calculated from the bursting

intensity time series. The EDFRL dynamics were reduced to symbolic dynamics by imposing a threshold on the burst envelopes. A synchronization measure was defined using the normalized zero-lag cross-correlation of the symbolic dynamics. Using this synchronization measure to study burst synchronization as a function of modulation strength, a clear transition to synchronization was demonstrated for both broad-band noise and sinusoidal modulation, Fig. 7.9. Surprisingly, the noise modulation was nearly as effective as the sinusoidal modulation. There were no obvious correlations between the modulation signals and the EDFRL intensity time series. The noise induced burst synchronization observed suggests generalized synchronization of the EDFRLs with the modulation signal, as indicated by the auxiliary system method [44].

Despite this dramatic shift to synchronized bursting dynamics with modulation of the optical injection, the qualitative and statistical features of the dynamics were unaffected.

8.5 Continuing and Future Research

8.5.1 EDFRL Mode Dynamics

While we understand that the wandering EDFRL mode interactions with the injected light field result in the bursting dynamics, we have yet to address the origins of the mode wandering itself. The phenomenological Class B injected laser model proposed in Section 6.4 successfully reproduced qualitative and quantitative features of the injected EDFRL bursting dynamics. However, the model did nothing to address the deeper question of the origins of the mode wandering. Possible connections between the fluorescence time $\tau_f = 10ms$ and the slow time scale of the mode wandering need to be addressed, and the contribution of the broad gain region of Er^{3+} doped fiber to the dynamics needs to be understood. Nonlinearities due to the fiber cavity need to be addressed as well. In order to explain these wandering

dynamics it may be necessary to utilize the delay differential model presented in Section 3.5.4, while incorporating the nonlinear effects of the optical fiber cavity and the multimode interactions.

Understanding the origins and dynamics of the observed EDFRL mode wandering may have significant applications to the development of high power fiber laser arrays, while also improving our fundamental understanding of the system. Straightforward methods of constraining the mode dynamics, such as introducing a Faery-Pérot filter to the ring cavity, may be a beneficial line of inquiry.

8.5.2 Identifying the Mechanism of Noise Induced Burst Synchronization in EDFRLs

Improving our understanding of the mode wandering mechanism may also provide insight into the mechanism responsible for noise induced synchronization. As previously stated, experimental heterodyne measurements of the injected EDFRL system have identified longitudinal mode wandering as the source of the bursting dynamics. However, exactly how the modulation of the injection signal leads to the synchronization of the mode wandering, and hence the observed bursting dynamics is still an open question. Preliminary simulations using the simplified Class-B laser model, Eqns. (6.18), with modulation of the E_{inj} parameter alone, have been unable to reproduce the synchronization observed experimentally.

A variety of nonlinear effects intrinsic to the ring laser and the modulation of the injection signal may cooperate to produce the observed burst synchronization. The simple modulation of the injected field amplitude mentioned above produces oscillations in the frequency-locking range that are common to both ring lasers. However, this effect alone is too weak to explain the observed noise induced burst synchronization. An additional weak effect of injection modulation is the resulting modulation of the effective cavity length, nL, due to the optical Kerr effect, Eqn. 3.31. As the cavity length determines the standing wavelengths supported by

the cavity, the modulation of the injection intensity may therefore directly effect the frequency of the modes supported. The range of the optical frequency modulation is written as

$$\Delta\nu_{Kerr} = \frac{mc}{n^2 L}\Delta n, \tag{8.1}$$

where m is the ratio of the cavity length L to the peak wavelength of the laser $\lambda = 1.58\mu m$. The index of refraction of the single mode fiber is $n = 1.44$, and $\Delta n = n_2 \Delta I_{inj}$. The Kerr index $n_2 \approx 3 \times 10^{-}20$, and $\Delta I_{inj} = M_{noise} P_{inj}/\pi a^2$, where $a = 5\mu m$ is the effective radius of single mode optical fiber. With these parameters, the frequency modulation is only $\Delta\nu_{Kerr} \approx 0.1Hz$. Even incorporating the full $30dB$, small signal gain of the erbium doped fiber amplifier $\Delta\nu_{Kerr}$ is only on the order of $100Hz$. This is far too weak to entrain the intrinsic MHz mode wanderings of the EDFRL, but may contribute to the synchronization.

Another possible contributing effect of the modulation is frequency modulation of the optical injection related to the modulation of the injection laser. The lithium niobate electro-optic modulator functions by rotating the polarization of the electric field between two linear polarizers, hence modulating the amplitude of the transmitted field. This phase modulation between the linear polarizers is intrinsically related to frequency modulation [149], which may assist in the synchronization of the EDFRL bursting dynamics. Experimental, numerical, and analytical studies of the degree of frequency modulation, as well as of its effects, are needed.

Contributing synchronization effects may be identified by multimode interactions, such as cross-phase modulation and four wave mixing [62] due to nonlinearities imposed on the system by the fiber optic cavity. Additional effects may be due to the broad gain region of the erbium doped fiber.

8.5.3 EDFRLs With Variable Coupling

A rich coupled laser experiment that will allow us to experimentally investigate the interactions of the wandering modes and synchronization of coupled EDFRLs has been constructed. The experiment, pictured in Fig. 8.1, consists of two nearly iden-

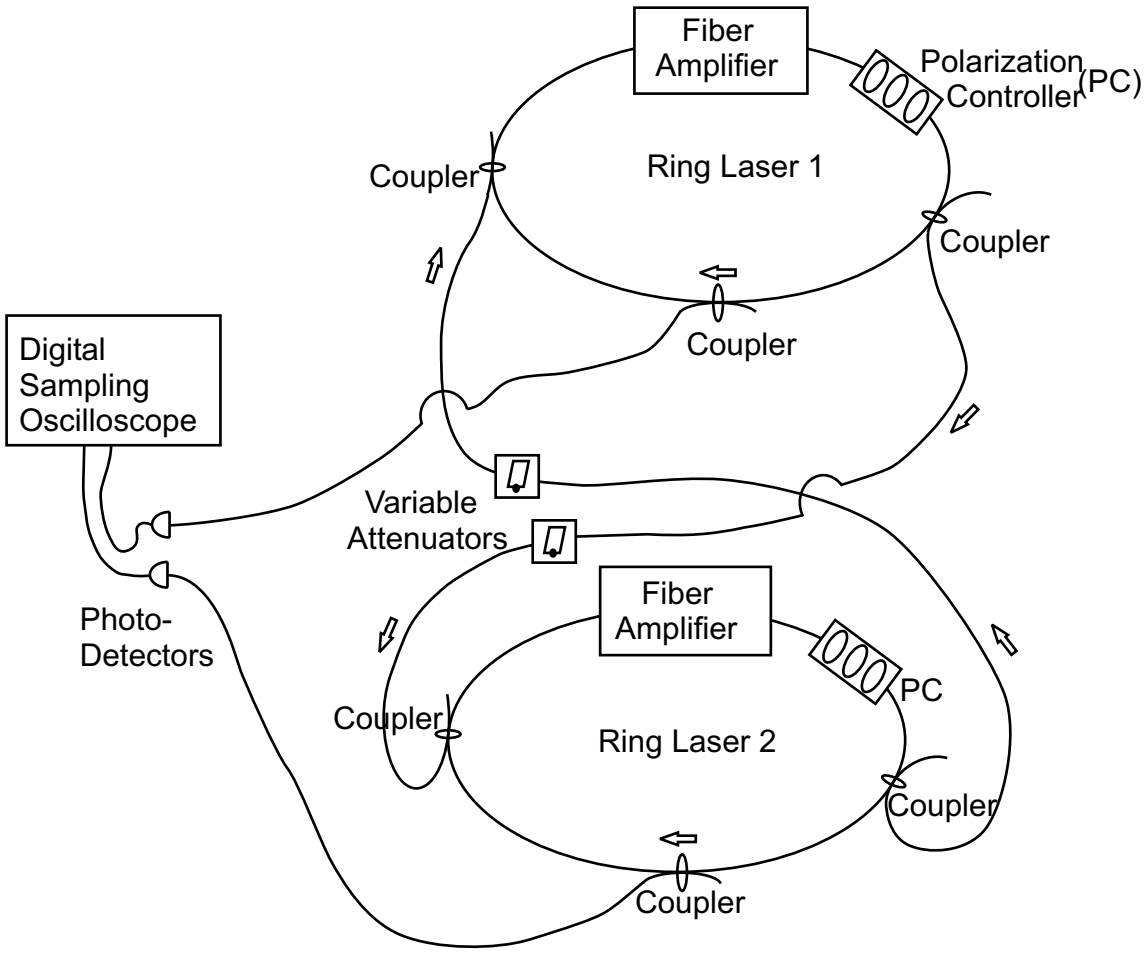

Figure 8.1: Variable coupling EDFRL experiment. The nearly identical fiber ring lasers are coupled through mutual injection. This configuration gives independent control of the two coupling channels, allowing one-way, symmetric and asymmetric coupling and synchronization studies of chaotic systems.

tical ring lasers with coupling through mutual injection. Fiber lengths throughout are carefully matched, and arrows indicate the direction of light propagation. Hopefully, analysis of the mode dynamics of the coupled ring lasers will provide further insight into their origins and behavior.

The variable attenuators in the coupling channels in Fig. 8.1 will allow the experimenter to independently control the proportion of light being injected from one ring laser into the other. Hence, we will be able to investigate unidirectional, symmetric, and asymmetric coupling configurations, as well as the synchronization, if any, that results. In this case, the fast dynamics of the ring lasers are likely

to dominate, and it will be necessary to utilize a delay differential model such as Eqns. (3.45, 3.46, & 3.47) in order to numerically study the dynamics. Introducing electro-optic elements such as phase modulators and electro-optic modulators into the ring cavities will allow experimental investigations of the propagation and communication of perturbations of one ring laser to the other in a variety of coupling configurations.

These experiments will allow for investigation and development of measures of information transfer, and for development of detection algorithms for identifying drive-response relationships in chaotic systems [150, 151, 152]. The results of these studies may prove applicable to studies of complex dynamics systems in which the nature of the coupling between the system elements is unknown, and in which there is only limited experimental control. Such systems are pervasive in chemistry and biology.

BIBLIOGRAPHY

[1] Edward Ott. *Chaos in Dynamical Systems*. Cambridge University Press, Cambridge, 1993.

[2] S.H. Strogatz. *Nonlinear Dynamics and Chaos*. Perseus Books, Cambridge, MA, 1994.

[3] H. D. I. Abarbanel. *Analysis of Observed Chaotic Data*. Springer-Verlag, New York, NY, 1996.

[4] H. Kantz and T. Schreiber. *Nonlinear Time Series Analysis*. Cambridge University Press, Cambridge, 1999.

[5] A.L. Schawlow and C.H. Townes. Infrared and optical masers. *Phys. Rev.*, 112(6):1940–9, 1958.

[6] T.H. Maiman. Stimulated optical radiation in ruby. *Nature*, 187(4736):493–4, 1960.

[7] A. Yariv. *Quantum Electronics*. John Wiley & Sons Inc., New York, 3rd edition, 1967.

[8] M. Born and E. Wolf. *Principles of Optics*. Cambridge University Press, New York, NY, 7th edition, 1999.

[9] R. Loudon. *The Quantum Theory of Light*. Oxford Science Publications, New York, NY, 2nd edition, 1983.

[10] O. Svelto. *Principles of Lasers*. Plenum, New York, 3rd edition, 1989.

[11] H. Haken. *Light. Vol. 2: Laser Light Dynamics*. North Holland Physics Publishing, Amsterdam, 1985.

[12] C.O. Weiss and R. Vilaseca. *Dynamics of Lasers*. VCH, Weinheim, Germany, 1991.

[13] K. Otsuka. *Nonlinear Dynamics in Optical Complex Systems*. KTK, Tokyo, 1999.

[14] G.D. VanWiggeren. *Chaotic Communication with Erbium Doped Fiber Ring Lasers*. PhD thesis, Georgia Institute of Technology, 2000.

[15] L.M. Pecora, T.L. Carroll, G.A. Johnson, D.J. Mar, and J.F. Heagy. Fundamentals of synchronization in chaotic systems, concepts and applications. *Chaos*, 7(4):520–43, 1997.

[16] A.S. Pikovsky, M. Rosenblum, and J. Kurths. Phase synchronization in regular and chaotic systems. *Int. J. Bif. Chaos*, 10(10):2291–305, 2000.

[17] J.R. Terry, K.S. Thornburg, Jr., D.J. DeShazer, G.D. VanWiggeren, S. Zhu, P. Ashwin, and R. Roy. Synchronization of chaos in an array of three lasers. *Phys. Rev. E*, 59(4):4036–43, 1999.

[18] D. J. DeShazer, R. Breban, E. Ott, and R. Roy. Detecting phase synchronization in a chaotic laser array. *Phys. Rev. Lett.*, 87(4):4101–4, 2001.

[19] D. J. DeShazer, R. Breban, E. Ott, and R. Roy. Phase synchronization and entrainment in a driven chaotic laser array. *In preparation*, 2002.

[20] D.J. DeShazer, J. García-Ojalvo, and R. Roy. Bursting dynamics in injected fiber lasers. *Submitted to Phys. Rev. E*, 2002.

[21] D. J. DeShazer, B. P. Tighe, J. Kurths, and R. Roy. Experimental observation of noise-induced burst synchronization. *Submitted Phys. Rev. E Rapid Commun.*, 2002.

[22] E.N. Lorenz. Deterministic nonperiodic flow. *J. Atmos. Sci.*, 20:130, 1963.

[23] O.E. Rössler. Equation for continuous chaos. *Phys. Lett. A*, 57(5):397–8, 1976.

[24] J.-P. Eckmann. Roads to turbulence in dissipative systems. *Rev. Mod. Phys*, 53(4 pt.1):643–54, 1981.

[25] J.P. Gollub and H.L. Swinney. Onset of turbulence in a rotating fluid. *Phys. Rev. Lett.*, 35(14):927–30, 1975.

[26] J. F. Heagy, N. Platt, and S. M. Hammel. Characterization of on-off intermittency. *Phys. Rev. E*, 49(2):1140–50, 1994.

[27] S.C. Venkataramani, T.M. Antonsen, Jr., E. Ott, and J.C. Sommerer. On-off intermittency: Power spectrum and fractal properties of time series. *Physica D*, 96(1-4):66–99, 1996.

[28] M.J. Feigenbaum. Quantitative universality for a class of nonlinear transformations. *J. Stat. Phys.*, 19(1):25–52, 1978.

[29] M.J. Feigenbaum. The universal metric properties of nonlinear transformations. *J. Stat. Phys.*, 21(6):669–706, 1976.

[30] A. Libchaber, C. Laroche, and S. Fauve. Period doubling cascade in mercury; a quantitative measurement. *J. Physique Lett.*, 43:L211, 1982.

[31] F.R. Arecchi and F. Lisi. Hoping mechanism generating 1/f noise in nonlinear systems. *Phys. Rev. Lett.*, 49(2):94–8, 1982.

[32] L.F. Olsen and H. Degn. Chaos in biological systems. *Quart. Rev. Biophys.*, 18:165, 1985.

[33] Y. Pomeau and P. Manneville. Intermittent transition to turbulence in dissipative dynamical systems. *Commun. Math. Phys.*, 74(1):189–97, 1980.

[34] N. Platt, E.A. Spiegel, and C. Tresser. On-off intermittency: A mechanism for bursting. *Phys. Rev. Lett.*, 70(3):279–82, 1993.

[35] T. John, U. Behn, and R. Stannarius. Fundamental scaling laws of on-off intermittency in a stochastically driven dissipative pattern-forming system. *Phys. Rev. E*, 65(04):6229, 2002.

[36] T. Yamada and H. Fujisaka. Stability theory of synchronized motion in coupled-oscillator systems. ii. *Prog. Theor. Phys.*, 70(5):1240–8, 1983.

[37] T. Yamada and H. Fujisaka. Stability theory of synchronized motion in coupled-oscillator systems. iii. *Prog. Theor. Phys.*, 72(5):885–94, 1984.

[38] V.S. Afraimovich, N.N. Verichev, and M.I. Rabinovich. Stochastic synchronization of oscillators in disspative systems. *Inv. VUZ Rasiofiz.*, 29:795–803, 1986.

[39] L.M. Pecora and T.L. Carroll. Synchronization in chaotic systems. *Phys. Rev. Lett.*, 64(8):821–4, 1990.

[40] M.G. Rosenblum, A.S. Pikovsky, and J. Kurths. From phase to lag synchronization in coupled chaotic oscillators. *Phys. Rev. Lett.*, 78(22):4193–6, 1997.

[41] A.S. Pikovsky. *Sov. J. Commun. Electron.*, 30:85, 1985.

[42] E.F. Stone. Frequency entrainment of a phase coherent attractor. *Phys. Lett. A*, 163(5-6):367–74, 1992.

[43] N. F. Rulkov, M. M. Sushchik, L. S. Tsimring, and H. D. I. Abarbanel. Generalized synchronization of chaos in directionally coupled systems. *Phys. Rev. E*, 51(2):980–94, 1995.

[44] H. D. I. Abarbanel, N. F. Rulkov, and M. M. Sushchik. Generalized synchronization of chaos: The auxiliary system approach. *Phys. Rev. E*, 53(5):4528–4535, 1996.

[45] J.D. Jackson. *Classic Electrodynamics*. John Wiley & Sons Inc., New York, 3rd edition, 1998.

[46] E. Merbacher. *Quantum Mechanics*. John Wiley & Sons Inc., New York, 3rd edition, 1998.

[47] G.R. Gray. *Noise in Semiconductor Lasers*. PhD thesis, Georgia Institute of Technology, 1990.

[48] K.S. Thornburg, Jr. *Synchronization of Coupled Solid-State Lasers*. PhD thesis, Georgia Institute of Technology, 1998.

[49] E. Hecht. *Optics*. Addison-Wesley, Reading, Massachusetts, 3rd edition, 1998.

[50] H. Haken. Analogy between higher instabilities in fluids and lasers. *Phys. Lett. A*, 53A(1):77–8, 1975.

[51] C.O. Weiss, W. Klische, P.S. Ering, and M. Cooper. Instabilities and chaos of a single-mode NH_3 ring laser. *Opt. Commun.*, 52(6):405–8, 1985.

[52] F.T. Arecchi, G.L. Lippi, G.P. Puccioni, and J.R. Tredicce. Deterministic chaos in laser with injected signal. *Opt. Commun.*, 51(5):308–14, 1984.

[53] J.E. Geusic, H.M. Marcos, and L.G. Van Uitert. Laser oscillations in Nd-doped yttrium aluminum gallium+gadoinium garnets. *App. Phys. Lett.*, 4(10):182, 1964.

[54] T. Kimura and K. Otsuka. Response of a cw Nd^{3+}:YAG laser to sinusoidal cavity perturbations. *IEEE J. Quant. Electron.*, 6:764–9, 1970.

[55] W. Koechner. *Solid State Laser Engineering*. Springer-Verlag, Berlin, 5th edition, 1999.

[56] L. Fabiny. *Dynamics of a Coupled Solid State Laser Array*. PhD thesis, Georgia Institute of Technology, 1992.

[57] E. Desurvire. *Erbium Doped Fiber Amplifiers: Principles and Applications*. John Wiley & Sons Inc., New York, 1994.

[58] G.P. Agrawal. *Fiber-Optic Communication Systems*. John-Wiley & Sons Inc., New York, 2nd edition, 1997.

[59] Quinton L. Williams. *Fast Temporal Dynamics of the Erbium-Doped Fiber Ring Laser*. PhD thesis, Georgia Institute of Technology, 1996.

[60] G.D. VanWiggeren and R. Roy. Transmission of linearly polarized light through a single-mode fiber with random fluctuations of birefringence. *App. Opt.*, 38(18):3888–92, 1999.

[61] G.P. Agrawal. *Nonlinear Fiber Optics*. Academic Press, San Diego, 2nd edition, 1995.

[62] D.L. Hart. *Nonlinear Dynamics of Multiwave Mixing in an Optical Fiber*. PhD thesis, Georgia Institute of Technology, 1996.

[63] H.D.I. Abarbanel, M.B. Kennel, and C.T. Lewis. Chaotic dynamics in erbium doped fiber ring lasers. *Phys. Rev. A*, 60(3):2360–74, 1999.

[64] Q.L. Williams, J. Garciía-Ojalvo, and R. Roy. Fast intracavity polarization dynamics of an erbium-doped fiber ring laser: Inclusion of stochastic effects. *Phys. Rev. A*, 53(3):2376–86, 1997.

[65] H. E. Haemeier and S. R. Robinson. Field properties of multiple coherently combined lasers. *App. Opt.*, 18(3):270–280, 1979.

[66] N. G. Basov, E. M. Belenov, and V. S. Letokhov. Synchronization of oscillations in a semiconducting laser having several p-n junctions. *Sov. Phys. Solid State*, 7(1):275–276, 1965.

[67] G. G. Basov, E. M. Belenov, and V. S. Letokhov. Diffraction synchronization of lasers. *Sov. Phys. Tech. Phys.*, 10(6):845–850, 1965.

[68] G. D. VanWiggeren and R. Roy. Optical communication with chaotic waveforms. *Phys. Rev. Lett.*, 81(16):3547–3550, 1998.

[69] S. Tang and J.M. Liu. Message encoding decoding at $2.5 Gbits/s$ through synchronization of chaotic pulsing semiconductor lasers. *Opt. Lett.*, 26(2):1843–5, 2001.

[70] L. Fabiny, P. Colet, R. Roy, and D. Lenstra. Coherence and phase dynamics of spatially coupled solid-state lasers. *Phys. Rev. A*, 47(5):4287–96, 1993.

[71] K.S. Thornburg, Jr., M. Möller, R. Roy, T.W. Carr, R.-D. Li, and T. Erneux. Chaos and coherence in coupled lasers. *Phys. Rev. E*, 55(4):3865–9, 1997.

[72] R. Roy and K.S. Thornburg, Jr. Experimental synchronization of chaotic lasers. *Phys. Rev. Lett.*, 72(13):2009–12, 1994.

[73] H.G. Winful and L. Rahman. Synchronized chaos in arrays of coupled lasers. *Phys. Rev. Lett.*, 65(13):1575–8, 1990.

[74] R. Adler. A study of locking phenomena in oscillators. *Proc. IEEE*, 61:1380–5, 1973.

[75] M.K.S. Yeung and S.H. Strogatz. Nonlinear dynamics of a solid state laser with injection. *Phys. Rev. E*, 58(4):4421–35, 1998. erratum, Phys. Rev. E **61**, p. 045207 (2002).

[76] T. Erneux, S.M. Baer, and P. Mandel. Subharmonic bifurcation and bistability of periodic solutions in a periodically modulated laser. *Phys. Rev. A*, 35(3):1165–71, 1987.

[77] I.B. Schwartz. Infinite primary saddle-node bifurcation in periodically forced systems. *Phys. Lett. A*, 126(7):411–8, 1988.

[78] F.T. Arecchi, R. Meucci, G. Pucciono, and J. Tredicce. Experimental evidence of subharmonic bifurcations, multistability and turbulence in a q-switched gas laser. *Phys. Rev. Lett.*, 49(17):1217–20, 1982.

[79] W. Klische, H.R. Telle, and C.O. Weiss. Chaos in a solid state laser with a periodically modulated pump. *Opt. Lett.*, 9(12):561–3, 1984.

[80] Y.C. Chen, H.G. Winful, and J.M. Liu. Subharmonic bifurcations and irregular pulsing behaviour of modulated semiconductor lasers. *App. Phys. Lett.*, 47(3):208–10, 1985.

[81] H.G. Winful, Y.C. Chen, and J.M. Liu. Frequency locking quasiperiodicity and chaos in modulated self-pulsing semiconductor lasers. *App. Phys. Lett.*, 48(10):616–8, 1986.

[82] R.F. Fox, I.R. Gatland, R. Roy, and G. Vemuri. Fast, acccurate algorithm for numerical simulation of exponentially correlated colored noise. *Phys. Rev. A*, 38(11):5938–40, 1988.

[83] M. Oka, H. Masuda, Y. Kaneda, and S. Kubota. Laser diode-pumped phase-locked Nd:YAG laser arrays. *IEEE J. Quant. Electron.*, 28(4):1142–7, 1992.

[84] J.R. Terry. Detuning and symmetry breaking in a system of coupled chaotic lasers. *J. Opt. B*, 1(2):245–50, 1999.

[85] J.R. Tredicce, N.B. Abraham, G.P. Puccioni, and F.T. Arecchi. On chaos in lasers with modulated parameters: A comparitive analysis. *Opt. Commun.*, 53(2):129–32, 1985.

[86] E. Ott, C. Grebogi, and J.A. Yorke. Controlling chaos. *Phys. Rev. Lett.*, 64(11):1196–99, 1990.

[87] R. Roy, T.W. Murphy, Jr., T.D. Maier, and Z. Gills. Dynamical control of a chaotic laser: Experimental stabilization of a globally coupled system. *Phys. Rev. Lett.*, 68(9):1259–62, 1992.

[88] A. Garfinkel, M.L. Spano, W.L. Ditto, and J.N. Weiss. Controlling cardiac chaos. *Science*, 257(5074):1230–5, 1992.

[89] J.N. Weiss, A. Garfinkel, M.L. Spano, and W.L. Ditto. Chaos and control in biology. *J. Clin. Invest.*, 93(4):1355–60, 1994.

[90] J. Buck. Synchronous rhythmic flashing of fireflies, ii. *Quart. Rev. Biol.*, 63(3):265–89, 1988.

[91] F.E. Hanson. Comparative studies of firefly pacemakers. *Fed. Proc.*, 37(8):2158–64, 1988.

[92] A. Pikovsky, M. Zaks, M. Rosenblum, G. Osipov, and J. Kurths. Phase synchronization of chaotic oscillations in terms of periodic orbits. *Chaos*, 7(4):680–7, 1997.

[93] M.A. Zaks, E.H. Park, M.G. Rosenblum, and J. Kurths. Alternating locking ratios in imperfect phase synchronization. *Phys. Rev. Lett.*, 80(21):4228–31, 1999.

[94] E.H. Park, M.A. Zaks, and J. Kurths. Phase synchronization in the forced Lorenz system. *Phys. Rev. E*, 60(6):6627–38, 1999.

[95] F.T. Arecchi, R. Meucci, and W. Gadomski. Laser dynamics with competing instabilities. *Phys. Rev. Lett.*, 85(21):2205–8, 1987.

[96] E. Allaria, F. T. Arecchi, A. Di Garbo, and R. Meucci. Synchronization of homoclinic chaos. *Phys. Rev. Lett.*, 86(5):791–4, 2001.

[97] M. G. Rosenblum, A. S. Pikovsky, and J. Kurths. Phase synchronization of chaotic oscillators. *Phys. Rev. Lett.*, 76(11):1804–7, 1996.

[98] P. Tass, M.G. Rosenblum, J. Weule, J. Kurths, A.S. Pikovsky, J. Volkmann, A. Schnitzler, and H.-J. Freund. Detection of n:m phase locking from noisy data: Application to magnetoencephalography. *Phys. Rev. Lett.*, 81(15):3291–4, 1998.

[99] C.M. Ticos, E. Rosa, Jr., W.B. Pardo, J.A. Walkenstein, and M. Monti. Experimental real-time phase synchronization of a paced chaotic plasma discharge. *Phys. Rev. Lett.*, 85(14):2929–32, 2000.

[100] I. Wallace, D. Yu, W. Lu, and R.G. Harrison. Synchronization of power drop outs in coupled semiconductor lasers with external feedback. *Phys. Rev. A*, 63(1):013809/1–5, 2001.

[101] D. Gabor. Theory of communication. *J. IEEE London*, 93:429, 1946.

[102] R.B. Larson and B.M. Tinsley. Star formation rates in normal and peculiar galaxies. *AstroPhys. J.*, 219(1):46–59, 1978.

[103] M.-H. Ulrich, L. Maraschi, and C.M. Urry. Variability of active galactic nuclei. *Ann. Rev. Aston. & Astrophys.*, 35:445–502, 1997.

[104] R.C. Elson, A.I. Selverston, R. Huerta, N.F. Rulkov, M.I. Rabinovich, and H.D.I. Abarbanel. Synchronous behavior of two coupled biological neurons. *Phys. Rev. Lett.*, 81(25):5692–5, 1998.

[105] J.R. Tredicce, F.T. Arecchi, G.L. Lippi, and G.P. Puccioni. Instabilities in lasers with an injected signal. *J. Opt. Soc. Am. B*, 2(1):173–83, 1985.

[106] J.L. Boulnois, A. Van Lerberghe, P. Cottin, F.T. Arecchi, and G.P. Puccioni. Self pulsing in a CO_2 ring laser with an injected signal. *Opt. Commun.*, 58(2):124–9, 1986.

[107] E.M. Izhikevich. Synchronization of elliptic bursters. *SIAM Rev.*, 43(2):315–44, 2001.

[108] F.C. Hoppenstead and E.M. Izhikevich. *Weakly Connected Neural Networks*. Springer, New York, NY, 1997.

[109] M.B. Spencer and W.E. Lamb, Jr. Laser with a transmitting window. *Phys. Rev. A*, 5:884, 1972.

[110] R. Lang. Injection locking properties of a semiconductor laser. *IEEE J. Quant. Electron.*, 18(6):976–983, 1982.

[111] W.H. Chung, L.Y. Chan, H.Y. Tam, P.K.A. Wai, and M.S. Demokan. Output polarization control of fiber DFB laser using injection locking. *IEEE Photon. Tech. Lett.*, 14(7):920–2, 2002.

[112] D.G. Slavov and M.N. Nenchev. A comparative study of approaches for spectral control of Ti:saphire pulsed lasers. *Opt. Commun.*, 200(1-6):283–301, 2001.

[113] C.O. Weiss, E. Bava, A. deMarchi, and A. Godone. Injection locking of an optically pumped FIR laser. *IEEE J. Quant. Electron.*, 16(5):498–9, 1980.

[114] Y. Braiman, T.A.B. Kennedy, K. Wiesenfeld, and A. Khibnik. Entrainment of solid-state laser arrays. *Phys. Rev. A*, 52(2):1500–6, 1995.

[115] E.G. Lariontsev, I. Zolotoverkh, P. Besnard, and G.M. Stéphan. Injection locking properies of a microchip laser. *Euro. Phys. J. D*, 5(1):107–17, 1999.

[116] B. Krauskopf, W.A. van der Graaf, and D. Lenstra. Bifurcations of relaxation oscillations in an optically injected diode laser. *Quant. Semiclass. Opt.*, 9(5):797–809, 1997.

[117] S. Wieczorek, B. Krauskopf, and D. Lenstra. A unifying view of bifurcations in a semiconductor laser subject to optical injection. *Opt. Commun.*, 172(1-6):279–95, 1999.

[118] B. Krauskopf and S. Wieczorek. preprint. 2002.

[119] T.B. Simpson. Phase-locked microwave-frequency modulations in optically-injected laser diodes. *Opt. Commun.*, 170(1-3):93–8, 1999.

[120] S. Wieczorek, T.B. Simpson, B. Krauskopf, and D. Lenstra. Global quantitative predictions of complex laser dynamics. *Phys. Rev. E*, 65(4):045207/1–4, 2002.

[121] T.B. Simpson and J.M. Liu. Phase and amplitude characteristics of nearly degenerate four-wave mixing in Fabry-Perot semiconductor lasers. *J. App. Phys.*, 73(5):2587–9, 1993.

[122] Photonetics, Versailles. *Tunics-BT, Wavelength Tunable Laser Diode Source; User's Guide*, February 1998.

[123] G.D. VanWiggeren and R. Roy. Communication with dynamically fluctuating state of light polarization. *Phys. Rev. Lett.*, 88(9):0979036/1–4, 2002.

[124] G.D. VanWiggeren and R. Roy. Transimission of linearly polarized light through a single-mode fiber with random fluctuations in birefringence. *Appl. Opt. LP*, 38(18):3888–92, 1999.

[125] Amos Maritan and Jayonth R. Banavar. Chaos, noise, and synchronization. *Phys. Rev. Lett.*, 72(10):1451–54, 1994.

[126] Arkady S. Pikovsky. comment on 'Chaos, noise, and synchronization'. *Phys. Rev. Lett*, 73(21):2931, 1994.

[127] L. Longa, E.M.F. Curado, and F.A. Oliveira. Round-off induced coalescence of chaotic trajectories. *Phys. Rev. E*, 54(3):R2201–R2204, 1996.

[128] E. Sanchez, M.A. Mathias, and V. Perez-Munuzuri. Analysis of synchronization of chaotic systems by noise: An experimental study. *Phys. Rev. E.*, 56(4):4068–71, 1997.

[129] C.-H. Lai and C.S. Zhou. Synchronization of chaotic maps by symmetric common noise. *Europhys. Lett.*, 43(4):376–380, 1998.

[130] C.S. Zhou and J. Kurths. Noise-induced phase synchronization and synchronization transitions in chaotic oscillators. *Phys. Rev. Lett*, 88(23):230602/1–4, 2002.

[131] J.M.R. Parrondo, C. van den Broeck, J. Buceta, and F.J. el la Rubia. Noise-induced spatial patterns. *Physica A*, 224(1-2):153–61, 1996.

[132] R. Benzi, A. Sutera, and A. Vulpiani. The mechanism of stochastic resonance. *J. Phys. A*, 14(11):L453–L457, 1981.

[133] B. McNamara, K. Wiesenfeld, and R. Roy. Observation of stochastic resonance in a ring laser. *Phys. Rev. Lett*, 60(25):2626–9, 1988.

[134] L. Gammaitoni, P. Hanggi, P. Jung, and R. Marchesoni. Stochastic resonance. *Rev. Mod. Phys.*, 70(1):223–87, 1998.

[135] A.A. Zaikin, J. Kurths, and L. Schimansky-Geier. Doubly stochastic resonance. *Phys. Rev. Lett.*, 85(2):227–231, 2000.

[136] K. Matsumoto and I. Tsuda. Noise-induced order. *J. Stat. Phys.*, 31(1):87–106, 1983.

[137] H. P. Herzel and W. Ebeling. The decay of correlations in chaotic maps. *Phys.Lett. A*, 111:1, 1985.

[138] L. Yu, E. Ott, and Q. Chen. Transition to chaos for random dynamical systems. *Phys. Rev. Lett.*, 65(24):2935–8, 1990.

[139] H. P. Herzel and J. Freund. Chaos, noise and synchronization reconsidered. *Phys. Rev. E*, 52(3):3238–41, 1995.

[140] G. Malescio. Noise and synchronization in chaotic systems. *Phys. Rev. E*, 53(6):6551–4, 1996.

[141] P. M. Gade and C. Basu. The origin of non-chaotic behavior in identically driven systems. *Phys. Lett. A*, 217(1):21–27, 1996.

[142] R. Toral, C. R. Mirasso, E. Hernandez-Garcia, and O. Piro. Analytical and numerical studies of noise-induced synchronization of chaotic systems. *Chaos*, 11(3):665–73, 2001.

[143] L. Baroni, R. Livi, and A. Torcini. Transition to stochastic synchronization in spatially extended systems. *Phys. Rev. E*, 63(3):6226, 2001.

[144] G. Baier, G. J. Escalera Santos, J. Perales, M. Rivera, M. Müller, R. Leder, and P. Parmananda. Self-exciting chaos as a dynamic model for irregular neural spiking. *Phys. Rev. E*, 62(6):R7579–R7582, 2000.

[145] L. Kocarev and U. Parlitz. Generalized synchronization, predictability, and equivalence of unidirectionally coupled dynamical systems. *Phys. Rev. Lett.*, 76(11):1816–9, 1996.

[146] D. Y. Tang, R. Dykstra, M. W. Hamilton, and N. R. Heckenberg. Observation of generalized synchronization of chaos in a driven chaotic system. *Phys. Rev. E*, 57(5):5247–51, 1998.

[147] M. A. Zaks, E.-H. Park, M. G. Rosenblum, and J. Kurths. Alternating locking ratios in imperfect phase synchronization. *Phys. Rev. Lett.*, 82(21):4228–31, 1999.

[148] A. Papoulis. *Probability, Random Variables and Stochastic Processes*. McGraw-Hill, New York, NY, 3rd edition, 1991.

[149] D.S. Elliott, R. Roy, and S.J. Smith. Extracavity laser band-shape and bandwidth modification. *Phys. Rev. A*, 26(1):12–18, 1982.

[150] L.M. Pecora and T.L. Carroll. Detecting chaotic drive-response geometry in generalized synchronization. *Int. J. Bif. Chaos*, 10(4):875–89, 2000.

[151] R.Q. Quiroga, J. Arnhold, and P. Grassberger. Learning driver-response relationships from synchronization patterns. *Phys. Rev. E*, 61(5):5142–8, 2000.

[152] T. Schreiber. Measuring information transfer. *Phys. Rev. Lett.*, 85(2):461–4, 2000.